UNIVERSITA' DEGLI STUDI DI NAPOLI "FEDERICO II"

DIPARTIMENTO DI INGEGNERIA CHIMICA, DEI MATERIALI E DELLA PRODUZIONE INDUSTRIALE

DOTTORATO IN INGEGNERIA DEI PRODOTTI E DEI PROCESSI INDUSTRIALI
XXXIII CICLO

INNOVATIVE COMPOSITE MATERIALS WITH HIGH GRAPHENE CONTENT

DOTTORATO INNOVATIVO CON CARATTERIZZAZIONE INDUSTRIALE
XXXIII CICLO

Ph.D. Thesis

Fabrizia Cilento

Tutors:
Prof. Ing. Giuseppe Mensitieri
Prof. Ing. Michele Giordano
Dott. Ing. Alfonso Martone
Coordinatore
Prof. Ing. Andrea D'Anna

May 2021

ABSTRACT

Nanocomposites based on the biomimetic brick and mortar architecture are gathering great attention recently due to the outstanding properties of the natural analogues. Thanks to the very high in-plane orientation of nanoplatelets and the low matrix content, these materials exhibit good mechanical performance combined with excellent functional properties based on the nanoplatelets characteristics. Key feature of these materials is the presence of a regular nanostructure that consists of alternated nanoplatelet and matrix layers.

This thesis addresses the study of mechanical and functional properties of nacre-like composite materials based on graphite nanoplatelets (GNPs). Particular attention is devoted to providing an insight into stress transfer mechanism in high filler content composites and describing the parameters that influence the efficiency of stress transfer. GNPs have been chosen as filler thanks to the good combination of mechanical, thermal and electrical properties, and the very low cost. This would allow the mass production of graphene-based material with remarkable properties that could give a breakthrough in the materials field and industrial applications. In particular, nacre-like GNPs/Epoxy thin films at different filler content have been prepared by a top-down manufacturing technology and their mechanical properties in tension have been experimentally evaluated. The elastic modulus has been found to exhibit a maximum of ~15 GPa between 53-67 vol% filler content and then it starts dropping at higher loadings. This is attributed to a discontinuous polymeric matrix layer, and thus to an incomplete GNP surface coverage at high filler content. As a result, the effective area for stress-

I

transfer is considerably reduced at the expense of the reinforcement efficiency. To better understand the quality of stress transfer between the two phases, a microscopic investigation has been carried out by micro Raman spectroscopy, highlighting the poor stress transfer between the two phases at high filler content. In the light of this, a model is proposed for predicting the stress transfer characteristics in brick-and-mortar systems by paying attention to possible non-uniform matrix distribution over the nanoplatelets. It has been observed that at relatively high filler content, the elastic modulus of these systems drops after a critical concentration deviating from the expected behaviour, which dictates that the higher the filler content the higher the macroscopic elastic modulus. Thus, understanding the mechanism at the base of stress transfer in composite with brick and mortar architecture is of great importance and allows the definition of design strategies for the optimization of the mechanical properties of this class of material. The proposed analysis captures well the observed effects and paves the way for the development and further improvement of this new class of engineering materials.

The material architecture of GNPs based films also contribute to the excellent thermal end electrical conductivity of the material. Also, the high anisotropy between in plane and cross-plane conductivities of GNPs is reproduced at the macroscale by the thin films. In fact, at 70 vol%, GNPs/Epoxy films exhibit in plane and cross plane thermal conductivities of 216 W/mK and 8 W/mK respectively and sheet resistance of 0.33 Ω/sq. This makes the material an excellent shield for high radiative heat flux and electromagnetic waves. Therefore, these exceptional multifunctional properties and the good structural performances of GNP/Epoxy films, can be exploited to improve those of FRP. They can be easily integrated into fibre reinforced polymers (FRP), without adding any additional steps in the fabrication process, and without compromising the weight and mechanical performances of the material. In this thesis, it has been investigated the possibility of improving fire resistance of composites by integrating on their surface protective coatings. Graphene rich films have been bonded on the heat-exposed surface of Carbon Fibres Reinforced Plastic (CFRP) laminates observing a significant reduction of the temperatures on the heated surface and of the damaged area when exposed to high power radiative heat fluxes. The behaviour of CFRP composite has also been assessed through cone calorimeter test and the effect of graphene films protection has been investigated. In addition, the reaction of CFRP composite to high power radiative heat flux have been further investigated by laser spot heating. The effect of the protective layer thickness has been tested with different laser power (25, 50, 75, 100, 150 kW/m^2), simulating standard testing conditions

(AC 20-135 and ISO 5660-1 Standards). Finally, damage level and residual mechanical of exposed samples have been assessed as a function of the level of protection. A significant improvement of the post-heat flexural moduli and a significant reduction of the damaged areas have been obtained in graphene films protected laminates.

ACKNOWLEDGEMENTS

«ἐὰν μὴ ἔλπηθαι ἀνέλπιστον οὐκ
ἐξευρήσει, ἀνεξερεύνητον ἐὸν
καὶ ἄπορον»

«Se l'uomo non spera l'insperabile
non lo troverà
perché esso è introvabile ed inaccessibile»

Eraclito, Frammento B18

CONTENTS

LIST OF FIGURES

LIST OF TABLES

1. MIMICKING NATURE: NACRE-INSPIRED MATERIALS

1.1 Introduction

Recently, innovative materials inspired from nature have raised huge interest thanks to their remarkable mechanical properties and impressive performance [1]. Their hierarchical and well-organized structure provides interesting structural properties. In particular a great deal of attention is paid to composite materials consisting of 95 vol% of inorganic filler and 5 %vol of organic binder, such as nacre and mollusc shell [2–4]. Actually, the material architecture at high filler content involves complex deformation mechanisms: the coexistence of a soft-domain (mortar) and a hard domain (bricks) affects the molecular mobility leading to an increase of ductility and energy dissipation. Moreover, the well-oriented microstructure and the low matrix content in brick-and-mortar materials ensure also other functionalities, such as gas barrier characteristics and good electrical and thermal conductivities, at reduced weight. The combination or structural and multi-functional properties makes this class of materials promising for several industrial applications.

1.2   Overview of hierarchical structure of nacre

In the last decades, many researchers have shown a huge interest in biomimetic materials. These are innovative materials inspired from nature, which have interesting structural proprieties and are organized in a hierarchical structure.

Among all biomimetic materials, nacre has drawn great attention of the scientific community, thanks to superior levels of strength and toughness and its brick-and-mortar (B&M) architecture. Nacre is the iridescent inner shell layer of many species of seashells from the gastropods and bivalves groups. It consists of a 3D assembly of hard lamellar aragonite ($CaCO_3$) tablets glued together with a low amount (5 vol%) of soft organic materials (proteins and polysaccharides). This hierarchical organized microstructure and the small fraction of biopolymers are responsible for the unique mechanical behaviour. In addition, the mineral bridges that connect the different tiles at nanoscale level are capable of preventing crack extension and provide toughness and impact resistance [3,4]. Although nacre is composed by fragile material, it exhibits a ductile behaviour, allowing plastic deformations and exhibiting high toughness, which is three order of magnitude higher than its main constituents.

Nacre consists of a brick-and-mortar like (B&M) structure, in which hard aragonite tablets are glued together with soft organic materials to form tiles. Lamellar micro-architectures of hard composite tiles with soft organic layers in between prevent crack deflection and ensure slip in order to provide toughness and impact resistance [3][4]. Therefore, the shells of molluscs offer a perfect example of a lightweight, tough armour system. It denotes how species have adapted to the external environment among years, turning brittle minerals into much tougher materials, capable to protect themselves from external agents.

From the engineering point of view, the exceptional behaviour of the material is given by the complex hierarchical structure, organized over several length scales: from macroscale to nanoscale.

1. *Macroscale* (Figure 1.1a). At the macroscale, the shell is composed by three main layers: the outer layer (periostractum) composed of hardened protein is brittle and hard and provides resistance to penetration from external impact; the middle layer (prismatic) is composed of columnar calcite; the inner layer (nacre) composed by aragonite and organic material provides toughening, by allowing the dissipation of the mechanical energy [1].
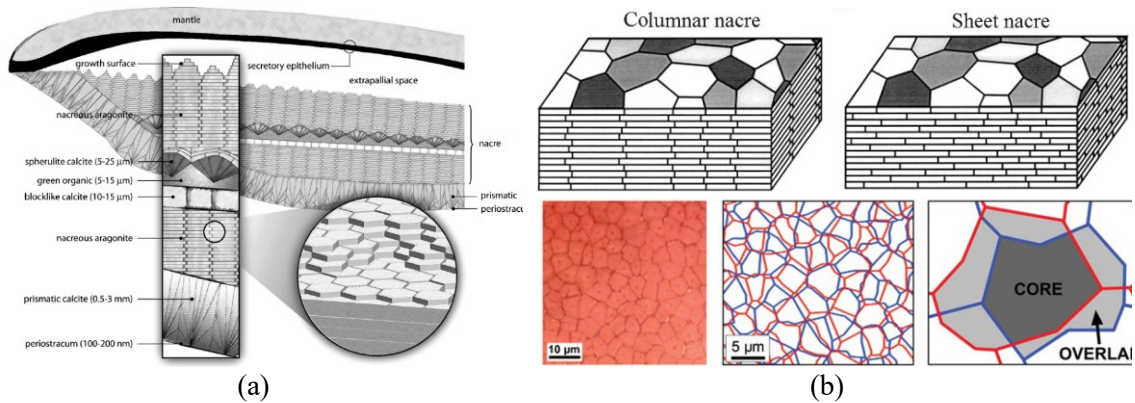
Figure 1.1. Hierarchical structure of red abalone nacre at macroscale (a) and microscale (b) [3]

2. *Mesoscale*. At this level some hardening mechanisms take place. The surfaces of the tablets are rough with many nano asperities, forcing bricks to climb obstacles in order to slide on one another. Either in tension or shear, strain hardening is the key to large deformation and is essential for the remarkable mechanical performance of nacre. In addition, the organic material at the interface have to maintain strong adhesion with the bricks, also over long sliding distances [4].

3. *Microscale* (Figure 1.1b). It is represented by the 3D brick and mortar architecture where the bricks are the aragonite polygonal grains held together by biopolymers matrix. There are two structures of nacre: columnar nacre or sheet nacre, depending on the stacking mode of the tablets.

   In the columnar nacre platelets are stacked in columns such as it is possible to identify a core and overlap regions, while in the sheet nacre platelets are stacked in a more random arrangement without well-defined core and overlap regions. In both configurations, the bricks are perfectly oriented in plane direction.

   Generally, columnar nacre is found in *gastropods*, whereas sheet nacre occurs more in *bivalves*. In columnar nacre, viewed from the top, the polygonal tablets form neighbouring layers overlap in such a manner that the inter-tablet boundaries form tessellated bands perpendicular to the lamellae boundaries, shown in Figure 1.1b. While in sheet nacre, the inter-tablet boundaries are distributed randomly. The overlap region in columnar nacre covers around 1/3 of the area of a tablet, whereas in sheet nacre no distinction can be made between the core and overlap areas [3,5]. The distinction between these two regions is important as they experience significantly different stress states. The tablets in nacre are often described and modelled as being flat on the microscale; it was actually observed that

the interfaces between the tablets show significant waviness, contributing to energy dissipation [5].

4. *Nanoscale*. In both nacre types there are mineral bridges connecting different tiles. These bridges, which protrude through the organic matrix, not only allows continued mineralization on the organic layers, but also improve their mechanical properties and prevent crack extension of nacre [3].

During the growth of the shells, the prismatic layer is deposited first, and the nacreous layer is added as the shell thickness increases with time. Successive nucleation of aragonite crystals gives birth to the aragonite component of the composite. The formation process differs in columnar nacre and sheet nacre; in the first tablets grow following a "Christmas-tree pattern" [6,7], while in the second tablets grow forming lower tower (Figure 1.2).

(a)   (b)
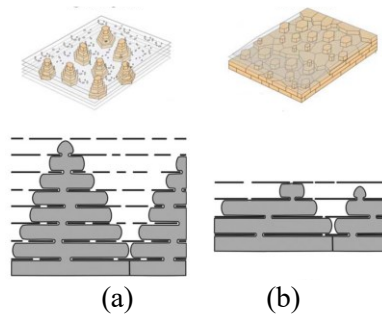
Figure 1.2 Formation process in columnar nacre (a) and sheet nacre (b) [3]

1.2.1 Mechanical properties and fracture mechanisms

Due to its structure, nacre behaves differently according to the direction of the applied compressive or tensile load. In general, nacre's compressive strength is higher when the load is applied perpendicular to the tiles, while tensile strength is higher when loaded parallel to the tiles [3]. Compressive strengths are also generally higher than tensile strength in both parallel and perpendicular directions. These results were obtained by Barthelat et al. [5], who performed tests on sample cubes of 5 mm sides. These tests were done under two different conditions: dry (ambient condition) and hydrates (soaked in water).

(a)   (b)
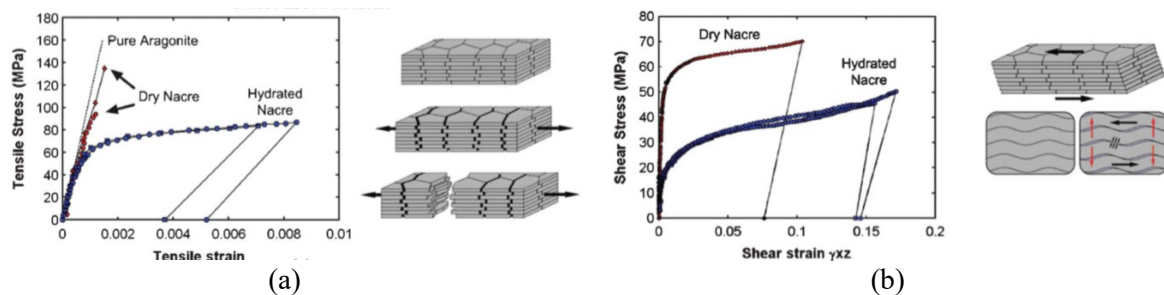
Figure 1.3. Tensile (a) and shear (b) stress-strain curves for nacre in red abalone [3,5]

Figure 1.3 shows the behaviour of nacre under tensile and shear stress. Nacre behaves differently when under dry or hydrated conditions. In Figure 1.3a there is a comparison of stress-strain behaviour of pure aragonite, dry nacre and hydrated nacre. The behaviour of dry nacre is similar to that of pure aragonite, which exhibits a brittle failure. On the other hand, hydrated nacre exhibits a ductile failure with an initial linear response, similar to dry nacre, followed by a region of larger inelastic strain, starting from a stress of 70 MPa. This points out not only the importance of water for the ductile behaviour of nacre, but also the relevance of the organic matrix. Even though it represents only 5% of its composition, it is responsible for the high toughness of nacre.

Also shear test highlighted the influence of water on shear modulus and shear strength. The behaviour of both hydrated and dry nacre in shear is reported in Figure 1.3b. It shows that the mechanical properties of nacre reduce in case of hydrated nacre, with respect to dry nacre.

Nacre behaviour at nanoscale is described through nanoindentation test [8]. The elastic modulus of tiles is between 60 and 80 GPa, which is similar to the one of pure aragonite (81 GPa), while the elastic modulus of the organic matrix is between 2.85 and 15 GPa. From the test, it also appears the viscoelastic nature of nacre, which is subjected to plastic deformations and pile-ups. Figure 1.3a also shows the deformation of nacre sample during tensile test. In particular, when the stress reaches 70 MPa the organic matrix yields and the tablets locally slides on one another, until nacre fractures as tablet pull-out mode.

Wang et al. [9] proposed a model to describe two different fracture mechanisms based on the aspect ratio of the platelets. In particular, they defined a critical value of the aspect ratio:

$$s_c = \frac{\sigma_p}{\tau_y} \tag{1.1}$$

If the actual aspect ratio, is greater than the critical one ($s>s_c$), fragile fracture is dominant and the platelet fracture occurs, while if $s<s_c$ the platelets starts sliding one on the another until they are pulled out from the soft matrix (Figure 1.4).
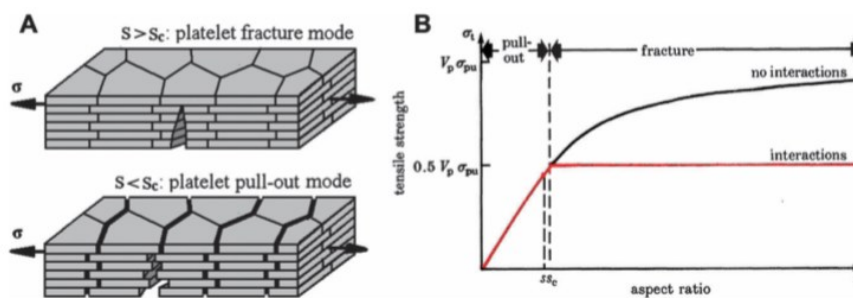
Figure 1.4. Fracture mechanisms [9]

1.2.2 Inter-tile toughening mechanism

The peculiarity of nacre is its high toughness, which is three order of magnitude higher than its main constituents. The high toughness of nacre is related to different mechanisms: (i) nanoasperities of the aragonites tiles; (ii) organic layer acting as viscoelastic glue after the elongation of biopolymer; (iii) mineral bridge relocking after fracture; (iv) tile interlock due to the microscale waviness and dovetail of tiles.
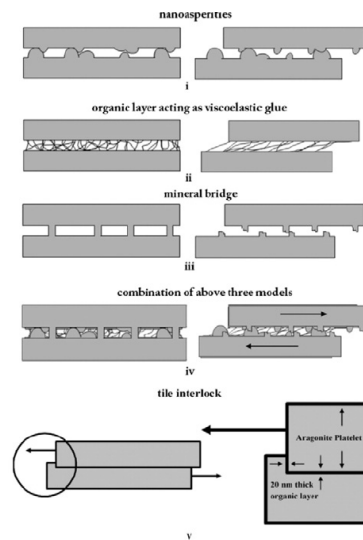
Figure 1.5. Different model for sliding between tiles [6]

Mechanisms (i) and (iii) make the sliding of contiguous tiles more difficult and increase friction; in fact, they are responsible for shear resistance. Whereas the stretching of biopolymers fibrils is responsible for the load transfer across nacre's structure, in fact the polymeric layers acting as a strong adhesive, increases the tensile strength of the composite. Another mechanism which contribute to nacre high toughness is the incremental thickness of tiles near the edges with a shape similar to a dovetail [3]; in this way, when tiles are pulled their sliding is limited because they locks. All these mechanisms allow inelastic deformation, contributing to the enhancing of the nacre toughness.

In substance, nacre represents a perfect example of the evolution of species over millions of years, where animals had to adapt to the external environment. The highly sophisticated microstructure ensures optimal performance, such that it inspires the design of the next generation of synthetic composites material. It follows, the interest in material engineering to mimic nacre's architecture, with the purpose of fabricating nacre-like materials with exceptional structural and functional properties.

1.3 Biomimetic materials

Synthetic materials, inspired by the complex structure of nacre, gave rise to a new trend in biomimetic materials, which includes several nanoparticles and polymers, different fabrication methods and design strategies, with the sole purpose of producing a novel material which combines the good mechanical properties with other functionalities.

In particular, paper-like structures have been widely investigated. They are composites with high content of lamellar nanofillers, organized in a well-oriented microstructure and bonded with low amount of polymer. Their structure, which resembles the brick-and-mortar architecture of nacre, is able to reproduce at the macroscale the behaviour of the nanoscale reinforcement, also ensuring other functionalities, such as good electrical and thermal conductivities, and gas and vapour barrier characteristics at reduced weight. Such behaviour makes this class of materials promising for several applications, such as protective coatings for fire-resistance, thermal interface materials (TIM), EMI shielding, lightning strike protection, heat spreader and thermal barrier [10,11].

Among 2D nanoplatelets, graphene represents the most promising candidate as filler, due to its exceptional combination of physical properties [12]. Actually, graphene is the strongest material ever produced exhibiting a tensile strength of 130 GPa and a Young's modulus of 1 TPa [13,14], and shows excellent thermal [15,16] and electrical properties [17]. In light of that, graphene and its related materials have widely been adopted for the fabrication of nacre-like materials [18–27].

For instance, graphene oxide (GO) [18,19] and reduced graphene oxide (rGO) [20,21] graphite nanoplatelets (GNPs) [22] [23], but also ceramic brick, such as montmorillonite (MTM) [28], alumina [29], boron nitride [30] have been employed as nanofillers, combined with a broad variety of polymers, both thermoset and thermoplastic. The common parameters are the well-aligned microstructure and the high filler content (>50 vol%).

In order to reproduce a material with such behaviour at very high filler content, given the low amount of polymer, an exact control of the structural organization (both vertical and lateral) of the two phases should be ensured. Both bottom-up and top-down technologies have been employed, the first are more able to fine-tune the nanometric alternance of the two phases [31] but remain mostly confined to the lab, while the second are more suitable for an industrial scale-up, but still ensuring a well-aligned architecture.

Design strategies [32–34] and models [35–37] to predict the elastic modulus and strength of brick and mortar composites have also been proposed for nacre-like architectures. These

models assume perfect bonding between the two phases and efficient load transfer to the particles, and that the matrix consists of a uniform and continuous layer between the nanoplatelets. Under these assumptions, the strength and the elastic modulus of the composites increase with the amount of filler, reaching the best performance, equal to those of the reinforcement, at very high filler content (90-95 wt%). Modelling the mechanical behaviour of the material, enable to better understand the complex mechanism at the base and to establish a design process, aimed to optimize the mechanical properties of the composites.

1.4   Aim of the thesis

The PhD programme is part of the project "Dottorati innovativi-PON Ricerca e Innovazione 2014-2020" supported by MIUR. This activity has been carried out in collaboration with NANESA (Arezzo), a company that produce graphene-based nanomaterials and with professor Galiotis of Department of Chemical Engineering of University of Patras, and the FORTH/ICEHT institute (Greece).

The aim of this thesis is to fabricate composites with *laminated nano-biomimetic architecture* capable of retaining at the macroscale the structural and functional properties of its main constituent. Graphite nanoplatelets (GNPs) have been chosen as filler thanks to the good combination of mechanical, thermal and electrical properties, and the very low cost. This would allow the mass production of graphene-based material with remarkable properties that could give a breakthrough in the materials field and industrial applications.

However, the main challenge is to obtain a material, which dissipate energy with localized plastic deformations, without experiencing global failure. In fact, as described before, nacre toughening behaviour is associated with several mechanisms, which are difficult to reproduce in synthetic composite materials. The material architecture involves complex deformation mechanisms, which underline a novel composites concept. Particular attention must be focused on the nature of the matrix, because it can affect not only the composite behaviour, but also the interface and so the stress transfer between the two phases. In fact, a very strong interface, although allows efficient stress transfer, enable crack propagation through the nanolaminate, decreasing the toughness. On the contrary, a weak interface improves the fracture toughness.

For this purpose, an accurate critical analysis of literature data has been conducted in Chapter 2, providing an insight into stress transfer mechanism in high filler content composites and describing the parameters that influence the efficiency of stress transfer and the strategies to improve it. In fact, the mechanical response of brick-and-mortar materials is influenced by

many factors, such as the filler content, the matrix molecular mobility and the compatibility between the two phases, in terms of interaction at atomic level.

According to this, in Chapter 3 the mechanical response of composites with high graphite nanoplatelets (GNPs) content have been investigated. First, a set up procedure for the production of films with high lamellar filler content has been assessed, following a top-down approach, then the material has been widely characterized through experimental investigations. Morphological analyses have been conducted in order to assess the resin distribution within nanoplatelets, using Scanning Electron Microscope (SEM) and Atomic Force Microscopy (AFM). Particular attention has been paid to the mechanical behaviour and in particular to the reinforcement efficiency vis-a-vis filler content ($v_f > 50$ wt%). For this purpose, films with different amount of resin have been prepared and mechanical properties in tension have been evaluated. Also, the thermal conductivity of the material as function of filler content and the electrical properties have been investigated.

To better understand the quality of stress transfer between the two phases, a microscopic investigation has been carried out by micro Raman spectroscopy, in Chapter 4. This technique has been found to be a very powerful tool for the study of micromechanics of composite; it is an excellent instrument for the evaluation of the mechanism of stress transfer in graphene-based material [14]. It is a reliable, well-established and non-destructive testing methodology for composite micromechanics since reinforcement can be actually adopted as a strain or stress sensor embedded into the composite.

In Chapter 5, the effectiveness of reinforcement has been discussed by invoking a shear-lag load transfer mechanism, suitably modified to take into account the actual resin distribution between the particles, evaluated through Atomic Force Microscopy (AFM). The accuracy of the proposed analytical model has been then assessed through comparison with experimental and literature data, and the influence of polymer distribution and nanoparticle surface coverage on the efficiency of stress transfer has also been examined. In addition, design strategies able to improve the structural organization of the matrix have been described and implemented with the production of a more mechanically efficient composite.

Finally, in Chapter 6, possible industrial applications of high content GNP papers have been reported. In particular, regarding the improvement of fire performances of CFRPs. In fact, GNP/Epoxy films can be easily integrated into common composite process, such as autoclave, without adding any additional steps. The addition of a thin layer on the surface of CFRPs, can significantly improve the performance of the material, without impacting its mechanical

properties and weight, while offering a new surface protection approach for additional applications. Consequently, the excellent properties of films with brick and mortar architecture can be exploited to improve the thermal and electrical conductivities of other materials, such as CFRPs, making them competitive for different applications, such as fire resistance, thermal barrier coatings, EMI shielding effectiveness, and lightning strike protection.

2. STATE OF ART ON HIGH FILLER CONTENT COMPOSITES: NACRE-LIKE MATERIALS

Inspired to nature, a new broad class of biomimetic materials was born. In the last decades, researchers have made many attempts in mimicking the hierarchical structure of natural materials, such as mussels' shells and bones, in order to fabricate materials with exceptional structural and functional proprieties. Specifically, a new class of materials, called nacre-like materials, inspired to nature has developed.

As already described in Chapter 1, these materials have a laminated architecture, constituted by well-oriented thin laminae. Although nacre is composed by fragile material, it exhibits a ductile behaviour, allowing plastic deformations. In fact, it is able to dissipate energy without experiencing global failure [38], thanks to the mineral bridges that connect the different tiles at nanoscale level, which are capable of preventing crack extension and provide toughness and impact resistance [3,4]. Most importantly, these materials are capable of reproducing at the macroscale interesting mechanical properties and impressive performance [39,40].

As it will be explained in this chapter, artificial nanolaminates are constituted by a high quantity of stiff but brittle nanoparticles, bonded together by a small amount of soft polymeric phase. To guarantee optimal mechanical performances, the interface mechanisms have to be

accurately adjusted, to allow stress and strain transfer from one phase to the other. Particular attention has also to be paid to the nature of the matrix, because it can affect the interface, and thus the overall composite behaviour. However, nacre toughening behaviour is difficult to reproduce in synthetic composite materials since it is associated to several mechanisms acting at nanoscale.

In the following sections, a review on nacre like composite materials is reported, highlighting fabrication methods employed and raw materials used and comparing structural and functional properties.

2.1   Engineering materials based on 2D nanoparticles

Inspired to nacre several synthetic materials with brick-and-mortar structure, have gathered the attention of scientists worldwide. In particular, a large variation of systems has been studied and several platelet/polymer structures have been investigated. Particular attention has been devoted to paper-like materials reinforced with lamellar fillers, which are able to reproduce on the macroscopic scale the mechanical characteristics of the nanoscale reinforcement.

The mechanical and functional properties of this class of material can be designed according to the filler and matrix nature [41], as described in Table 2.1. The mechanical performances in terms of strength and stiffness are regulated by the filler properties, while the energy dissipation is regulated by the matrix brittle or ductile behaviour. However, the overall behaviour depends on the quality of stress transfer between the two phases and on their interactions. On the other hand, thermal and electrical properties depend only on the nature of the filler, due to the low amount of polymer, and are characterized by high anisotropy between in plane and cross plane conductivities [42,43].

Table 2.1. Mechanical and functional behaviour of composites with high content 2D nanofiller

Filler	Polymeric matrix behaviour	Composite mechanical behaviour	Composite conductivities
Graphitic (GO, RGO, GNP, Pyrolytic Graphite…)	Brittle	Pseudo-elastic	Electrically Conductive in plane – High ratio in plane/trough thickness thermal conductivity
	Ductile	Plastic	
Ceramic (MTM, Alumina, Silica…)	Brittle	Pseudo-elastic	Isolating
	Ductile	Plastic	

Table 2.2. Comparison between 2D nanoplatelets

Particle	Costs	Geometry	Elastic modulus	In plane - Therm. Cond.	Elec. Cond.
Graphene	200-300 € per flake	Monolayer	1 TPa [44]	5000 W/mK [44]	10^7–10^8 S/m [44]
GO	2-5 layers 48 €/g	2-5 layer BET 420 m^2/g	250 GPa [45]	72 W/mK with an oxidation degree of 0.35 [46]	270 S/m [47]
RGO	2-5 layers 68 €/g	2-5 layer BET 1562 m^2/g	250-350 GPa [48]	670 W/mK with an oxidation degree of 0.05 [46]	4480 S/m [49]
GNP	6-10 €/g	>10 layer BET 30 m^2/g	25-40 GPa [50]	300-470 W/mK [43]	$2x10^6$ S/m [22]
MTM	<1 €/g	BET 750 m^2 very high (nm × μm) aspect ratio	207 GPa [51]	16 W/m [52]	25 to 100 mS/m [52]

In literature several attempts have been done to mimic and design artificial nacre. For this purpose, different materials have been employed as bricks and mortar. The most employed nanoparticles used as reinforcement are listed in Table 2.2 and a comparison in terms of costs, mechanical properties and thermal and electrical conductivities is presented.

2.1.1 Graphene

A huge number of works based on graphitic nanoparticles can be found in literature. After the discover in 2004 by the scientists Geim and Novoselov, graphene has been in the spotlight involving many researchers for possible applications in several industrial sectors thanks to its outstanding electronic, optical, thermal conductivity and mechanical properties. Graphene is an allotrope of carbon in the form of a single layer of atoms in a two-dimensional hexagonal lattice [53]. The sp^2 hybridisation and the very thin atomic thickness (of 0.345 nm [54]) enable graphene to break so many records in terms of strength [14,44], electricity [17] and heat conduction [15,42,55]. In nature, isolated graphene sheets do not exist, they represent the

stacking of sheets which form graphite, held by weak interactions, van der Walls forces, that can be easily broken. With the discover of fullerene in 1985, a new allotropic form of carbon has drawn the attention of the scientific community [56]. This interest grew when other nanostructure has been discovered: single, double and multi walled carbon nanotubes, (SWCNTs, DWCNTs, MWCNTs) [57]. The single graphene sheet was isolated for the first time in 2004 by Geim and Novoselov at the University of Manchester [12], who awarded the Nobel Prize in Physics in 2010, and was prepared by using the scotch tape method. The sub-nanometric thickness of carbon-carbon bonding, makes graphene the strongest material in the world, stronger than steel and Kevlar, with tensile strength of 130 GPa and a Young's modulus of 1 TPa [14,44]. It is elastic, returning to initial dimensions after the stretching and it lightweight (0.77 mg/m^2) [58] and able to absorb light [59].

Those characteristics make the material very attractive for scientific research and industrial applications especially in development of optical electronic materials. However, all these properties refer to an ideal material, since producing monolayer graphene sheets without defects is extremely expensive and challenging. For this reason, other graphitic particles, with similar characteristics are widely employed in the research field. Graphene based materials [60] are classified according to physical and chemical parameters: average lateral size, number of layers and carbon/oxygen ratio (C/O) as shown in Figure 2.1.

They are graphene oxide (GO), reduced graphene oxide (RGO) and graphite nanoplatelets (GNPs). They differs from graphene for physical and chemical features such as average lateral size, number of layers and carbon/oxygen ratio (C/O) [60]. In fact, by increasing the number of layers of graphene, i.e. the thickness, or by decreasing the C/O ratio, both mechanical properties and conductivity of the material are negatively affected [61]. The average lateral size ranges in a quite large interval, from nanometric to micrometric scale (10 nm to 20 μm) and influences the strain of the material. The number of layers determines the thickness and the superficial, specific surface area (BET), and the elasticity of the material. In fact, reducing the number of layers it is supposed that the tendency of grafting other molecular and polymeric species increases. This parameter also influences the thermal and electrical conductivities which are maximum for graphene monolayer. The C/O ratio refers to the chemistry of the material and its surface, influencing the hydrophobicity and the capacity of interact with other polymeric and molecular species. GO, in fact, is characterized by hydrophobic areas incorporated into hydrophilic areas, with different reactivity. It is a chemically modified

graphene, with several oxygen distributed on the surface and on the edges. It is characterized by excellent solubility and dispersibility in aqueous solution and reasonable colloidal stability.
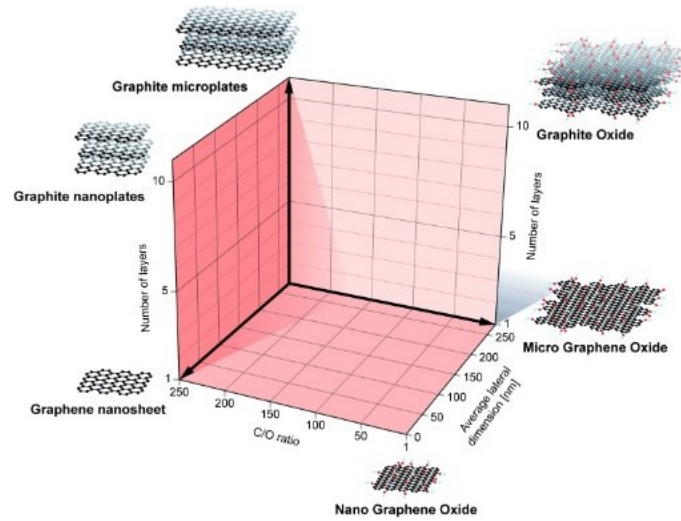
Figure 2.1 Graphene based material classification [60]

In general, graphene synthesis can be carried out via four different methods: (1) scotch tape method which mechanically exfoliates graphene sheets from highly-oriented graphite flakes [53]; (2) chemical vapor deposition (CVD) on metallic catalyst [62]; (3) epitaxial growth of graphene films on an electrical insulating substrate (e.g. Si) [63]; (4) mechanical and chemical exfoliation of graphite [64]; (5) oxidation of and chemical reduction of natural graphite flakes.

No defects graphene sheets can be prepared with CVD and epitaxial growth techniques. These methods, however, are not suitable for mass production. More in detail, CVD consists in depositing gaseous reagents, made of hydrocarbon, on a surface [65]. Usually, a mixture of methane and hydrogen are used and channelled on polycrystalline nickel films, previously heated at 900-1000°C. During this process, hydrocarbons break and the single carbon atoms dissolve on the metallic film forming a solid solution. Then a cooling process with an inert gas allows the diffusion of carbon atoms toward the solid solution, which aggregate forming graphene (Figure 2.2). More controlled formation of monolayer graphene can be obtained using copper as catalysator, thanks to the lower solubility of carbon on it.
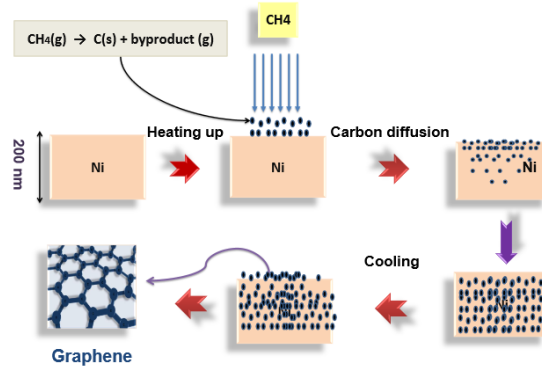
Figure 2.2 CVD graphene

Exfoliation of graphite along the crystalline planes is guaranteed by the low intermolecular interactions, van der Waals forces (2 eV/Nm^2) between the graphitic layers. Different approaches can be followed to exfoliate graphite: mechanical and chemical, such as intercalation with organic or inorganic elements [64]. These methods are less expensive than the others, because of the cheap raw material (graphite), and are also versatile and suitable for mass production.

Mechanical exfoliation consists in subjecting graphite to an external force able to break the interaction between the layers. The most diffused techniques are ultrasonication, intercalation and thermal treatment. During ultrasonication, micrometric bobbles apply shear stresses on graphite particles dispersed in a liquid, causing separation of the layers, as shown in Figure 2.3a. This method allows the production of high-quality graphene with high crystallinity and conductivity and low defects. Exfoliation of graphene can also be done starting from expanded graphite or from intercalated graphite (Figure 2.3b). Atoms and molecules, such as sodium or potassium or inorganic acids, are infiltrated between graphite layers, increasing the distance between them, and thus weakening their interactions [66]. In this case, the performances of the technique are higher than the direct exfoliation, but the material has more defects.

Thermal exfoliation of graphite has more advantages than mechanical exfoliation and allows the production of monolayer graphene. It is time saving and the process at very high temperature last few seconds. Furthermore, thermal exfoliation method produces graphene in gas environment, which can be advantageous for some application such as electrodes and lithium-ion batteries, where graphene must be dry.

<div align="center">(a)   (b)</div>
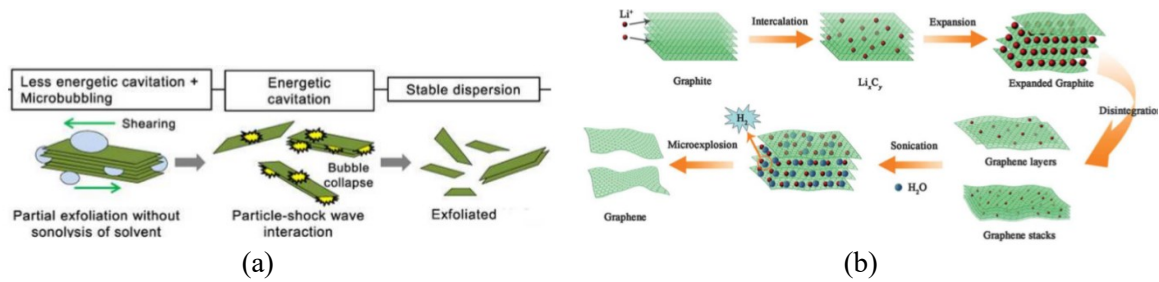
Figure 2.3 Exfoliation of graphite by: (a) ultrasonication; (b) intercalation
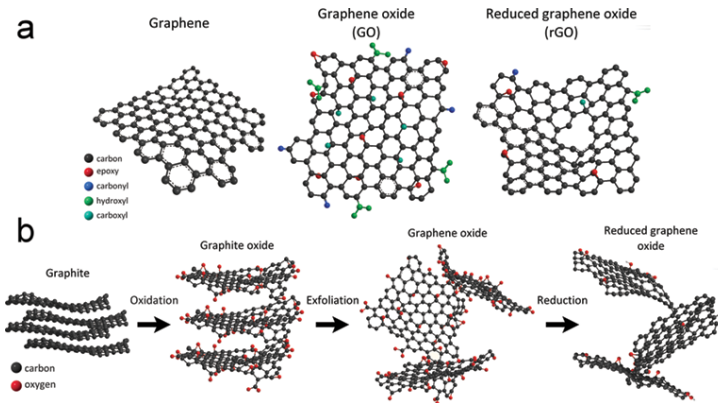
Figure 2.4 (a) Graphene oxide (GO) and reduced graphene oxide (RGO); (b) Oxidation and reduction of graphene

GO is produced by direct oxidation of graphite (Figure 2.4), following Hummer's [67] and Brodie's [68] methods, developed in 1957 and 1859 respectively. The difference between the two methods is based on the initial treatment, the first is done with a mixture of sulfuric acid, sodium nitrate and potassium permanganate while the second with potassium chlorate and fuming nitric acid. During the oxidation, the interactions between graphite layers are weakened, allowing the exfoliation of monolayer GO sheets. Although graphite is strongly hydrophobic, GO is hydrophilic, because of the oxygen functions, and thus can be easily exfoliated in water. GO can be considered as an insulating material because contains several oxygen atoms which interrupts the carbon atoms lattice [69].

By chemically reducing GO [70], it is possible to partially recover the electrical conductivity of the material, obtaining reduced graphene oxide (RGO), which still maintains the defects of GO (Figure 2.4). By using GO as precursor, thermal exfoliation produces directly reduced graphene oxide. During heating, functional groups bonded to graphitic layers are decomposed and produce gasses, which generates pressure on the adjacent layers. For this reason, GO, expanded graphite and intercalated graphite, are preferred to simple graphite as raw materials in the thermal exfoliation processes.

(a)   (b)
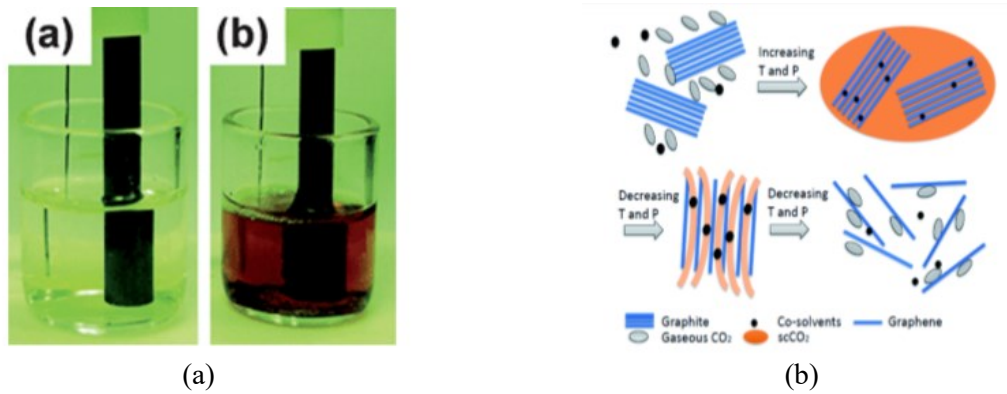
Figure 2.5 Electrochemical exfoliation (a) and supercritical fluid-facilitated exfoliation (b)

In addition to mechanical, chemical, and thermal methods, recently other processes have been developed for producing graphene. Electrochemical method consists in applying a potential difference to graphite electrodes in a conductive solution, gradually destroying the graphitic planes and generating graphite nanosheets (Figure 2.5a). Supercritical fluid-facilitated exfoliation consists in intercalating graphite with supercritical fluids, which expands applying pressure and separating the layers (Figure 2.5b).

Consequently, the price of graphene is linked to its quality and to the technique used for its production. Mechanically exfoliated graphene (obtained with "scotch tape" technique [12]) comes in small, high-quality flakes, not nearly enough for applications with price of the order of several thousand euros per flake. Whereas GO and GNPs, produced by oxidation and exfoliation of graphite, can be mass-produced, cutting the costs to tens euro per grams.

According to the desired application, the production method and thus the graphene characteristics have to be chosen. For example, scotch tape methods are widely used for physical and mechanical characterization of graphene on laboratory scale. CVD and epitaxial growth techniques, which are able to produce large graphene sheets with no defects can be employed in case of electronic devices. Thermal exfoliation, which produces graphene in gas environment, can be advantageous when graphene must be dry such as in case of electrodes and lithium-ion batteries. Mechanical exfoliation and oxidation can easily scaled up to mass production and thus, can be employed in the composite fields.

2.1.2 Ceramic bricks

Also, nanoclays are widely used to fabricate nacre-like composites, thanks to their low costs (<1 €/g) combined with remarkable mechanical properties. These are a broad class of natural inorganic minerals, of which montmorillonite (MTM) is the most commonly used as reinforcing material in composite applications [71]. According to the nature of the clay the

nanoplatelet elastic modulus ranges from 50 to 180 GPa [51]. MTM nanoplatelets consists of ~1 nm thick aluminosilicate layers stacked together to form a thicker multilayer (700 nm-10 µm) plate-like nanoparticles with very high aspect ratio. They exhibit low thermal and electrical conductivities (in the order of mS/m), thanks to the porous nature of clay minerals, making it a good candidate for thermal barrier and flame-retardant applications [52].

2.2   Technologies enabling industry applications – Fabrication processes

By combining the knowledge of the biological materials with the processing technique, synthetic materials with remarkable mechanical and functional properties can be designed. Several methods have been used for the production of nacre-like materials, capable to reproduce the hierarchical well-organized microstructure of nacre, with particle aligned in the longitudinal direction and bonded together by a thin matrix layer [40,72].

Generally, production methods follow two different approaches: top-down and bottom-up. For definition, top-down methods go from a general to a specific level, while bottom-up begins at a specific and moves to a general level. More specifically, in top-down technologies the material is fabricated starting from a suspension of nanoparticles and polymer mixed together and assembled in such a way as to ensure a layered structure (Figure 2.6a). Whereas, in bottom-up technologies the material is specified in great detail, by alternatively arrange the two phases and build up a layered structure (Figure 2.6b).
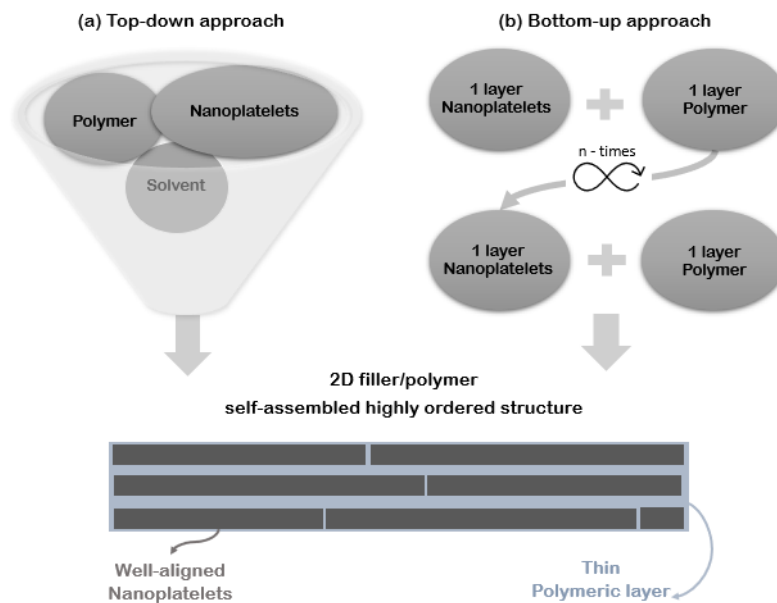
Figure 2.6. Top-down (a) and bottom-up (b) approaches

In general, bottom-up technologies are more able to fine-tune the nanometric alternance of the two phases [31] but remain mostly confined to the lab. Differently, top-down manufacturing processes are suitable for an industrial scale-up but are still far from obtaining the expected material architecture. In the following section are reported a summary of some of those methods [40,72].

2.2.1 Bottom up

(a)

(b)

(c)

(d)
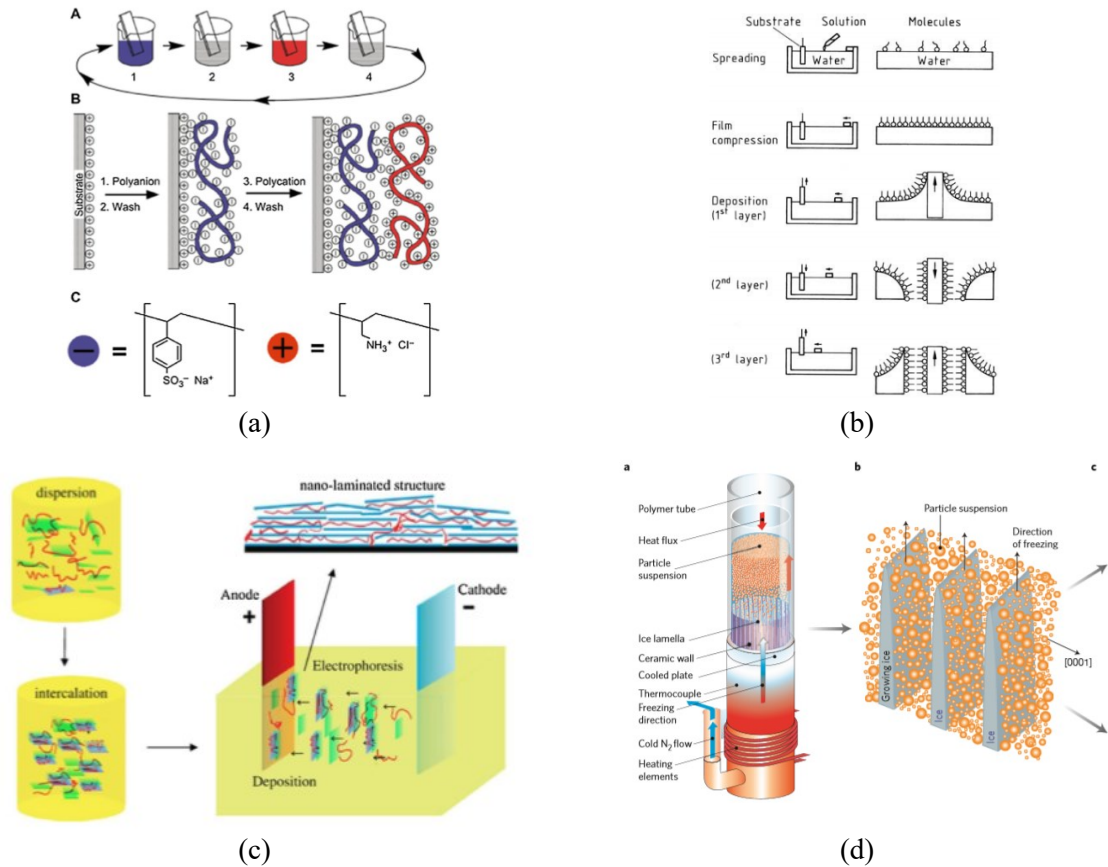
Figure 2.7. Bottom up methods: (a) Layer by Layer [73]; (b) Langmuir-blogdett [74]; (c) Electrophoretic deposition [73]; (d) Freeze casting [46]

Composites fabricated with bottom-up technologies, exhibit excellent mechanical properties, and are able to reproduce rigorously the brick-and-mortar structure of nacre by accurately alternating layers of polymer and nanofillers. They exploit the interactions between the phases, such as hydrogen and covalent bonds or π-π, electrostatic and hydrophobic interactions. Thanks to the good control during the stratification process, this method allows the production of homogeneous nanocomposites with very high filler content. The most widely used techniques are layer by layer, Langmuir-blogdett, electrophoretic deposition and freeze casting.

Layer by Layer (LbL) deposition process is based on electrostatic attraction between nanometric thick monolayers [73]. It consists in alternatively dipping a clean substrate into two solutions, constituted by positive and negatively charged polyelectrolytes, several times in order to obtain a film with a practical thickness and a multi-layered structure (Figure 2.7a). This process is governed by the absorption time of each layer, which can vary from several seconds to few hours, according to the concentration of the solution, making the whole process time-consuming. The principle at the base of the process is the interactions between the phases. Typically, these are hydrogen or covalent bonds or π-π, electrostatic or hydrophobic interactions. Thanks to the good control during the stratification process, this method allows the production of homogeneous nanocomposites with very high filler content.

The Langmuir-blogdett (LB) technique is based on the principle of the molecular film balance on water surfaces [74]. It is an assembly technique, consisting in dipping a substrate into a solution, which contains a floating film of molecules. Once the molecules layer reaches a suitable constant surface tension, the molecules are transferred on the substrate by dipping it into the solution (Figure 2.7b). The obtained deposition has nanometric thickness, which depends on to the number of dipping steps (i.e. number of layers). The method allows to accurately control the molecules orientation for each layer as well as their nature and the molecular interaction within the film optimizing its properties, such as the wettability and conductivity [75].

The electrophoretic deposition (EPD) process is simple, cheap and easily replicable to large scale [76]. With this technique it is possible to fabricate films with a stratified and well-aligned microstructure. The deposition process is regulated by the formation of an electric field in a particle suspension: the suspended particles, which are attracted by the electrodes, are deposited on them to form a nano-laminated structure (Figure 2.7c). Nanocomposites fabricated with electrophoretic deposition have lower mechanical properties than those produced by LbL deposition due to a low interface optimization and to the not perfect alignment of the particles. Although the method is simple and scalable, the achievement of low mechanical properties limits its use for industrial application.

Freeze casting process, also named ice templating [77–79], exploits the anisotropic solidification of water to create porous, layered materials. The process consists in freezing in a controlled manner a suspension of particles in water (Figure 2.7d). When freezing, ice crystals are formed, and the particles are intercalated and trapped between them. After water sublimation, the structure becomes homogeneous, forming a layered scaffold, which

architecturally represents the negative replica of the ice structure. This structure can be filled with a soft phase, having a hard-soft layered composite with B&M architecture. By controlling the speed of the freezing front, it is possible to manipulate the thickness and roughness of the lamellas. Roughness influences the relative sliding between bricks, which is the dominant mechanism for controlling the ductility of the material.

2.2.2 Top down
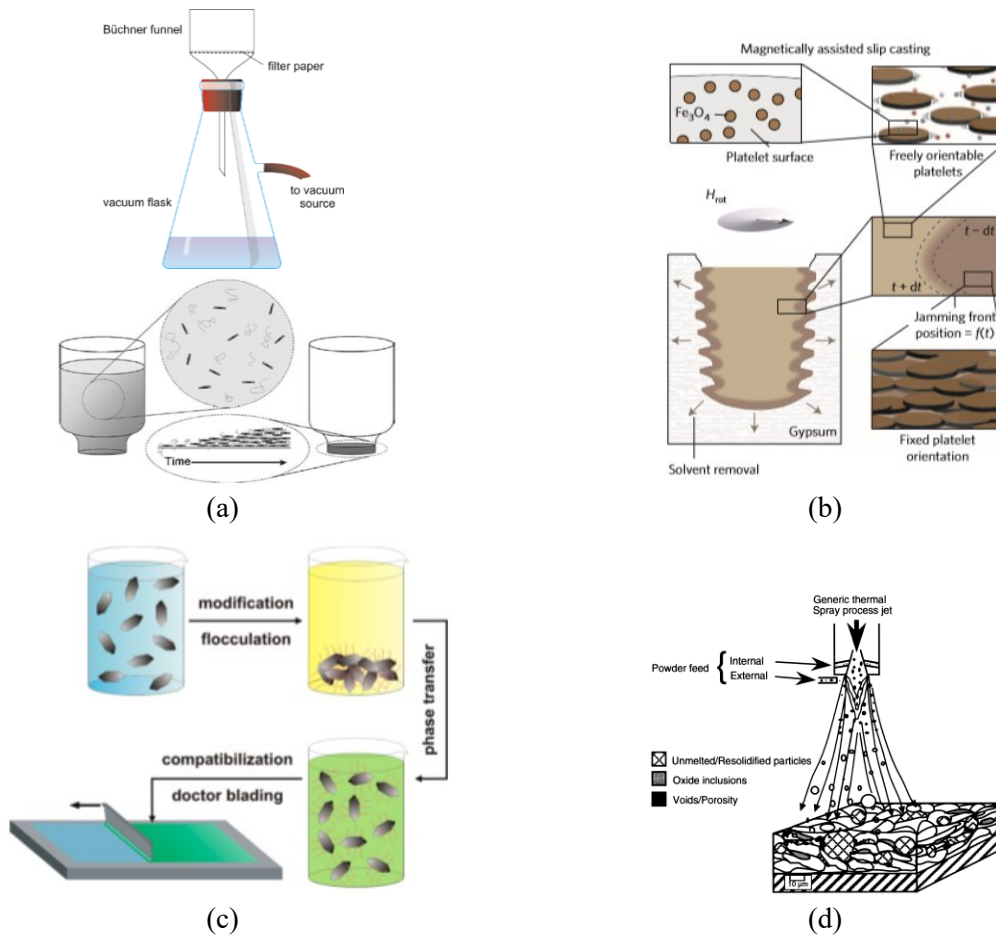
Figure 2.8. Top-down methods: (a) Vacuum assisted filtration [80], (b) Doctor blading [29], (c) Magnetically assisted slip casting [81] and (d) Spray deposition [82]

Top-down technique allow the production of thick and robust film in a single-step process, which would be very laborious to achieve with bottom up technique. It is worth mentioning as top-down methodology vacuum assisted filtration, doctor blading, magnetically assisted slip casting and spray deposition. These are easily scalable to mass production and are able to fabricate composites with very high filler content and well-aligned microstructure.

Vacuum-assisted filtration process, usually used in laboratory to separate a solid phase from a liquid, has been adapted for the fabrication of film with high level of nanoplatelet orientation

and with high filler content. The process consists in pouring a mixture of particles, polymer, and solvent into the Büchner funnel and filter with a filter paper (Figure 2.8a). Thanks to the vacuum pump, the solid part accumulates arranging in an ordered manner on the filter paper, while the liquid is pulled in the flask. The simplicity and rapidness of this method allow the fabrication of astonishingly well-aligned self-assembled structures. Composites fabricated with this technique exhibit excellent mechanical properties on par with LbL technique [80]. Furthermore, because it consists in a single step process, it allows the fabrication of thick materials (fraction of millimetres), which would be extremely laborious with LbL or other sequential approaches.

Doctor blading (or tape casting) [29] is one of the most used technique for making thin films. The process is very fast and allows the fabrication of large area films with constant thickness very. It consists in spreading a paste on a substrate by means of a blade or a spiral bar (Figure 2.8b). The relative movement between the blade and the surface allows the deposition of a thin film, whose thickness varies from 20 to 100 μm according to the geometry of the device, the wettability of the substrate and the rheological properties of the paste. The actual thickness of the deposition is about 60-70% of the nominal one, while the final thickness of the coating depends on the dry weight content. Doctor blading systems are equipped with a blade or a spiral bar. The second one is generally used for coating of leather, fabrics, or other flexible materials with irregular surface.

The magnetically assisted slip casting (MASC) is employed to produce materials with complex shapes and architecture, controlling the orientation and distribution of a particle suspension through magnetic field. This method also allows the production of composite functional materials with high filler content [81]. Initially, a particle suspension is deposited in a mould with a defined geometry through a slip casting process, as shown in Figure 2.8c. The mould is porous, and the dimension of the holes must be lower than that of the particles. The porosity of the mould generates in the suspension capillary forces, which absorb the liquid phase depositing a particle layer on the mould walls, called "cake layer". By applying a magnetic field on the outer side of the mould in the desired direction it is possible to monitor the orientation of the particles. To do that, the particles must be magnetic; thus, a layer of superparamagnetic iron oxide (SPIONs) particles can be added. Changing the direction of the magnetic field, it is possible to obtain heterogeneous composites with the desired orientation of the particles.
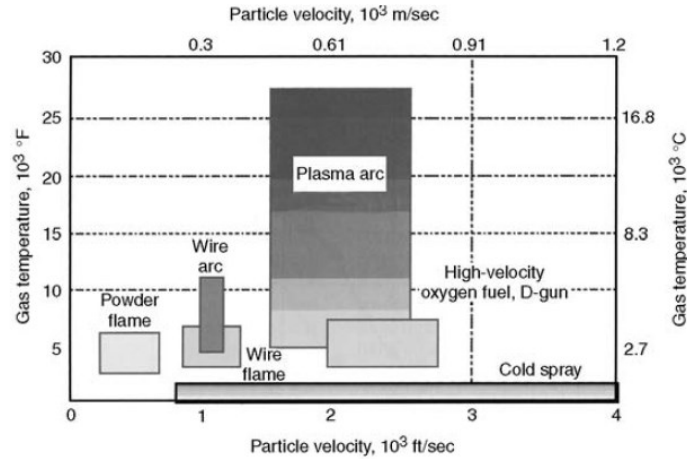
Figure 2.9. Spray deposition processes classification [82]

Spray deposition process is easily scalable to industrial application. According to the velocity and temperature used, it can be classified in thermal and cold spray processes (Figure 2.9). Thermal spraying (TS) was primarily used to produce coatings or thin films before the invention of cold spraying (CS). The process is typically used for superficial treatments of metallic and not-metallic coatings. The treatments are divided in three categories, according to the heat: flame spray, electric arc spray and plasma arc spray [82]. It is a fusion-based technology, where the material, once heated, is sprayed at high velocity on a surface. The impact with the surface allows the formation of a coating with lamellar structure, which microstructure depends on the process conditions such as, impact velocity and cooling rate. The main advantage of thermal spray process is the possibility of using a variety of materials and thus its versatility. However, it is not able to cover small and deep cavities outside the line-of-sight areas.

Cold spraying (CS) deposition process is a relatively new technique, which exploits the supersonic fluid dynamics and the high-speed impact dynamics [83]. It allows the deposition of ductile materials, such as metals and polymers, but not of fragile materials like ceramics. It consists in spraying relatively small particles in the solid state, ranging in size from approximately 1 to 50 µm in diameter at high velocities (typically 300 to 1200 m/s) on an appropriate substrate. High temperature compressed propulsive gas passes through a nozzle, generating a supersonic flow inside and outside the nozzle. The cold spray system basically consists of a compressed gas delivery system, a gas heater, a powder feeder, a supersonic nozzle, a robot arm, and an operation system as schematized in Figure 2.8d. The mechanism of bonding of the particles with the substrate is associated to the impact at high speed, which creates an atomic contact thanks to the pressure and temperature of the interface during the

process. The cold spray process, differently from hot spray process, enables to produce coatings at low temperatures, in the range of 0 to 700 °C, a range that is generally lower than the melting temperature of the particle used for the coating. The nozzle exit temperature is substantially lower than the gas preheat temperature, such that deleterious effects of high temperature associated with thermal spray method and which employs a liquefaction step are minimized or eliminated [82].

In Table 2.3 a comparison between bottom-up and top-down techniques is reported. Top-down technologies are easily scalable to mass production and are not time consuming. The assembly of the material, though, is not easy to control, making it impossible to fine tuning the nanometric matrix layer. On the contrary, bottom-up technologies are much more accurate at nanometric level, ensuring a good alternance between the two phases. However, the level of precision is at expenses of the velocity of the process and consequently to its scalability.

Table 2.3. Comparison between top-down and bottom-up techniques

	Top-down	Bottom-up
Time required	Rapidness	Time consuming
Scalability	Yes	No
Accuracy (polymer film)	Impossibility of fine tuning the nanometric matrix layer	Nanometer-level control over the architecture.
Particles alignment	Very good alignment	Very good alignment
%vol filler	>50%wt	>50%wt

Nevertheless, the final assembly of the bulk material is governed by different driving forces, which are involved during the fabrication process, both in bottom-up and top-down technologies. Suter et al. [84] found that the formation of highly-ordered brick and mortar structure depends on the interaction forces between the two phases. If the flakes are relatively uncharged, the bonds between the flakes and the polymer drive the self-assembly to the final highly ordered structure. This means that the properties of a macroscopic bulk material strongly depend on the interaction at atomic levels, including Van der Waals (vdW) force, hydrogen, ionic and covalent bonds and in most cases, on their synergetic effect. Of all the assembly interaction, vdW bond and π-π interactions are the weakest and covalent bond is the strongest, while hydrogen and ionic bond are in between them [85–87].

2.3   Mechanical performances – Experimental observation of literature data

Experimental evidence demonstrated that the mechanical performances of brick-and-mortar composites depend on filler and matrix nature and on their interactions. The choice of the two phases and their compatibility is fundamental for achieving the desired performances.

Figure 2.10 shows an Ashby plot of strength and elastic modulus of artificial nacre with bricks of various nature. Graphene oxide (GO) nanoparticles, and in particular reduced graphene oxide (RGO), guarantee the best performances in terms of strength of the material, while exhibit elastic moduli in the range of 15-40 GPa and 3-15 GPa, respectively. On the other hand, composites with ceramic bricks, such as montmorillonite (MTM) show low values of strength but high elastic moduli (10-35 GPa). Finally, graphene nanoplatelets (GNPs) composites exhibit the lowest values of strength but discrete elastic moduli in the range of 20-30 GPa. The low number of points indicates that they are not widely used as reinforcement in brick-and-mortar composite because of the difficulty of the nanoplatelets to be well dispersed in polymers.
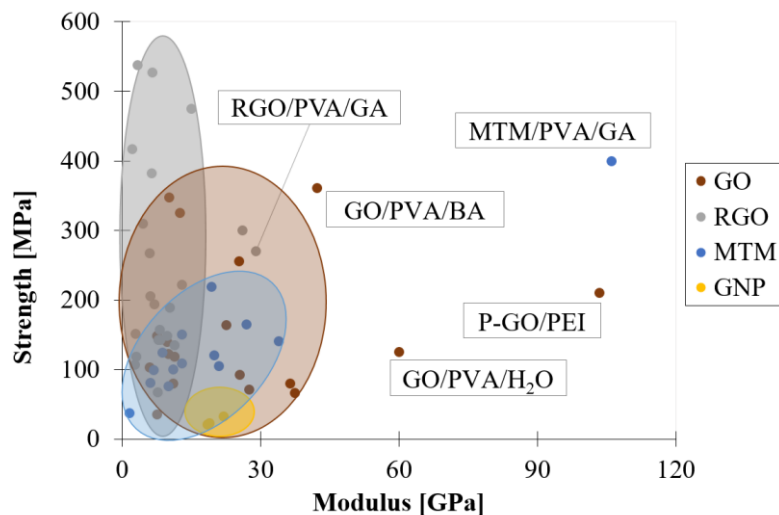
Figure 2.10 Ashby plot of strength vs modulus of brick-and-mortar composite with bricks of various nature: GO [24,25,95–98,26,88–94]; RGO [49,88,106–109,96,99–105]; MTM [28,110–115]; GNP [23,116,117]

Anyway, these ranges are wide and depend on different factors, such as: volumetric filler content, range of motion of the polymeric chains and the filler/matrix compatibility. The best performances can be achieved by improving the compatibility between nanoparticles and the polymers and their interaction, for example by chemically functionalizing the nanoplatelets or improving crosslinking. In fact, the highest values of elastic moduli are achieved when the chemical affinity between the two phases is improved, for example by using glutheraldeyde

(GA) [108,111], or boric acid (BA) [92] or water (H_2O) [93] or by functionalizing GO with polydopamine (P-GO) [26], as emerged from Figure 2.10.

2.3.1 Influence of filler content

From a critical analysis of the mechanical behaviour of composites with nano-lamellar reinforcement at relatively high filler content, it emerges that the elastic modulus of these systems drops after a critical concentration deviating from the expected behaviour, which dictates that the higher the filler content the higher the macroscopic elastic modulus. This unusual behaviour is reported by many authors in literature.

Wu and Dzral [22] fabricated a self-standing graphite paper consisting of graphite nanoplatelets by vacuum filtration and impregnated it with different amount of polyetherimide (PEI). By adding 30 wt% of polymer the tensile modulus reaches 22 GPa but then drops for further increase of PEI content. Likewise, Li et al [23] produced high content GNP polyetherimide (PEI) papers by filtration and hot-press. They investigated the tensile properties at various filler contents and showed a maximum in the elastic modulus for filler content of 60 wt%. This behaviour was observed also in composite prepared with graphene oxide and alumina. In fact, highly ordered GO/PVA papers, with high nanofiller concentrations, prepared using vacuum-assisted self-assembly technique, showed a reduction in the elastic modulus from 36.4 GPa to 27.6 GPa for 50 wt% to 75 wt% filler content respectively [24]. In the same way, GO/PVA paper fabricated through simple solution-casting method showed a maximum at 80 wt% of GO with an elastic modulus of 11.4 GPa [25]. Tian et al. [26] fabricated graphene-based paper via vacuum filtration with low amount of polymer (<45 wt%). They used GO doped with polydopamine (PGO) to prepare PGO/PEI papers and functionalized them by a crosslinking reaction. The mechanical properties increased with the addition of PEI, showing a maximum in strength (209.9 MPa) and modulus (103.4 GPa) for PEI loading of 14.7 wt%. GO/Thermoplastic polyurethane (TPU) films, with nacre-like laminated structure, are fabricated via solution casting with different matrix content achieving the best performances for 20 wt% of polymer [89]. Also in alumina/chitosan nacre-like composite fabricated with doctor blading technique, the mechanical properties are found to drop at high filler content [29]. In fact, at very high tablet concentration (>50 vol%), the material failed in a brittle fashion, due to a misalignment of the tablets and inability of the polymer to infiltrate the open spaces between tablets. Cao et al. [101] fabricated RGO/PVA composite with an ordered layered structure and with a molecular level coupling between RGO sheets and PVA molecules. PVA

chains strongly couple with RGO sheets at the molecular level and the neighbouring RGO sheets are linked by PVA molecules through hydrogen bondings and the C–C covalent bondings in the PVA polymer chains, forming a stronger multi-connected bridge as a continuous load-transfer pathway. The films display extremely high strength and Young's modulus and the optimal content of PVA was found to be 70 vol%. Wang et al. [114] fabricated Montmorillonite/poly(vinyl alcohol) (MTM/PVA) nanocomposites spanning the complete range of MMT content (0–100 wt%) by simple evaporation-induced assembly. In the range of 30–70 wt%, the nanocomposites show a nacre-like layered structure with alternating MTM platelets and PVA layers. Composites reached the maximum value in terms of elastic modulus and strength for MTM content of 70 wt%, then for higher filler content the layered structure is transformed to tactoids, which deteriorate mechanical properties. This suggests that partial MTM platelets are restacked and form tactoids, probably because the PVA is too little to fully cover all the MTM platelets.

These evidences demonstrate that the mechanical performances of composites with high content of 2D nanoparticles are regulated by the efficacy of the thin polymeric layer to transfer load, via shear transfer mechanism. In particular, the efficiency of reinforcement, η, is defined, according to the modified rule of mixture and is based on elastic modulus of the composite, E_c):

$$\eta = \frac{E_c - E_m(1 - v_f)}{v_f E_f} \tag{2.1}$$

Figure 2.11 shows the unusual behaviour of this class of material for which with the increasing filler content, the efficiency drops below one, indicating that the stress transfer between filler and matrix is poor. As a consequence, the elastic modulus deviates from the rule of mixture, exhibiting a decreasing behaviour (Figure 2.11b). The drop of elastic modulus at high volume fraction is due to a bad interaction between the two phases and specifically to a bad compatibility. This compatibility is governed by the chemical interactions between nanoplatelets and matrix and also by the matrix wettability and its capacity to cover the entire nanoplatelet surface.
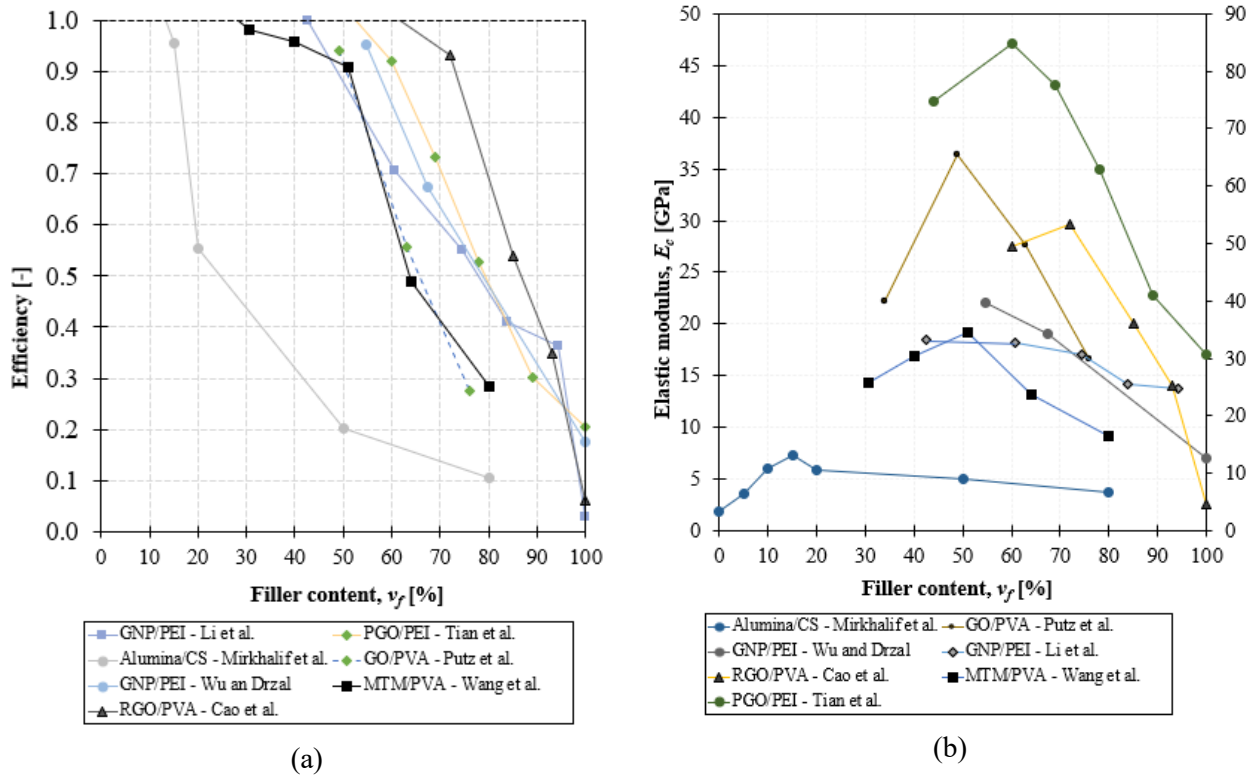
Figure 2.11. Drop of elastic modulus (a) and efficiency (b) at high filler content, state of art [22–26,29,89,101,114,118]

2.3.2 Influence of matrix - Effect of matrix molecular weight

Also, the matrix choice can be discriminating for the optimal mechanical performances of the material. The higher is the molecular mobility of the polymer and the capacity to intercalate between nanoplatelets, the better will be the stress transfer at the interface and thus the performances of the material even at high filler content. Short polymer chains are able to diffuse between nanoparticles during assembly, while very long polymer chains ability to navigate around the layered nanosheets is more limited [24,119]. Evidence of this behaviour can be found by comparing the volumetric filler fraction for which the drop of efficiency occurs, and the matrix molecular weight (Figure 2.12). It can be seen that for high molecular weights (150-300 kDa) the drop of efficiency occurs for very low volumetric filler content (20-30 vol%). Whereas for low molecular weight (<100 kDa), the drop occurs for filler content greater than 40 vol%.

This indicates that the matrix molecular mobility affects the efficiency of reinforcement, which decreases as the molecular weight increases. The dependence of the efficiency from the matrix molecular weight is also shown in Figure 2.13, for different nanoplatelets, especially for MTM and GO. In case of RGO, there is little evidence of this behaviour since the efficiency is very low (<10%) (Figure 2.13c).
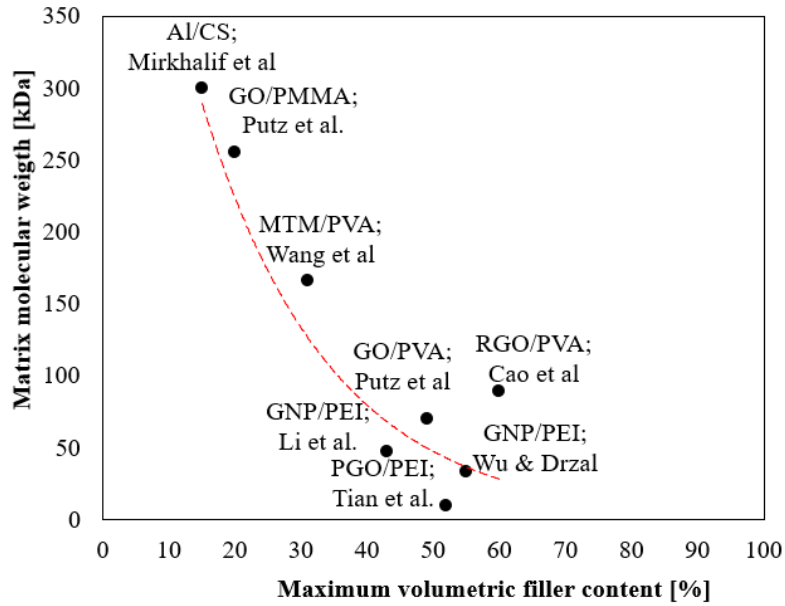
Figure 2.12. Dependence of maximum volumetric filler content before drop on matrix molecular weight

(a)

(b)

(c)
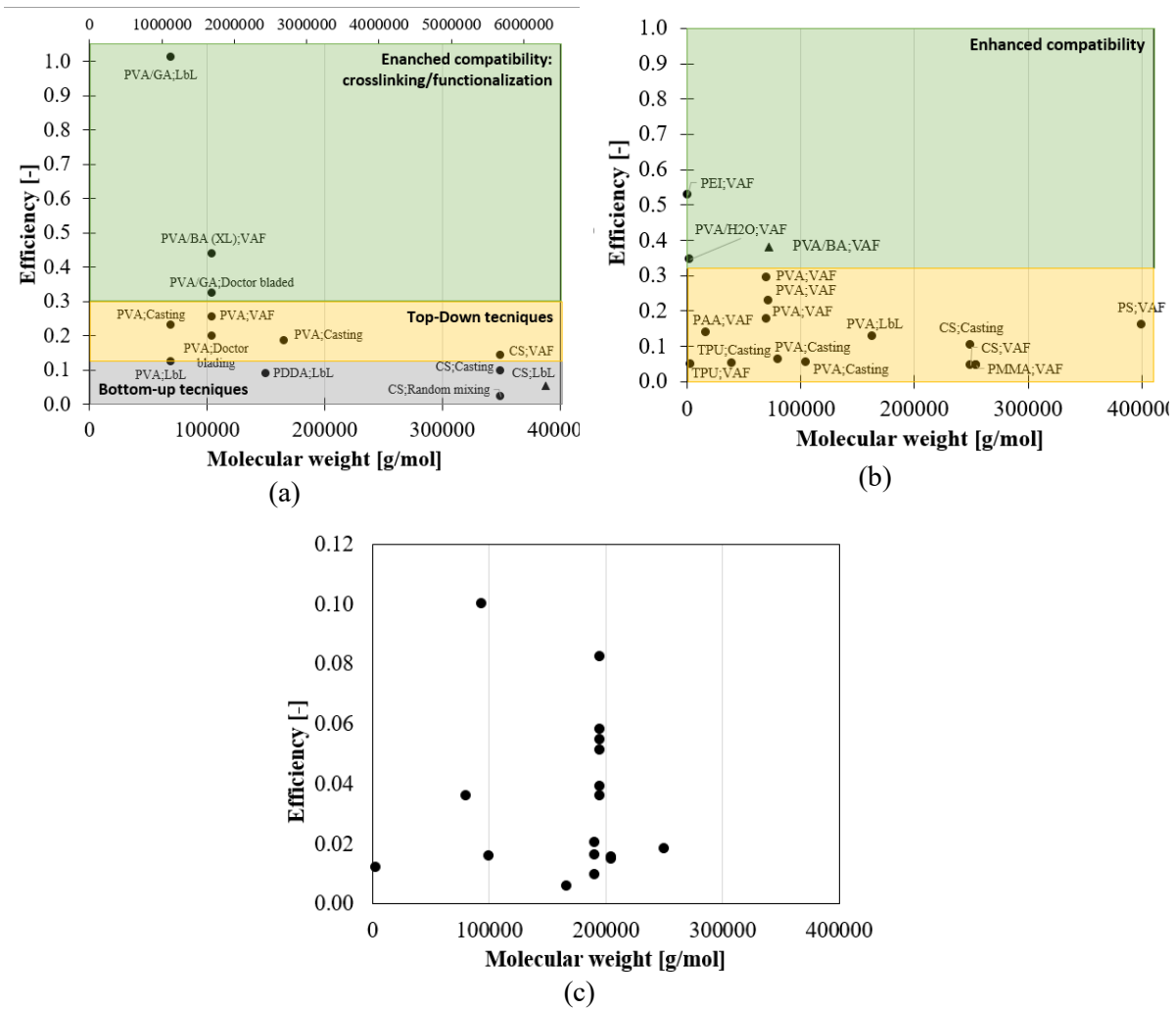
Figure 2.13. Efficiency vs Molecular weight: (a) MTM; (b) GO; (c) RGO

This phenomenon has been found by other authors in literature. Podsiadlo et al. [120] observed that the polymer flexibility directly affects the stress dissipation and load transfer from the organic matrix to the inorganic nanoscale component. In particular, they compared the mechanical response of B&M composites reinforced with MTM, observing that the elastic modulus of MTM/PDDA is greater than that of MTM/Chitosan (CS), even though the elastic modulus of CS is higher than that of PDDA. This can be explained by the high rigidity of CS and the poor MTM/CS interactions, which contribute to lowering the mechanical properties. The CS chains cannot find an optimal conformation on the surface of the MTM, due to lack of flexibility, which instead is possible for PDDA, where the strength of adhesion is about four time higher than that of MTM/CS and the attraction energies include electrostatic attraction, hydrogen bonding, and van der Waals forces.

Also, Putz et al. [24] investigated the hydrophilicity and hydrophobicity of polymers, fabricating GO films with poly(vinylalcohol) (PVA) and poly(methyl methacrylate) (PMMA). They observed poor interactions between GO sheets with hydrophobic PMMA, which limits improvement in stiffness at high nanofiller concentration.

The importance of matrix molecular weight in the fabrication process of this class of material can also be understood by comparing the theoretical and the measured matrix layer thickness at different filler content. According to the representative volume element (RVE) of Figure 2.14, matrix thickness decreases with increasing filler content and is computed with Eq. (2.2).
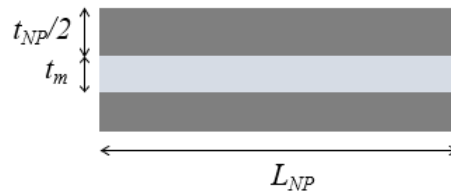
Figure 2.14. Representative volume element (RVE) of composites with high filler content

$$t_m = \frac{1 - v_f}{v_f} \cdot t_{NP}$$
(2.2)

In reality, from experimental data reported for GO/PVA [24], PGO/PVA [26], RGO/PVA [101] systems, this value deviates from the theoretical one starting from the volumetric filler fraction which corresponds to the drop of mechanical properties, as shown in Figure 2.15. In fact, when the matrix content is very low, the polymer thickness should be very small (< 1 nm), but it is incompatible with the mobility of the polymeric chains, especially when the matrix molecular weight is high. In fact, Putz et al. [24] found that at high filler content the polymer

thickness is almost twice in composites with PMMA (17 nm) with respect to PVA (9 nm) due to the higher molecular weight, which is 254 kDa for PMMA and 70 kDa for PVA.
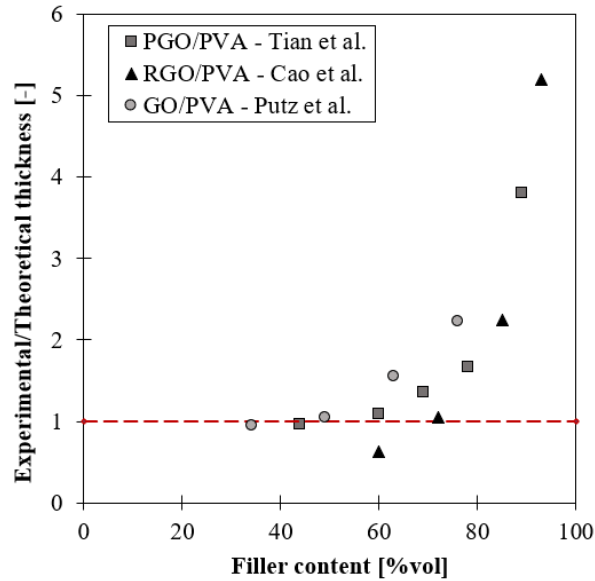
Figure 2.15. Comparison between experimental and theoretical matrix thickness in GO/PVA composites as function of filler content

Consequently, the polymer reaches a minimum thickness, which depends on matrix molecular weight, after which it does not decreases anymore. This results in a partial uncovering of nanoparticle surface at high filler content. In other words, the matrix thickness must be compatible with the gyration radius of the polymer [121], otherwise dewetting of nanoparticles surface can occur. This condition prevents full covering of the nanoparticle and compromises the performance of the brick-and-mortar material. Parameters influencing the wettability of the thin polymeric films include molecular weight, temperature, film thickness, substrate interaction and a combination of these parameters [122,123]. This negatively affects the stress transfer and thus the composites mechanical behaviour, leading to a drop of strength and stiffness, especially at very high filler content (>70 wt%).

Another interesting observation that emerges from Figure 2.13a is that the best mechanical performances are achieved when the nanoparticles are functionalized. This is the case of Podsiadlo et al. [111] and Walther et al. [28] who used glutaraldehyde (GA) to improve PVA crosslinking to connect nanoclays. GA is an efficient cross-linking agent for PVA, because it improves the interaction with MTM platelets and the load transfer between particles. Despite all, the improvement of mechanical properties is more significant in sample prepared by Podsiadlo et al., where both strength and elastic modulus improve of about three times and ten times respectively at the expense of the ultimate tensile strain, maximizing the efficiency, rather

than those prepared by Walther et al. This difference is attributed to the process. In fact, Podsiadlo et al. used LbL to produce MTM/PVA composites and immersed it in GA solution gradually, every 0.05 μm, for about 30 steps. On the other hand, Walther et al. produced MTM/PVA composites with doctor blading and directly immersed the 200 μm thick paper in GA solution. The excellent barrier properties provided by the well aligned microstructure of the material, make it difficult to GA to penetrate in the bulk, especially in samples prepared by Walther et al. Thus, the treatment done by Podsiadlo et al. is much more rigorous than the second one and involves a higher the volume, justifying the significant improvement of the mechanical properties.

2.3.3 Filler/matrix compatibility – chemical bondings

As shown so far, the best mechanical performances are achieved when the chemical interactions between the two phases are improved [85]. It was found in literature that, functionalization with glutheraldeyde (GA) [111], boric acid (BA) [124], water (H_2O) or polydopamine are very efficient, as can be seen in Figure 2.10. This effect can also be observed in GO films without binder. In Figure 2.16 is reported the efficiency for GO films with chemical bonds of various strength: covalent bond using BA [125], hydrogen bond using H_2O [24] and ionic bond using Al^{3+}, Mg^{2+} ions [126], and GA [127]. As expected, BA crosslinking creates strong covalent bonding, which significantly improve the elastic modulus of 240% with respect to not functionalized GO films. On the other hand, functionalization with H_2O slightly increases the modulus of 25%, while ions lower the mechanical properties of the material due to the increase of the spacing between nanosheets.
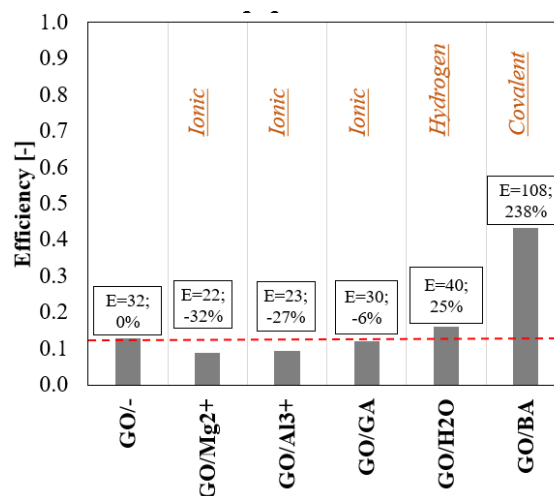
Figure 2.16. Effect of functionalization on the efficiency and elastic modulus of GO films without binder

Graphene oxide (GO) free-standing paper [128] with macroscopic flexibility and stiffness are fabricated via vacuum filtration exhibits average modulus, strength, and maximum strain of 32 GPa, 120 MPa and 0.6% respectively, thanks to the unique interlocking-tile arrangement of the nanoparticles. The use of a very low quantity of borate (0.0094 wt%) significantly improves stiffness and strength of the material. Remarkable improvements arise from the formation of covalent bonds between borate ions and the hydroxyl groups on the graphene oxide nanosheet, similar to the borate cross-links in plants. Therefore, these improvements are at the expense of ductility. In fact, the strain to failure in the borate modified material is about 0.24%, while in the unmodified is 1.4%. In the absence of borate, graphene oxide thin films exhibit plastic deformation because hydrogen bonds can adapt to strains during tension testing and can accommodate high amounts of deformation. Cross-linking with borate ions strongly reinforces the thin-film structure, improving strength by nearly 25% to 160 MPa. However, once broken, these covalent bonds cannot be readily reformed, leading to a more brittle behavior under tension [124].

Another excellent crosslinker for GO sheets is dopamine (DA). The DA molecules not only react with GO sheets creating strong covalent cross-linking, but also self-polymerize into long chain polymer of PDA, suppling enough space for GO sheets slippage and absorbing much more energy during the loading. Strong integrated artificial nacre based on graphene oxide (GO) sheets and dopamine (DA) cross-linking are fabricated via evaporation-induced assembly process obtaining GO/PDA composite [49]. Similar criterion has been followed by Tian et al. [26], who used polydopamine to functionalize GO (PGO). They fabricated graphene based PGO/PEI paper via vacuum filtration and with low amount of polymer (<45 wt%), showing excellent mechanical properties, with a maximum strength of 209.9 MPa and modulus of 103.4 GPa for PEI loading of 14.7 wt%. Also Wang et al. reduced GO with simultaneous coating by polydopamine (PDA) obtaining PDA reduced GO, called PDG [104]. PDG nanoplatelets has been assembled with PVA with a vacuum-assisted process, obtaining a nacre-like structure. This treatment acts on the hydrogen bonding, improving the adhesion and friction between PDG nanosheets and PVA chains. The stress in PDG−PVA materials could be effectively transferred due to the strong interface interaction. The adhesion of PDA and strong covalent cross-linking between PDA and GO enhance interlayer contact and interactions of sheets, also increasing the friction between adjacent PDG sheets. When the paper is loaded, PDG nanosheets extensively slide against each other and the PVA coiled long-chain molecules, which are interpenetrated into the interlayer, stretch along the sliding direction. The

nanocomposite shows enhanced mechanical properties thanks to the interface mechanisms between PDG and PVA, exhibiting tensile strength, elongation at break and toughness of 327 $\pm$19.3 MPa, 8 $\pm$0.2% and 13.0 $\pm$0.7 MJ/m^3 respectively, with 7.3 wt% PVA.

Although in GO paper without binder the mechanical properties of the film reduce when a small amount of these divalent metal ions is added, in other cases modification with a Mg^{2+} and Ca^{2+} ions is possible, thanks to their ability to bind readily to oxygen functional groups [126]. In fact, the effect of ions crosslinking on mechanical properties, can be seen in the case of GO/carboxymethylcellulose (CMC) composites [129]. Multivalent cationic (M^{n+}) ions, cross-linking with plenty of oxygen-containing groups, serve as the reinforcing evocator, working together with other cooperative interactions (e.g., hydrogen-bonding) to strengthen the GO/CMC interfaces. GO nanosheets serve as bricks, while CMC polymers are taken as mortar, and M^{n+} ions are invoked as the reinforcing evocator. Graphene oxide/carboxymethylcellulose (GO/CMC) films are prepared via vacuum filtration and then intercalated with three different types of M^{n+} ions. The measurements of macro−micromechanical properties show that the chemical cross-linking reactions between M^{n+} ions and oxygen-containing groups of the two components can dramatically strengthen/toughen the GO/CMC interfaces, which significantly restrict the relative slip of between GO nanosheets and CMC layers, resulting in a great improvement of strength and toughness. The reinforcing strategies of different types of M^{n+} ions reflect the diverse increases in mechanical properties. Gong et al. also fabricated GO– CMC films [106] and placed them in a manganese chloride solution in order to improve the synergistic hydrogen and ionic bonding. After introducing ionic cross-linking with Mn^{2+}, the mechanical properties of GO–CMC– Mn^{2+}, nanocomposite films are dramatically enhanced, with a tensile strength of 329MPa and a toughness of 3.64MJ/m^3, thanks to the synergistic effect of intermolecular hydrogen bond crosslinking and ion-crosslinking. Wan et al. improved the synergistic interfacial interactions of covalent and ionic bonding, effectively suppressing the crack propagation in the fatigue process, by using small amount Ni^{2+} ions (0.7 wt%), achieving maximum tensile strength of 417.2 MPa and toughness of 19.5 MJ/m^3.[105].

However, the strength of chemical bonds also depends on the nature of the filler. For examples, graphitic nanoplatelets, such as GO, RGO, GNP, are really different from a chemical point of view. In particular, GO contains oxygen atoms on the surface, which interact with the polymeric matrix, establishing covalent, ionic or hydrogen bonds. After oxidation, the oxygen content of RGO reduces significantly and with it the possibility to create strong chemical bonds

with the matrix. As a consequence, the mechanical performances are very poor, as demonstrated previously (Figure 2.13c).

Consequently, the efficiency of reinforcement sharply decreases with increasing carbon/oxygen ratio (C/O) as shown in Figure 2.17. Typical values C/O ratio lies around 2 for GO and increases in case of RGO being greater than 4 [130].
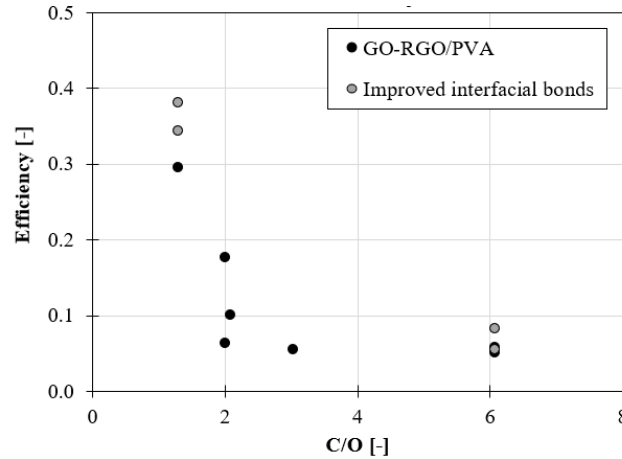
Figure 2.17. Influence of chemical interactions between filler and matrix: efficiency vs C/O ratio in GO and RGO/PVA films

Suter et al., investigated the variation of GO/PVA structure with C/O ratio [84]. They found that GO self-assembly can be controlled by changing the degree of oxidation, varying from fully aggregated to intercalated assemblies with polymer layers between sheets. The architecture varies according to the degree of oxidation. In case of zero oxidation (RGO) it comes predominantly aggregated, with no polymer resident between the flakes and with the majority of flakes directly interacting with each other via attractive van der Waals interactions. When increasing the degree of oxidation, systems preferentially self-assemble, with a tendency toward forming intercalated morphologies, with GO flakes lying directly above each other and with the polymer between the flakes. The high oxidation degree allows highly attractive interaction between PVA molecules with the hydroxyl groups on GO flakes, leading to a very dense layer of immobile polymer on each flake [93].

Same discussion can be done for GNPs, which can interact only with weak vdW bonds and π-π interactions. Current performance of GNPs as a reinforcing filler is limited by their agglomeration and weak interfacial interaction with certain polymer matrices. Kim et al. [131] proposed an approach to produce noncovalently functionalized GNPs (F-GNPs), by one-step functionalization process with melamine, to improve the interfacial adhesion and dispersion in an epoxy matrix. They used a conventional ball-milling process, in which GNP flakes are functionalized through the aromatic ring in melamine by π–π interactions. The amine groups

(NH_2) react with the epoxide groups to provide strong chemical adhesion at the interface between the GNP flakes and the polymer matrix, improving the mechanical properties of nanocomposites of 94.3% and 35.3% enhancements in Young's modulus and tensile strength, respectively than those of the unfilled pure epoxy. Addition of 2 wt% provides the best improvement, the Young's modulus and ultimate tensile strength of the nanocomposites reach 3.49 GPa and 63.32 MPa, which further increase when melamine functionalization is employed. Vadukumpully et al. [132] fabricated GNP/poly(vinyl chloride) (PVC) ultrathin composite films of surfactant via solution blending, drop casting and annealing route with 2 wt% loading. This material exhibits Young's modulus of 2 GPa, which corresponds to an increase of 58% with respect to the pure PVC film. A lightweight and flexible composite paper has been successfully fabricated by incorporating nanofibrillated cellulose (NFC) with graphite nanoplatelets (GNPs) using vacuum filtration [133]. Specifically, the hybrid film with 75 wt% GNPs a satisfactory tensile strength of 46.39 MPa. The network formed of NFC even at a small amount of 25 wt% makes great contribution to the mechanical properties of the composite paper. The neat GNP paper has very low values of tensile strength and Young's modulus, which is attributed to the weak interaction between the GNPs. With the addition of NFC, the tensile strength and Young's modulus of the composite papers increase. It is believed the enhancement of the mechanical properties is mainly originated from the NFC networks formed in the composite paper. Prolongo et al. [134] studied the advantages and disadvantages of the addition of graphene nanoplatelets to epoxy resins according to the GNP content (from 1.5 to 8.0 wt%). They found that the storage modulus increases when GNPs are added to epoxy, while strength and elongation at break reduce due to the poor interface between the nanofiller and matrix. Debelak et al. [116] investigated the influence of particle sizes and filler content (from 0.1 to 20%wt) on GNP/Epoxy nanocomposites. The addition of exfoliated graphite gradually increased the modulus of the base polymer after the percolation threshold was achieved. However, the strength seemed to reduce within an increase in concentration due to slip in the graphite planes and to a lack of interface between graphite and polymer. The excellent conductivities achieved in the polymers can be attributed to the dispersion of graphitic sheets throughout the polymer, forming a unique conductive network. Multilayered GNP/NFC, produced via vacuum filtration, followed by pressing, showed excellent tensile mechanical properties without any surface treatments [135]. The optimum composition was found at 1.25 wt% graphene multilayers, giving a Young's modulus of 16.9 GPa, ultimate strength of 351 MPa, strain of 12%, and work-of-fracture of 22.3 MJ/m^3. Physical interaction between NFC

and graphene multilayers generates the basis for the excellent mechanical properties. These remarkable properties suggest that the mechanical strength of the composite is improved through interactions that are mediated by binding between graphene and NFC (π-interactions). Also an increase of toughness is showed thanks to the non-covalent bonding between GNPs and NFC fibrils, which allow relative sliding.

2.3.4 Ternary systems

Ternary artificial nacre are hybrid materials fabricated by coupling bricks of different nature. An example is the robust ternary artificial nacre constructed through synergistic toughening of graphene oxide (GO) and molybdenum disulfide (MoS_2) nanosheets via a vacuum-assisted filtration self-assembly process [90]. The ternary GO-MoS_2/TPU artificial nacre shows an excellent integration of tensile strength and toughness, much higher than the binary GO-TPU nanocomposites. The tensile strength and toughness of binary GO-TPU increase with GO content. Thus, the initial inorganic content was determined to be 90 wt% for constructing the GO-MoS_2/TPU composite. By reducing GO, the tensile strength and toughness of RGO-MoS_2/TPU reach 235.3 MPa and 6.9 MJ/m^3, respectively, which are 40% and 100% higher than RGO-TPU (90:10).

Wan et al. synthetized an ultrahigh fatigue resistant graphene-based nanocomposite via tungsten disulfide (WS_2) [136]. The graphene-based freestanding GO-WS_2 hybrid film (Figure 2.18a) was assembled via vacuum-assisted filtration of a dispersion of GO and WS_2 nanosheets and then was grafted with PCDO via esterification reaction by soaking the GO-WS_2 hybrid film into premixed tetrahydrofuran/PCDO solution. After reduction with hydriodic acid (HI), the mechanical properties significantly improve, reaching tensile strength of 413.6 MPa, elastic modulus of 14 GPa and toughness of 17.7 MJ/m^3. The WS_2 nanosheets contributes to the stretching of the material improving toughness, while the coiled cross-linked PCDO chains bridges the crack propagation during the stretching of the material as shown in Figure 2.18. Moreover, compared with the physical van der Waals' force between graphene nanosheets and lubrication of WS_2 nanosheets, the covalently cross-linking via the PCDO long chain could provide much stronger interfacial strength, dissipating much more energy during the fatigue testing process.

(a)   (b)
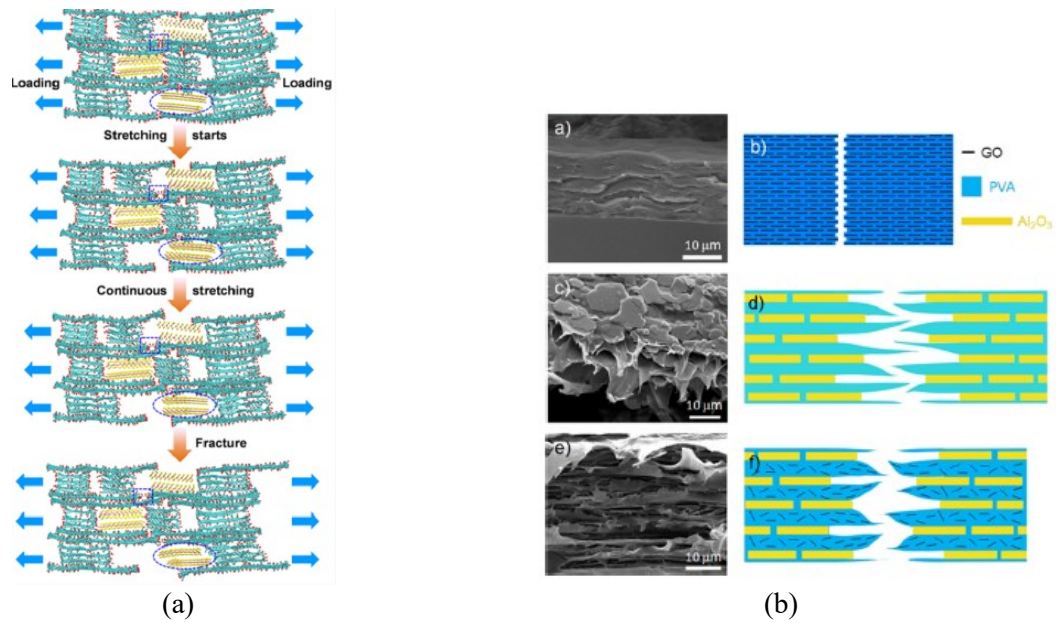
Figure 2.18. Example of ternary systems: (a) GO/WS$_2$/PCDO [136]; (b) Al$_2$O$_3$/GO−PVA [137]

Likewise, Duan et al. [138] introduced covalent bonding between adjacent GO nanosheets through synergistic toughening of graphene oxide (GO) and nanofibrillar cellulose (NFC). Binary GO-NFC layered nanocomposites were assembled via evaporation process and then were covalently cross-linked through 10,12-pentacosadiyn-1-ol (PCDO), resulting in the GO-NFC/PCDO ternary nacre-like nanocomposites. After chemical reduction with hydroiodic acid (HI), the RGO-NFC-PCDO ternary artificial nacre nanocomposites with 94.7 wt% GO content demonstrates ultimate stress of 314.6 MPa and a toughness of 9.8 MJ/m^3 and high electrical conductivity 162.6 S/cm.

Another strong and tough ternary bioinspired nanocomposite was fabricated by Gong et al. [139], who exploited the synergistic toughening and covalent bonding of reduced graphene oxide and double-walled carbon nanotube (DWNT). GO-DWNT hybrid layered materials are fabricated through an evaporation process, then immersed into the 10,12-pentacosadiyn-1-ol (PCDO)/tetrahydrofuran (THF) solution and finally chemically reduced by hydroiodic acid (HI). PCDO chains under UV irradiation form the covalent cross-linking between adjacent GO nanosheets, leading to the GO-DWNT/PCDO nanocomposites. After covalent cross-linking with PCDO, the mechanical properties of RGO and DWNT films were dramatically enhanced. The tensile strength and toughness of this kind of ternary bioinspired nanocomposites, with only 2.24 wt% of PCDO reaches 374.1 MPa and 9.2 MJ/m^3.

Ming et al. [140] combined graphene oxide (GO) and montmorillonite (MMT) bricks with poly(vinyl alcohol) (PVA) via a vacuum-assisted filtration self-assembly process, obtaining a

multifunctional bioinspired nanocomposite (GO:MMT:PVA=81:9:10). By reducing GO with hydroiodic acid (HI) the RGO–MMT/PVA ternary bioinspired nanocomposite was obtained exhibiting tensile strength and tensile toughness of 356.0 MPa, and 7.5 MJ/m^3, high fatigue-resistant properties.

Alumina microplatelets−graphene oxide nanosheets−poly(vinyl alcohol) (Al$_2$O$_3$/GO−PVA) artificial nacre was successfully constructed through layer-by-layer bottom-up assembly, in which Al$_2$O$_3$ and GO−PVA act as "bricks" and "mortar", as shown in Figure 2.18b, respectively [137]. The artificial nacre exhibits excellent strength (143 ± 13MPa) and toughness (9.2 ± 2.7 MJ/m^3), maintaining plastic deformation of PVA. The sharp reinforcement by GO nanosheets and strain amplification by Al$_2$O$_3$ microplatelets are therefore combined simultaneously bringing about high strength and toughness.

Li et al. [141] fabricated low cost hybrid composite with GO noncovalent functionalized boron nitride nanosheets (BNNS) by means of vacuum filtration. The addition of small amount of PVA (1.7 wt%) into the composite films, fills gaps between the packed nanosheets to connect GO and BNNS, improving the mechanical properties of the material and showing tensile strength and modulus of 41.0 MPa and 14.0 GPa.

2.4   Multifunctionalities and applications

As well as for mechanical properties, experimental observations indicate that to obtain composites with a high thermal and electrical conductivities, it is necessary to comprehensively consider the filler intrinsic properties and dispersion, the filler/matrix interface compatibility, and the filler content and orientation [142].

First of all, the intrinsic nature of the filler determines the thermal and electrical conductivity of the material, as described in Table 2.1. Bidimensional lamellar nanoparticles, such as graphene are characterized by high thermal and electrical conductivities and have intrinsic barrier properties. Their excellent properties can be reproduced on the macroscale by assembling nanoparticles into a brick-and-mortar architecture. Oriented nanoplatelets form a conductive path along the in-plane direction, resulting in a higher in-plane conductivity rather than the out-of-plane conductivity [30,43]. As for mechanical properties, the functionalization of filler/matrix interface is beneficial and improves the thermal conductivity of the composites. In fact, it ensures the formation of effective heat conduction paths, reduces interfacial thermal resistance between the two phases and prevent agglomerations. In addition, the well aligned

microstructure, and the low amount of polymer of brick-and-mortar materials creates a tortuous path, which ensures gas barriers properties and water resistance.
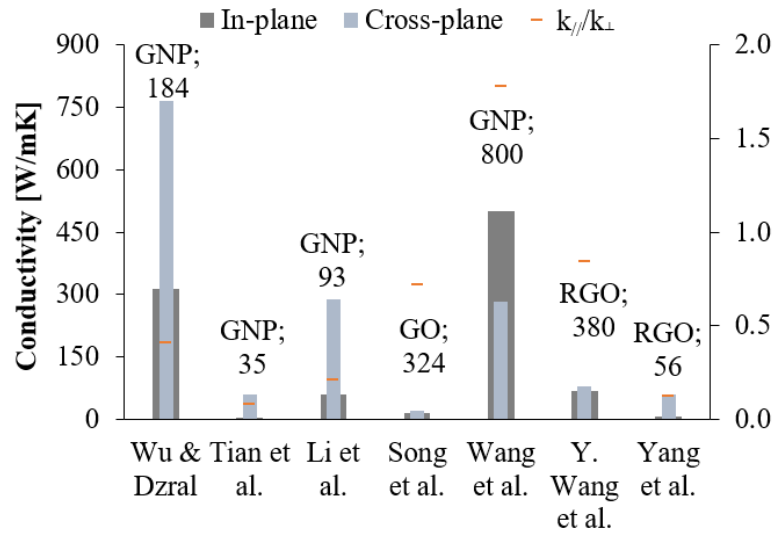
Figure 2.19 Anisotropy of thermal conductivity

Brick and mortar architecture makes the thermal conductivity of the material highly anisotropic, with high ratio between in-plane and through-thickness thermal conductivity. This behaviour is shown in Figure 2.19, where both conductivities are reported for films with graphitic nanoplatelets. In graphene papers the low cross plane thermal conductivity depends on the excessive van der Waals interfaces and plentiful air pockets among sheets, which increase the phonon scattering and further limit the heat transport [104]. Song et al. [143] fabricated RGO/nanofibrillated cellulose (NFC) membranes by means of layer-by-layer (LbL) technique, with in-plane and the cross-plane thermal conductivity of 12.6 W/mK and 0.042 W/mK respectively, such that the ratio k_X/k_Z is 279. Likewise, ultrathin and highly aligned RGO/cellulose nanofiber (CNF) films [107] show strong anisotropy of thermal conductivity. With 50 wt% RGO composition, films showed anisotropic index of k_X/k_Z =56, with in-plane thermal conductivity of 7.3 W/mK and low cross-plane thermal conductivity of 0.13 W/mK. At the same time, the material in-plane electrical conductivity reaches 4057.3 S/m, and markedly increases with an increase in the RGO content. In addition, the large number of highly aligned RGO layers and excellent electrical conductivity ensure that the electromagnetic microwaves that penetrated the sample, decay, thus resulting in an excellent EMI shielding performance.

To improve the thermal properties, Wang et al. [144] proposed sulfuric/nitric acidification of graphite films. This treatment improves the through thickness thermal conductivity of 19% from 0.528 W/mK of the control film to 0.626 W/mK after 5 min, while decreases the in plane

thermal conductivity from 641 W/mK to 501 W/mK. Same behaviour has been observed by Li et al. [133] for GNP/NFC films and by Wu & Drzal [117] for GNP/PEI films, in which the ratio between in plane and cross plane thermal conductivities (k_X/k_Z) was ~93 and ~184 respectively. The anisotropic behaviour makes this material ideal for thermal interface application (TIM) [145].

As stated before, thermal and electrical conductivities of graphene-based material often go hand in hand, especially in brick-and-mortar material, as reported in Figure 2.20.
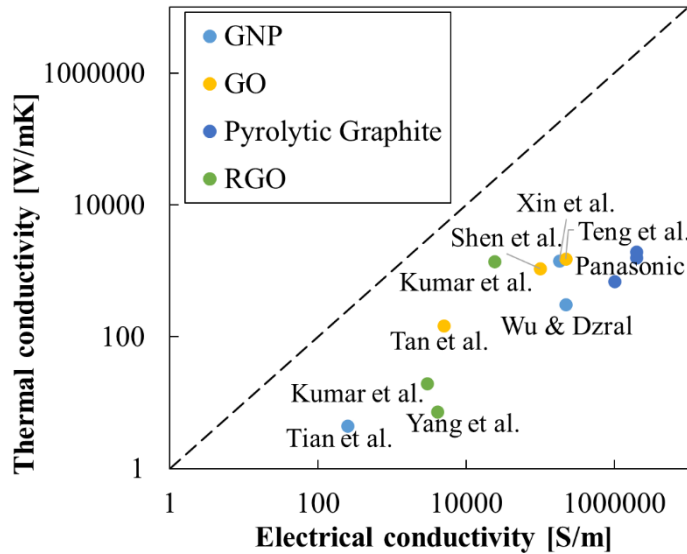
Figure 2.20. Thermal and electrical conductivities of graphene-based brick and mortar material

Kumar et al. fabricated RGO/poly (vinylidene fluoride-co-hexafluoropropylene) (rLGO/PVDF-HFP) composite films through simple solution casting with low polymer content (27 wt%), showing excellent thermal and electrical conductivities [18,146]. Xin et al. [147] prepared graphene papers by electro-spray deposition (ESD) with excellent thermal and electrical conductivities to 1434 W/mK and 1.83×10^5 S/m ideal for heat spreading applications. The alignment of the graphene nanosheets in the paper structure can be controlled by electrospray deposition and further improved by mechanical press and high temperature. The effect of annealing temperature on the thermal conductivity of RGO films was investigated by Song et al. [21]. The thermal conductivity increases up to 1043.5 W/mK with the annealing temperature up to 1200°C, which is attributable to the removal of the oxygen-containing functional groups with a simultaneous restoration of the graphite lattice. Annealing under mechanical compaction [148], diminishes the holes, eliminates the vacancies, decreases the interlamellar spacing and crosslinks the adjacent graphene sheets, resulting in higher thermal conductivity [149,150]. At higher annealing temperature (2000°C), reduction and

graphitization of GO occurs as shown in other works [19,151], providing to the material excellent electrical and thermal conductivities and EMI shielding effectiveness. This indicates that the graphitization of GO film could be considered as an alternative way to produce excellent thermal conductive material with efficient EMI shielding.

However, thermal and electrical conductivities depend on the filler content. When increasing the amount of reinforcement in the composites, the number of contacts between the particles increases, allowing heat flows and promoting phonon diffusion [152,153]. Zhu et al. [154] showed that there is a nearly linear relationship between the mass fraction and the thermal conductivity of composite. Even though the thermal conductivity increases with filler content, the best performances are achieved with a small amount of polymer. In fact, it acts as a solder, connecting the adjacent graphene sheets via covalent bonding and evolves into oriented graphitic structure after the graphitization treatment [155].

Enhancements in thermal conductivity can be achieved either by improving the filler/matrix compatibility or by exploiting the synergistic effects of multiple filler. Upon this, some authors investigated the possibility of incorporating glycidyl methacrylate-grafted graphene oxide (g-GO) in the PI matrix, showing better performance compared to GO, particularly when the filler content increases [156]. Alternatively, other authors [141,157] demonstrated that by adding boron nitride sheets (BNNS) to GO significantly improve the thermal conductivity of the material, since these particles acts as thermally conductive bridges, connecting GO particles and allowing better heat transfer. Likewise, hybrid CNT/GO films [158] combine high thermal conductivity (up to 1056 W/mK), excellent mechanical properties. The alternance of CNTs GO sheets ensure a mechanically strong and conductive scaffold, in which aligned CNTs act as a strong and conducing skeleton, and graphene sheets provide an efficient connection path for heat, electricity and force. However, the electrical conductivity is influenced by the interactions between the particles and the matrix. In fact, by reducing GO [102] [136] and by improving the bonding and the synergistic interactions between the two phases, the electrical conductivity enhances [88,99] as well as by annealing the material at high temperature [47].

In addition to thermal and electrical conductivities, nacre-like materials also possess good barrier properties [159–161] and optical transmittance [115,162], thanks to the well aligned structure of the platelets and to the binder function. These multifunctionalities combined with good mechanical properties, opening the possibility of employing the material for several applications (Table 2.4), such as fire-resistant coatings [163,164], thermal interface materials (TIM) [142,145], EMI shielding [64,76,77,79], and lightning strike protection [165–167].

Table 2.4 Multifunctionalities and corresponding applications of brick-and-mortar composites

Multifunctionalities	Applications
Thermal conductivity anisotropy, gas and vapour barrier	Fire resistant coatings, Thermal interface materials (TIM), Heat spreader
Electrical conductivity	EMI shielding, Lightning strike protection

2.4.1 Applications

Thanks to the anisotropic thermal behaviour [30,43], and vapour and gases barrier properties [168,169], in the latest years has risen a great interest for the use of materials with brick and mortar architecture as fire resistant coatings [28,170]. These engineered properties may favourably influence the fire resistance by managing the conductive heat exchange, block the oxygen and pyrolysis products diffusion towards the flame [171] and reflecting the incoming radiative heat flux.

When the material is exposed to a flame, the high temperatures spread on the entire surface, exploiting the high in plane thermal conductivity of the material. The preferential conduction path in plane with respect to cross plane direction, slow down the increase of the temperature from the outside atmosphere to the inside, lowering the possibility for the internal samples to contact with oxygen and thus difficult to ignite. This results in high fire-retardant performance.

Good fire retardant properties have been showed by RGO-MMT/PVA composites [140]. When exposed to open flame, the film initially burnt quickly and generated a certain amount of gas due to the presence of PVA and residual oxygen groups of RGO. After that, it retains its shape and did not burn any more even when exposed to fire, owing to the formation of an inorganic framework composed of a high content of interlocked MTM nanosheets and RGO sheets. In the same way, laminated structure with alternated layers of clay and nanofibrillated cellulose (NFC), fabricated by vacuum filtration [113,172], showed exceptional fire retardance and oxygen barrier properties. The cellulose nanofiber network forms the continuous matrix phase with random-in-the-plane fibril orientation distribution, conferring toughening, while MTM guarantees fire retardance and oxygen barrier properties. The clay nanopaper showed self-extinguishing characteristics when subjected to open flames delaying thermal degradation of cellulose, thanks to the favorable gas barrier properties of ordered clay platelets. Although the oxygen barrier properties of pure cellulose nanopaper are exceptionally good in the dry state, the addition of montmorillonite improves barrier properties considerably at higher relative humidity.

High demand of material with high thermal conductivity materials interests the microelectronics fields. In fact, a serious problem involving thermal management in this fields, is associated to the heat generation, which is responsible deterioration of device efficiency and service lifetime. Consequently, effective heat transfer technology is an essential requirement for a reliable operation of electronic devices. Thermal interface materials (TIMs) come to the aid for reducing the thermal contact resistance between the chip and heat spreader. They should have high thermal conductivity with a minimal thickness, without leakage from interface, and should not deteriorate over time, all this guaranteeing good mechanical characteristics [173,174]. An example of thermal interface material widely diffused on the market, there are Panasonic thin flexible graphite sheets [175]. They are used to provide thermal management or supplemental heatsinking in addition to conventional means. Made from pyrolytic graphite, they exhibit very high in plane thermal and electrical conductivity, which strongly depend on the film thickness. However, low through-plane thermal conductivity limits the direct use of B&M composites for TIM applications. Gao et al. [173] fabricated lightweight TIM based on hierarchically structured graphene paper with superior through-plane thermal conductivity, by inserting thermally conductive materials between horizontal graphene layers, made up of a randomly oriented small graphene sheets. The practical performance test achieved a remarkable enhancement in cooling efficiency by ≈ 2.2 times compared to the state-of-the art commercial thermal pad.

Another interesting field is that of electromagnetic interference (EMI) shielding. Nacre-like materials, in fact, respond to the rising demand of EMI shielding materials, followed by the advancements in wireless technology and increased signal sensitivity in electrical/electronic devices, especially for the safety of aircraft and other structures. Also, lightning strike damages are becoming the major concern, thus multifunctional structural composites are required to act as an EMI shield for the avionic equipment such as flight recorders, navigation units, flight-control systems [165,176].

Composites with brick-and-mortar architecture work as efficient EMI shielding, being ideal candidate for these applications. They are capable of replacing metals, thanks to their low weight combined with excellent electrical conductivity, high thermal stability and anti-corrosion properties [18].

In general, attenuation of an incident EM wave is given by three contributions: absorption, reflection, and multiple reflections. Reflection is a surface phenomenon, while absorption happens in the composite's volume, and consequently is dependent on the thickness of the

material (Figure 2.21). A quantitative measure of the EM shielding is the shielding effectiveness (SE), which is measured in decibels (dB) [177]. Typical values of SE for many industrial applications are around 30 dB and provides an attenuation EM waves of 99.9% [178]. The EMI shielding ability is positively related to the electrical conductivity and thickness according to theoretical Simon's formula. The electrical conductivity of the materials needs to be at least higher than 1 S/m to obtain excellent EMI shielding performance.

Ceramic materials are electrical insulators and do not absorb well the EM waves in the microwave spectral region, while carbon allotropes such as graphene and few-layer graphene demonstrated better performance, since they are characterized by high electrical and thermal conductivity. Barani et al. [179] investigated the SE of graphene/epoxy composites with 19.5 vol% filler. The material exhibits total shielding efficiency in the X-band frequency of 65 dB in sample of 1 mm thickness, which even improves with increasing temperature. Same behaviour was observed in GNP/PEI papers [180], which exhibited good SE increasing with paper thickness. GNPs composites also works as microwave absorber in S-band for practical applications. Parida et al. [181] investigated the EM shielding effectiveness of GNP/ethylene vinyl acetate (EVA)/Ethylene-octene copolymer (EOC) blend composite in S-band and observed that at 30 wt% of GNP loading a SE of 67.63 dB and was achieved mainly due to absorption mechanism. This is attributed to increase in electrical conductivity, that reaches 455 S/m, thanks to the formation of a conducting network within the insulating the matrix.

Good EMI shielding performances are also exhibited by flexible multi-layered MXene/thermoplastic polyurethane (TPU) films with brick and mortar architecture, prepared via a simple layer-by-layer spraying technique [182]. Samples with 28.6 wt% MXene content and 52-μm thickness exhibit high electrical conductivity of 1600 S/m, excellent EMI shielding effectiveness of 50.7 dB in the X-band, and outstanding specific shielding effectiveness of 7276 dB cm^2/g. In addition, the composite films have stable EMI shielding performance during continuous bending.

With increase in concentration of filler loading, the gap between the fillers decreases, impedance mismatch and multiple reflections increases and contribute to the absorption rather than reflection. Moreover, absorption is the primary mechanism where fillers are unevenly distributed, and reflection is the major contributor where fillers are uniformly distributed in the polymer matrix. In a laminated compact structure as Figure 2.21a, the SE is mainly governed by reflection, since the densely stacked platelets are more favourable for reflecting the EM

waves. On the other hand, in porous structure (Figure 2.21b), waves pass through the surface of the material, moving a in cell-like configuration.

(a)

(b)
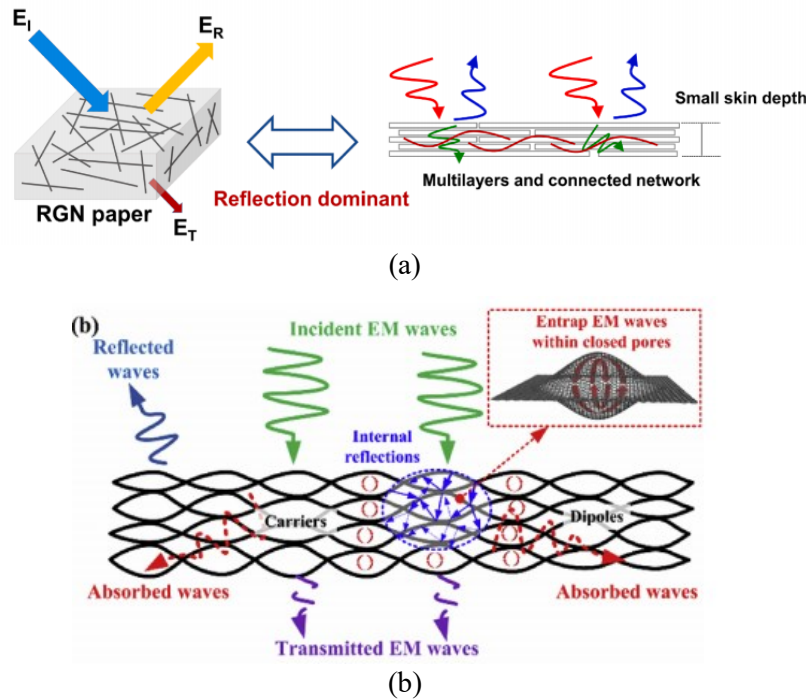
Figure 2.21 Schematic representation of microwave transfer across in nacre-like paper with compacted [183] (a) and porous architecture [184] (b)

The EM wave attenuation repeats in the internal layer, which acts as a reflecting surface and gives rise to multiple internal reflections. In addition, the repeated reflection and scattering greatly enhance the transfer of EM energy, which is dissipated as heat in the form of microcurrent, leading to the enhancement in SE absorption. The entrapped EM waves continue to bounce off the graphene cell walls until they are completely absorbed within this structure. Finally, Lai et al. [184] investigated the SE of GO paper with porous architecture. These materials are able to block and absorb 99.99995% of the incident radiation, and exhibit a SE of 63.0 dB and a very high specific SE/thickness of 49750 dB cm^2/g.

2.4.2 Integration in FRP

Brick and mortar composites can be easily integrated into common composite processes, such as autoclave, without adding any additional steps. Adding a thin layer on the surface of FRPs, can significantly improve the performance of the material, without impacting their mechanical properties and weight, while offering a new surface protection approach for additional applications. Consequently, the excellent properties of these type of material can be exploited to improve the thermal and electrical conductivities of other materials and making

them competitive for different applications, such as fire resistance, thermal barrier coatings, EMI shielding effectiveness, and lightning strike protection.

Even if fire resistant properties of such thin films have been published [28,113,115,140,185,186], only few papers have been devoted to evaluate the effect of the application of such coating on the fire resistant properties of CFRP composite. The addition of a protective coating on the surface of the laminate has several advantages: the fire-resistant properties are concentrated at the surface eliminating compatibility issues with the matrix and, more importantly, the functional and structural properties of the composite are not impacted.

Previous works have demonstrated that bucky papers are an optimal solution to improve the electrical and thermal conductivity of CFRP [187], but the addition of GNPs can further improve the behavior of the material. Multi wallet carbon nanotube (MWCNT)/GNP coating on CFRP [163] can significantly improve the fire resistance, especially in terms of peak on heat release rate (HRR); 7.5 wt% GNP causes a reduction in PHRR of 35% with respect to CFRP. In particular, MWCNT/GNP hybrid membranes have better barrier effect compared to MWCNT, since GNPs create a tortuous path in the structure improving the barrier effect of the buckypaper.
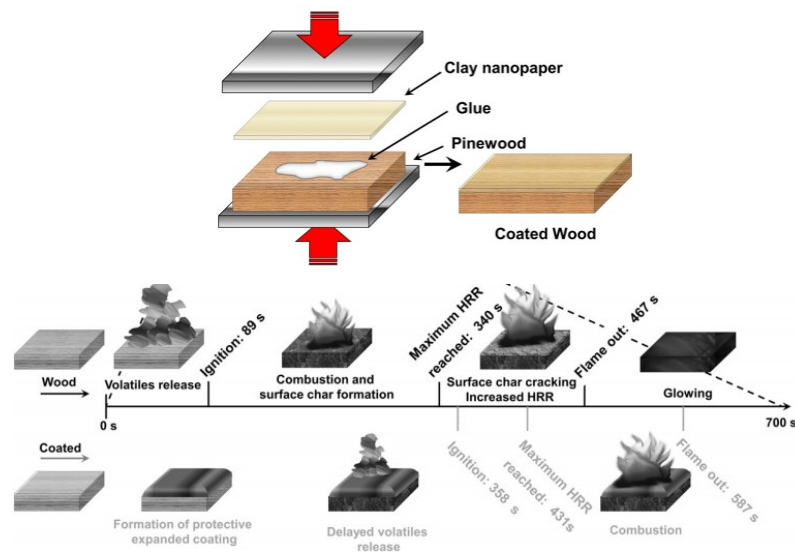
Figure 2.22. Use of brick and mortar coating as fire retardant [164]

Clay nanopaper composed of montmorillonite and cellulose nanofibers, characterized by brick and mortar structure has been used as fire protective coating for wood [164]. The authors demonstrated a strong increase in the time required to reach ignition and a reduction (−33%) in the total heat release during combustion when exposed to a heat flux typical of developing fires (35 kW/m^2). The heat transmitted to the wood substrate is substantially reduced (−81%).

48

The clay nanopaper also has favourable gas barrier properties, hindering diffusion of both oxygen and degradation products coming from the flame. Both functions, of thermal shielding and gas barrier, contribute to delayed thermal degradation of substrate and delayed emission of volatile combustible gases.

Another application can be found in the lightning strike protection (LSP) field. Brick and mortar composites can be used to replace or reduce the weight of the current metallic mesh used to disperse lightning strikes at the surface of the composite structure of the aircraft [167]. Thanks to their high electrical conductivity, they form a crosslinked conductive network on the surface of the material. It has been demonstrated that the lightning damage resistance of CFRP can be improved by depositing a uniform and sufficient protection layer of RGO on CFRP through a liquid composite moulding process [166]. The presence of the coating changes the electrical path, flowing through the conductive layer rather than through the inner CFRP, significantly improving the electrical conductivity (Figure 2.23). The damage caused by the lightning strike is extremely reduced, halving the extension in depth with respect to the uncoated CFRP (Figure 2.24).

Other works [165] showed that the combined use of carbon nanotubes (CNTs) and graphene nanoplatelets (GNPs) synergistically reduced the CFRPs surface resistivity by four orders of magnitude and increased the thermal conductivity by more than 7 time, opening up possibilities for the replacement of metallic mesh structures for EMI shielding and LSP. Long and tortuous CNTs can bridge adjacent GNPs and inhibit their aggregation, resulting in a larger specific surface area and more conductive pathways and faster surface heat transfer through the coating layer. A facile method, for instance, is spray coating, which is able to deliver CNTs and GNPs into CFRPs in a controllable and scalable manner.
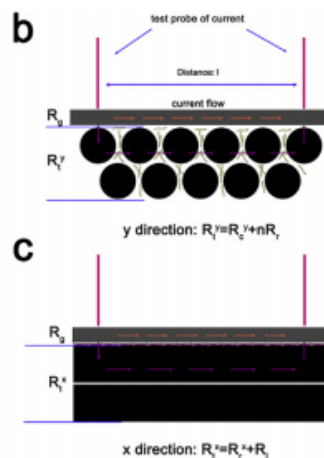
Figure 2.23. Use of brick and mortar coating to improve LSP of CFRPs [166]
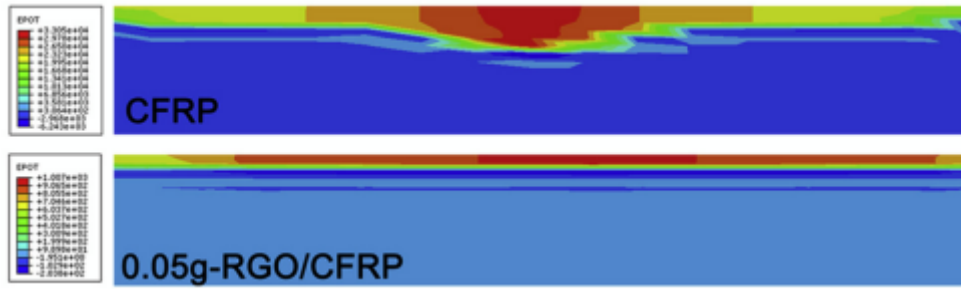
Figure 2.24. Electrical potential distribution in the cross-section view with and without coating [166]

GNP papers can also be embedded in GFRP composites to improve the EMI shielding effectiveness [180]. Even though improvements in electrical conductivity were found by embedding exfoliated graphene nanoplatelet paper in GFRP, the presence of the inner GNP layer negatively affects the overall mechanical behaviour of the material. This suggests that an effective way to improve EMI shielding effectiveness of GFRP, without modifying the mechanical behaviour of the composites could be by inserting the graphitic paper as an outer layer.

2.5 Strategy to optimize the mechanical and functional properties of high filler content composites

From a critical analysis of the literature data, it emerges that the best mechanical properties in composites with high content of 2D nanofillers are achieved when the bonding and interactions between nanoparticles and the polymer are strong and when the matrix molecular mobility is such that the polymer intercalates between nanoplatelets, covering their entire surface. This means that high-performance and mechanical improvements need high interfacial attraction between fillers and the surrounding matrix able to guarantee the load transfer.

One way to maximize the interfacial interactions is by improving chemical bonds between the filler and matrix by functionalizing nanoparticles, using covalent, ionic or hydrogen bonding forces and by accurately selecting the matrix [188,189].

Basically, the filler/matrix compatibility is at the base of the optimal performance of the material. Both the chemical bonding and the matrix wettability have to be chosen in order to optimize the compatibility between the two phases (Figure 2.25).
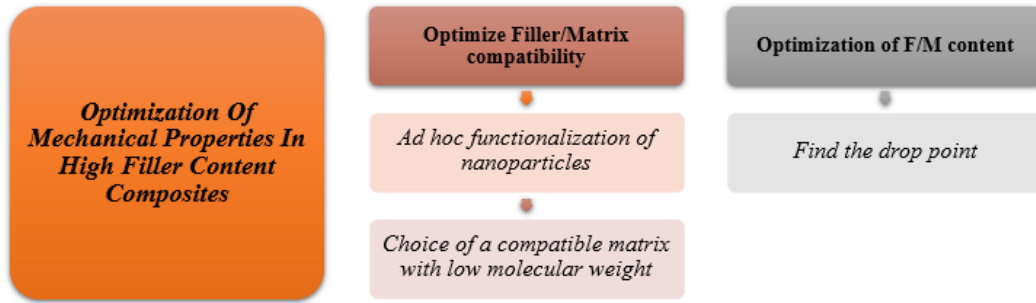
Figure 2.25. Strategy to optimize the mechanical properties of high filler content composites

At the same time, these features also influence the multifunctional properties of nacre like material. In fact, both thermal and electrical conductivities strongly depend on the filler intrinsic properties and dispersion, the filler/matrix interface, and the filler content and orientation.

In conclusion, by improving the mechanical properties of the material and by exploiting its functionalities it is possible to fabricate multifunctional innovative materials with outstanding characteristics that can be employed in different fields and several applications.

3. MANUFACTURING AND EXPERIMENTAL CHARACTERIZATION OF COMPOSITES WITH HIGH GNPS CONTENT

In this chapter, the morphological, mechanical and thermal behaviour of composite with high filler content is investigated. Experimental investigation is fundamental for the characterization of materials properties. The objective of the study is to investigate the mechanical and functional properties of composite reinforced with high content of lamellar nanoplatelets, in particular, graphite nanoplatelets (GNPs). First, a set up procedure has been developed for preparing nacre-like materials with high filler content and with well aligned lamellar architecture. Then, both morphological, mechanical, and thermal analyses are performed. In particular, the influence of filler content, matrix type and nanoplatelet aspect ratio on mechanical and thermal behaviour is investigated.

3.1 Materials

Graphite nanoplatelets (GNPs), called G2Nan, used for the experimental campaign are produced by NANESA srl, industrial partner of the PhD programme. The single particle has average lateral size and thickness of 30 μm and 14 nm respectively and a specific surface area (BET) > 30 m^2/g (Figure 3.1a-b) [190]. GNPs consist of small stacks of graphene layers

obtained from exfoliation of graphite. The graphene sheet that forms the basal plane of these platelets is identical in composition to the graphene wall of a carbon nanotube, but in a flat sheet form. The size and morphology of nanoplatelets makes these particles especially effective at providing barrier properties, while their graphene structure makes them excellent thermal and electrical conductors.

The micro-Raman spectroscopy characterization (Figure 3.1c) shows that: D band has a low density and width, while the G band has high intensity and sharpness, indicating low concentration of defects on the surface of the material. Furthermore, G2Nan has a L_D ratio of 3.10, which indicates that it is highly exfoliated.

(a)   (b)

(c)
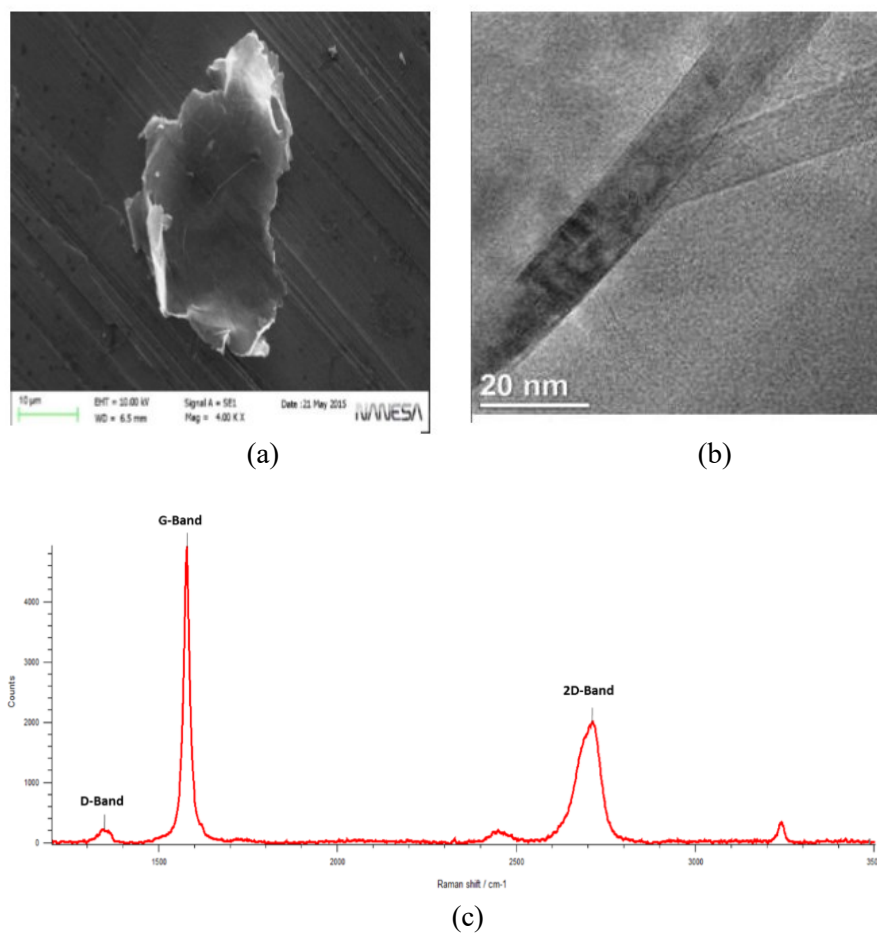
Figure 3.1 G2NAN characterization: a) SEM micrograph. The scale is 10 μm; b) HRTEM micrograph of G2Nan section. The scale is 20 nm: c) Raman spectrum

A sustainable set up fabrication procedure to produce composites with high GNP content is developed by NANESA S.r.l. Pre-impregnated papers with variable thickness of 10 to 100 μm, called GPregs are fabricated. They consist in flexible thin sheets with high filler loading, variable from 50 to 95 wt%, bonded together by a low content polymeric matrix (50 to 5 wt%).

GPregs with different fillers and matrixes are fabricated in order to investigate different behaviour. As filler, in addition to G2Nan, other GNPs with higher aspect ratio are chosen: AVA1240, with lateral size 30 μm and thickness of 4 nm and AVAN GRP 440 with a lateral size of the single particle of 96 x 42 μm and a thickness of 8 nm and a specific surface area (BET) 56 m^2/g, both produced by the Spanish company AVANZARE.

As binder, both thermoset and thermoplastic polymers have been employed in order to investigate different behaviours: two aeronautic epoxy resin, HexFlow® RTM6 and ALTANA, a polyurethane ICAFLEX ADB562 and then a thermoplastic vinyl copolymer VINNOL® H 40/50. RTM6 is a degassed monocomponent resin purchased from Hexcel, specially developed to fulfil the requirements of the aerospace and space industry in advanced resin transfer moulding processes (RTM) [191]. ICAFLEX ADB562 is an aromatic polyester polyurethane (PU) with high hydrolysis resistance and excellent bending resistance [192]. VINNOL® H 40/50 is an extremely tough vinyl copolymer; it shows permanent flexibility, abrasion resistance, little tendency to swell in the presence of water and low gas permeability [193].
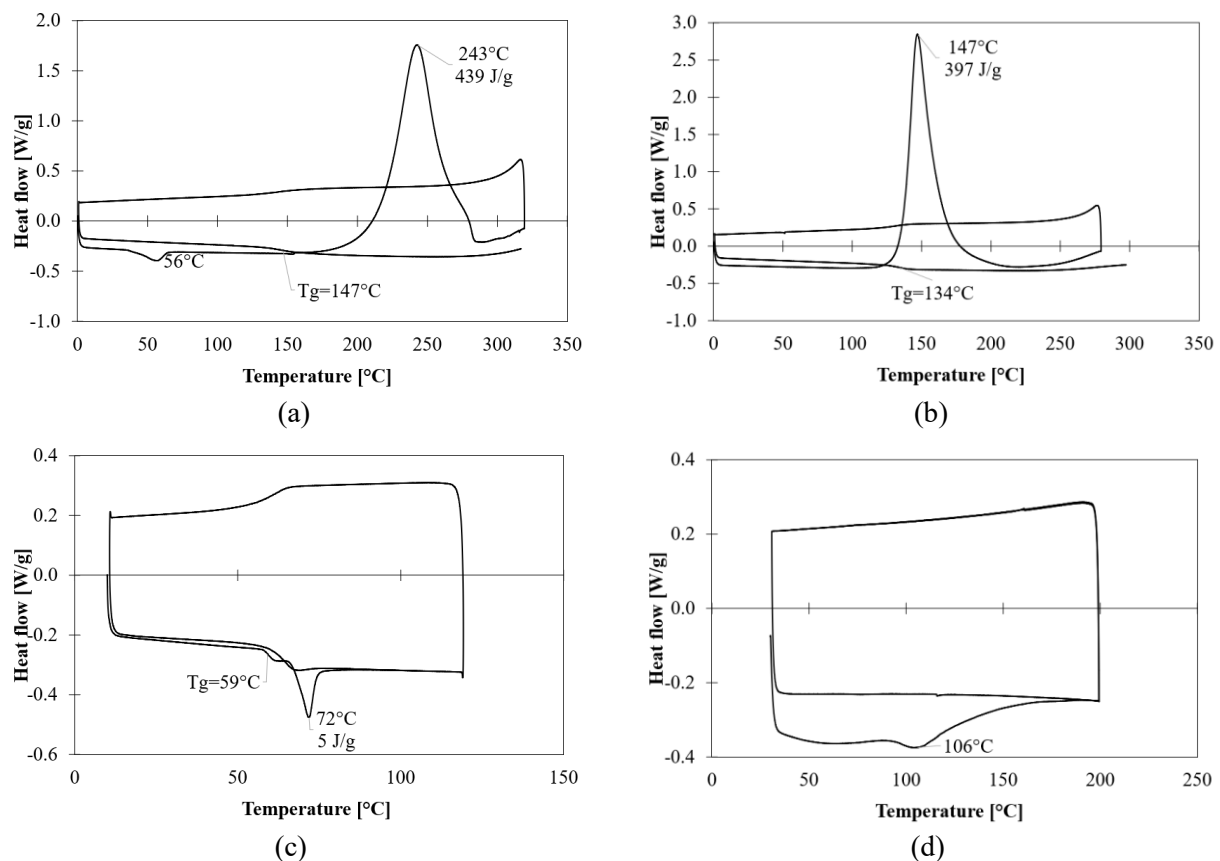
Figure 3.2 DCS on: (a) RTM6; (b) ALTANA; (c) VINNOL H40/50; (d) PU ICAFLEX

All the matrices have been characterized by differential scanning calorimeter (DSC), using DSC Discovery [194]. Samples are heated with temperature ramp of 10°C/min from room temperature to a specific temperature, avoiding the degradation of the material. Double scan is considered, with an intermediate cooling ramp of 10°C/min. RTM6 exhibits high glass transition temperatures, around 147°C, and a reticulation peak at 243°C with an energy of 439 J/g (Figure 3.2a); ALTANA shows the reticulation peak at 147°C with an energy of 397 J/g (Figure 3.2b) and the thermoplastic H40/50 shows a fusion peak at 72°C and a glass transition temperature (T_g) at 59°C (Figure 3.2c). Finally, the polyurethane ICAFLEX, which does not have the hardener, shows a flat heat flow curve. The peak at 100°C indicates the evaporation of the solvent, in which it is diluted (Figure 3.2d). For RTM6 a cure cycle at 160°C for 90 min is chosen, followed by a post-cure cycle at 180°C for 1 hour, as described in ref. [195].

3.1.1 Spray deposition process

GPregs are fabricated by spray deposition process. This process is simple and easily scalable to massive production. The GNPs particles are dispersed in acetone and mixed with a solution of epoxy diluted in acetone previously prepared (10 wt% of epoxy) by ultra-sonication (Figure 3.3a). The obtained paste is then deposited on a silicon non-sticky support by means of a semiautomatic tri-axes pantograph (Figure 3.3b). The material is then dried all night at room temperature to let the solvent to evaporate (Figure 3.3c). Then, the deposition is calendared to compact the material, reducing the thickness of four times respect to the initial deposition and to promote particle orientation; the final pre-impregnated layer is obtained by pressing the layer at increasing compaction pressure up to 10 bars (Figure 3.3d) [196,197]. Finally, the GNP/Epoxy films are cured according to the resin polymerization process. This process allows to produce paper of 20×20 cm^2 of variable thickness (Figure 3.4), from 10 to 100 μm, with different matrix content (from 50 wt% to 90 wt%) [43,118,198]. Pure GNP films (100 wt%) are fabricated in a similar manner: firstly, the film is prepared with a very low amount of resin (<5 wt%) and then it is burned in order to eliminate the polymer.

This process allows the fabrication of flexible thin paper reinforced with high content of lamellar nanoparticles. Their geometry (i.e. high aspect ratio) combined with the processing technology ensure that the nanoparticles are well aligned in plane, thus resembling the nacre nanoarchitecture. Therefore, these materials exhibit an isotropic behaviour in plane, and an anisotropic behaviour out of plane, as it will discussed in the following sections.
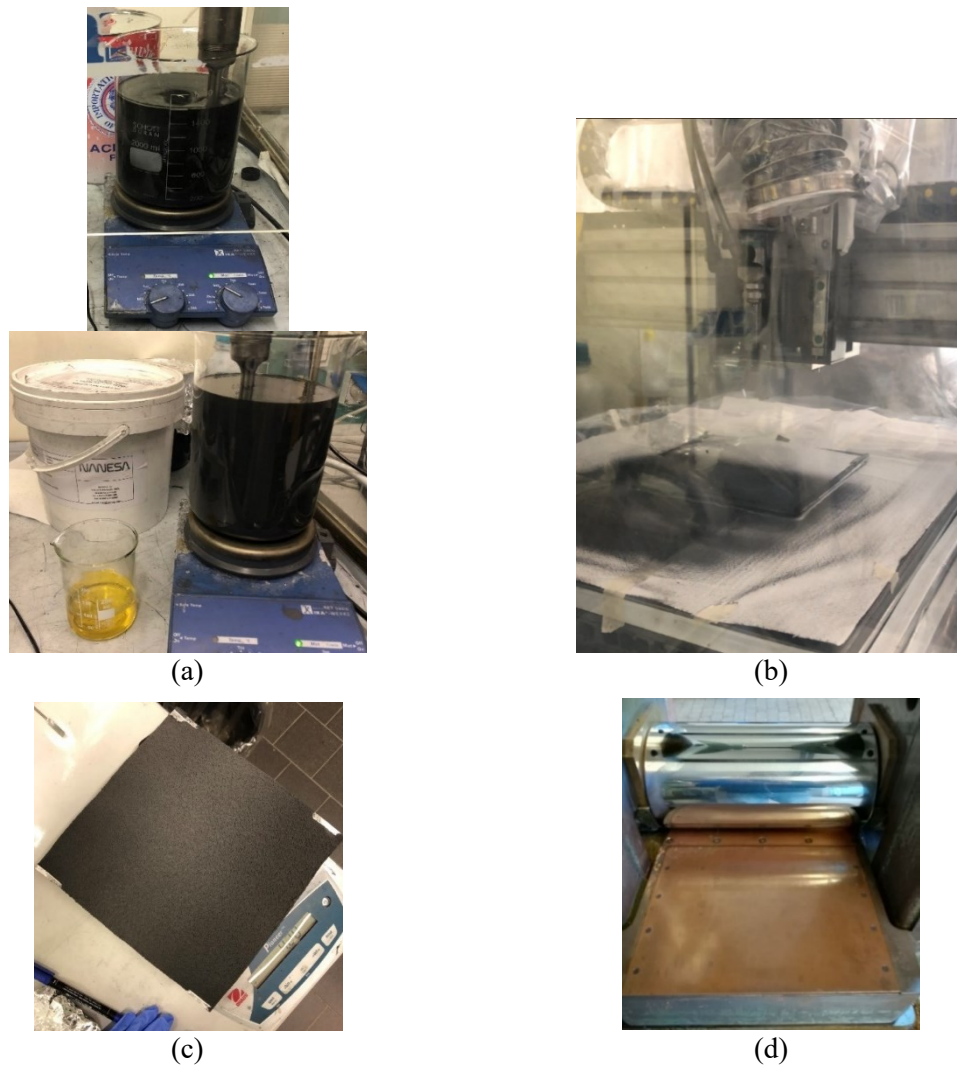
Figure 3.3. GPres manufacturing process: a) Dispersion and mixing of GNP particles in acetone with epoxy; b) Cold spray deposition; c) Solvent evaporation at room temperature; d) Calendaring
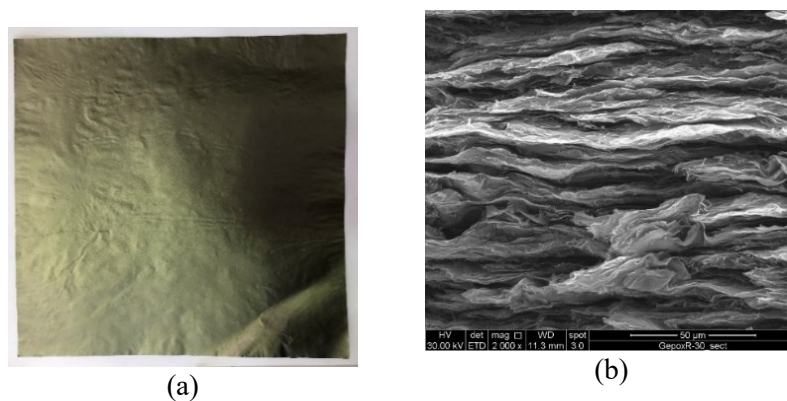
Figure 3.4. GNP-Epoxy thin film: a) Compacted paper; b) SEM image of film cross section

3.1.2 Evaluation of GPregs uniformity and of resin distribution

Thermogravimetric analysis (TGA) is employed both to evaluate the actual content of GNP in the samples and to evaluate the resin distribution within the paper. GPreg is divided in three main areas as shown in Figure 3.5: centre, side, corner. For each part, three square specimens of side 1 cm and a weight of 7-9 mg are cut.
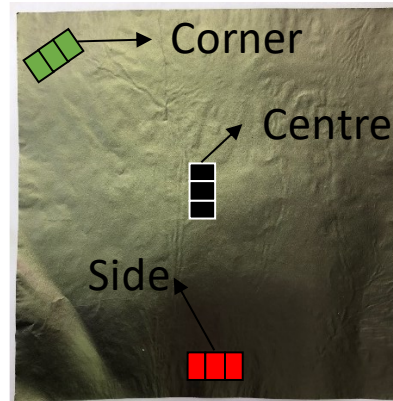
Figure 3.5. GPreg mapping

All the analyses are performed in inert atmosphere, using nitrogen gas, with a temperature ramp of 10°C/min from room temperature to 800°C. The weight loss is evaluated at 600°C, temperature at which the percent residue from heating the pure resin is 10.3% [195,199].

During the fabrication process, (deposition phase and calendaring) the samples can be affected by inhomogeneity:

- During the spray deposition, the flow could be not uniform in terms of quantity and content, making the deposition thicker in the centre with respect to the edges (Figure 3.6a).
- During calendaring process, the very small gap between the rollers, while reducing the thickness, can cause a resin flow from the centre to the edges (Figure 3.6b).

a)

b)
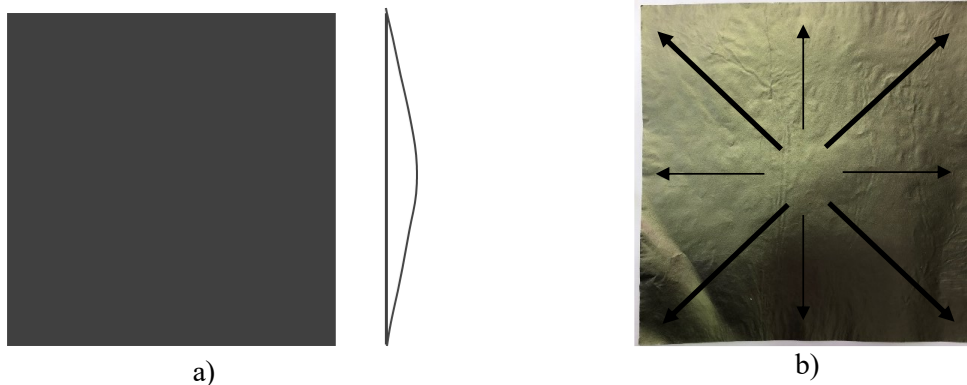
Figure 3.6. Causes of not uniformity of resin distribution within GPregs before (a) and after (b) calendaring

However, from the analysis, it appears that the resin distribution in the paper is almost uniform, as shown in Figure 3.7, confirming the good quality and reproducibility of the process.

(a)   (b)
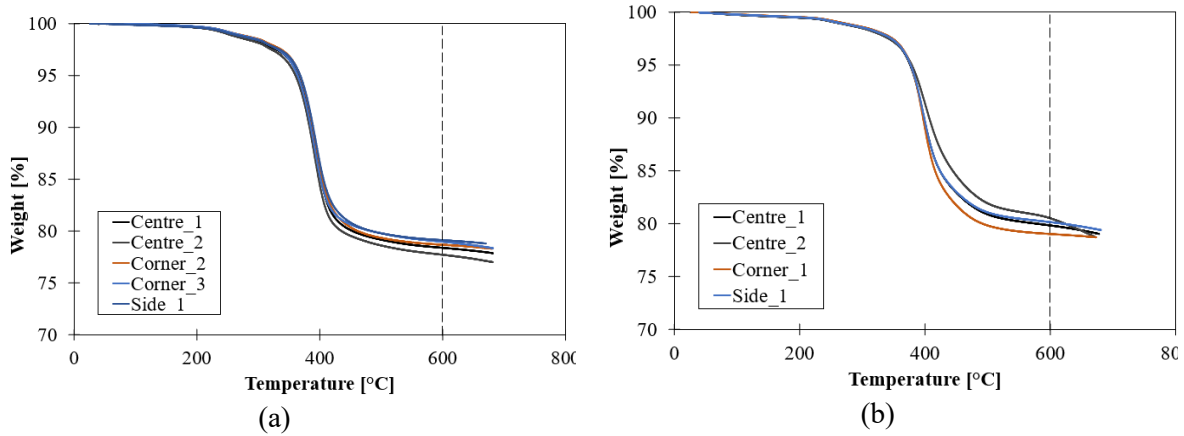
Figure 3.7. TGA mapping results on GPregs with 70%wt GNP: a) Before, b) After calendaring

3.2   GPreg characterization

Table 3.1 GPreg charachterization test list

	TGA	SEM	Mechanical properties in tension	Thermal properties
Filler content	✓	✓	✓	✓
Binder type	✓	✗	✓	✗
Filler aspect ratio	✓	✗	✓	✓

3.2.1   Thermogravimetric analysis (TGA)

Thermogravimetric analysis (TGA) (TA Instruments Q500) is adopted to evaluate the actual content of GNP in the samples. All the analyses are performed in inert atmosphere, using nitrogen gas, with a temperature ramp of 10°C/min from room temperature to 800°C and the weight loss is evaluated at 600°C. When calculating the real matrix content in GPregs and laminates, the weight loss of epoxy is considered. In particular, at 600°C it is 90% as shown in Figure 3.8.
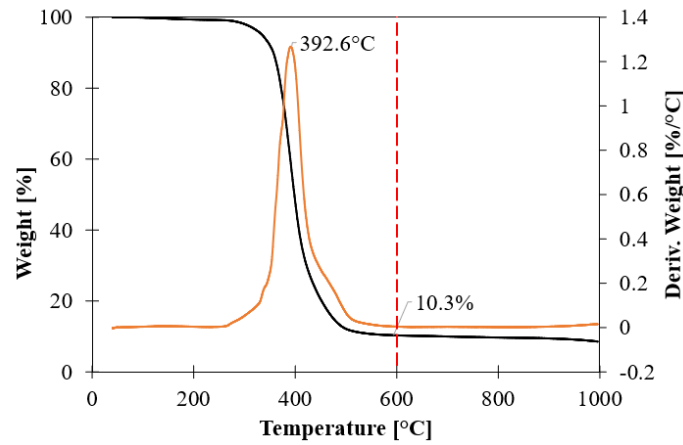
Figure 3.8. TGA in nitrogen for RTM6

The residual weight, obtained from TGA on composites, is the sum of the residual weights associated to the filler and to the matrix:

$$
\begin{aligned}
W_{residual} &= W_f + Y \cdot W_m = \\
&= w_f W_C + Y \cdot w_m W_C = \\
&= w_f W_C + Y \cdot (1 - w_f) W_C
\end{aligned}
\tag{3.1}
$$

Where W_f is the filler weight, Y is the residual weight obtained when burning only the polymer, W_m is the resin weight, W_C is the composite weight and w_m e w_f are the filler and resin weight fractions.

Consequently, the filler weight fraction can be expressed as follow:

$$
w_f = \left(\frac{W_{residual}}{W_C} - Y \right) \cdot (1 - Y)
\tag{3.2}
$$

Finally, the volume fractions v_f are computed starting from the real weight fractions and according to Eq. (3.3).

$$
v_f = \frac{w_f}{w_f + (1 - w_f) \cdot \dfrac{\rho_f}{\rho_m}}
\tag{3.3}
$$

Where ρ_f and ρ_m are the filler and matrix densities (equal to 2 g/cm^3 for GNPs and 1.4 g/cm^3 for RMT6).

Thermogravimetric analysis on GNP/Epoxy (RTM6) films shows that the nominal filler content slightly underestimates the real one, as shown in Figure 3.9 and Table 3.2.
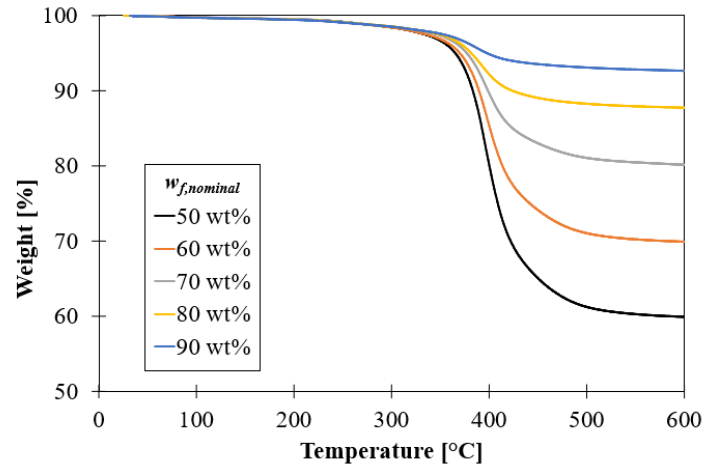
Figure 3.9. TGA for GPregs for different filler/matrix content

Table 3.2. Real matrix content in GNP/Epoxy films

Nominal weight fraction	Actual weight fraction	Volume fraction filler
$w_{f,nominal}$ [%wt]	$w_{f,real}$ [%wt]	v_f [%vol]
50	56	42
60	67	53
70	78	67
80	89	82
90	94	91
100	100	100

3.2.2 Morphological assessment (SEM; AFM)

The morphology of GNP/Epoxy films has been investigated employing scanning electron microscopy (SEM) (FEI Quanta 200 FEG). Samples are fractured in nitrogen to have a picture of the internal section. Figure 3.10 shows SEM images of the cross section (fractured surface) of GNP/Epoxy films with nominal filler content of 50, 60, 70, 80 wt%. The morphological analysis shows that the particles are highly oriented in the longitudinal direction, with a laminated inner architecture and uniform texture. A closer inspection reveals that the particles are aligned, but wrinkled. Therefore, albeit the distribution of lamellar particles is overall good, some empty areas can be detected which can, in principle, affect the bonding between the nanoplatelets. In particular, by decreasing the resin content, the inner structure becomes organised with nanoplatelets leaned on the film plane up to a critical GNP content (70 wt%). Above this critical content the inner structure is threaten by dry spots and empty areas.
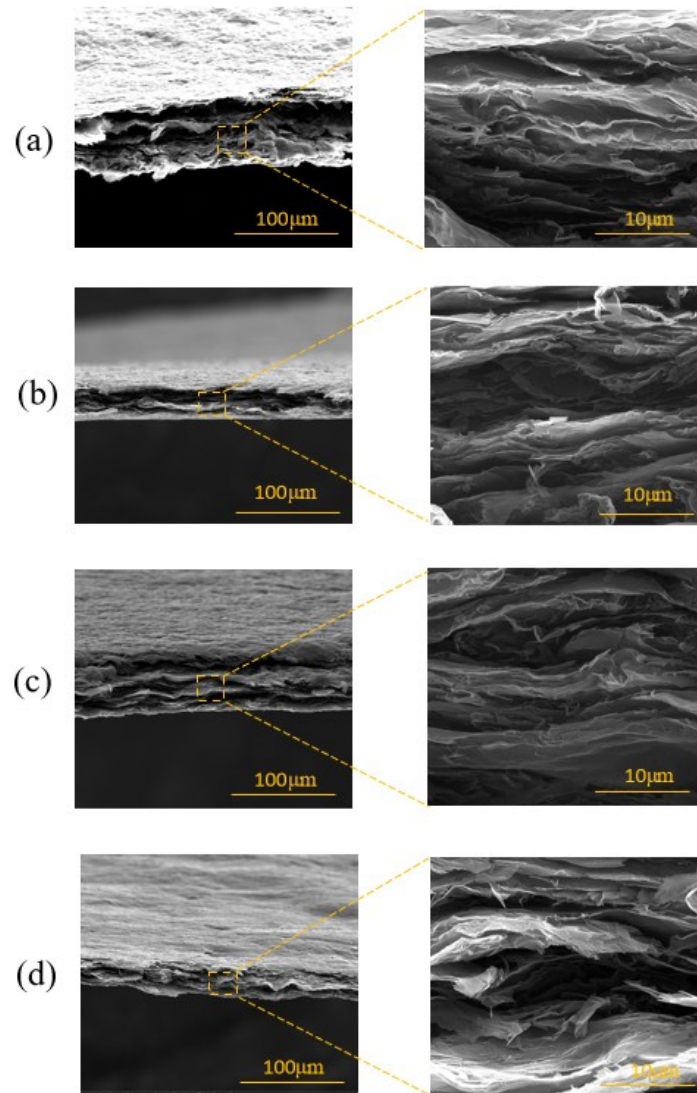
Figure 3.10. SEM images at two different magnifications of GNP/Epoxy filler with different nominal filler content: a) 50 wt%; b) 60 wt%; c) 70 wt%; d) 80 wt%

Atomic force microscopy (AFM) is employed to investigate the topography of the sample and the resin distribution within the films. High-resolution pictures are taken to investigate the topography of the samples using Bruker Dimension Icon atomic force microscope with ScanAsyst in the PeakForce Tapping mode (tip stiffness 0.4N/m, frequency ~70kHz). Analysis of morphological features has been carried out using the cross-section tool of the Gwyddion software.

AFM allows for better investigation of material morphology. The topography of an internal layer of the GNP/Epoxy film with 60 wt% and 70 wt% filler content is shown in Figure 3.11a-b, confirming that it consists of an assembly of stacked GNPs, with typical structural corrugations (wrinkles and folds). A further inspection into higher resolution AFM images (Figure 3.11c-d) reveals the presence of several droplet-like features, which could be attributed

to a discontinuous polymeric phase. The morphology of the material does not vary in samples with 60 wt% to 70 wt% filler content, but the average size of the droplets decreases with the increase of filler content. In particular, the sample with 60 wt% filler content showed several clusters of lateral size of about 650-1000 nm. Accordingly, the matrix partial coverage of the nanoplatelets could affect the mechanical properties of the composite, causing the observed reduction of the elastic modulus and tensile strength at very high filler content.
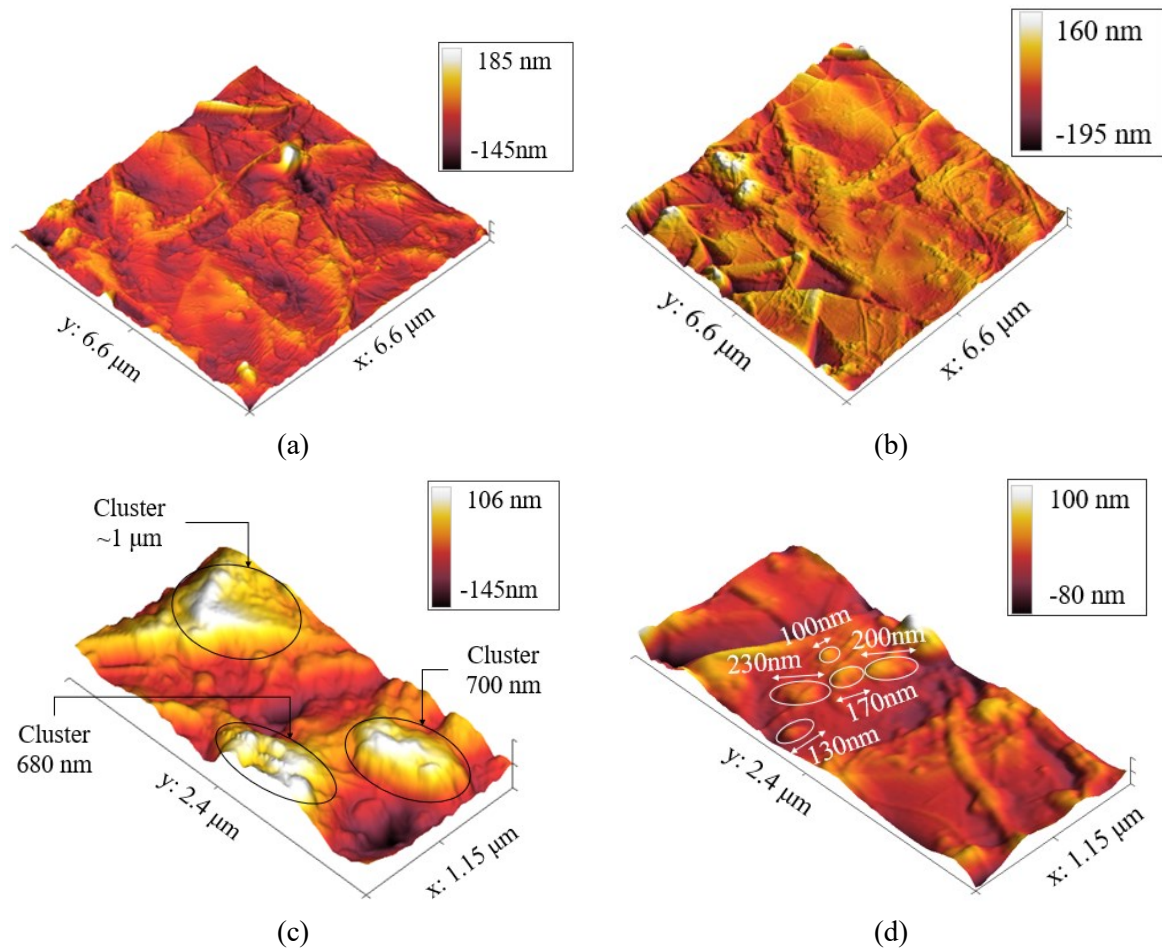
Figure 3.11. AFM images of GNP/Epoxy films: Topography of sample with 60 wt% (a) and 70 wt% filler content and respective magnification with droplet-like features (c, d)

3.2.3 Mechanical characterization

Mechanical characterization of the GNP/Epoxy films is performed by using a micro-tensile tester (DEBEN MT200), equipped with a 200 N loadcell. Tensile tests are conducted by applying an incremental strain rate of 0.012 min^{-1}. Rectangular specimens of dimensions 5 mm × 40 mm are clamped at both ends and are aligned with dual threaded leadscrews. Thickness is measured with a digital micrometre in several locations of the gauge length and ranges between (0.06-0.08) μm.

(a)

(b)

(c)
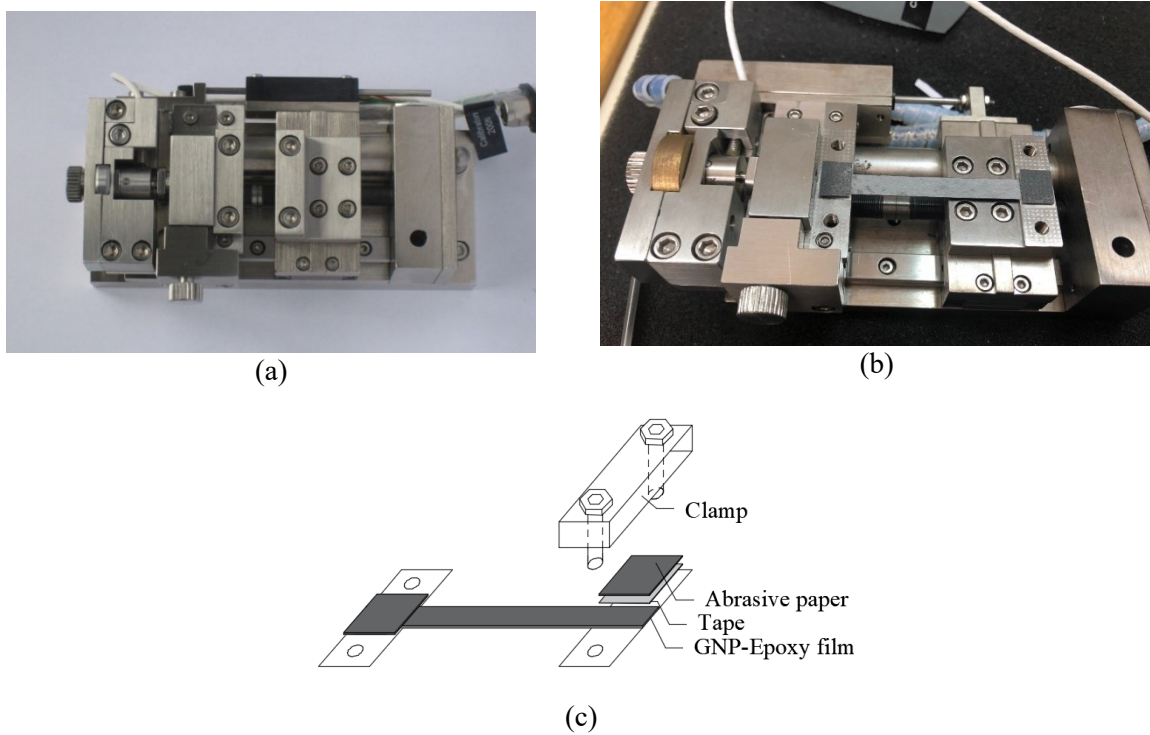
Figure 3.12. Tensile tester: (a) Instrument; (b) Sample positioning; (c) Schematic representation of clamping system
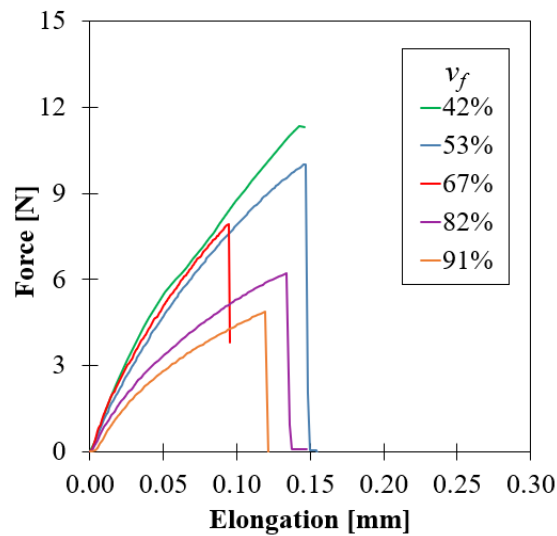
Figure 3.13. Force-elongation plot acquired from the tensile test

Samples are mounted horizontally, clamped to a pair of jaws, and supported on stainless steel sliding bearings, as shown in Figure 3.12. A dual threaded leadscrew drives the jaws symmetrically in opposite directions, keeping the sample centred in the field of view. The load cell and elongation sensors' high sensitivity allow the measurements of small force and displacement changes. The acquired force-elongation data of Figure 3.13 are analysed, and stress-strain data are computed according to Eq. (3.4) [200].

$$\varepsilon = \frac{\Delta l}{l}$$
$$\sigma = \frac{F}{A}$$

(3.4)

The elastic moduli at very low strain (0-0.05%) are evaluated according to Eq. (3.5):

$$E_{0-0.05\%} = \frac{\sigma(0.05\%)}{0.05\%}$$

(3.5)

Stress strain curves (Figure 3.14a) obtained from tensile tests show that the material has a pseudo-elastic behaviour: for small deformations, the behaviour is linear, as shown in Figure 3.14b, then the slope slowly decreases until a brittle failure occurs [118]. The elastic modulus at very low strain, evaluated in the range 0-0.05%, exhibits a maximum for filler content of 67 vol% (Figure 3.14c). For low filler content, the elastic modulus of the composite is well approximated by the rule of mixture with GNP modulus of 25 GPa, resembling that of graphite [50]. With the increasing filler content the elastic modulus of the composite drops, deviating from the rule of mixture, as shown in Figure 3.14c. Likewise, the tensile strength exhibits the maximum value for filler content of 53 vol% (Figure 3.14d). Similar mechanical behaviour has already been observed in literature for nacre-like composites [22–27,29] where at very high platelet concentration, the material failed in a brittle fashion, due to possible misalignment of the bricks and issues associated to polymer infiltration between the nanoplatelets [29].

This phenomenon could be ascribed to an inefficient load transfer between matrix and nanoplatelets attributable to a discontinuous resin distribution within the nanoplatelets, as observed from AFM analysis. Therefore, since nanoplatelets are partially covered, the stress transfer is negatively affected and the mechanical properties at high filler content are deteriorated.

Table 3.3. Results of tensile test on GNP/Epoxy films

Volume fraction filler v_f [vol%]	Elastic modulus E_c [GPa]	Tensile strength σ [MPa]	Elongation at break ε [%]
42	11.28±0.61	26.72±1.48	0.37±0.02
53	14.39±1.55	32.98±2.68	0.35±0.04
67	14.76±1.03	24.44±1.49	0.25±0.02
82	12.11±1.70	23.38±1.61	0.33±0.06
91	11.53±1.43	20.73±3.30	0.30±0.06

(a)

(b)

(c)

(d)
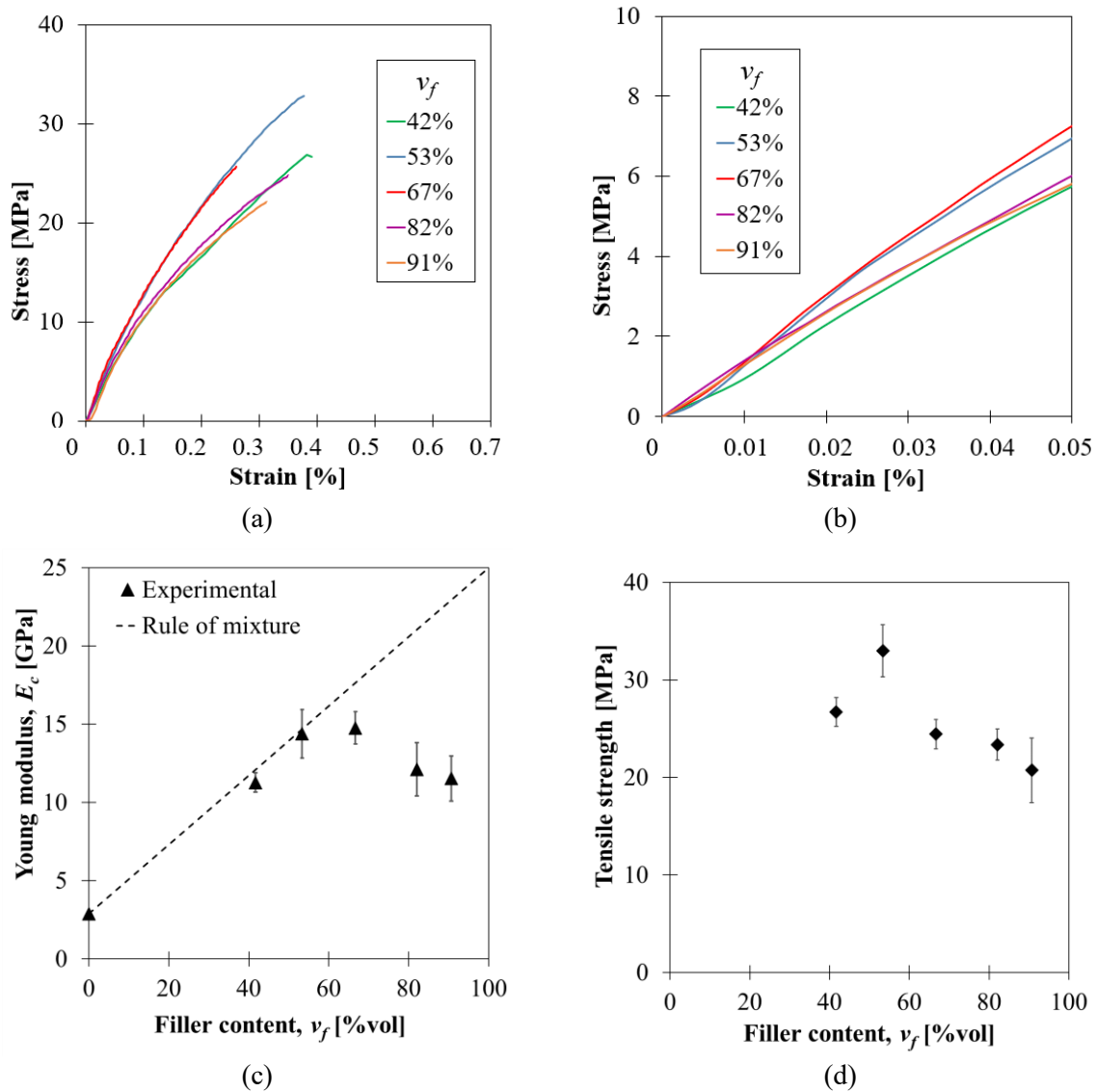
Figure 3.14. Mechanical properties in tension of the produced GNP/Epoxy films: (a) Stress-strain curves; (b) Enlargement in the range of 0-0.05% strain; (c) Tensile strength; (d) Young's modulus

The dissipative behaviour of GPregs with no binder and of GPregs with GNP content of 80 and 70 wt% has been evaluated by dynamic mechanical analysis (DMA) with TA Instrument Q800. Test were conducted in bending studying the frequency response at room temperature. Table 3.4 compares the storage modulus and the damping factor, tanδ, of manufactured laminates. The storage modulus shows a trend dissimilar to the elastic modulus evaluated by tension film tests: it increases with compaction pressure, but the increase of the resin content results in a slight decrease of the bending modulus. GNP neat paper shows a very high capacity to dissipate mechanical energy in bending mode. The damping factor of GPregs strongly decrease respect to the neat paper, but it keeps the same order of magnitude of the damping factor tanδ of the polymer matrix (RTM6 @room temperature @1 Hz tanδ=0.021). The

65

damping effect of GNP in high content composites may be attributed to the heterogeneity of the system during dynamic loading and to an excellent intrinsic damping property of GNPs. In addition, the coexistence of a soft-domain (polymeric mortar layer) and a hard domain (graphitic bricks) could affect the molecular mobility leading to an increased energy dissipated.

Table 3.4. DMA data for GPregs at different filler content

Filler content [wt%]	P=1 bar		P=100 bar	
	E [MPa]	tanδ [–]	E [MPa]	tanδ [–]
100	0.71±0.64	0.44±0.04	-	-
80	0.55±0.30	0.04±0.02	17.8±7.0	0.027±0.014
70	0.50±0.19	0.02±0.01	11.2±4.7	0.018±0.006

Also, the effect of variation of nanoplatelet aspect ratio and matrix type has been investigated. GPregs with different fillers and matrices are fabricated with filler/matrix content of 70/30 wt/wt. Varying the aspect ratio of GNPs particles from 2143 for G2Nan to 7500 for AVA, the mechanical properties of the composite do not show significant modifications. Comparing the results in Figure 3.15a, there is not a substantial difference in terms of modulus, while strength slightly increases for sample with higher aspect ratio. On the other hand, the influence of the matrix type is significant. The behaviour changes from brittle to ductile according to the nature of the matrix (Figure 3.15b). In fact, the overall behaviour of the composite is governed by matrix behaviour, whether it is linear elastic as in the case of epoxy, or elastoplastic as in the case of vinyl copolymer and polyurethane. For all the samples, a good reproducibility of the results is observed.
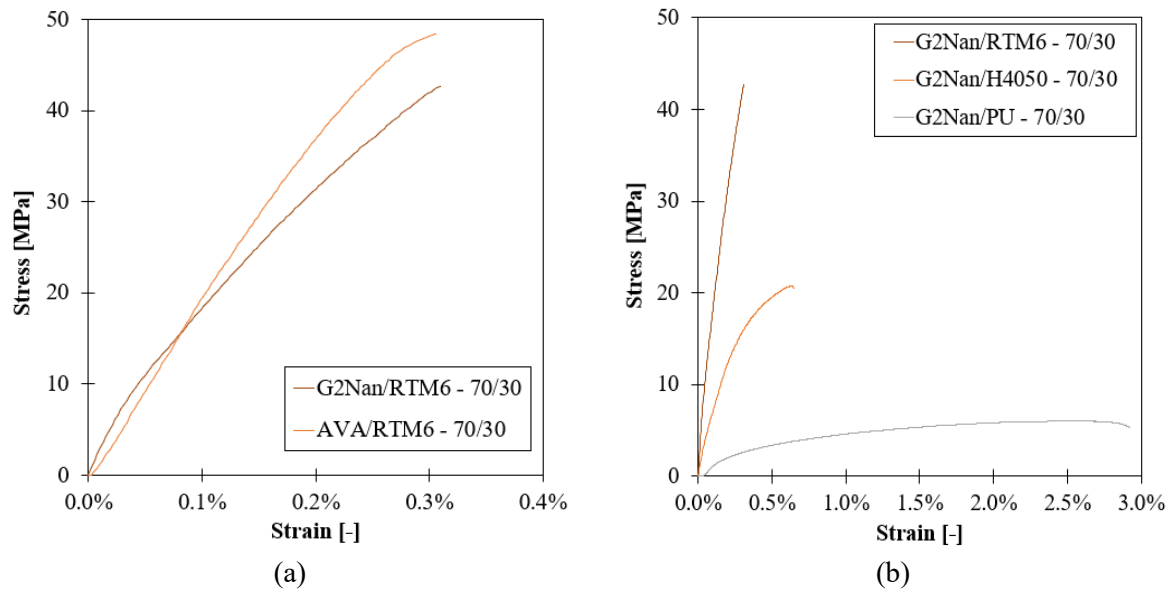
Figure 3.15. Results of tensile tests on GNP-Epoxy film varying filler aspect ratio (a) and matrix type (b)

3.2.4 Thermal properties

The film thermal diffusivities, in plane and cross plane, have been investigated through light flash analysis (LFA), with NETZSCH instrument. This technique is currently the most widely accepted method for precise measurement of the thermal diffusivity. The principle at the base of the measurement is described by Parker et al. [201]. A few millimetres thick specimen is heated by a high-intensity short-duration light pulse, and the resulting temperature history of the rear surface is measured by a thermocouple and recorded [202]. The time needed to heat the rear surface is correlated to the thermal diffusivity of the material and the thermal conductivity is computed as the product of the heat capacity, thermal diffusivity, and the density, according to Eq. (3.6). The higher the thermal diffusivity of the sample, the faster the energy reaches the backside.

GNPs display intrinsic anisotropic thermal behaviour, which is reproduced in GPregs thanks to the good alignment of the nanoplatelets in plane direction respect to cross plane. The in plane thermal diffusivity of GPregs linearly increases with the increasing filler content (Figure 3.16a) as it is expected. In fact, the addiction of polymer, reduces the thermal diffusivity, it means that for high filler content, there are lots of GNP-GNP bridges which allow the heat transfer. Whereas the cross plane thermal diffusivity (Figure 3.16b) is quite constant and slightly increases in the case of pure GNP paper, indicating that the polymer does not affect the thermal properties in the cross plane direction [43]. GPregs with filler content greater than 70 wt% exhibit high thermal diffusivity, higher than that of copper (115mm^2/s). The higher is the filler content the higher is the in plane thermal diffusivity, while cross-plane diffusivity has not a real trend fluctuating close to that of pyrolytic graphite ($\alpha_\perp$=3.6mm^2/s) [203].

Figure 3.17 reports the thermal conductivity as function of the content of GNPs. It is computed as [204]:

$$K = c_p \cdot \rho \cdot \alpha \tag{3.6}$$

$$c_p = \sum_{i=1}^{n} c_{p_i} \cdot w_i \tag{3.7}$$

Where ρ and α are the density and the thermal diffusivity of GPregs and are measured experimentally. c_p is the global thermal capacity of the composites; it is calculated as a combination of the thermal capacities of the single components according to their weight fractions, w_i. The thermal capacity of GNPs and epoxy are 0.71 J/gK and 1.67 J/gK respectively.

(a)   (b)
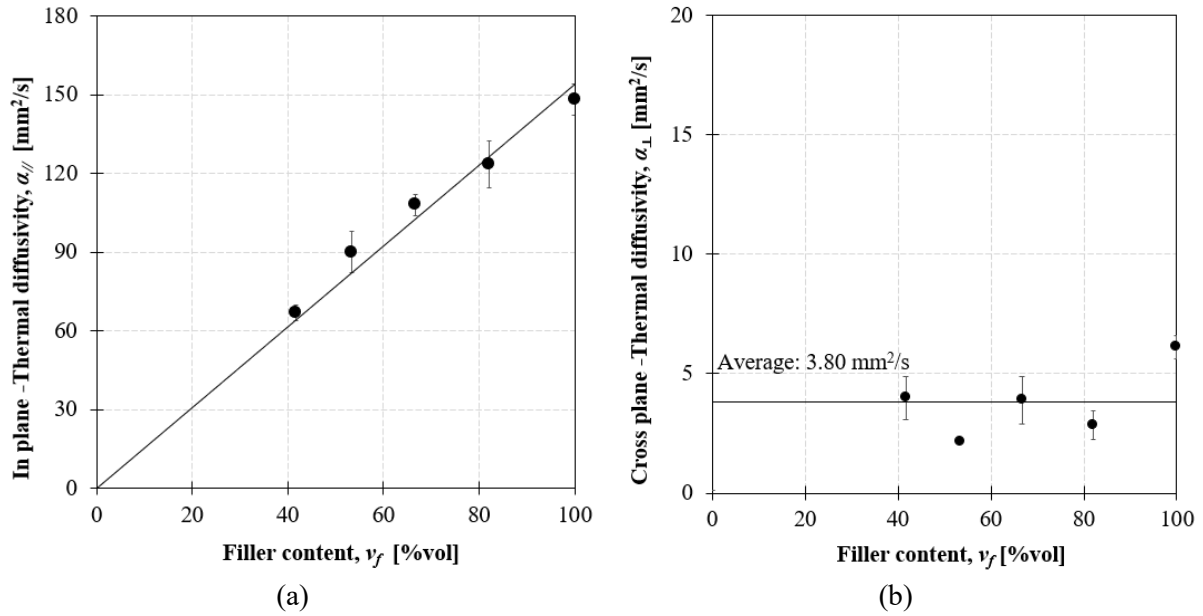
Figure 3.16. Thermal diffusivity trend of GPregs for different filler content: a) In plane; b) Cross plane

Table 3.5. Thermal conductivity of GPregs for different filler content

Filler content [vol%]	ρ [g/cm^3]	Porosity [-]	$\alpha_{in plane}$ [mm^2/s]	$K_{in plane}$ [W/mK]	$\alpha_{cross plane}$ [mm^2/s]	$K_{cross plane}$ [W/mK]
42	1.4	7%	67	146	4.00	8.57
53	1.5	6%	90	181	2.17	4.37
67	1.4	18%	108	216	3.90	7.88
82	1.4	24%	123	232	2.83	5.36
100	1.8	10%	148	242	6.11	4.37
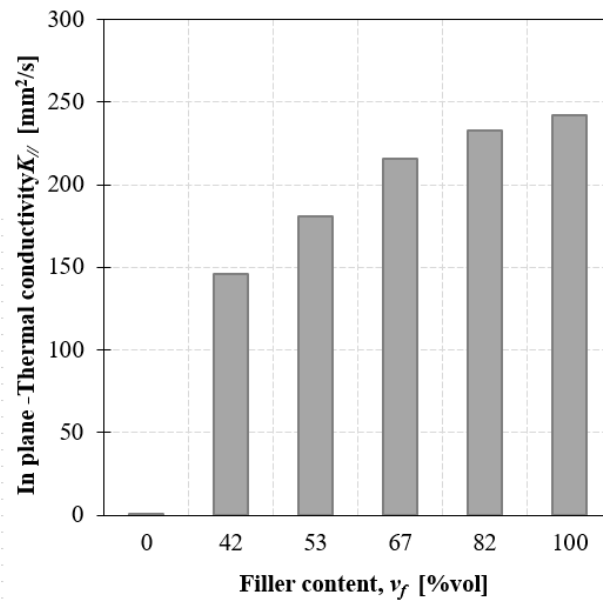
Figure 3.17. In plane thermal conductivity of GPregs

Also, thermal conductivity has an increasing trend with increasing filler content, as shown in Figure 3.17, reaching a maximum of 242 kW/mK for GNP content of 100 wt%.

Therefore, the adopted fabrication route is able to reproduce the anisotropic thermal properties of the graphite nanoplatelet, the only issue is the high porosity detected (Table 3.5). It is evaluated as the variance of the measured density from the nominal density. The voids negatively affect the cross-plane diffusivity, while the good alignment guaranteed by the calendaring stage ensure good correlation between the resin content and the material diffusivity.
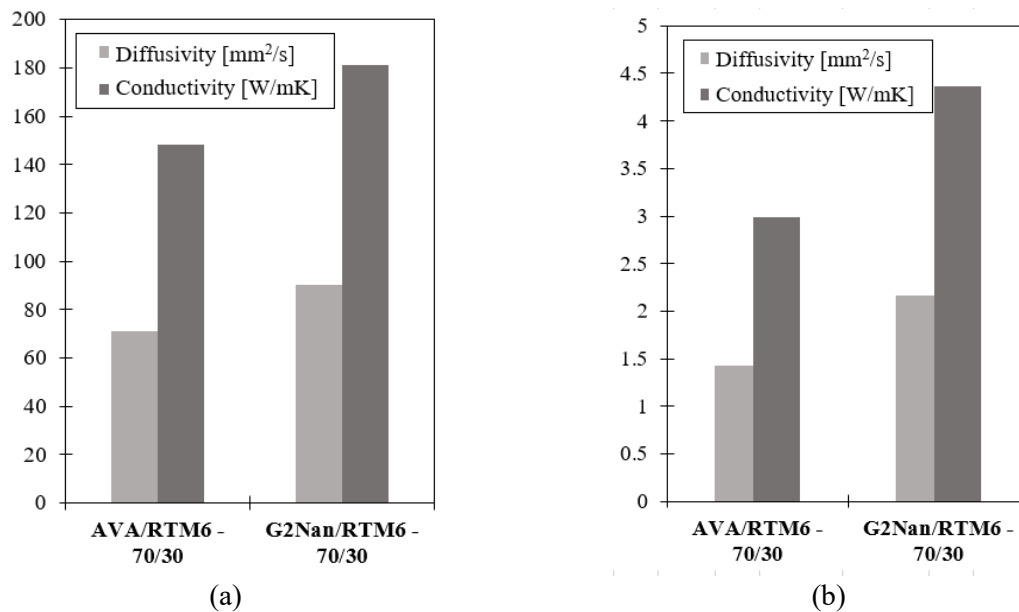
Figure 3.18. Influence of filler aspect ratio on in-plane (a) and cross-plane (b) thermal diffusivity and conductivity

Also, the influence of nanoplatelets aspect ratio is investigated. Thermal behaviour in plane and cross plane of composite produced with G2Nan and AVA nanoplatelets is reported in Figure 3.18. Results show that the increasing of platelets aspect ratio, negatively affected the thermal behaviour.

3.2.5 *EMI shielding*

GNP/Epoxy films could respond to the rising demand of EMI shielding materials. They would be capable of replacing metals, thanks to their low weight combined with excellent electrical conductivity, high thermal stability and anti-corrosion properties [18]. In fact, GNP/Epoxy film with 70 wt% filler content and 65 μm thickness shows a sheet resistance (Rsheet) of 0.33 Ω/sq. This measure is representative of the electrical resistivity of bidimensional systems, which thickness is very small compared to the plane area.

The EMI shielding ability is positively related to the electrical conductivity and thickness of the material, according to theoretical Simon's formula. The electrical conductivity needs to be at least higher than 1 S/m to obtain excellent EMI shielding performance. In general, attenuation of an incident EM wave is given by three contributions: absorption (A), reflection (R), and multiple reflections (B). Reflection is a surface phenomenon, while absorption happens in the composite's volume, and consequently is dependent on the thickness of the material.
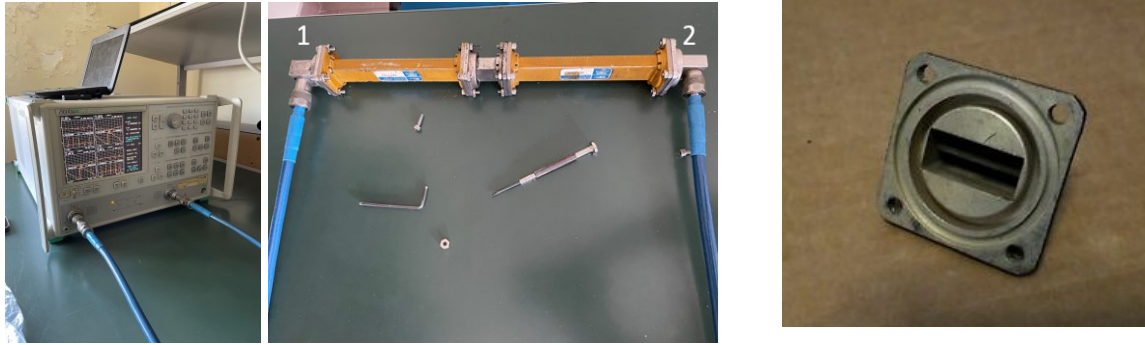
Figure 3.19 X-Band waveguide measurement setup

In this section, the shielding ability of of GNP/Epoxy films with different filler content (from 10 wt% to 90 wt%) is investigated, following the X-band waveguide measurement technique. Preliminary tests are performed at Department of Electrical Engineering and Information Technology of University of Naples Federico II. The X-band refers to a band of frequencies in the microwave radio region of the electromagnetic spectrum within 8-12 GHz. It is used for radar, satellite communication, and wireless computer networks. For these measurements, rectangular samples of dimensions 22.86 mm x 10.16 mm are placed in the middle section of a rectangular guide of the same size (Figure 3.19). During the test, an electromagnetic wave (EM) passes through the guide from one side (1) and is detected at the other side (2). The reflected signal (S11) and the transmitted signal (S21) are recorded, and five measurements are collected for each sample. The signal analysis gives an estimation of the capability of the material to attenuate the electromagnetic waves. The reflection, absorption and transmission contributions are computed according to Eq. (3.8) [179].

$$
\begin{aligned}
R &= |S11|^2 \\
T &= |S21|^2 \\
A &= 1 - (R + T)
\end{aligned}
\tag{3.8}
$$

Figure 3.20 and Figure 3.21 report the signals S11 and S21 for samples with 10 wt% and 90 wt% filler content. Test showed that for high GNP content, the EM is mostly reflected, while for low GNP content this contribution is lower. In both cases the trasmitted signal is low.
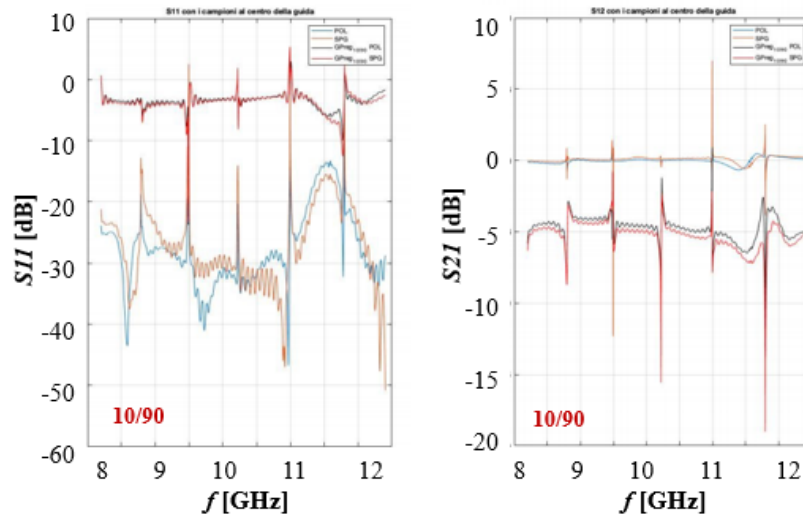
Figure 3.20 Reflected and transmitted signals in GNP/Epoxy films with 10 wt% filler content
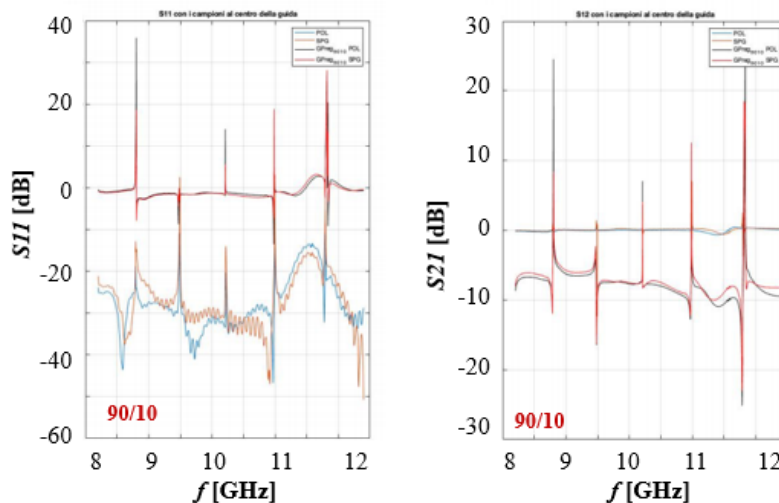
Figure 3.21 Reflected and transmitted signals in GNP/Epoxy films with 90 wt% filler content

The absorption contribution, computed according to Eq. (3.8), for different filler content is reported in Figure 3.22. This contribution decreases with the increasing filler content, since it is associated to the inner structure of the material. In fact, while the reflection efficiency is directly related to the surface electrical conductivity, the absorption efficiency depends on the thickness of the sample and involves the overall volume of the composite. By observing the SEM images of Figure 3.23, it appears that for high filler content, the material has a well-ordered nanostructure with nanoplatelets oriented in plane direction. In this configuration, when the EM wave crosses the material, it is mainly reflected. On the contrary, for low filler

content, the nanostructure is less organized, with nanoparticles randomly oriented in the volume. In this case, a small absorption contribution appears, highlighting the ability of the GNPs to dissipate the EM waves in the plane direction.
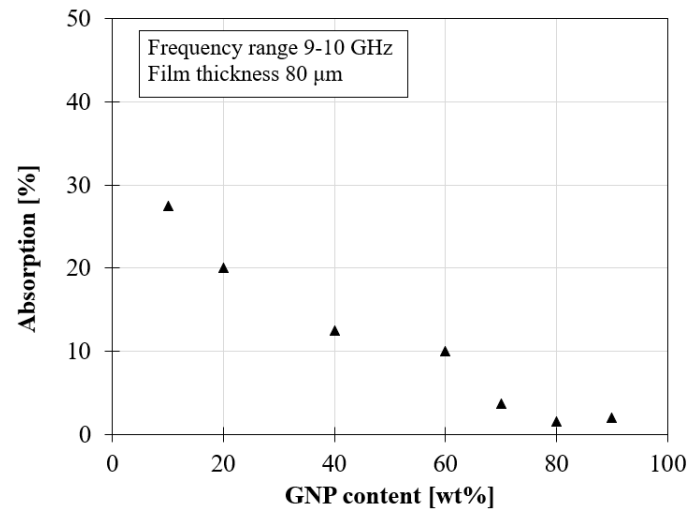
Figure 3.22 Absorption contribution vs filler content
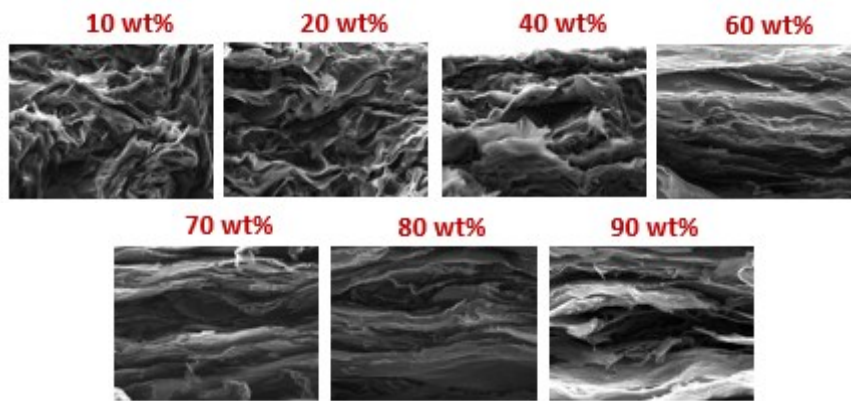
Figure 3.23 SEM images (10 μm) of GNP/Epoxy films with filler content from 10 wt% to 90 wt%
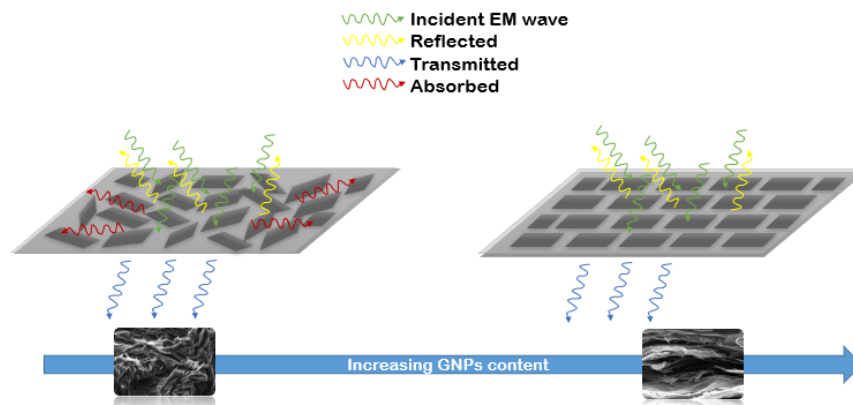
Figure 3.24 Schematic representation of electromagnetic field in GNP/Epoxy films for different filler content

Consequently, at low filler content, given the randomly orientation of nanoplatelets within the volume, the EM waves are partly absorbed. On the contrary at high GNP content, given the high level of organization and alignment in the plane of the nanoparticles, the EM waves are mostly reflected (Figure 3.24).

3.2.6 Contact angle

(a)   (b)

(c)
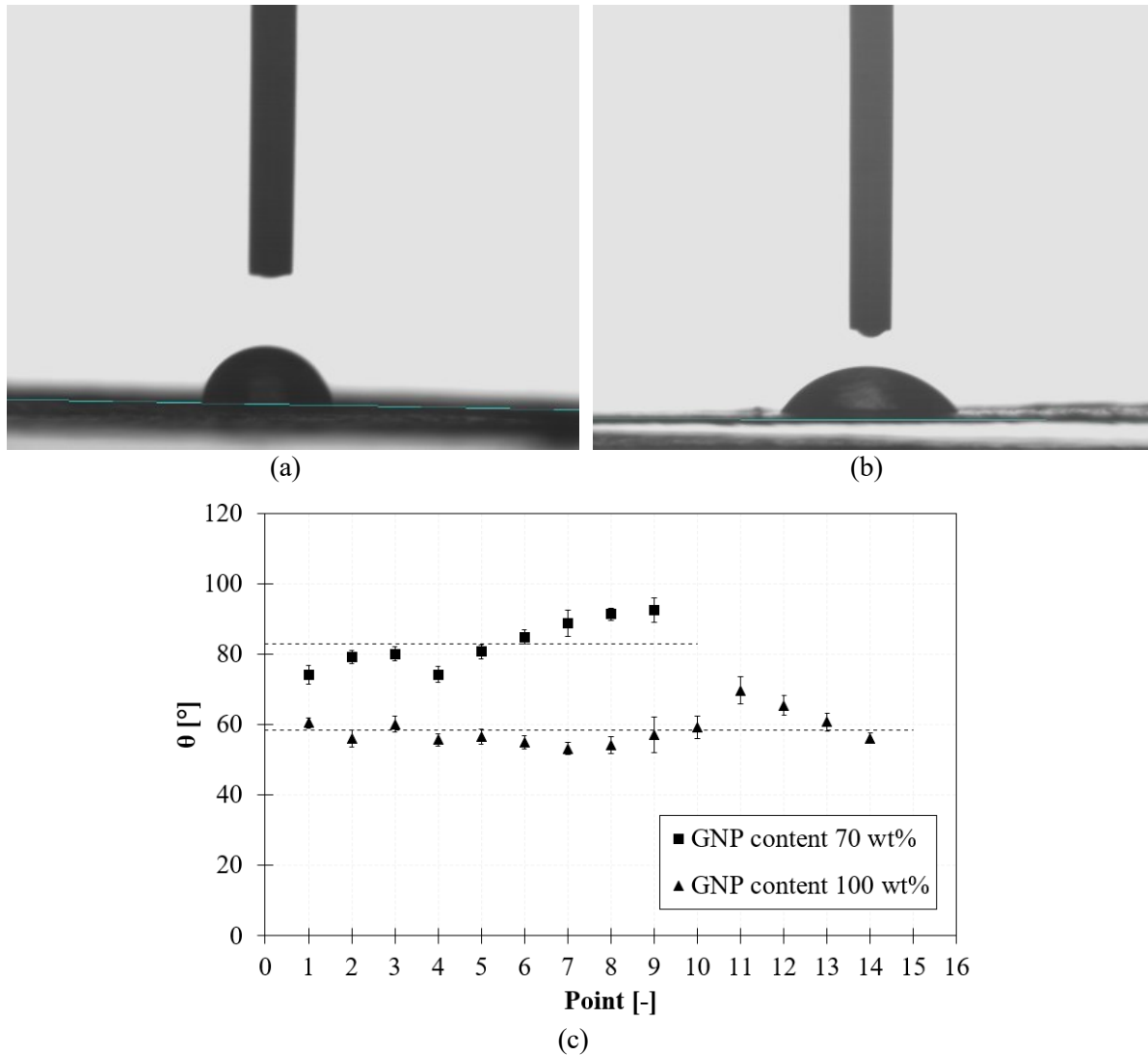
Figure 3.25. Contact angle measurements on GPreg with 70 wt% GNP (a) and 100 wt% GNP (b) and results (c)

Contact angle measurements on GPregs with 70 wt% of GNP and 100 wt% GNP are taken, using optical contact angle measuring (OCA 20 DataPhysics) and contour analysis systems. Contact angle, θ, gives information about the wettability of the material. Test are conducted using distilled water drops of 1 mL. The contact angle is geometrically defined as the angle formed by the liquid with the solid surface. Results of Figure 3.25, show that the material wettability changes according to the polymer content. In fact, samples with 30 wt% resin

content showed an average contact angle of 83° and samples without binder showed and average contact angle of 59°. This suggests that the polymer hydrophobicity affects the wettability of the material, compared to pure GNP paper. In fact, the angle reduces of about 30% from paper with 70 wt% to 100 wt% [205].

3.3   Laminates characterization

Table 3.6 Laminates charachterization test list

	TGA	SEM	Mechanical properties 3-point bending	Damping
Filler content	✓	✓	✓	✓
Binder type	✓	✓	✓	✓
Filler aspect ratio	✓	✓	✓	✓

Since GPregs are impregnated with polymer, they can be assembled to fabricate laminates of 1 mm thickness, through compression moulding process. GPregs laminae of 20 mm width and 65 mm length are stratified as shown in Figure 3.26, and placed in a mould, consisting in two metallic plates and a frame of 1 mm thickness. The system is placed in a platen press (P200E Collin) and the resin cure cycle is applied. To improve the alignment of GNPs within the material and to decrease the porosity, during the processing a pressure of 40-50 bar is applied. Both samples with filler content from 50 to 80 wt% and with different binder and nanoplatelets are manufactured at a nominal thickness of 1 mm. Also in this case, the effect of resin content, filler and matrix type on the final mechanical performances is investigated.
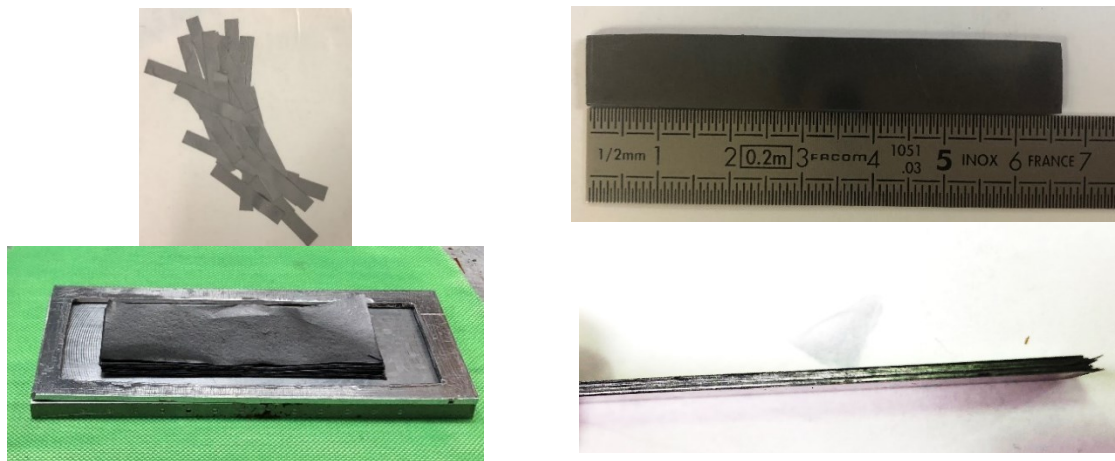
Figure 3.26. Laminate's fabrication process

3.3.1 *Thermogravimetric analysis (TGA)*

Thermogravimetric analyses are conducted according to §3.2.1. Figure 3.27 shows that the nominal filler content of laminates underestimates the real one, as also reported in in Table 3.7.

Table 3.7. Matrix content of GNP/Epoxy laminates

Nominal weight fraction	Real weight fraction	Volume fraction filler
$w_{f,nominal}$ [%wt]	$w_{f,real}$ [%wt]	v_f [%vol]
50	61	47
60	70	57
70	78	68
80	89	81
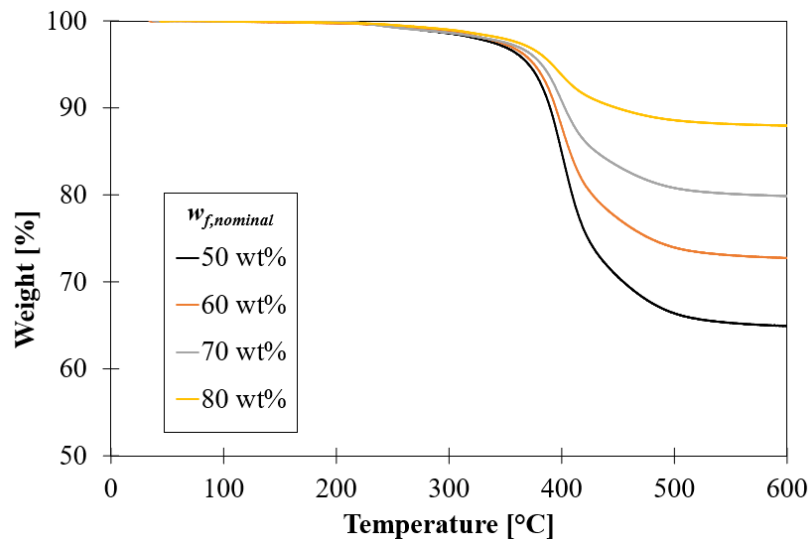
Figure 3.27. TGA for laminates (GNP/Epoxy) with different filler/matrix content

3.3.2 *Morphological assessment (SEM)*

Morphological analyses are conducted in order to study the alignment of the particles and the bonding between plies for samples with filler content of 50, 70, and 80 vol%.

Figure 3.28 shows SEM images of the cross section (fracture surface) of thick GNP laminate with actual matrix content of ~50 vol%. To achieve the final thickness at least 25 GNP films were stacked and the compacted, the micrograph shows an inner structure where the single layers are clearly recognizable. Border lines which identify the contact between adjacent layers is evident indicating a bad adhesion between layers. Furthermore, Figure 3.28b shows two different textures, an area where the particles are well aligned reproducing a nacre-like structure and the other where with wrinkles, indicating a worse alignment. Figure 3.29 shows fracture surface at a matrix content of ~30 vol%. Here, the alignment of GNP in the plane is

greatly improved, the cross section exhibits a uniform texture. Even if the overall distribution of lamellar particle is good some voids are still present. Empty areas represent weak points and affect the bonding between layers. A further increase of GNPs content does not improve the material architecture, in fact, the resin seems to be worse dispersed (Figure 3.30) entailing an inner structure not perfectly aligned, moreover some voids are still detectable.

(a)   (b)
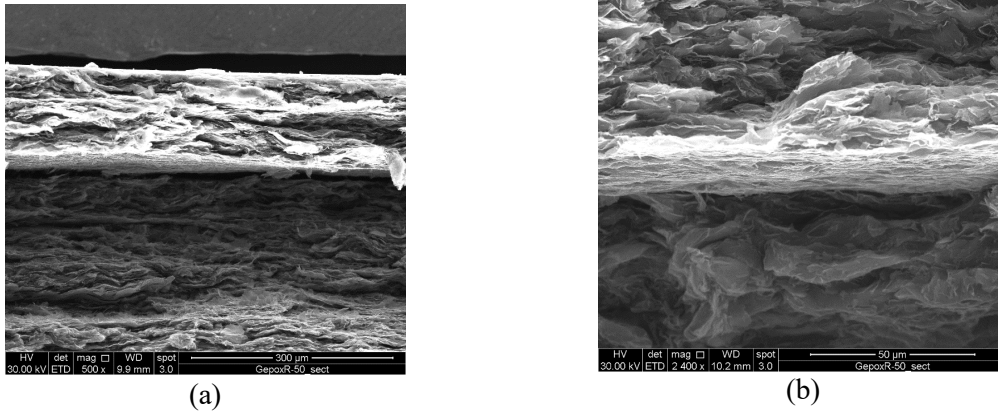
Figure 3.28. SEM Fracture surfaces, actual composition GNP/Epoxy 53/47 vol%

(a)   (b)
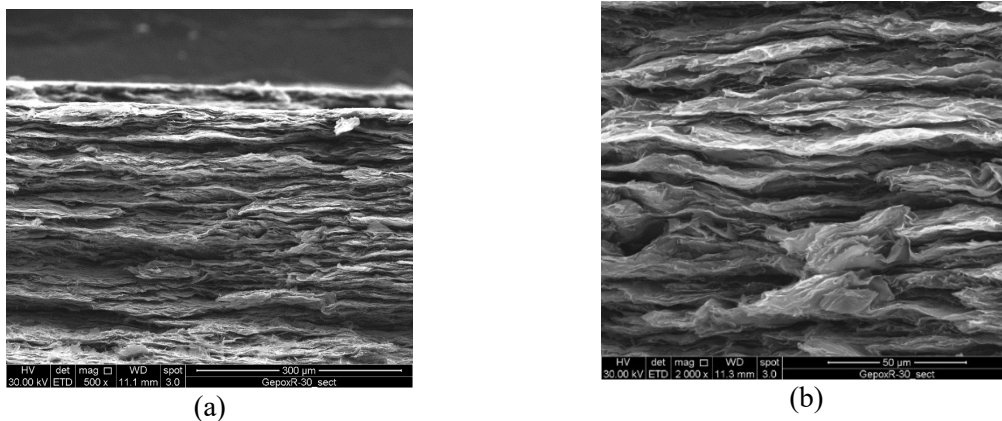
Figure 3.29. SEM Fracture surfaces, actual composition GNP/Epoxy 66/33 vol%

(a)   (b)
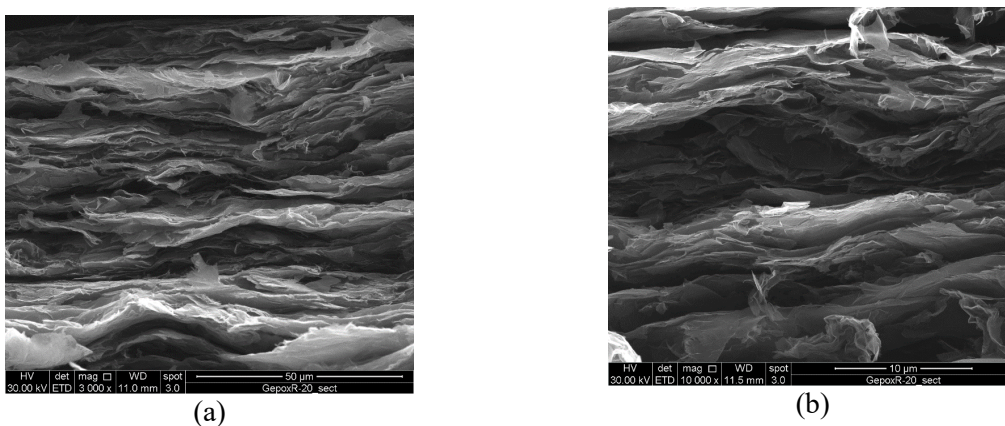
Figure 3.30. SEM Fracture surfaces, actual composition GNP/Epoxy 80/20 vol%

3.3.3 *Mechanical characterization*

Mechanical characterization of laminates is performed with TA instrument DMA-Q800 equipped with 3-point bending clamp. Three-point bending tests were preferred to tensile tests, in order to avoid cracking of the sample in the clamp. The sample is supported at both ends and loaded in the middle section. Monotonic tests at room temperature were performed on rectangular specimens (50 mm x 10 mm x 1 mm) at room temperature with a displacement rate of 500 μm/min. Data are elaborated according to the ASTM D790 standard for flexural behaviour of composites [206]. Moduli at very low strain (0-0.05%) are evaluated according to Eq.(3.5). Also, the dynamic behaviour of the material has been investigated in the Multi-Frequency Strain mode, heating the sample from room temperature to 250°C with 3.00°C/min speed.

Mechanical tests carried out on laminates follow the trend of those conducted in the single ply (cfr. §3.2.3), as shown in Figure 3.31. The higher compaction load improved the mechanical performances of laminates with respect to GPregs. The increase in stiffness is probably related to the higher ordering achieved and to the decrease of void content.

Figure 3.32 shows the results of flexural tests conducted on laminates in terms of elastic moduli, evaluated at very low strain (0-0.05%). For filler content lower than 70 vol% the elastic modulus follows the direct rule of mixture, while at higher filler content (>70 vol%) the elastic modulus abruptly drops. The reduction of the modulus can be associated to low resin content, which is not able to efficiently transfer load.

(a)	(b)
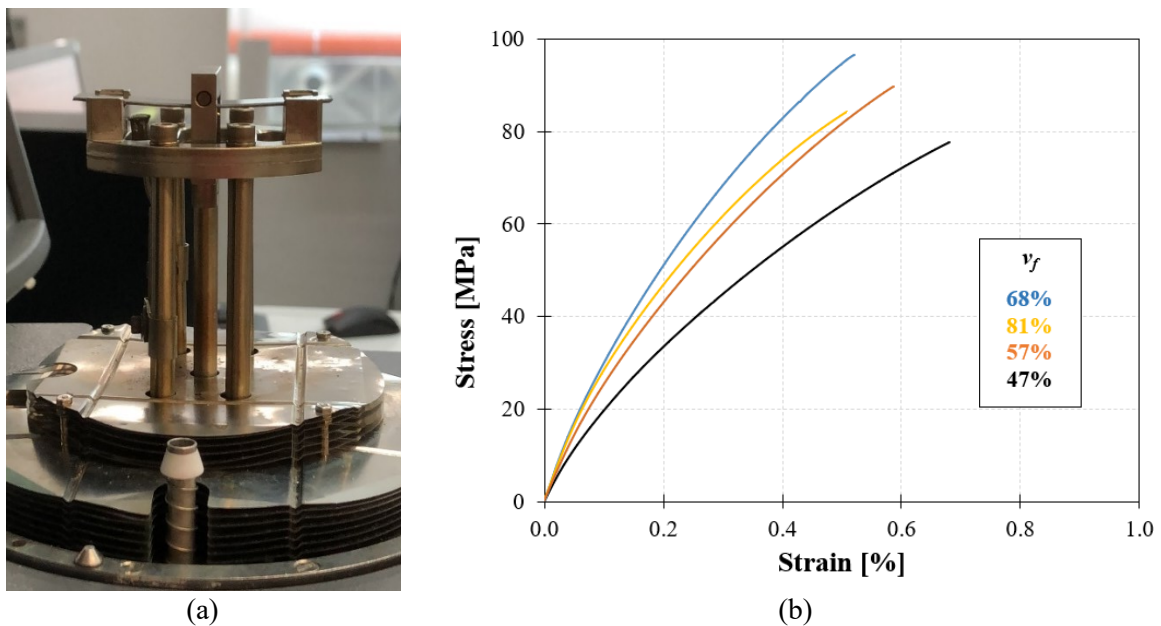
Figure 3.31. (a) Bending test set-up; (b) Stress strain curve of bending test conducted on laminates with G2/Epoxy (RTM6) at different filler content
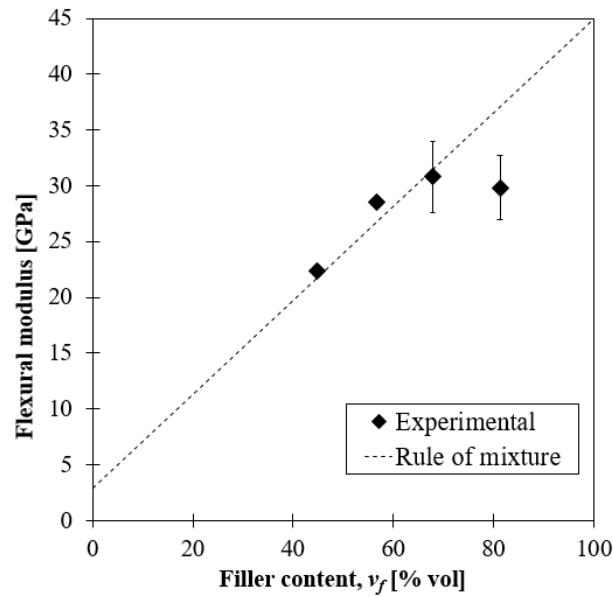
Figure 3.32. Flexural moduli of nanolaminates in bending evaluated in 0-0.05% strain range

Mechanical tests on laminates, varying the filler aspect ratio and the matrix type (Figure 3.33), are in accordance with the results obtained on GPregs of Figure 3.15. In fact, varying the aspect ratio of GNPs particles from 2143 for G2Nan, 7500 for AVA to 8600 for AVA440 there is not a substantial difference in terms of modulus, while strength slightly increases for sample with higher aspect ratio. On the other hand, the influence of the matrix type is significant. The behaviour changes from brittle to ductile according to the nature of the matrix. However, toughness is almost the same for all samples, it slightly increases with filler aspect ratio, as reported in Figure 3.34a.

(a)

(b)
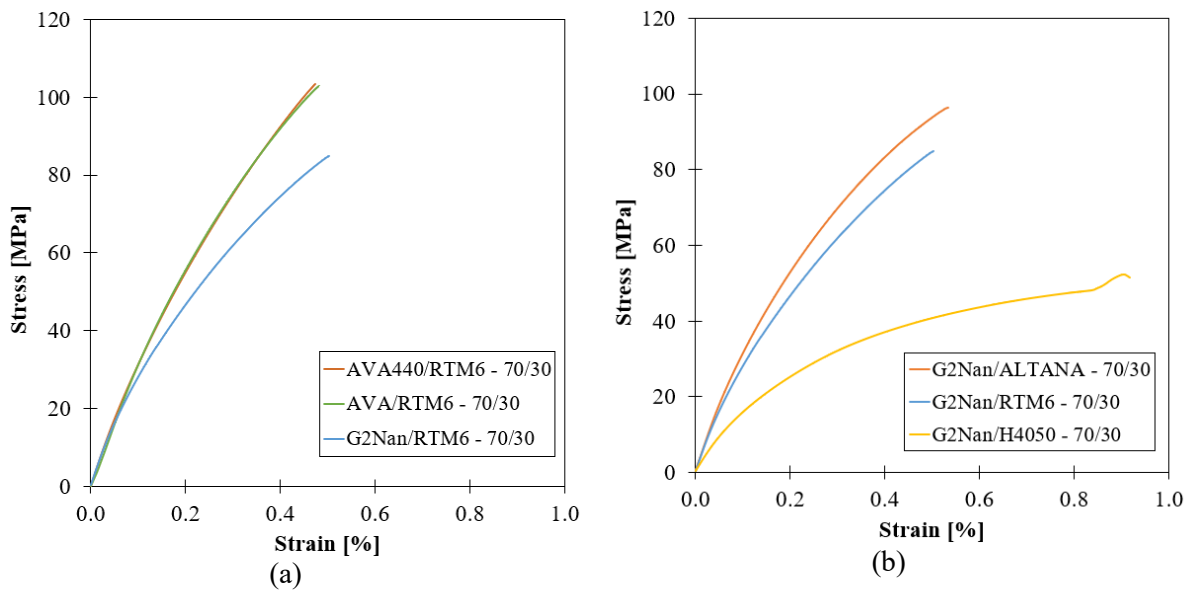
Figure 3.33. Results of bending tests on laminates varying a) Filler aspect ratio; b) Matrix behaviour

78

Furthermore, dynamic analyses conducted on the same samples showed that the composites fabricated with the thermoplastic vinyl copolymer (H4050) have the highest dissipative capacity. Damping values are reported in Figure 3.34b.
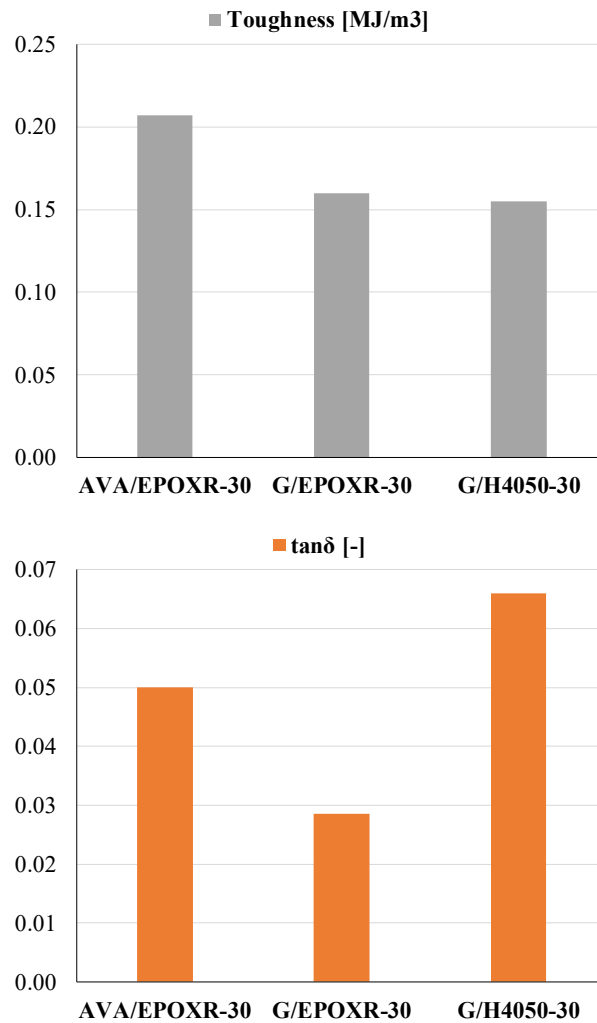
Figure 3.34. Influence of matrix and filler type on toughness (a) and damping (b)

4. MICROMECHANICAL INVESTIGATION USING MICRO RAMAN SPECTROSCOPY

4.1 From macro- to micromechanical investigation

The macro-mechanical characterization of GNP/Epoxy (RTM6) films showed that for high filler content (>50 vol%) there is a drop of efficiency of reinforcement, with consequent reduction of the Young's modulus. This phenomenon could be ascribed to an inefficient load transfer between matrix and nanoplatelets. From AFM analysis it has been observed that the resin distribution within the nanoplatelets is discontinuous due to the presence of polymeric several droplet-like features. Therefore, since nanoplatelets are partially covered, the stress transfer is negatively affected and the mechanical properties at high filler content are deteriorated.

For this reason, a micromechanical investigation based on micro Raman spectroscopy (μRS) has been carried out and the quality of stress transfer has been investigated. Micro Raman spectroscopy is widely used to investigate the deformational processes in nanocomposites, particularly in case of graphitic reinforcements, since the peak frequencies of the Raman bands in these materials are sensitive to the level of applied strain [207]. This technique is based on the fact that the frequencies, or wavenumbers, of the Raman bands shift under the application of a macroscopic strain (or, analogously, stress). In other words, when the material is subjected

to an external load, the particles and their chemical bonds are stressed, resulting in a translation of the spectrum peaks [14].

Consequently, this technique is adopted to determine the efficiency of stress transfer in GNP/Epoxy films at different filler content in order to assess the macroscopic response of the film.

4.2   Fundamentals of Raman spectroscopy

Raman spectroscopy is an inelastic scattering technique that probes the vibrational modes of chemical bond into materials [208,209]. Raman spectroscopy takes its name from the scientist who first observed the inelastic scattering in 1928: the Indian scientist C. V. Raman, who also won the Nobel Prize for Physics in 1930 for his work on the scattering of light.

In the last decades it has been drawing particular attention since its versatility in providing a fingerprint of molecules over several ambient conditions. For this reason, it can be used to identify specific substances. Nowadays this technique is employed in several fields, from medical diagnostic to solid state physics and materials science and not only for academic purpose, but also for industrial analytical purposes, for example to identify contaminants appearing during production. Thanks to Raman's high chemical selectivity, it is possible to study many different types of polymers and other substances. Therefore, this technique not only provides basic phase identification, but also can be used to assess nano-scale structural changes and characterize micromechanical behaviour.

Based on light scattering, Raman spectroscopy can provide information on the molecular structure and characteristics of the material, exploiting the specific vibrations of molecules and their relative movements. When light hits the molecules, most of the photons are dispersed and diffused with the same energy and vibration of the incident photons, determining the "elastic scattering" or "Rayleigh scattering". Only one photon on one million, scatters with a different frequency, which represents the "inelastic scattering" or "Raman effect" (Figure 4.1). Raman scattering allows the examination of specific vibrational characteristic of a molecule, giving information of its structure and of the interaction with adjacent molecules.
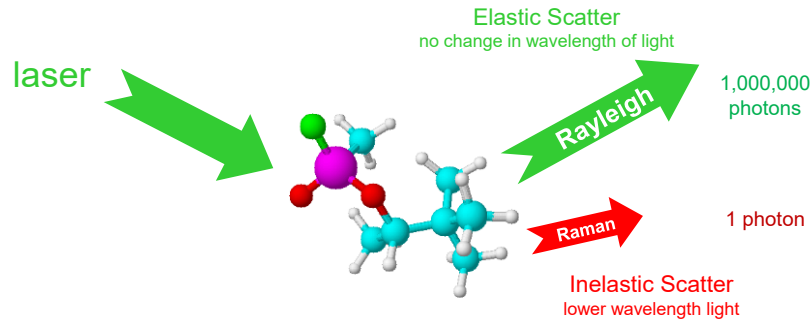
Figure 4.1 Light scattering

Phonons are collective excitations, often designated as quasiparticles, that occurs in a crystal and can be represented by the superposition of plane waves that virtually propagate to infinity [210], called normal modes of vibration. Modes can be classified as either stretching (ν), bending (δ), torsional (η) or librational (R'/T' pseudorotations/translations) and lattice modes (the latter include the relative displacement of the unit cells). There are modes characterized by in-phase oscillations of neighbouring atoms (acoustic vibrations) and modes characterized by out of phase oscillations (optical vibrations), as shown in Figure 4.2.
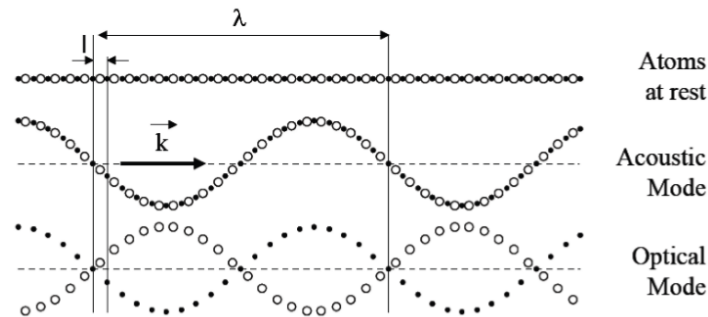
Figure 4.2 Phonons movements

As a group of atoms vibrates, the electron cloud, and thus the polarizability, changes instantaneously. The interaction of the periodic change in the charge distribution with an imposed electromagnetic field is the origin of several types of light scattering phenomena including infrared (IR) and Raman effects.

In other words, when a solid is excited by an energy source $\bar{E}$ the dipole moment vector $\bar{P}$ can be defines as:

$$\bar{P} = \bar{\bar{\alpha}} \cdot \bar{E}$$
(4.1)

where $\bar{\bar{\alpha}}$ is the polarizability tensor.

In particular, in the case of a laser input of amplitude $\bar{E}_0$ and frequency $ν_0$, the polarization vector $\bar{P}$ of the dipoles becomes:

$$\overline{P} = \overline{\overline{\alpha}} \cdot \overline{E}_0 \cos(2\pi v_0 t) \tag{4.2}$$

If the nuclei are not fixed, but oscillate with their own frequency v'_{vib}, the internuclear distance, r, can be expressed as follow:

$$r = r_0 \cos(2\pi v_{vib} t) \tag{4.3}$$

The polarizability varies with the internuclear distance and can be written as:

$$\overline{\overline{\alpha}} = \overline{\overline{\alpha}}_0 + \left(\frac{\partial\overline{\overline{\alpha}}}{\partial r}\right) r_0 \cos(2\pi v_{vib} t) \tag{4.4}$$

By substituting Eq. (4.4) in Eq. (4.2), the dipole moment caused by the induced electrical field becomes:

$$\overline{P} = \overline{\overline{\alpha}}_0 \cdot \overline{E}_0 \cos(2v'_0 t) + \left(\frac{\partial\overline{\overline{\alpha}}}{\partial r}\right)_0 \overline{E}_0 \cdot r_0 \cos(2\pi v'_{vib} t)\cos(2\pi v'_0 t) \tag{4.5}$$

Manipulating Eq. (4.5), the dipole moment vector can be rewritten as the sum of three terms:

$$\overline{P} = \overline{\overline{\alpha}}_0 \cdot \overline{E}_0 \cos(2v'_0 t) + \frac{1}{2}\left(\frac{\partial\overline{\overline{\alpha}}}{\partial r}\right)_0 \overline{E}_0 \cdot r_0 \cos\left[2\pi(v'_0 + v'_{vib})t\right] +$$
$$+ \frac{1}{2}\left(\frac{\partial\overline{\overline{\alpha}}}{\partial r}\right)_0 \overline{E}_0 \cdot r_0 \cos[2\pi(v'_0 - v'_{vib})t] \tag{4.6}$$

In Eq. (4.6) are defined the two components of scattered light: the quasi-elastic of frequency v'_0 and the inelastic of frequency $v'_0 \pm v'_{vib}$, which occurs only if the exciting vibrations produce a variation of polarizability $\left(\partial\overline{\overline{\alpha}}/\partial r \neq 0\right)$. The first term indicates the Rayleigh scattering, the second and third the anti-Stokes and Stokes scattering respectively [211,212].
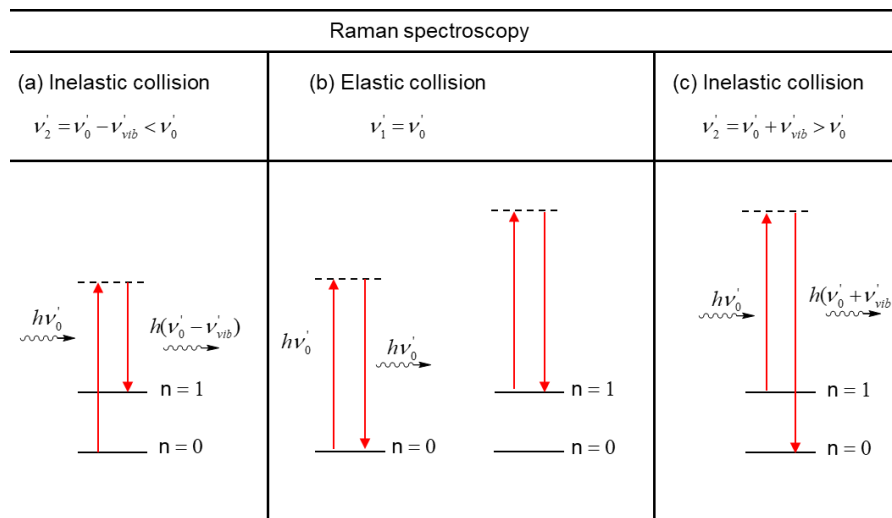
Figure 4.3 Energy level diagram of various vibrational spectroscopic transitions

Thus, when a material is excited, the molecules vibrate and the polarizability changes instantaneously. According to quantum mechanics, the excited molecules move to a superior virtual energetic level ($n \neq 0$). In this condition, different situations can occur, as shown in Figure 4.3:

(a) *Stokes scattering*. When the system is excited, the electrons move to a different vibrational energetic level (from $n=0$ to $n=1$). In this case the frequency of vibration changes being lower than the initial one ($\nu'_0 - \nu'_{vib} < \nu'_0$). The difference between the energy associated to the incident and the scattered photons is the Raman shift.

(b) *Elastic scattering*. When the molecule is excited with a vibration frequency equal to its natural frequency ($\nu'_1 = \nu'_0$), it remains to the initial energetic level.

(c) *Anti-Stokes scattering*. In this case, the system, which is already in an excited state ($n=1$), move to a lower energetic virtual level ($n=0$). The frequency of vibration changes being higher than the initial one ($\nu'_0 + \nu'_{vib} > \nu'_0$).

In an excited system, the elastic scattering is preponderant and only $1/10^6$ photons has inelastic scattering. For this reason, the frequencies have to be filtered in order to eliminate ν'_0 and acquire only the Stokes (or anti-Stokes) ones.

Raman spectroscopy is based on the polarizability variation of the molecular bonding. When the laser light hits a molecule, it deforms the electronic cloud, causing a polarizability variation. The condition for a vibrational mode to be Raman active requires that its molecular polarizability should be neither maximum nor minimum when the atoms are at their equilibrium positions.

It is commonly used to refer to vibration modes by their wavenumber (expressed in cm^{-1} unit):

$$\bar{\nu} = \nu/c \tag{4.7}$$

Where c is the speed of light. By using this notation and considering the electromagnetic theory of radiations from oscillating dipole, the Raman peak Lorentzian shape is described by the following expression:

$$I(\bar{\nu}) = I_0 \cdot \int \frac{d^3\bar{k}}{\left[\bar{\nu} + \bar{\nu}(\bar{k})\right]^2 + \left(\dfrac{\Gamma_0}{2}\right)^2} \tag{4.8}$$

where $\bar{\nu}(\bar{k})$ represents the dispersion branch to which the mode belongs and Γ_0 is the half-width for the ordered reference structure.

4.2.1   Harmonic model

The harmonic model can be adopted to study the oscillation of chemical bonds. It considers that all vibrations are purely harmonic, and the potential energy of the system is the sum of the quadratic terms whose coefficients are the force constants. The bonds can be modelled as a spring of length l_b, reduced mass μ, and constant stiffness k_b, as shown in (Figure 4.4).
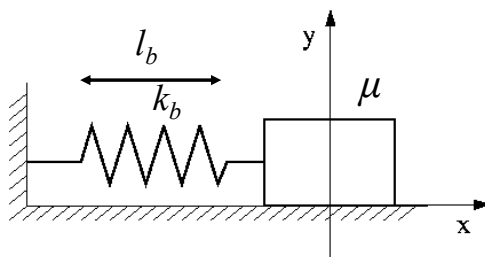
Figure 4.4 Harmonic oscillator

In this model, potential energy is a parabolic function (Figure 4.5), which expression is:

$$V = \frac{1}{2} k_b (l - l_0)^2 \tag{4.9}$$

and

$$k_b = \frac{\partial^2 V}{\partial l_b^2} \tag{4.10}$$

$$\bar{v}_{vib} = \frac{1}{2\pi c} \sqrt{\frac{k_b}{\mu}} \tag{4.11}$$

$$\mu = \frac{m_1 \cdot m_2}{m_1 + m_2} \tag{4.12}$$

This oscillation is harmonic, and its frequency v does not depend on the distance from the equilibrium position l_0. The quantum theory of the harmonic oscillator has a selection rule that allows only one transition between adjacent energy states ($\Delta v = \pm 1$). These energy states are represented in Figure 4.5 by the green line.

Actually, in the real system the oscillating masses (m_1 and m_2) are not comparable, and the selection rule is not valid. Also, phenomena like overtones, combination bands, or difference bands cannot be explained by the simplistic harmonic theory; the real interatomic potential is not harmonic but includes attractive and repulsive contributions. In addition, concepts like bond breaking at high deformations demands a different approach for the potential energy function. Thus, an anharmonic oscillator gives a better approximation of this behaviour. Such

an approximation is the Morse function (Figure 4.5), where the potential energy is a function of the dissociation energy D_e, or the energy required to break the bond:

$$V = D_e \left(1 - e^{-a(\Delta l)}\right)^2 \tag{4.13}$$

Where Δl is the displacement of the interatomic distance l from the equilibrium value l_b, and a is a constant, which controls the width of the potential function.

In this model, the quantum theory accounts for more than one transition between energy levels.
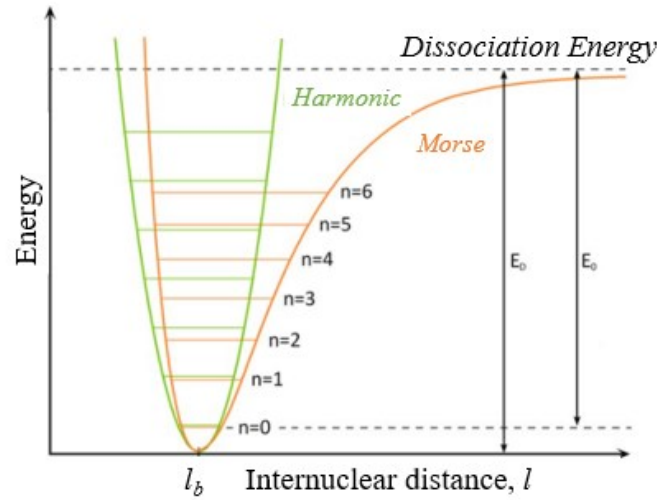
Figure 4.5 Harmonic and Morse potential

4.2.2 Stress dependence of the vibrational frequency

In the harmonic model, the stiffness k_b is constant and does not depend on the relative displacement Δl (Eq. (4.10)). Consequently, the wavenumber does not depend on the distance from the equilibrium position. In the case of Morse potential, the second derivative of Eq. (4.13) with respect to Δl is:

$$k_b = 2a^2 D_e \left(2e^{-2a(\Delta l)} - e^{-a(\Delta l)}\right) \tag{4.14}$$

It changes gradually with the Δl. Figure 4.6a shows the trend of the force constant with the interatomic distance for both models. Therefore, if the bond distance is increased ($\Delta l > 0$) by a tensile force, the corresponding force constant slightly reduces, as shown in Figure 4.6b, resulting in a low frequency shift of the stretching vibrational mode ($\bar{v}_{vib} \propto k_b$). From a macroscopic point of view, a tensile (or compressive) stress is expected to decrease (or increase) the wavenumber $\bar{v}$.
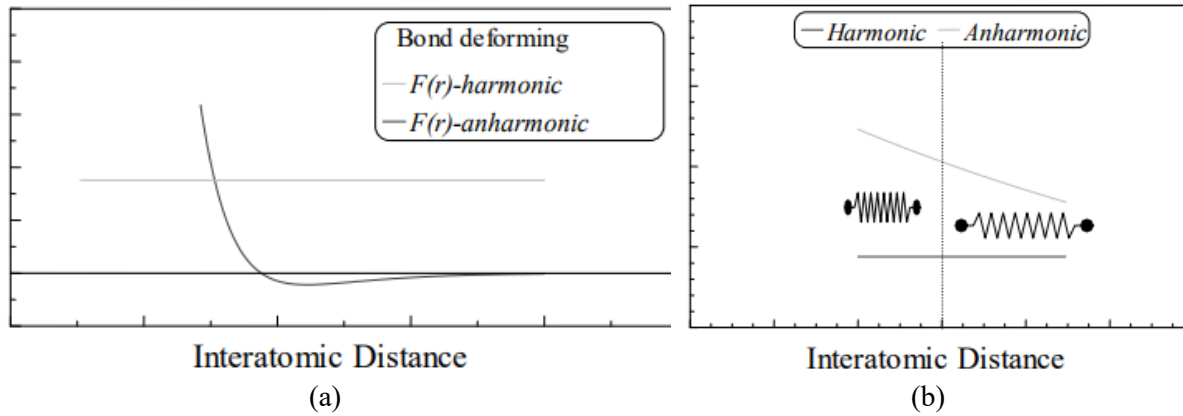
Figure 4.6 Dependence of force constant k_b on interatomic distance

The above principle provides the theoretical background for the frequency shift of distinct Raman bands when the molecule is subjected to external load. The theoretical calculation of the expected shift has been presented for simple molecules [213,214]. More complicated analyses include the lattice dynamical theory to predict stress induced shifts in polymeric chains.

For small displacements, the stress dependence may be regarded to a good approximation as proportional to the applied stress field. Bretzlaff and Wool [215] propose the following:

$$\Delta v_\sigma = v(\sigma) - v(0) = \alpha_x \cdot \sigma \tag{4.15}$$

Where Δv_σ is the mechanically induced peak frequency shift, α_x is the mechanically induced frequency shifting coefficient at constant temperature T, and σ is the applied uniaxial stress.

The key feature that links the stress dependence of the molecule to any macroscopic induced deformation is whether this deformation affects the material at a molecular level. Amorphous materials do not show detectable stress sensitivity, while highly crystalline materials, such as carbon, exhibit measurable stress sensitivity [207].

Experimental calibration curves may be employed to correlate Raman frequency shifts and absolute strain. In most cases, a direct proportionality of the shift to the applied strain is adequate [216]. In particular, there is a proportionality factor that links the wavenumber shift to the macroscopic strain in isotropic material:

$$\Delta \bar{v} = S^\varepsilon \cdot \Delta \varepsilon \tag{4.16}$$

where S^ε [cm^{-1}/%] is the proportionality factor and $\Delta \varepsilon$ [%] is the macroscopic strain. For elastic materials, the validity of the Hooke's law, lead to a direct relationship between the stress induced Raman shift and the bond stiffness or the Youngs modulus of a macroscopic structure.

$$\Delta\bar{v} = S^{\sigma} \cdot \Delta\sigma \qquad\qquad (4.17)$$

These relationships allow for universal plots that correlate the strain induced Raman shift with the moduli of known fibres [217].

4.2.3   Raman technique and instrumentation

Since the Raman effect is intrinsically weak, the optics components of Raman spectrometer must be optimized and combined. In particular, such applications require often a high spatial resolution that can be achieved by focusing monochromatic light with standard optical microscopy techniques. The so-called micro Raman spectroscopy (µRS) is characterized by a spatial resolution that typically ranges between 1 and 5 µm and is limited by the quality of the optical components and the optical arrangement used to focus the beam. This high spatial resolution makes µRS the best tool to map phase and strain distributions in many materials. Raman spectroscopy is a non-destructive, non-invasive, and fast technique and can be applied on solids, powders, liquids, gas without any preparation, at ambient pressure and temperature. The principal components for Raman spectroscopy are: (1) sources (Figure 4.7), (2) monochromators, (3) sampling systems, (4) detectors, (5) systems for data managing and elaboration.

For micromechanical investigation of composites two systems are commonly adopted (Figure 4.8): the conventional Raman microprobe set-up and the remote Raman microprobe (ReRam) [218]. In the conventional microprobe set-up, the laser beam is directed to a microscope that focus it, through a micrometric spot, on the sample mounted on a tensile jig. The scattered beam is then collected by the microscope, sent to the spectrometer and finally directed to a charged coupled device (CCD). The ReRam apparatus utilizes fibre-optic cables for laser delivery and collection; as previously, the laser is first focused on the sample, sent to the spectrometer and then collected by the CCD. However, the use of a flexible fibre optic permits operation of the microprobe in horizontal, vertical and multi-angle position, thus allowing investigation of specimens of different size and shape, mounted on common universal testing machine, and under different environmental conditions. The first system has high spatial resolution and allows depth investigation on a volume lower than 1 µm^3, while the second system is useful for in-situ analysis, for industrial process monitoring and in art and forensic applications.
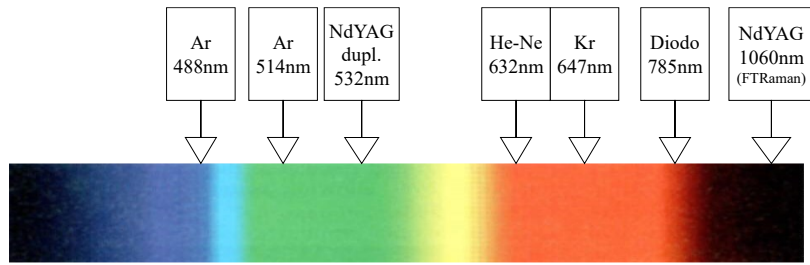
Figure 4.7 Common laser used in Raman spectroscopy

(a)   (b)
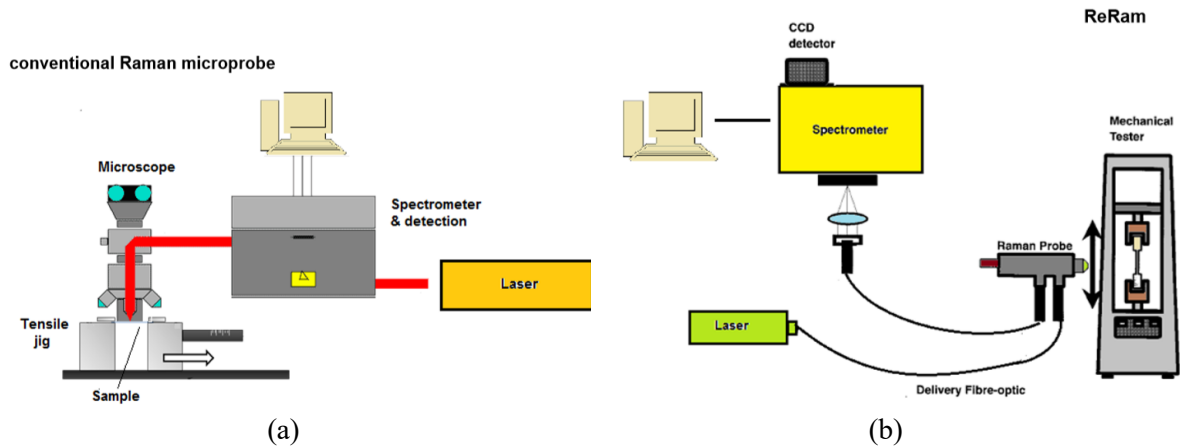
Figure 4.8 Schematisation of micro Raman spectroscopy experimental set up: (a) conventional microprobe; (b) ReRam

By analysing the Raman spectrum in terms of band position, intensity, shift, and width, it is possible to collect qualitative and quantitative information about a certain material. The band position is used in qualitative studies, allowing the identification of functional groups; the band intensity gives information about the concentration and molecular orientation. The band shift is useful for stress and strain measurement and band width identifies amorphous/crystalline phases (Figure 4.9).
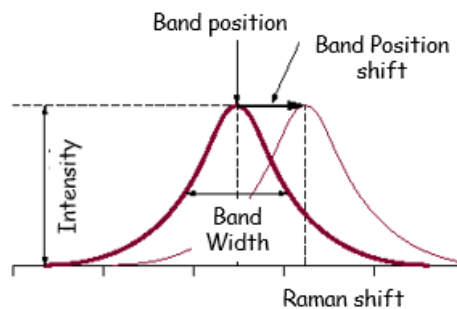
Figure 4.9 Raman spectrum analysis

This technique interests academic and industrial field and allow the study of relationships between microstructure and macroscopic physical properties in polymers and composite. In fact, has opened the way for a powerful technique for the micromechanical studies at the fibre/matrix interface [219].

4.3   Raman spectroscopy in composites

In the last decades Raman spectroscopy has been gained ground among all the experimental techniques for micromechanical investigation of composites. In particular, a new branch of µRS, the so called 'micro Raman extensometry' (µRE) was born, by exploiting the dependence of Raman band shift with the macroscopical solicitation [217]. As described before, the frequencies or wavenumbers of the Raman bands of many high-performance fibres shift when an external solicitation in applied, due to the application of stress in the fibres [216,220,221]. In other words, given the anharmonicity of atomic bond, the variation of the vibrational frequency (or wavenumber) is determined by a change in the interatomic force and interatomic distance caused by the macroscopical applied strain. Therefore, this technique is a valuable tool for understanding the relationship between the macroscopic deformation and the deformation mechanism at molecular or microstructural level.

Based on this approach, the reinforcement in a composite acts as a 'mechanical probe' [222]. Once the Raman peak shift is calibrated for the specific fibre (or nanoplatelet) by loading it individually, it acts as internal stress/strain sensor in the composite. However, the matrix must be reasonably transparent (or must not interfere with the Raman spectrum) and the reinforcement must possess a high crystallinity. Consequently, by monitoring the Raman wavenumber shift with applied stress or strain for the fibre embedded in the matrix and by comparing this value with that of the reference value (fibre tested in air), it is possible to understand the quality of stress transfer between the two phases.

Since the mechanical performances of composites are regulated by the matrix efficacy to transfer load, via shear transfer mechanism, the effective performances of the material can be investigated through Raman spectroscopy, quantifying the efficiency of stress transfer between the matrix and the filler, thanks to the sensitiveness of the Raman band to the level of applied strain [207]. When the material is subjected to an external load, the particles and their chemical bonds are stressed, resulting in a translation of the spectrum peaks [14]. By monitoring the wavenumber shift of the Raman bands when a macroscopic stress/strain is applied, it is possible to determine the stress level within the particles and thus the capability of the matrix to transfer load. Specifically, when the particle is loaded in compression, the peak shifts to higher wavenumber, while when it is loaded in tension, the peak shifts to lower wavenumber (Figure 4.10) [14].
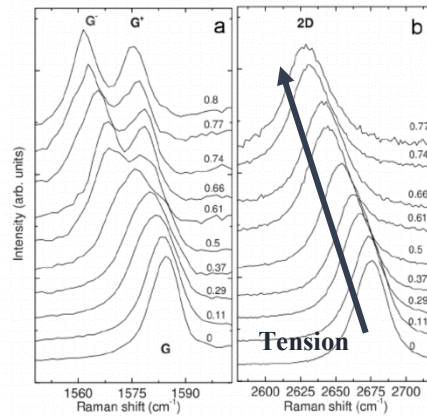
Figure 4.10 Raman band shift of graphene spectrum when loaded in tension
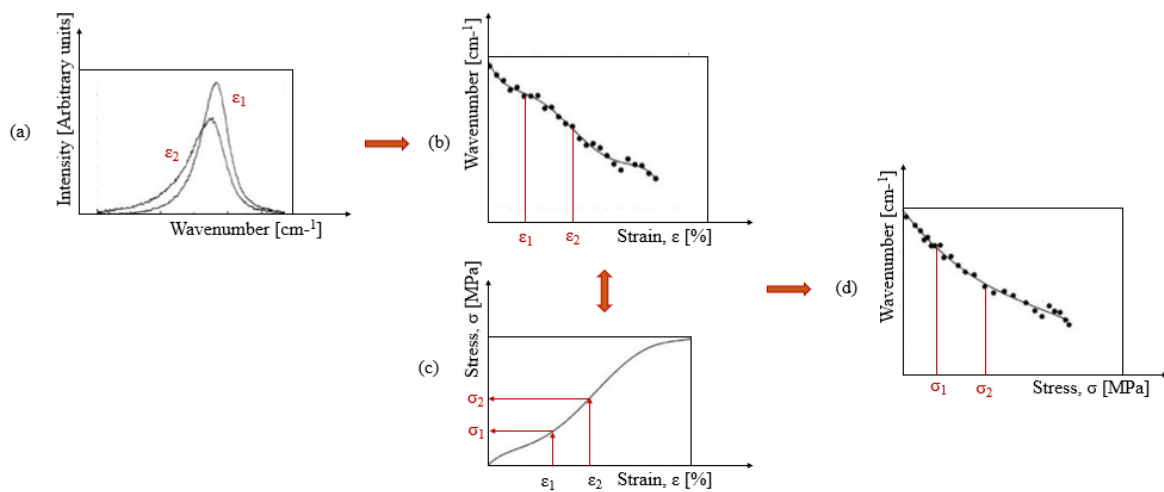
Figure 4.11 Fundamental steps of micromechanical investigation with Raman spectroscopy

The steps for the micromechanical investigation of the quality of stress transfer via Raman spectroscopy are summarized in Figure 4.11.

First, Raman spectra are acquired in the midpoint of the sample at different level of axial strain ($\varepsilon_1 < \varepsilon_2 < \dots \varepsilon_n$) (Figure 4.11a) and a graph of Raman peak position (wavenumber) as a function of the applied strain in built, as shown in Figure 4.11b. Then, the stress strain curve of the material is determined by means of tensile test performed by imposing an effective strain rate equivalent to the one adopted in the Raman test (Figure 4.11c). Finally, knowing the relationship between stress and strain, it is straightforward to calculate the dependence of Raman peak position on stress (Figure 4.11d). From this, it is possible to plot the stress profiles along the fibre/nanoparticle.

4.4   Graphene Raman spectrum

Raman spectroscopy has been employed extensively for the study of the micromechanics of reinforcement in nanocomposites, especially in case of graphitic nanoparticles.

91

Graphene's electronic structure is uniquely captured in its Raman spectrum [223]. The strong resonant Raman scattering, even from a one-atom-thick graphene flake, produces a well-defined Raman signal and enables the observation of several interesting phenomena under various conditions. Raman fingerprints for single-, bi- and few-layer graphene reflect the changes in the electronic structure and electron-phonon interactions allowing unambiguous, non-destructive identification of graphene layers. Consequently, Raman spectrum changes with increasing number of layers.
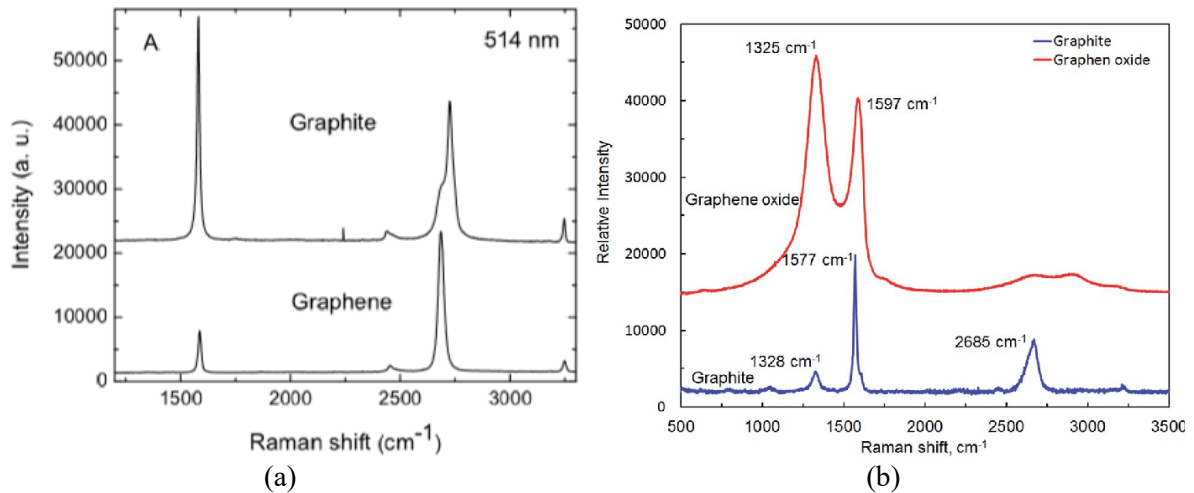
Figure 4.12 Comparison of Raman spectra of: (a) bulk graphene and graphite [224]; (b) graphene oxide and graphite [225]
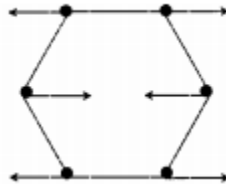
Figure 4.13 Relative motion of sp^2 carbon atoms in graphene planes (E$_{2g}$ phonon mode) [226]

Figure 4.12a compares the Raman spectra of graphene and bulk graphite. The two most intense features are the *G* peak at 1580 cm^{-1} and a *G′* (or 2*D*) band at 2700 cm^{-1}. The *G* peak is related to the doubly degenerate E$_{2g}$ phonon mode at the Brillouin zone centre (Figure 4.13). The symmetry of the E$_{2g}$ modes restricts the motion of the atoms to the plane of the carbon atoms [227]. Zone-boundary phonons give rise to a peak at 1350 cm^{-1} in defected graphite, called *D* peak [227]. The defect-induced *D* band is usually found in different forms of graphitic carbon, in particular in the case of imperfect graphene prepared by methods such as chemical vapour deposition (CVD) and thermal expansion, while it is very prominent in graphene oxide (Figure 4.12b) as a result of defects, vacancies and distortions induced during oxidation [225].

Finally, the strongest feature in the second order spectrum is at 2 x 1350 cm^{-1}. It represents the 2*D* band, which has nothing to do with the *G* peak, but is related to the second order of zone boundary phonons. Since zone-boundary phonons do not satisfy the Raman fundamental selection rule, they are not seen in first order Raman spectra of defect-free graphite [228].

Raman spectroscopy is a useful tool to characterize the different number of layers of graphitic flake, because each nanoparticle has typical features that allow to distinguish them. Figure 4.14 shows Raman spectra of monolayer, bilayer and many-layer graphene. For the case of monolayer graphene, the intensity of the characteristic 2*D* band is twice the intensity of the *G* band, while in the case of bilayer graphene flakes, the 2*D* band is comparable or even weaker than the *G* band. It changes in shape and intensity because of the resonance effects in the electronic structure. In particular, it is characterized by 4 components, which could be attributed to two different mechanisms: the splitting of the phonon branches [228,229] or the splitting of the electronic bands [226]. On the other hand, in bulk graphite the 2*D* peak consists of two components 2*D*$_1$ and 2*D*$_2$ [228], roughly 1/4 and 1/2 the height of the *G* peak, respectively. With increasing number of layers, the 2*D* band shifts to even higher wavenumbers. For more than five layers the Raman spectrum becomes hardly distinguishable from that of bulk graphite, in fact, many-layer graphene spectrum resembles that of bulk graphite [227].
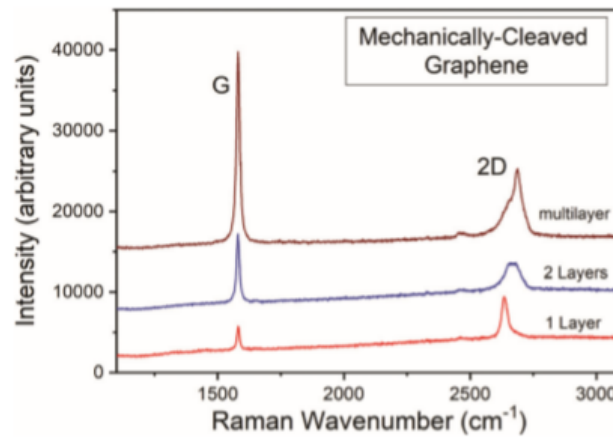
Figure 4.14 Raman spectra of graphene (mono- ,bi-, multi-layer)

The average number of layers of multilayer graphene could quantitatively be estimated, by calculating a metric, *M*, related to flake thickness [150]:

$$M = \frac{I_{graphene(\omega=\omega_{p,graphite})}\big/I_{graphene(\omega=\omega_{s,graphite})}}{I_{graphite(\omega=\omega_{p,graphite})}\big/I_{graphite(\omega=\omega_{s,graphite})}} \tag{4.18}$$

The factors I are the intensities of graphite and graphene $2D$ peak (p) and $2D$ shoulders evaluated with Raman analysis. The average number of layers is then calculated starting from M according to an empirical equation:

$$N_G = 10^{0.84M + 0.45M^2} \qquad (4.19)$$

The sensitiveness of the Raman bands of graphene to the level of applied strain [14], allows to quantify the stress level in the nanoparticles by monitoring the shift of the band's wavenumber when a macroscopic stress/strain is applied.

The Raman shift rate in graphene related materials, depends on the number of layers of the nanoparticle and on the nature of the matrix support. In particular, it decreases with the increasing number of layers. Monolayer graphene deposited on a flexible substrate exhibits the highest downshift of $2D$ band in tension of -60 ± 5 cm^{-1}/% strain [230], which is consistent with a modulus of the order of 1 TPa. This value, confirmed in several studies [14], is generally considered in literature as a reference value of the Raman $2D$ band shift of graphene under tensile strain and is used as the calibration value for the evaluation of strain within monolayer graphene.
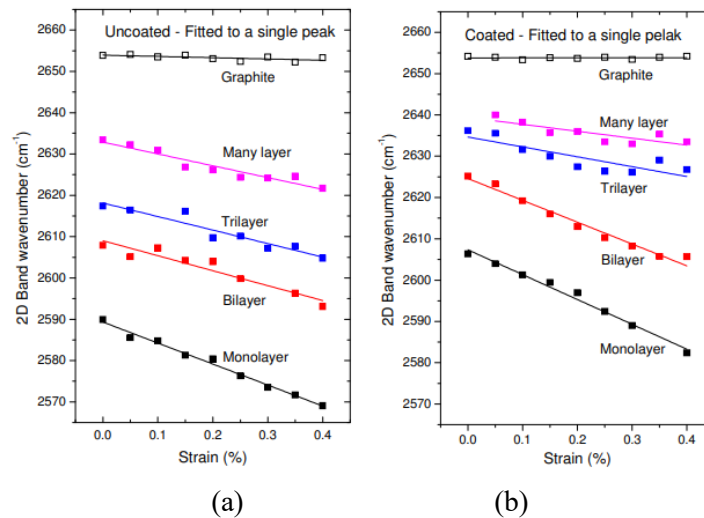
Figure 4.15 Raman band shift in monolayer, bilayer, tri-layer and many-layer graphene, for simply supported (a) and embedded nanoparticles (b) [231]

However, Raman band shift rate decreases significantly for bilayer and many-layer graphene, because of weak van der Waals forces, low internal stress transfer, and slippage between layers. Gong et al. [231] studied the effect of number of layer on the Raman band shift. They observed that from monolayer to bilayer graphene there is not a significant decrease of the $2D$ band shift, while starting from tri-layer it reduces, as shown in Figure 4.15. The tri-

layer graphene possesses a higher bending rigidity compared to the monolayer and its critical strain is four times smaller than the one found in single layer graphene.

Furthermore, Raman shift rate of graphene with more than one layer also depends on the nanoparticle configuration, whether it is simply supported (uncoated) or embedded in a matrix (coated) [231]. It was observed that in bilayer graphene, Raman shift rate is different in the two configurations, in particular it passes from -60 cm^{-1}/% when the particle is coated with polymer to -53 cm^{-1}/% when it is uncoated (Figure 4.16b). When bilayer graphene is uncoated, the stress transfers is affected by the poor stress transfer between the two graphene layers; this effect is more pronounced when the number of layer increases. On the contrary, when the bilayer nanoparticle is encapsulated in the polymeric matrix, no slippage between the layers occurs and the Raman shift rate is equal to that of monolayer graphene. Generally, the band shift rates are slightly higher in case of coated specimens but, even if when the number of layers increases, as for GNPs, this value is still very low. Differences with respect to the monolayer will therefore principally be a result of the efficiency of stress transfer between the different graphene layers.
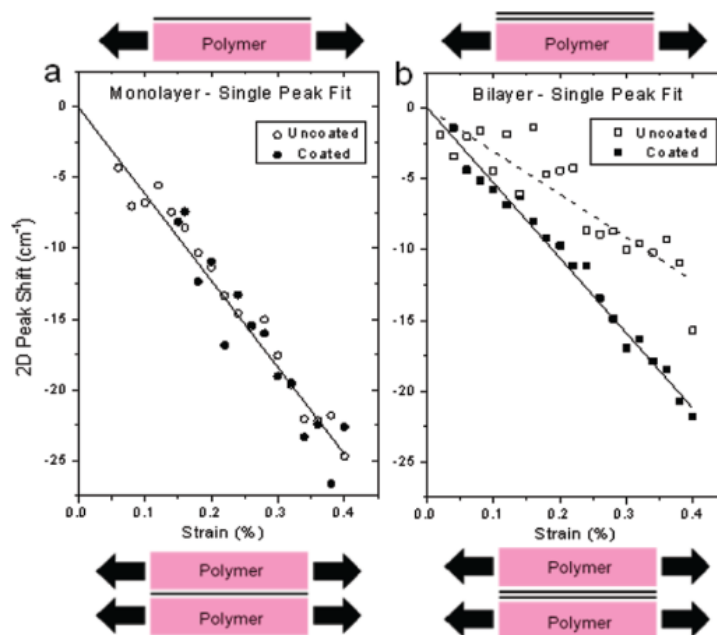
Figure 4.16 Raman shift with strain of 2D band of graphene monolayer (a) and bilayer (b) in the simply supported and embedded configuration [231]

Most importantly, Raman shift rate depends on the matrix mechanical behaviour [232]. For low stiffness matrix, such as thermoplastic elastomers (TPE) it is around -0.05 cm^{-1}/%, while

for high stiffness matrix, such as polypropylene (PP) or epoxy [233] it increases up to –5 cm^{-1}/% and 8 cm^{-1}/% respectively, as summarized in Figure 4.17.
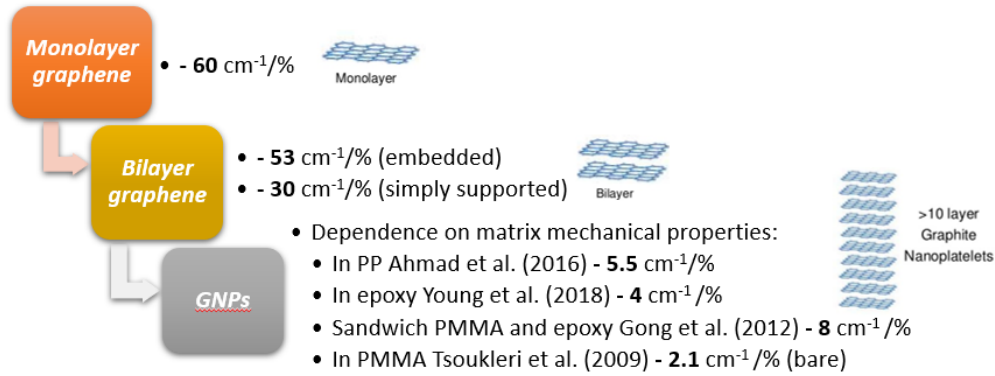
Figure 4.17 Raman band shift from monolayer to multilayer graphene

However, there is always the possibility that a variations in 2D band may be due to inhomogeneities or uneven stress transfer due to slippage [234]. Variations in the band shift are also known to occur due to differences in excitation wavelength, relative orientation of the graphene lattice to the straining direction, and direction of laser polarization [230,235].

There is a proportional correlation between the 2D Raman shift rate (dω$_{2D}$/dε) and the effective Young's modulus of the graphene (E_R). The effective Young's modulus of carbon-based materials can be estimated from the slope of the 2D Raman band position against strain. For graphene-related materials, where the characteristic downshift of the 2D band is in the order of −60 cm^{-1}/% the effective modulus can be estimated according to the following relationship:

$$E_R = \frac{\mathrm{d}\omega_{2D}}{\mathrm{d}\varepsilon} \frac{E_{graphene}}{\left(\mathrm{d}\omega_{2D}/\mathrm{d}\varepsilon\right)_{ref}}$$

(4.20)

Where $\mathrm{d}\omega_{2D}/\mathrm{d}\varepsilon$ is Raman shift rate of the 2D band, $E_{graphene}$ is the modulus of graphene of 1 TPa and $\left(\mathrm{d}\omega_{2D}/\mathrm{d}\varepsilon\right)_{ref}$ = –60 cm^{-1}/% is the characteristic downshift of the 2D band of graphene.

4.5 Experimental investigation

4.5.1 Materials and methods

Raman spectroscopy is employed to investigate the stress transfer in GNP/Epoxy (RTM6) films by monitoring the 2D peak position of GNPs during stretching of the material with inVia™ confocal Raman microscope by Renishaw.

The stress transfer efficiency has been assessed with Raman spectroscopy on GNP/Epoxy films for different filler content, from 40 vol% to 90 vol%. For each composition, five sample are tested. Rectangular specimens of dimensions 5 mm x 40 mm x 0.08 mm are clamped at both ends and are aligned with dual threaded leadscrews of DEBEN MT200 instrument, following the same procedure described in Chapter 3.

Raman spectra are acquired at different strain starting from unloaded configuration, with steps of 0.1%. Setting parameters are tuned in order to obtain the adequate spectra and to minimize the fluorescence effect associated to the epoxy resin (Figure 4.18a). The 2D peak position ($\sim$2635 cm^{-1}) of GNPs is monitored while the films are stretched, thus the spectral windows range is set from 2100 to 3000 cm^{-1}. For each step, 25 spectra are acquired on the surface of the sample, considering a rectangular grid of 25 points, using the 785 nm laser line and x100 objective lens (Figure 4.18b). To avoid the heating of the sample during the measurements, the power is kept under 1 mW with an exposure time of 30 sec. The 2D band is fitted to a single Lorentzian peak.

Table 4.1. Raman analysis settings

Laser	785 nm
Microscope objective lens	x100
Spectral window	2D $\sim$ 2600
Exposure time	30 s
Intensity	1%
Area	Rectangular grid – 25 points
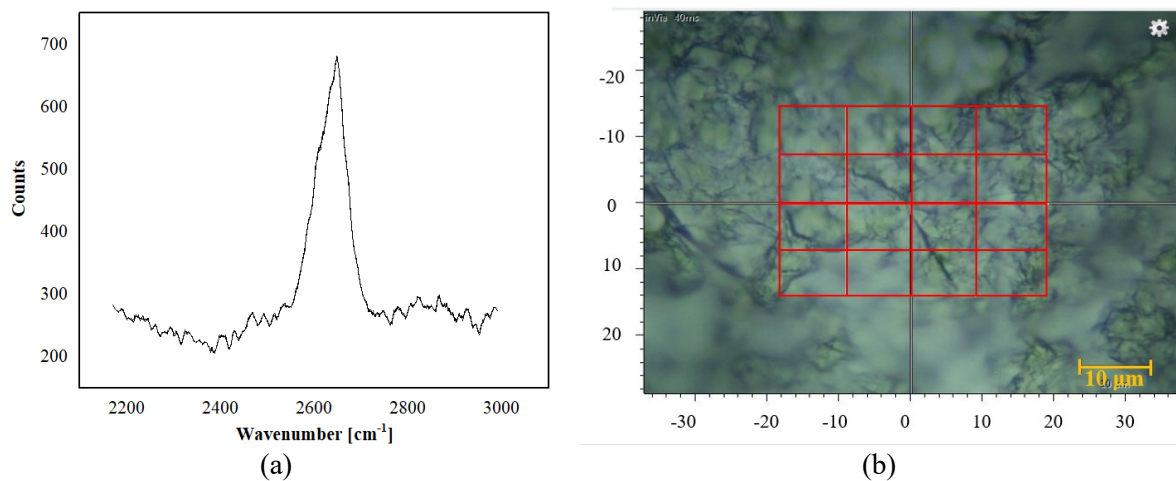
Figure 4.18 (a) Typical Raman spectra of GNPs/Epoxy (RTM6) films; (b) Rectangular grid
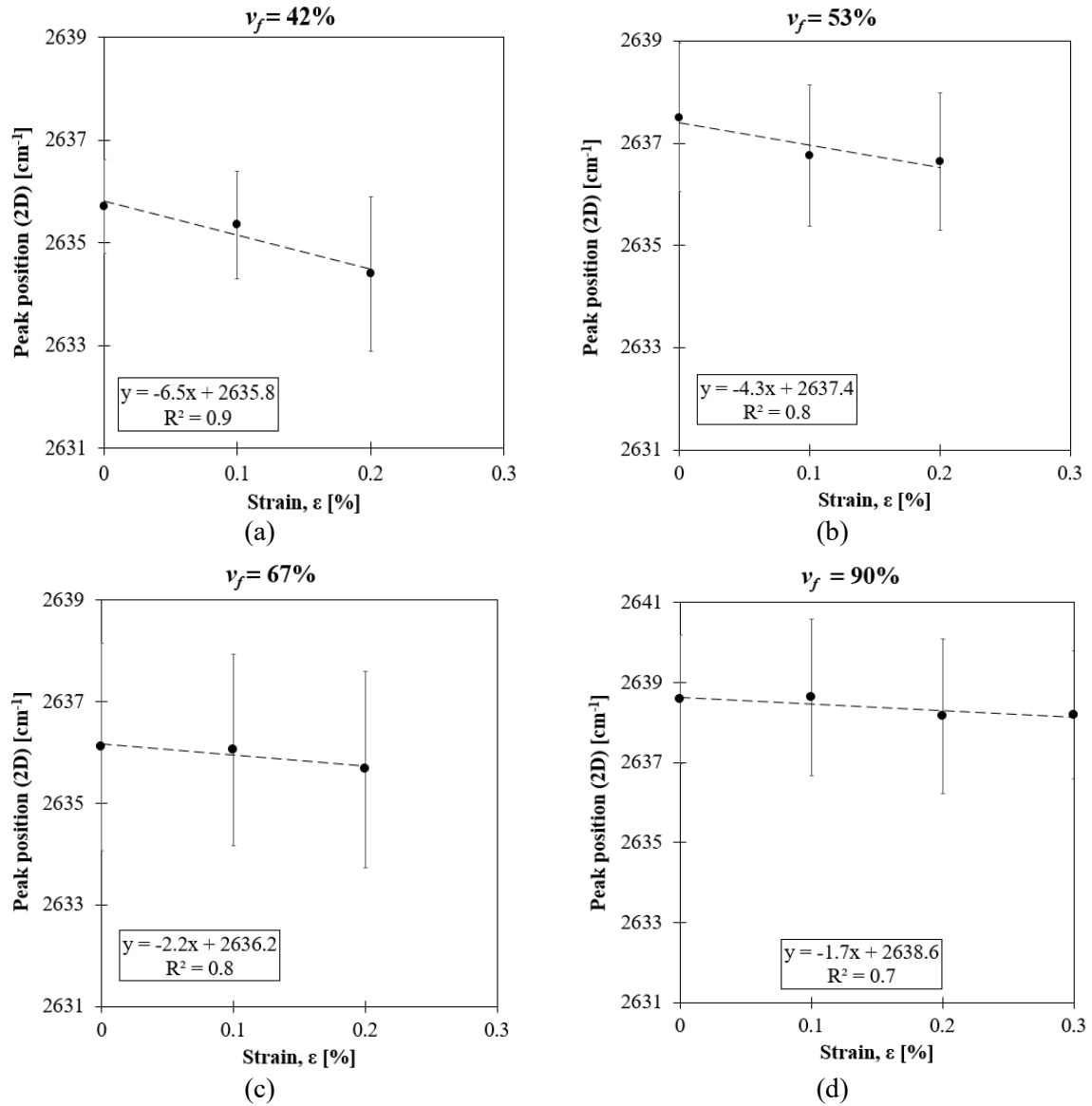
Figure 4.19 Raman shift rate for GNP/Epoxy film with different filler content: (a) 42 vol%; (b) 53 vol%; (c) 67 vol%; (d) 90 vol%

Table 4.2. Raman shift of GNP/Epoxy film with different filler content

Filler content [%vol]	Raman shift [cm^{-1}/%]
42	6.50
53	4.30
67	2.20
90	1.70

Figure 4.19(a-d) report the shift of the 2D peak position with applied macroscopical strain (ε=0.1, 0.2, 0.3%), for GNP/Epoxy films with different filler content. Raman band shift rate, which represents the slope of the plot, gives information about the quality of stress transfer in the composites. These values are listed in Table 4.2, for filler content from 40 to 90 vol%.

As stated before, Raman band shift is strongly dependent on the nanoplatelets number of layer and on the matrix in which they are embedded. For this reason, the Raman band shift associated to the optimal stress transfer that occurs between GNP and epoxy (RTM6) must be identified. For this purpose, two ideal systems have been considered:

(i).   Isolated nanoparticle embedded in the resin (Figure 4.20a);

(ii).   Interacting nanoplatelets aligned in the direction of the load (Figure 4.20b).

The first system is represented by nanocomposites with 0.5 wt% of GNPs fabricated via solution casting (Figure 4.20a). GNPs are dispersed in epoxy using dip sonication; then the mixture is poured in a mould and cured according to the resin cure cycle [195]. The second system is represented by GPregs coated with a thin layer of RTM6 (~10 μm) by means of spin coater (Figure 4.20b). The resin, diluted in acetone to reduce the viscosity, with an acetone-resin ratio of 10:1, is spin coated on the uncured GPregs with 2500 rpm for 1 minute and then cured according to the resin cure cycle [195]. The thickness of the resin layer is measured posteriori by using a digital micrometre in several locations.

(a)   (b)
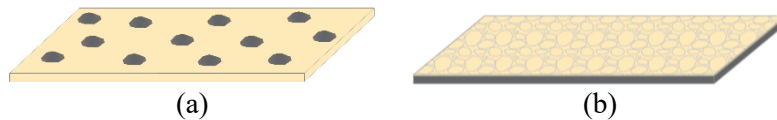
Figure 4.20 (a) Nanocomposite (0.5%wt); (b) GPregs coated;

Rectangular specimens of dimensions 40 mm × 5 mm are cut for both systems, and their thickness, (0.06-0.08) μm, is measured with a digital micrometre in several locations of the gauge length. Tensile tests have been performed on them using the micro-tensile tester (DEBEN MT200), equipped with 200 N loadcell and Raman spectra are acquired following the same procedure described before.

For system (i) the Raman shift rate obtained from the analysis is of ~8 cm^{-1}/% (Figure 4.21a), and is consistent with literature data for GNPs embedded in epoxy [233]; while for system (ii), the Raman shift rate is higher (~11 cm^{-1}/%) (Figure 4.21b). The reason why the system with GPreg coated with epoxy is characterized by higher value of Raman shift rate is related to the good alignment of the nanoplatelets and to their interactions unlike the dilute system.

In addition, for the second system, Raman spectra are acquired on coated sample with different filler content (from 40 to 90 vol%). These results show that the Raman shift rate is independent from filler content as shown in Figure 4.22 and equal to ~10.5 cm^{-1}/%. This finding is associated to the fact that Raman measurements on graphitic nanoparticles as GNPs are localized on the very superficial part of the material, and hence are representative exclusively

of the stress transfer between the GNPs on the surfaces of GPreg and the resin thin film. Consequently, Raman band shift does not depend on filler content but only on the stress transfer that occurs at the upper surface of the sample, i.e. between the aligned nanoplatelets and the thin resin film.

(a)   (b)
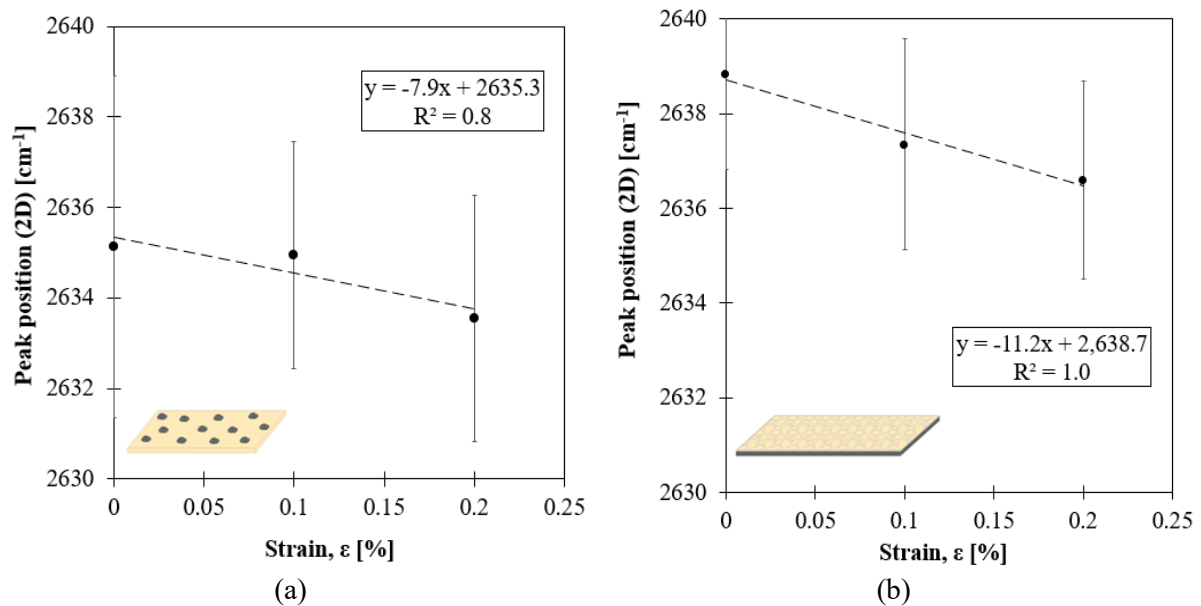
Figure 4.21. Raman shift rate for (a) nanocomposite with low filler content (0.5%vol) and (b) GPregs (90 vol%) coated with RTM6
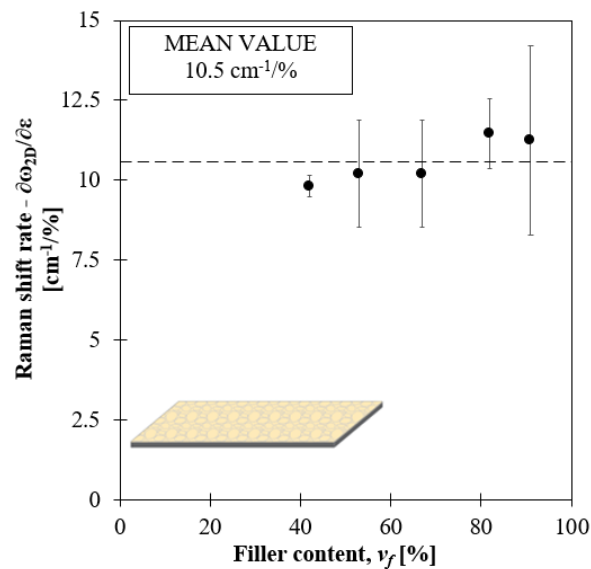
Figure 4.22. Variation of Raman shift rate with filler content for GPregs coated with RTM6

4.6 Efficiency of stress transfer

In Chapter 3 it has been found that the mechanical response of GNP/Epoxy films deteriorate with the increasing filler content, showing a drop of efficiency for filler fraction greater than 53 vol%, both for moduli evaluated in strain range of 0-0.05% and 0.2-0.3%. The same behaviour is found from Raman measurements as depicted in Figure 4.23b. In fact, the Raman shift linearly decreases for high filler content meaning that the stress transfer is poor. In addition, the values of Raman shift rate obtained from the analysis are lower than the optimal values calculated on both the ideal systems ((i) and (ii)). This indicates that the matrix is not able to efficiently transfer load to the particles and there is poor stress transfer between particles and matrix as shown in Figure 4.23.

The efficiency data obtained from tensile test are calculated according to Eq. (4.21). By comparing these results, referred to the composite elastic modulus evaluated in the range 0.2-0.3%, with Raman measurements in terms of efficiency (Eq. (4.22)), it appears that there is a strong correlation between the results (Figure 4.24).

$$\eta_{Tensiletest} = \frac{E_c - E_m(1 - v_f)}{v_f} \tag{4.21}$$

$$\eta_{Raman} = \frac{(d\omega_{2D}/d\varepsilon)_{v_f}}{(d\omega_{2D}/d\varepsilon)_{ref,GNP}} \tag{4.22}$$

Where $(d\omega_{2D}/d\varepsilon)_{ref,GNP} = 10.5 \ cm^{-1}/\%$

Consequently, this analysis allows a better understanding of the micromechanical behaviour of GNP/Epoxy films. It confirms the results obtained from tensile test, highlighting a bad stress transfer between the two phases, starting from filler content of 50 vol%.

(a)   (b)
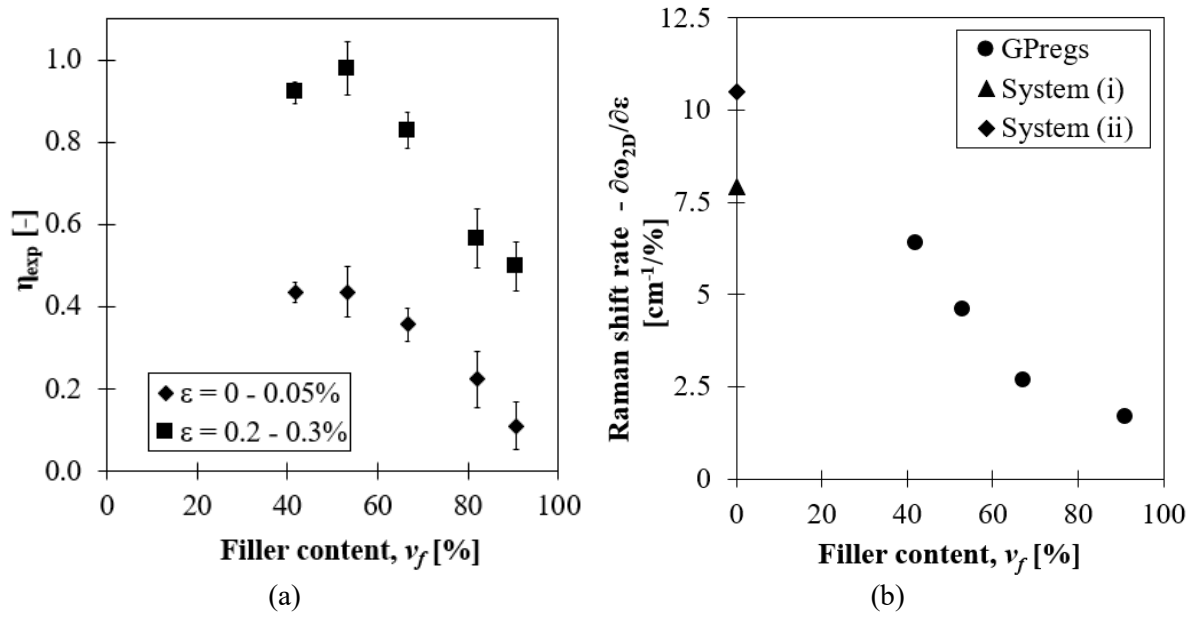
Figure 4.23. Efficiency of stress transfer: (a) tensile tests; (b) Raman measurements
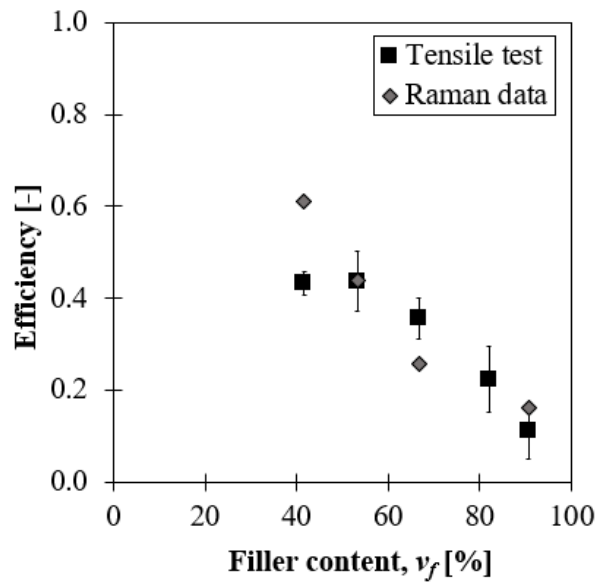
Figure 4.24 Affinity between the results obtained from tensile test and micro Raman spectroscopy

5. MODELLING OF MECHANICAL BEHAVIOUR OF HIGH FILLER CONTENT COMPOSITES

5.1 Mechanics of composite materials

The simplest way to evaluate the mechanical behaviour of composite materials is by characterizing them experimentally. In this way, the obtained properties refer to a specific system, constituted by a certain amount of reinforcement. Therefore, for the material design, there is the need of a tool for the estimation of the mechanical properties, which links the matrix and filler properties and their respective contents. In this respect, it is necessary to build analytical models, based on micromechanical considerations, that describe the composites behaviour from a macroscopic point of view. Although the material is microscopically inhomogeneous, because it is composed by two different phases, globally it can be considered homogeneous, and the composite elastic modulus can be evaluated as an average of the elastic moduli of the material in different points.

The analytical equations are derived from micromechanical considerations and constitute the contact point between micro- and macro-mechanics, they are based on the inhomogeneity of the material, and provide macroscopic moduli and strength.

Composites are divided in two main classes according to the length of the reinforcement. Long fibre composites are characterized by continuous oriented fibres immersed in an isotropic matrix (Figure 5.1a). Short fibre composites are characterized by discontinuous fibres that can be randomly or well oriented in the isotropic matrix, according to the filler content (Figure 5.1b-c). In the first case, for low filler content, the overall behaviour of the material is isotropic; in the second case, for high filler content, the preferential orientation of fibres/nanoplatelets conferees to the material an anisotropic behaviour through plane and isotropic in plane.

GNPs/Epoxy films are included in the last class, since nanoplatelets are well oriented in plane (Figure 5.1c). For this reason, this chapter will be focused on the macro and micro mechanical behaviour of this type of material.
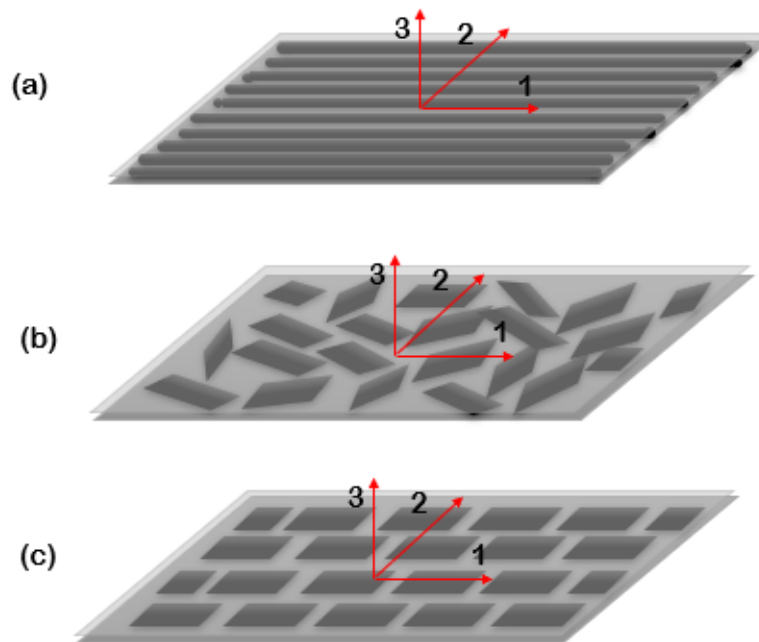
Figure 5.1 (a) Long fibre composites; (b) short fibre composites with randomly oriented particles; (c) short fibre composites with oriented particles

5.2 Long fibre composites: micro-mechanical model and rule of mixture

In long fibre composites, for the evaluation of the elastic modulus of the material in plane direction, some assumptions are made: (i) matrix and fibres are linear elastic; (ii) all fibres have the same elastic modulus E_f; (iii) perfect bonding between the two phases [236].

The last hypothesis means that when the film is loaded in tension, in the direction 1, the level of strain in the matrix and the reinforcement is the same:

$$\varepsilon_f = \varepsilon_m = \varepsilon_1 \tag{5.1}$$

Where the subscripts f and m refer to the fibre and the matrix, respectively.

According to the Hooke's law, the strain in the fibre and matrix can be defined as follow:

$$\varepsilon_f = \frac{\sigma_f}{E_f}$$

$$\varepsilon_m = \frac{\sigma_m}{E_m}$$

(5.2)

In the direction 1 of the lamina, the elastic modulus (Young's modulus) E_{11} is defined:

$$\varepsilon_1 = \frac{\sigma_1}{E_{11}}$$

(5.3)

Where σ_1 is the average stress in the generic cross section of the lamina.

From Eq. (5.1) and (5.2) it has:

$$\frac{\sigma_f}{\sigma_m} = \frac{E_f}{E_m}$$

(5.4)

Thus, the stress in the fibre and in the matrix are distributed according to their elastic moduli.

When the material is loaded in tension, in direction 1, the total load P applied to the lamina is divided in two parts, P_f and P_m, supported by the fibre and the matrix respectively:

$$P = P_f + P_m$$

(5.5)

Being:

$$P = \sigma_1 A$$

$$P_f = \sigma_f A_f$$

$$P_m = \sigma_m A_m$$

(5.6)

Where A_f and A_m are the area occupied by the fibre and the matrix respectively and A is the total cross section area.

Substituting Eq. (5.6) in (5.5) it has:

$$\sigma_1 A = \sigma_f A_f + \sigma_m A_m$$

(5.7)

Considering the filler and matrix volume fractions v_f and v_m:

$$v_f = \frac{A_f}{A}$$

$$v_m = \frac{A_m}{A}$$

(5.8)

Eq. (5.7) becomes,

$$\sigma_1 = \sigma_f v_f + \sigma_m v_m$$

(5.9)

According to Eq. (5.2), Eq. (5.9) can be rewritten:

$$\varepsilon_1 E_{11} = \varepsilon_f E_f v_f + \varepsilon_m E_m v_m$$

(5.10)

Which can be simplified according to Eq. (5.1):

$$E_{11} = E_c = E_f v_f + E_m v_m \qquad\qquad (5.11)$$

Eq. (5.11) is called *rule of mixtures*. It gives a simple reliable estimation of the Young's modulus of composites based on the modulus and volume fraction of each component.

It is the simplest and most straightforward relationship for the description of elastic modulus on composite with high modulus infinitely long and aligned fibres immersed in a low modulus matrix, for stress parallel to the fibre direction. Despite its simplicity, this relationship has been confirmed on numerous occasions to be effective in describing the essence of fibre reinforcement, especially at low fibre contents. Thus, when strain is applied to both the fibre and the matrix, the stress in the fibres is much higher than that in the matrix, with the fibres carrying most of the load and subsequently reinforce the low modulus matrix. The filler modulus scales with the matrix modulus, and stress is transferred more effectively when the matrix is stiffer.

According to Eq. (5.11) when v_f tends to 1, i.e. when the amount of matrix is very low, the elastic modulus is equal to that of the filler. This extreme value cannot be achieved for long fibre with circular section packed in a hexagonal lattice, since the occupied volume is of 0.906. Furthermore, for technological limitation the best content of fibre is between 0.6-0.7; for higher content fibre come into contact damaging.

5.3   Short fibre composites: modified rule of mixture

The rule of mixture is valid for long fibre composite and for low matrix content (<70 vol%). In reality, there are many factors, which affect the Young's modulus of the composite, particularly in the case of short fibres composites, such as the orientation, aspect ratio, particles shape and agglomeration. For these reasons, the rule of mixture has been modified, introducing an efficiency parameter, η:

$$E_c = E_m v_m + \eta \cdot E_f v_f \qquad\qquad (5.12)$$

The efficiency, η, was theorized by many researchers and specializes according to the orientation, length (or aspect ratio), agglomeration, waviness, and wrinkles.

The spatial orientation of the nanoparticles in polymer nanocomposites is very important, since the effect of reinforcement enhances when the particles are oriented in the direction of strain. The orientation factor, η_o, introduced by Krenchel [237], depends on the average

orientation and shape of the particle. It has a value between zero (for orientation perpendicular to the stress axis) and unity (for alignment with the stress axis). For aligned nanoplatelets or nanotubes it is equal to 1, for nanoplatelets and nanotubes oriented in two dimensions is equal to 1 and 3/8 respectively and finally for randomly oriented nanoplatelets and nanotubes is equal to 8/15 and 1/5 respectively, as shown in Figure 5.2 [238]. This factor can also be evaluated experimentally by Raman spectroscopy, correlating the degree of special orientation of the reinforcement with the mechanical properties of the nanocomposites [239].
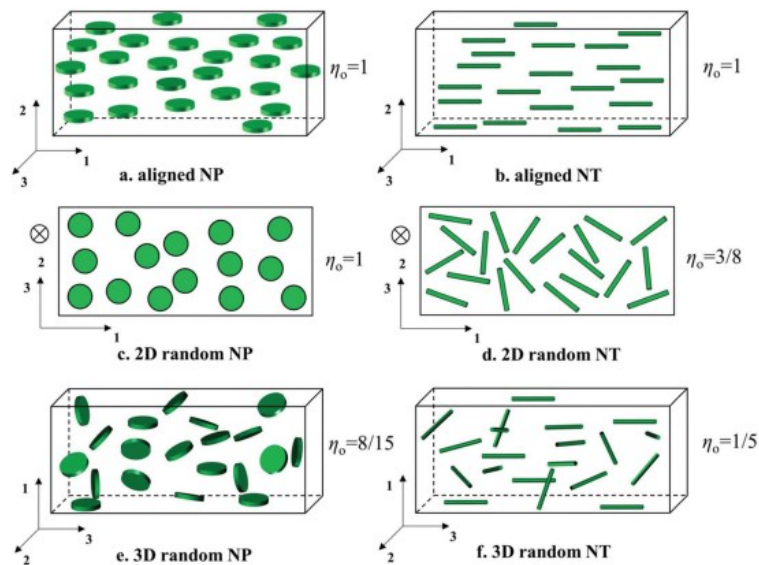
Figure 5.2 Krenchel orientation factor [238]

As agglomeration is dependent on the lateral dimensions and spatial orientation of the nanofillers, an agglomeration factor, η_a, can be introduced in Eq. (5.12). It is defined between 0 and 1: $\eta_a = 0$, indicated that all the particles are agglomerated hence they do not act as particle (nanoplatelets, nanotubes) but as bulk material instead, reducing the stress transfer. When $\eta_a = 1$, there is no agglomeration and all the particles are well dispersed in the matrix enabling efficient stress transfer [240]. In this case, the product $\eta_a v_f$ can be considered as the effective volume fraction, i.e. the volume fraction of the particles that bear load effectively as result of good dispersion.

The waviness and wrinkling induced during manufacturing especially for fillers at nano or micro-scale can also affect the mechanical properties of nanocomposites. Omidi et al. [241] modified the rule of mixture introducing shape function, length efficiency, orientation efficiency and waviness parameters and accounting for a non-linear relationship of the elastic modulus with filler content, especially at high loadings.

$$E_{c/m} = \left(\kappa_l \kappa_o \kappa_w \cdot E_{f/m} - 1 \right) \cdot v_f e^{\alpha \cdot v_f}$$

$$\text{With } E_{c/m} = \frac{E_c - E_m}{E_m},$$

$$\alpha = \frac{\ln \beta}{v_f} \text{ and } \beta = \frac{E_{c/m}}{\left(\kappa_l \kappa_o \kappa_w \cdot E_{f/m} - 1 \right) \cdot v_f}$$

(5.13)

In Eq. (5.13), the parameters κ_l, κ_o are the length and orientation factors described before, while κ_w is the waviness factor and assumes values from 0 to 1.

$$\kappa_w = 1 - \frac{a}{w}$$

(5.14)

Where a and w are indicated in Figure 5.3.
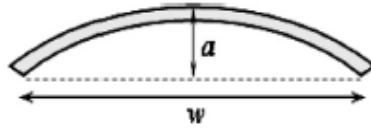
Figure 5.3 Curved CNT for evaluation of waviness factor

Wrinkles can significantly affect the roughness and the properties of the nanoplatelets. Although wrinkles reduce the aspect ratio of the platelets, they can affect the stress distribution around the matrix and improve the stress transfer due to enhanced filler/matrix adhesion and interlocking at the interface [242].

As it is known from numerous experimental studies on fibre-reinforced composites, short fibres are less effective in reinforcing composites compared to longer or continuous fibres. This phenomenon has been explained in detail by the shear lag and other theories, indicating that exists a critical length beyond which nanoparticles do not act as a reinforcement. The major parameters that affect the critical length are the aspect ratio of the nanoparticles and the interfacial interaction between the filler and the matrix. This effect is contained in the length factor, η_l, described by Cox equation [243]. The derivations of the efficiency of reinforcement in case of lamellar nanoplatelet are reported in the following section.

5.3.1 Shear lag theory applied to nanoplatelets

Passing from continuous to discontinuous composite materials, the assumptions at the base of the stress transfer between filler and matrix change. As discussed in the previous section there are some factors that negatively affect the mechanical behaviour of composite in terms

of interfacial adhesion. In particular, when the reinforcement length reduces to a finite length, the stress transfer drops.
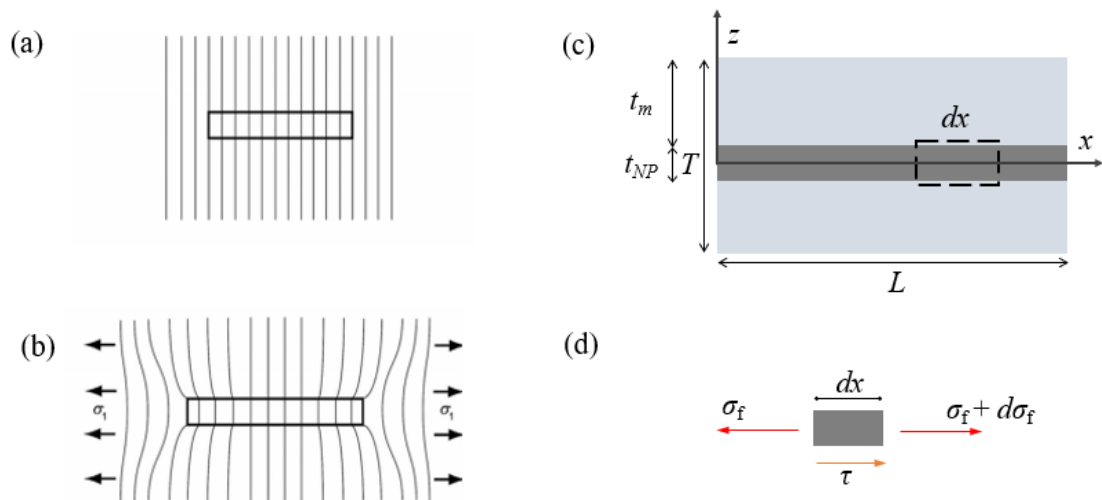
Figure 5.4 Short fibre composite material (in dilute condition): (a) undeformed state; (b) deformed state; (c) representative volume element of a platelet immersed in a matrix; (d) infinitesimal element

Kelly [244] discussed for the first time the stress transfer in discontinuous composites. When the material is loaded along fibre direction (Figure 5.4a-b), the fibre deforms the most in the central part and less in the edges, with consequent relative displacement between filler and matrix. The increment of axial stress is balanced by shear stress at the interface, which is highest at the edges.

This theory is at the base of shear lag model, which consider that the stress transfer from matrix to fibre is governed by interfacial shear stresses. An accurate model has been developed by Cox, for cylindrical fibre of length l and radius r [243], and by Kotha for rectangular platelets [245]. The models consider a fibre/nanoplatelet completely embedded in a continuous solid matrix, as sketched in Figure 5.4c. It is assumed that the interface does not carry tensile stresses and that the axial stress in the matrix is constant. The RVE is symmetric with overlapped platelets uniformly distributed and aligned in the direction of applied load and perfectly bonded by a uniform matrix layer. The matrix at the ends of the platelet is considered as an imaginary platelet with same thickness of the brick and with the mechanical properties of the matrix that acts as a shear spring transferring load from one platelet to the other. When the platelet/matrix system is loaded, the matrix strains homogeneously, but locally, around the platelet, the load transfer generates a perturbed state. The rate of transfer of load depends on the relative displacement between fibre and matrix. The stress field, which act on the

infinitesimal nanoplatelet element of length dx and thickness t_{NP} consists in normal stress, σ_f, and shear stress, τ (Figure 5.4d).

For equilibrium in x direction, on the infinitesimal element dx, it is possible to derive the shear stress:

$$\tau \cdot dx = (\sigma_f + d\sigma_f) \cdot t_{NP} \tag{5.15}$$

$$\tau = -\frac{d\sigma_f}{dx} \cdot t_{NP} \tag{5.16}$$

It shows that, the build-up of tensile stress in the nanoplatelet is determined from the distribution of interfacial shear stress.

The strain field around the fibre can be defined in terms of the displacement u of the matrix in the x-direction, relative to the original configuration. The displacement variation, du, along the z axis is connected to the shear strain γ, and hence to shear stress by the matrix shear modulus G_m. Thus, in the z direction, the shear strain can be expressed as follow:

$$\gamma = \frac{du}{dz} = \frac{\tau}{G_m} \tag{5.17}$$

By integrating Eq. (5.17) in z, the difference between the displacement in the matrix and in the platelet is given by the follow:

$$u_m - u_f = \int_{u_f}^{u_m} du = \int_{t_{NP}/2}^{T/2} \frac{\tau}{G_m} dz = \frac{T - t_{NP}}{2} \frac{\tau}{G_m} \tag{5.18}$$

The distance $T/2$ represents the far-field location, where the matrix is assumed to be uniform and not influenced by the presence of the platelet.

Integrating Eq. (5.18) with respect to x axis, it has:

$$\frac{du_m}{dx} - \frac{du_f}{dx} = \frac{t_m}{2G_m} \frac{d\tau}{dx} \tag{5.19}$$

Where du_m/dx and du_f/dx are the strain in the far field matrix and in the nanoplatelet respectively:

$$\frac{du_m}{dx} = \varepsilon_m$$
$$\frac{du_f}{dx} = \varepsilon_f \tag{5.20}$$

By substituting Eq. (5.2) and (5.20) in (5.19):

$$\varepsilon_m - \varepsilon_f = -\frac{t_m t_{NP}}{2G_m} \frac{d^2 \sigma_f}{dx^2} \tag{5.21}$$

Multiplying by the elastic modulus of the filler E_f:

$$E_f \varepsilon_m - E_f \varepsilon_f = -E_f \frac{t_m t_{NP}}{2G_m} \frac{d^2 \sigma_f}{dx^2} \tag{5.22}$$

Thus, the stress in the in the nanoplatelet can be evaluated by solving a second order differential equation in the unknown σ_f.

$$
\begin{aligned}
\frac{d^2 \sigma_f}{dx^2} &= \frac{2G_m t_{NP}}{E_f t_m} \frac{1}{t_{NP}^2} \left(\sigma_f - \varepsilon_m E_f \right) \\
\frac{d^2 \sigma_f}{dx^2} &= \frac{n^2}{t_{NP}^2} \left(\sigma_f - \varepsilon_m E_f \right)
\end{aligned}
\tag{5.23}
$$

Where n is the shear lag parameter for nanoplatelet.

$$n = \sqrt{\frac{2G_m t_{NP}}{E_f t_m}} \tag{5.24}$$

The ratio t_{NP}/t_m depends on the nanoplatelet distribution within the matrix and their volume fraction v_f. In particular, the exact relationship between t_{NP}/t_m and v_f depends on the platelets' arrangement. According to the RVE of Figure 5.4c, for platelets oriented in the x direction:

$$\frac{t_m}{t_{NP}} = \frac{1-v_f}{v_f} \tag{5.25}$$

The solution to the differential equation (5.23) is:

$$\sigma_f(x) = E_f \varepsilon_m + C \sinh\left(\frac{n \cdot x}{t_{NP}} \right) + D \cosh\left(\frac{n \cdot x}{t_{NP}} \right) \tag{5.26}$$

The constant C and D are evaluated by imposing the boundary conditions, i.e. normal stresses at the nanoplatelet edges are zero:

$$
\begin{aligned}
x = 0 &\rightarrow \sigma_f(0) = 0 \\
x = L &\rightarrow \sigma_f(L) = 0
\end{aligned}
\tag{5.27}
$$

Substituting Eq. (5.27) in (5.26):

$$
\begin{aligned}
0 &= E_f \varepsilon_m + C \sinh(0) + C \cosh(0) \\
0 &= E_f \varepsilon_m + C \sinh\left(\frac{n \cdot L}{t_{NP}} \right) + C \cosh\left(\frac{n \cdot L}{t_{NP}} \right)
\end{aligned}
\tag{5.28}
$$

$$D = -E_f \varepsilon_m$$

$$C = E_f \varepsilon_m \frac{\sinh\left(\dfrac{n \cdot L}{2t_{NP}}\right)}{\cosh\left(\dfrac{n \cdot L}{2t_{NP}}\right)} \tag{5.29}$$

Therefore, the stress in the nanoplatelet is given by:

$$
\begin{aligned}
\sigma_f(x) &= E_f \varepsilon_m + E_f \varepsilon_m \frac{\sinh\left(\dfrac{n \cdot L}{2t_{NP}}\right)}{\cosh\left(\dfrac{n \cdot L}{2t_{NP}}\right)} \sinh\left(\dfrac{n \cdot x}{t_{NP}}\right) - E_f \varepsilon_m \cosh\left(\dfrac{n \cdot x}{t_{NP}}\right) = \\[2mm]
&= E_f \varepsilon_m \left[1 - \frac{\sinh\left(\dfrac{n \cdot L}{2t_{NP}}\right)\sinh\left(\dfrac{n \cdot x}{t_{NP}}\right) - \cosh\left(\dfrac{n \cdot L}{2t_{NP}}\right)\cosh\left(\dfrac{n \cdot x}{t_{NP}}\right)}{\cosh\left(\dfrac{n \cdot L}{2t_{NP}}\right)} \right] = \\[2mm]
&= E_f \varepsilon_m \left[1 - \frac{\cosh\left(\dfrac{n \cdot L}{2t_{NP}} - \dfrac{n \cdot x}{t_{NP}}\right)}{\cosh\left(\dfrac{n \cdot L}{2t_{NP}}\right)} \right]
\end{aligned}
\tag{5.30}
$$

It builds up from 0 at the edges reaching a maximum in the middle of the platelets, as shown in Figure 5.5.
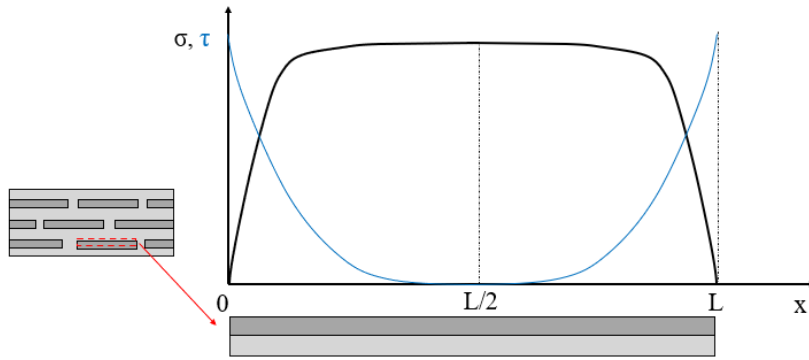
Figure 5.5 Typical example of axial and shear stress according to shear lag theory

The average stress in the nanoplatelet is calculated by integrating Eq. (5.30) between 0 and L and averaging on the whole platelet length L:

$$\bar{\sigma}_f = \frac{\int_0^L \sigma_f(x)dx}{\int_0^L dx} = E_f \varepsilon_m \left[1 - \frac{\tanh\left(\dfrac{n \cdot L}{2t_{NP}}\right)}{\dfrac{n \cdot L}{2t_{NP}}} \right] \tag{5.31}$$

The stress in the composite is defined by the rule of mixture:

$$\sigma_c = \sigma_m v_m + \bar{\sigma}_f v_f \tag{5.32}$$

By substituting Eq. (5.31) in (5.32):

$$\sigma_c = \varepsilon_m \left[E_m v_m + \left(1 - \frac{\tanh\left(\dfrac{n \cdot L}{2t_{NP}}\right)}{\dfrac{n \cdot L}{2t_{NP}}} \right) E_f v_f \right] \tag{5.33}$$

Since nanoplatelets and matrix in the longitudinal direction are acting in series, they carry the same strain $\varepsilon_c = \varepsilon_m = \varepsilon_f$, thus:

$$E_c = \frac{\sigma_c}{\varepsilon_m} = E_m v_m + \left(1 - \frac{\tanh\left(\dfrac{n \cdot L}{2t_{NP}}\right)}{\dfrac{n \cdot L}{2t_{NP}}} \right) E_f v_f =$$

$$= E_m v_m + \eta \cdot E_f v_f \tag{5.34}$$

Where,

$$\eta = 1 - \frac{\tanh\left(\dfrac{n \cdot L}{2t_{NP}}\right)}{\dfrac{n \cdot L}{2t_{NP}}} \tag{5.35}$$

Eq. (5.35) define the efficiency of reinforcement based on shear lag for rectangular platelet embedded in a matrix. Introducing the aspect ratio $AR=L/t_{NP}$, Eq. (5.35) can be rewritten as function of the platelet aspect ratio:

$$\eta = 1 - \frac{\tanh\left(n \cdot AR / 2\right)}{n \cdot AR / 2} \tag{5.36}$$

Eq. (5.34) defines the modified rule of mixture for lamellar nanoplatelets. Eq. (5.34) indicates that larger flakes are more effective in reinforcing polymer composites, as a result of better stress transfer than their smaller counterparts.

5.3.2 Semi-empirical models

In addition to shear lag models, there are other theoretical models that predict the elastic moduli of nanocomposites based on experimental observations, such as the Halpin-Tsai model [246] and the Mori-Tanaka relationship [247]. The assumptions at the base of the models are the same of the rule of mixture: particles and matrix are liner-elastic, isotropic and there is

perfect bonding between the two phases. The particles are also perfectly aligned in the direction of load and not agglomerated, and do not interact with each other.

Halpin-Tsai model [246] was obtained from the observation of micromechanical results of experimental tests. This model considers that the particles are ellipsoidal, have a constant aspect ratio and are aligned. It works better for relatively high aspect ratios.

The elastic modulus of the material is expressed as a function of the matrix and filler moduli, E_m and E_f:

$$E_c = \frac{1 + \zeta \cdot \eta \cdot v_f}{1 - \eta \cdot v_f} E_m \tag{5.37}$$

$$\eta = \frac{E_f/E_m - 1}{E_f/E_m - \zeta} \tag{5.38}$$

The value of ζ varies from 0 to infinity. If $\zeta = \infty$, Eq. (5.37) reduces to the rule of mixture and if $\zeta = 0$, it reduces to the transverse rule of mixture. It depends on the geometry of the reinforcement, particularly on the aspect ratio. For aligned short fibre composites the parameter ζ is estimated to be:

$$\zeta = 2\frac{l}{d} + 40 \cdot v_f \tag{5.39}$$

For low volume fraction it becomes $\zeta = 2l/d$ [248].

These models usually slightly overestimate the experimental data, because of the assumption of perfect bonding between the fibres and the matrix. This effect was taken into account in the Lewis-Nielsen model [249], by introducing other coefficients. The elastic modulus of the composites is given by:

$$E_c = \frac{1 + (k_E - 1) \cdot \beta \cdot v_f}{1 - \beta \cdot \mu \cdot v_f} E_m \tag{5.40}$$

Where k_E is the generalised Einstein coefficient and β and μ are constants. The first takes into account the relative modulus of matrix and fibres, while μ depends on the maximum volume fraction of the particles, v_{max}:

$$\beta = \frac{E_f/E_m - 1}{E_f/E_m - (k_E - 1)} \tag{5.41}$$

$$\mu = 1 + \frac{1 - v_f}{v_{max}}\left[v_{max}v_f + (1 - v_{max})(1 - v_f)\right] \tag{5.42}$$

The value of v_{max} is tabulated in Nielsen and Landel book [250] for a range of particle shapes and types of packing. It is the ratio between the true volume and the apparent volume occupied

by the filler. The lowest values, of 0.37, is for random close-packed agglomerated particles, while the highest, of 0.74, is for hexagonal close packed spheres. The Einstein coefficient k_E varies with the degree of adhesion between matrix and particle. For matrix with a Poisson ratio of 0.5, the coefficient is 2.5 if there is no slippage at the interface and is 1.0 if slippage occurs.

5.4 Analytical models for the prediction of mechanical properties of nacre like materials

All these models are not suitable for the predictions of the elastic properties of nacre like materials. At high filler content, the material architecture involves complex deformation mechanisms. The coexistence of a soft-domain (polymeric layer) and a hard domain (bricks) could affect the molecular mobility leading to an increase of ductility and energy dissipation.

Composites with brick-and-mortar architecture consist in a uniform assembly of bricks glued together by a uniform matrix thin layer (mortar), as schematized as in Figure 5.6. Actual biological and engineering structures, such as nacre, display spatial variations in overlap lengths, with different distributions which can be relatively narrow, as in the case of columnar nacre or very wide and even uniform, as in the case of sheet nacre.

However, modelling these complex micro-structures with a single unit cell gives a reasonable representation of the mechanical response of the material, which is sufficiently reliable to examine trends and establish broad design guidelines.
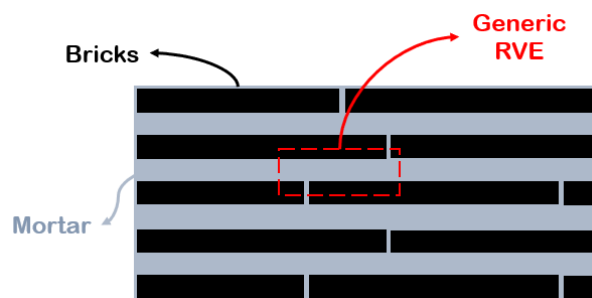
Figure 5.6. Schematic illustration of brick-and-mortar composites

Their behaviour in tension is described in Figure 5.7. At small strain both bricks and mortar move in the elastic field and the behaviour is linear. Then, four different failure mechanisms can occur [251]. If the brick is weaker than the matrix, there is an instant failure, which lead to a fragile behaviour of the structure. Otherwise, the matrix in the vertical interface yields, making the behaviour more ductile. In this case, for linear elastic matrices, the composite exhibits a pseudo-elastic behaviour and failure is attributed to the vertical junctions. Whereas,

for matrices with elastic-plastic behaviour, yielding in the horizontal direction occurs, allowing sliding between bricks. The composite failure can be attributed to the mortar break either in the vertical junctions or in the horizontal interfaces. In both cases, large strains are reached with consequent sliding between bricks and final pull-out mechanism.
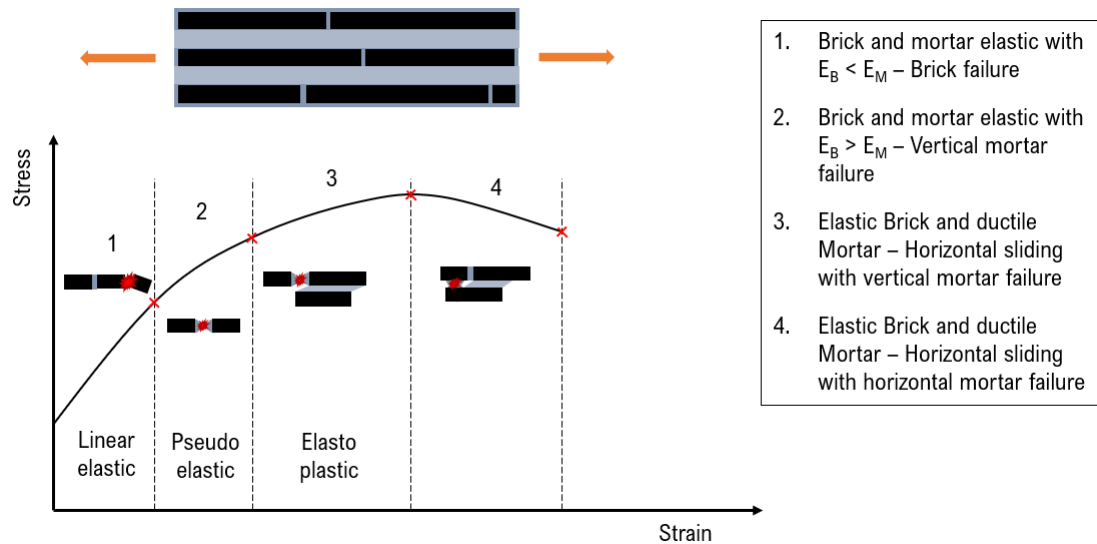
Figure 5.7. Stress-strain behaviour of B&M materials in tension

In modelling brick and mortar composites, it is assumed that the bricks behave elastically, while the mortar can have both elastic and elasto-plastic behaviour. Small plane strain deformations are assumed with zero strain in the *z*-direction, and zero stress in the *y*-direction. In addition, under uniaxial deformation, the horizontal interface experiences pure shear according to the relative displacements between adjacent bricks in different rows, while the vertical interfaces experience pure tension according to the relative displacements between adjacent bricks in the same rows. Finally, the horizontal mortar layer is considered very small such that the shear strain is uniform. The representative volume elements (RVE) are accurately chosen according to the analytical model and are depicted in Table 5.1.

The mechanical performance of these composites is regulated by the efficacy of the thin polymeric layer to transfer load, via shear transfer mechanism [243]. Thus, models [35–37,245] and design strategies [32–34] to predict the elastic modulus and strength of brick and mortar composites, based on the shear-lag theory, have been proposed in literature. These models assume perfect bonding between the two phases and efficient load transfer to the particles, and the existence of a continuous uniform matrix layer between the bricks.

Table 5.1. Analytical models for the prediction of composite's elastic modulus

Authors	RVE	Elastic modulus
(a) Cox et al. [243]		$E_c = E_m v_m + \eta \cdot E_f v_f$ $\eta = 1 - \dfrac{\tanh(AR_B \cdot n/2)}{AR_B \cdot n/2}$, with $AR_B = \dfrac{L_B}{t_B}$
(b) Kotha et al. [245]		$E_c = E_t v_f \dfrac{1}{1 + \coth \beta_0 / \beta_0}$ $\beta_0 = \rho_0 \sqrt{\dfrac{G_i}{E_t} \dfrac{v_f}{1 - v_f}} ; \rho_0 = \dfrac{L_0}{t_B}$
(c) Barthelat et al. [32].		$E_c = \dfrac{E_f v_f}{1 + \dfrac{\kappa}{\beta_0}\left[\coth \beta_0 + \coth\left(\dfrac{1-\kappa}{\kappa}\beta_0\right)\right]}$ $\beta_0 = \rho_0 \sqrt{\dfrac{G_i}{E_t} \dfrac{v_f}{1 - v_f}} ; \rho_0 = \dfrac{L_0}{t_B}$
(d) Begley et al. [251]		$\bar{E}_c \approx \dfrac{2\kappa_1 + \kappa_2}{2(1 + \kappa_1) + \kappa_2}$ $\kappa_2 = \kappa_{horizontal} = \sqrt{\dfrac{(1 - v_M)\bar{E}_M L_B^2}{2\bar{E}_B t_M t_B}}$ $\kappa_1 = \kappa_{vertical} = \dfrac{\bar{E}_M L_B}{\bar{E}_B h}$
(e) Wei et al. [252]		$E_c = E_f v_f \dfrac{1}{1 + \dfrac{\coth(\lambda L_0 / 2)}{\lambda L_0 / 2}}$ $\lambda = \dfrac{1}{t_B} \sqrt{\dfrac{G_m}{E_t} \dfrac{v_f}{1 - v_f}}$
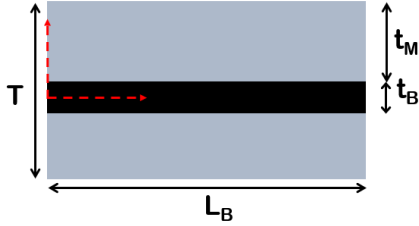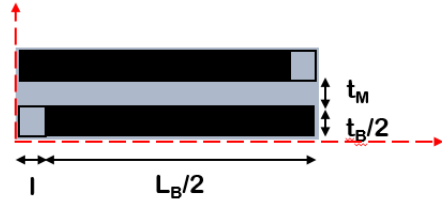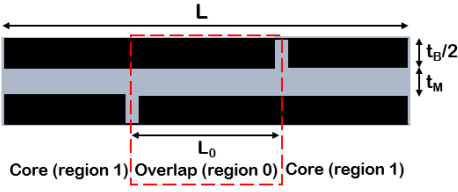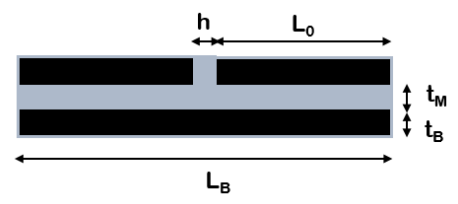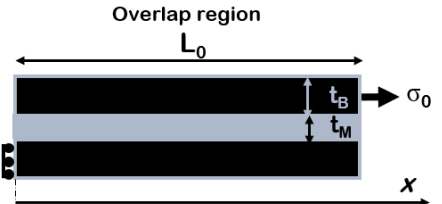
As described in the previous paragraph, shear lag theory has first been introduced by Cox, who developed an accurate model, for cylindrical fibre [243], and by Kotha et al. [245], who developed a similar model for the prediction of the mechanical properties of 2D platelet embedded in a continuous matrix. Based on this theory, several micromechanical models for the prediction of the mechanical behaviour of discontinuous composites have been developed.

Along this path, Barthelat [32] extended the model to the case of non-symmetric RVE, highlighting the impacts of the overlap length on the mechanical properties of the material.

According to the structure of nacre, the RVE is characterized by tablets with a well-defined arrangement and overlapped on a length L_0. The tablets are assumed linear elastic and brittle, while the matrix is modelled as a linear elastic-perfectly plastic material. The deformation mechanism is of shear-tension-shear, where the tablets are loaded in tension and the matrix in shear. For this reason, the vertical junctions between the tablet are assumed to be empty. According to the shear lag theory, the tensile stress in the brick and the shear stress at the interface are not uniform. Focusing on an individual overlap region within the composite, the distribution of shear stresses along the interface is governed by a non-dimensional elastic shear transfer number β_0, reported in Table 5.1.

When the interface is soft and/or the overlap ratio is small ($\beta_0 < 1$), the shear stress is quasi-uniform along the overlap length. On the contrary, when β_0 is large, the shear stresses become more concentrated at the overlap regions edges, accelerating failure. This is the case of low efficient structures, because in the central region of the overlap region, the interface does not carry any stress, and does not provide any contribution to the structural performance of the composite. Furthermore, for high brick concentration, variations in aspect ratio and overlap ratios have little effects on the overall modulus, leading to high modulus and resulting in more robust microstructures.

A more complex solution was found by Begley et al. [251], who included the vertical junctions in the model. A micromechanical analysis was developed for the uniaxial response of composites composed by elastic bricks bonded together with thin elastic perfectly plastic layers. The unit cell contains two bricks separated horizontally and vertically by a mortar layer, interlocked by a distance L_0. The model assumes that bricks are perfectly aligned, but with an arbitrary off-set between rows, and that the vertical interfaces carry load. The model is valid in case of very small mortar ratio and small mortar volume fraction and the material failure corresponds to that of interfaces.

Wei et al. [37] proposed an analytical model, based on shear lag theory in both elastic and plastic regime, capable of linking the mechanical properties of the constituents, to the mechanical behaviour of the reinforcement, their geometric arrangement, and to the chemistries used in their lateral interactions. In particular, the model aims to define design guidelines and to predict the characteristic overlap length for the optimization of the mechanical performances of the material. The RVE consists of two tablets connected by the matrix with an overlap length L_0. The system is subjected to a tensile load applied to the right end of the top tablet and fixed in the axial direction in the left end of the bottom tablet. The load transfer mechanism resembles

that of the shear lag model, with maximum shear stress at both nanoplatelets ends and maximum normal stress in the centre of the platelet, as in common biological composites.

The effect of both geometry and matrix constitutive law on the macroscopic behaviour of the composite material was investigated by Pimenta and Robinson [36], who developed a model for brick and mortar structure with nonlinear matrix response. They highlighted the relevant influence of platelet aspect ratio (AR) on the composite behaviour. In fact, for thick configuration, the strength increases with the aspect ratio, the overall stress strain curve resembles the matrix constitutive law and the distribution of shear stresses along the overlapping region is homogeneous. On the other hand, for slender configuration, the strength is independent from *AR*, the stress strain curve does not depend on the matrix behaviour but is governed by matrix fracture with crack tip at the platelets' ends and converges to a fracture criterion, as summarized in Table 5.2.

Furthermore, they highlighted the importance of matrix thickness on the composite behaviour. In particular, thick platelets and strain hardening matrices leads to a ductile composite, while thin platelets delay final failure and increase the strength of composites.

Table 5.2. Dependence of mechanical behaviour on aspect ratio

	Thick platelets (AR<10)	**Slender platelets (AR>30)**
Strength	Increase with AR	Independent from AR
Stress-Strain curve	Resembles the matrix constitutive law	Does not depend on the matrix behaviour
Behaviour	Ductile (Yield criterion)	Fragile (Fracture criterion)
Fracture	-	Matrix fracture with crack tip at the platelets' ends
Distribution of shear stresses	Homogeneous	-

However, these models assume perfect bonding between the two phases and efficient load transfer to the particles, and that the matrix consists of a uniform and continuous layer between the nanoplatelets. Under these assumptions, the strength and the elastic modulus of the composites increase with the amount of filler, reaching the best performance, equal to those of the reinforcement, at very high filler content (90-95 wt%). In order to reproduce a material with such behaviour at very high filler content, given the low amount of polymer, an exact control of the structural organization (both vertical and lateral) of the two phases should be ensured. Specifically, the matrix must spread into a continuous nanometric film with full coverage of the nanoplatelet surface [253] and this may be challenging due to defects associated to the fabrication process and to the polymer wettability issues [254].

Experimental data on GNP/Epoxy films at different filler content investigated in Chapter 3 and the critical analysis of the behaviour of other brick and mortar materials of literature (Chapter 2) have shown that, in reality, the mechanical performances at high filler content drop diverging from the theoretical behaviour. This trend is attributed to the difficulty of building a continuous nanometric matrix film able to fully cover the nanoplatelet surface [253,254].

In general, bottom-up technologies (e.g. layer-by-layer assemblies) are more able to fine-tune the nanometric alternance of the two phases [31] but remain mostly confined to the lab. Differently, top-down manufacturing processes are suitable for an industrial scale-up but are still far from obtaining the expected material architecture and final performance. In such processes, producing stable ultrathin polymer layers may be tricky and requires specific techniques. Very importantly, since the soft phase thickness must be compatible with the gyration radius [121], dewetting can occur thus leaving the particle surface partially uncovered. This condition prevents full covering of the nanoparticle and compromises the performance of the brick-and-mortar material. Parameters influencing the wettability of the thin polymer films include molecular weight, temperature, film thickness, substrate interaction and a combination of these parameters [122,123]. This may lead to a drop of strength and stiffness, especially at very high filler content. Therefore, knowing the issues associated to the loss of efficiency of the reinforcement is really important in the design process, in order to optimize the mechanical properties of these composites.

Starting from these observation, a new analytical model capable of describing the unusual behaviour (drop of modulus) that characterizes composites with lamellar reinforcement at high filler content has been developed [198].

5.4.1 *Model to predict the efficiency of reinforcement in aligned discontinuous composites with high filler content*

As discussed previously, in discontinuous composite materials, the stress transfer between matrix and filler is governed by interfacial shear stress [255] and the elastic modulus, E_c, of the composite is defined by the modified rule of mixtures of Eq. (5.34) [256].

A model for predicting the efficiency of stress transfer in brick-and-mortar systems, which accounts for a non-uniform matrix distribution over the nanoplatelets is proposed. It is evident that as the filler content increases, the nominal matrix layer thickness reduces to a fraction of the nanoplatelet thickness. However, exact control of the structural organization of the matrix layer at the nanoscale may be fairly difficult since localized non-homogeneous distribution of components, local dewetting and surface-induced roughening may occur [257]. In particular,

the minimum stable thickness of the matrix layer must be compatible with the gyration radius of the polymer and, at a critical thickness, dewetting phenomena may occur [258]. Also uneven lateral organization of the matrix layer may be due the random movements in the liquid dispersion film allowing for polymer rearrangements [31].
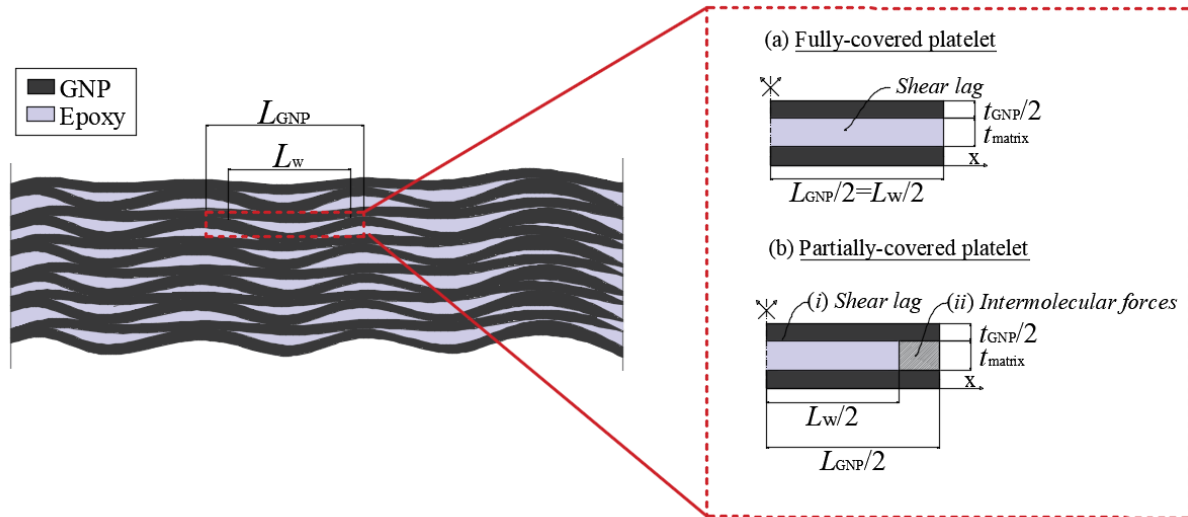
Figure 5.8. Sketch of resin distribution in GNP/Epoxy film and of the representative volume element (RVE) in the case of (a) fully-covered platelet and (b) partially-covered platelet

Figure 5.8 shows a sketch of the resin distribution between GNPs particles where the polymer is not able to wet the entire nanoplatelet surface and accumulates into small pockets or droplets, the height of which is of the order of magnitude of the gyration radius of the polymeric chains [123]. This assumption has been supported by AFM observation shown in Chapter 3. Also, it can be assumed that, in the case of partial nanoparticle surface coverage, the "wetted" length of the nanoplatelet reduces according to the increase of the filler content. A reduction of the wet-length of the nanoplatelet causes in turn a reduction of the effectiveness of the shear load transfer, with a consequent loss of the efficacy of the reinforcement.

For low filler content, the matrix can be assumed to cover the entire particle surface and the matrix length L_w is therefore equal to the lateral size of the particle ($L_w = L_{GNP}$) (Figure 5.8a). As the filler content increases, the amount of resin decreases and, due to the aforementioned thermodynamic and/or technological limitations to the minimum polymer thickness and distribution, partial nanoparticle coverage may occur ($L_w < L_{GNP}$), as shown in Figure 5.8b. In the latter case of partial surface coverage, the efficiency of load transfer can be assumed as the sum of two mechanisms acting on the particle length L_{GNP}:

(i)   the first active on the length L_w at the polymer/nanoplatelet interface described by the shear-lag theory [243];

(ii)   the second acting on the length L_{GNP}–L_w at the nanoplatelet/nanoplatelet interface based on constant intermolecular forces that develop at the particle-particle contact [259,260].

According to these assumptions, the average stress in the nanoplatelet of length L_{GNP} [243], defined in Eq. (5.31), is given by the two contributions and is defined as follows:

$$\bar{\sigma}_f = \frac{\int_0^{L_w/2} \sigma_f^{(i)}(x)dx + \int_{L_w/2}^{L_{GNP}/2} \sigma_f^{(ii)}dx}{\int_0^{L_{GNP}/2} dx} =$$

$$= \frac{\int_0^{L_w/2} E_f \varepsilon_m \left[1 - \frac{\cosh\left(\frac{n \cdot L_w}{2t_{GNP}} - \frac{n \cdot x}{t_{GNP}} \right)}{\cosh\left(\frac{n \cdot L_w}{2t_{GNP}} \right)} \right] dx + \sigma^{(ii)} \int_{L_w/2}^{L_{GNP}/2} dx}{\int_0^{L_{GNP}/2} dx} =$$

$$= \frac{E_f \varepsilon_m \left[1 - \frac{\tanh\left(\frac{n \cdot L_w}{2t_{GNP}} \right)}{\left(\frac{n \cdot L_w}{2t_{GNP}} \right)} \right] \cdot L_w + \sigma^{(ii)} \left(L_{GNP} - L_w \right)}{L_{GNP}} \tag{5.43}$$

Where $\sigma^{(ii)}$ describes the constant intermolecular forces arising from the contact interactions at platelet-platelet interface.

By substituting Eq. (5.43) in (5.32):

$$\sigma_c = \varepsilon_m \left[E_m v_m + \frac{\left(1 - \frac{\tanh\left(\frac{n \cdot L_w}{2t_{GNP}} \right)}{\left(\frac{n \cdot L_w}{2t_{GNP}} \right)} \right) \cdot L_w + \frac{\sigma^{(ii)}}{E_f \varepsilon_m} \left(L_{GNP} - L_w \right)}{L_{GNP}} E_f v_f \right] \tag{5.44}$$

Since the filler and matrix in the longitudinal direction are acting in series, they carry the same strain $\varepsilon_c = \varepsilon_m = \varepsilon_f$, thus:

$$E_c = \frac{\sigma_c}{\varepsilon_m} = E_m v_m + \frac{\left[\left(1 - \frac{\tanh\left(n \cdot L_w / 2t_{GNP}\right)}{\left(n \cdot L_w / 2t_{GNP}\right)}\right) \cdot L_w + \frac{\sigma^{(ii)}}{E_f \varepsilon_m}\left(L_{GNP} - L_w\right)\right]}{L_{GNP}} E_f v_f =$$

$$= E_m v_m + \frac{\eta^{(i)} \cdot L_w + \eta^{(ii)} \cdot \left(L_{GNP} - L_w\right)}{L_{GNP}} E_f v_f =$$

$$= E_m v_m + \eta \cdot E_f v_f \qquad (5.45)$$

Finally, the overall efficiency is a combination of the two contributions:

$$\eta = \frac{\eta^{(i)} \cdot L_w + \eta^{(ii)} \cdot \left(L_{GNP} - L_w\right)}{L_{GNP}} \qquad (5.46)$$

where $\eta^{(i)}$ represents the efficiency associated to the shear-lag mechanism defined in Eq. (5.36) dependent on an effective aspect ratio AR_w (ratio between the wet length of the particle, L_w, and its thickness, t_{GNP}) and the cohesive parameter $\eta^{(ii)} = \sigma_f^{(ii)} / E_f \varepsilon_m$ represents the ratio between the cohesive forces arising from the contact interactions at platelet-platelet interface [259,260] and the maximum load carried by the nanoplatelet at a certain level of strain ε_m.

Thus, introducing the effective aspect ratio $AR_w = L_w / t_{NP}$, Eq. (5.46) can be rewritten as follow:

$$\eta = \frac{AR_w}{AR_{NP}} \cdot \left(1 - \frac{\tanh(AR_w \cdot n/2)}{AR_w \cdot n/2}\right) + \left(1 - \frac{AR_w}{AR_{NP}}\right) \cdot \eta^{(ii)} \qquad (5.47)$$
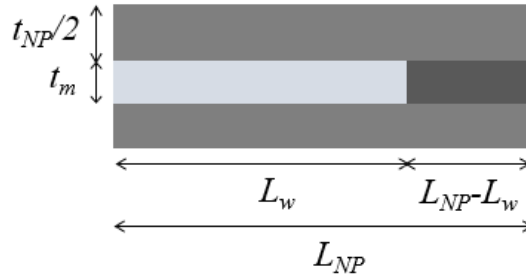
Figure 5.9. Representative volume element of the uncovered nanoparticle.

The effective aspect ratio AR_w, is a decreasing function of filler content. According to the RVE of Figure 5.9, the volumetric filler content is defined as the ratio between the area occupied by nanoplatelet area and the total area of the RVE:

$$v_f = \frac{A_{NP}}{A} = \frac{t_{NP} \cdot L_{NP}}{t_{NP} \cdot L_{NP} + t_m \cdot L_w} =$$

$$= \frac{1}{1 + \dfrac{t_m \cdot L_w}{t_{NP} \cdot L_{NP}}} = \frac{1}{1 + \dfrac{t_m}{L_{NP}} AR_w} \tag{5.48}$$

From which it is derived the effective aspect ratio as function of volumetric filler content:

$$AR_w = \frac{1 - v_f}{v_f} \frac{L_{NP}}{t_m} \tag{5.49}$$

The model, based on shear lag, incorporates two parameters that inherently capture the interfacial efficiency: (a) the minimum matrix thickness (t_m), which depends on the chemical affinity between the two phases and the matrix wettability and (b) the cohesive parameter (η^{ii}), which contains information about the molecular interactions that occur between adjacent nanoplatelets. In particular, interfacial properties are introduced in terms of nanoplatelets coverage, since poor wetting of nanoplatelet inhibits the stress transfer mechanism.

The efficiency, evaluated with Eq. (5.47), and the elastic modulus are compared with the experimental data for GNP/Epoxy nanocomposites, as shown in Figure 5.10a-b. The experimental efficiency of reinforcement, η_{exp} (based on modulus values, $E_{c,exp}$) is defined, according to the modified rule of mixture (Eq. (5.34)), as:

$$\eta_{\exp} = \frac{E_{c,\exp} - E_m(1 - v_f)}{v_f E_f} \tag{5.50}$$

It is interesting noting that the analytical model perfectly matches the experimental data (see Table 5.3 for properties and parameters) and the minimum matrix thickness is estimated to be 10 nm, which is compatible with the gyration radius of the polymer [123]. The cohesive parameter $\eta^{(ii)}$, which indicates the reduction of the stiffness of the material respect to the GNP nanoplatelet, E_f, due to GNP-GNP nanoplatelet poor molecular interaction, is equal to 43%. A best fitting methodology has been applied to find the best values of parameters, the minimum matrix thickness, t_m, and the cohesive parameter, $\eta^{(ii)}$, that minimize the error between experimental data and the model.

Table 5.3. GNPs and Epoxy properties and fitting parameters

L_{GNP} [nm]	t_{GNP} [nm]	AR_{GNP} [-]	E_f [GPa]	v_m [-]	E_m [GPa]	G_m [GPa]	t_{matrix} [nm]	$\eta^{(ii)}$ [-]
30000	14	2143	25	0.3	2.89	1.12	10	0.43

(a)   (b)
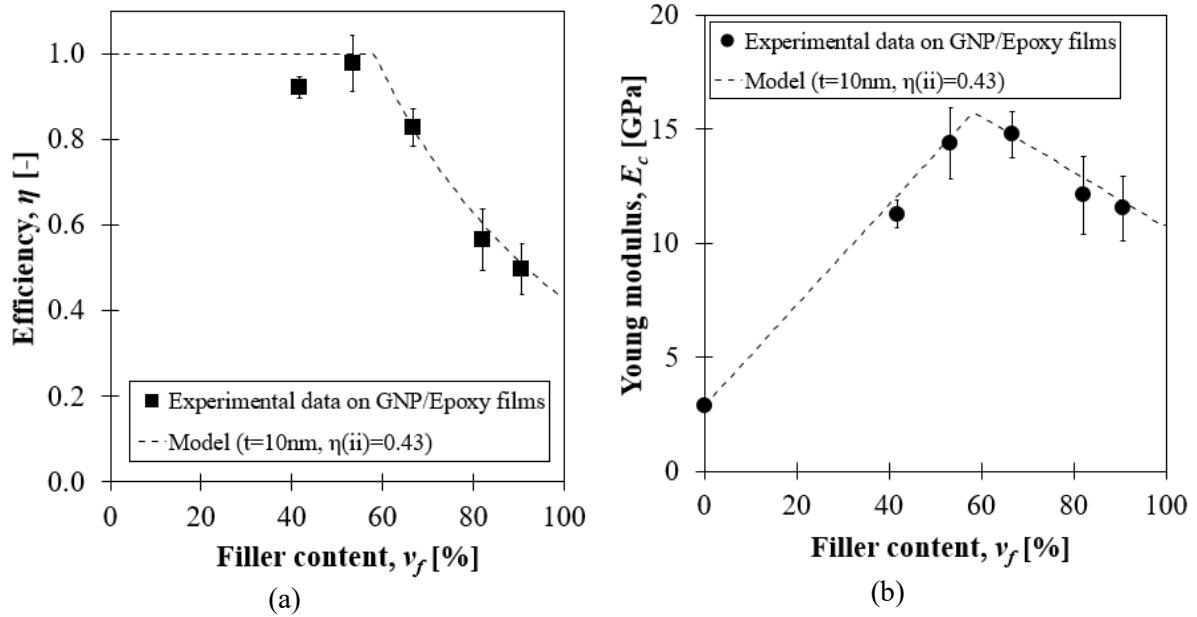
Figure 5.10. Comparison between experimental data and analytical model: (a) Efficiency parameter η and (b) Elastic modulus of the composite as a function of filler content

The proposed model has been also tested to fit literature experimental data. Li et al. [23] investigated the mechanical properties of high content GNP/PEI films. Also, in this case the mechanical efficiency decreases at increasing the nanoplatelet content. The GNP and PEI properties and the two fitting parameters are reported in Table 5.4.

Table 5.4. GNPs and PEI properties and fitting parameters (Li et al. [23])

L_{GNP} [nm]	t_{GNP} [nm]	AR_{GNP} [-]	E_f [GPa]	v_m [-]	E_m [GPa]	G_m [GPa]	t_{matrix} [nm]	$\eta^{(ii)}$ [-]
50000	14	3571	40	0.3	2.60	1.00	15	0.30

Figure 5.11, shows the comparison of the experimental data with the model prediction for both the efficiency and the elastic modulus with the values of parameters equal to a minimum matrix thickness of 15 nm and cohesive parameter, $\eta^{(ii)}$, of 30%.

(a)   (b)
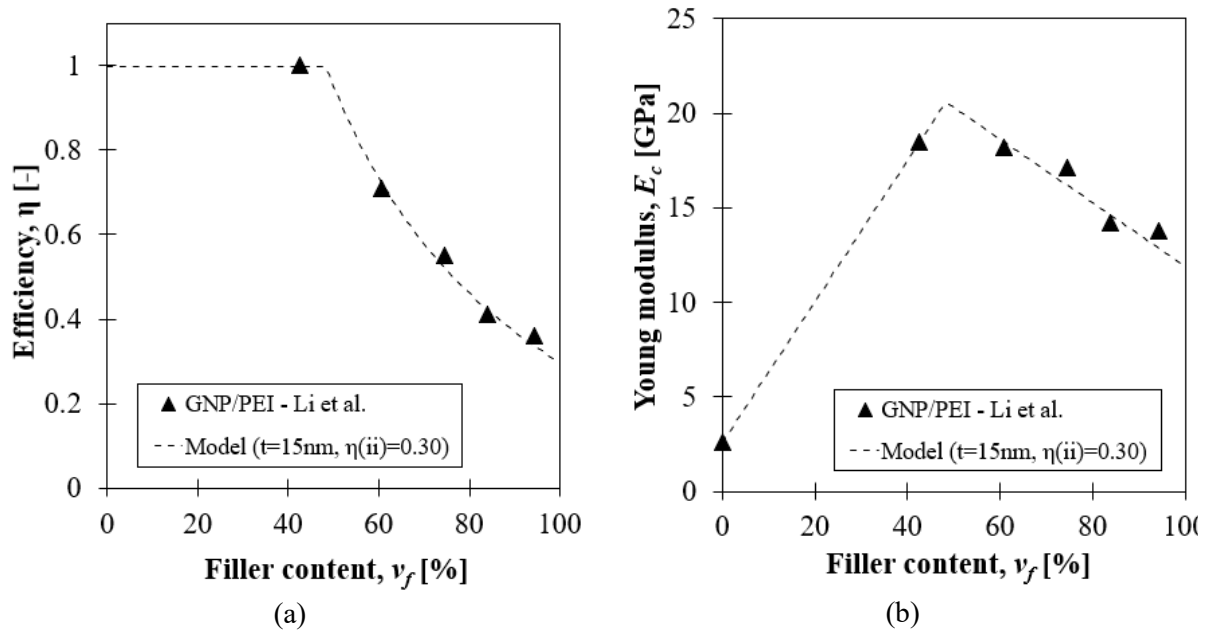
Figure 5.11. Comparison between literature data [23] and analytical model: (a) Efficiency parameter η and; (b) Elastic modulus of the composite as a function of filler content

(a)   (b)
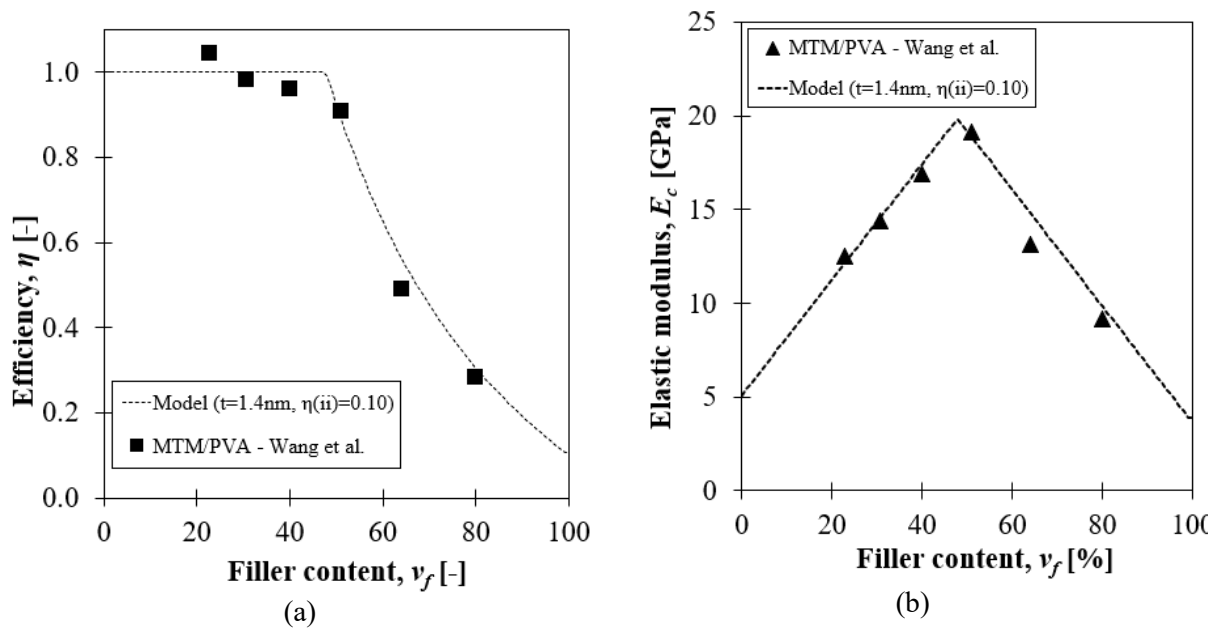
Figure 5.12. Montmorillonite (MTM)/PVA system [114]. Elastic modulus vs filler content and Efficiency vs filler content: comparison between experimental data and model with t_{matrix}=1.4 nm and η^{ii}=0.1

(a)   (b)
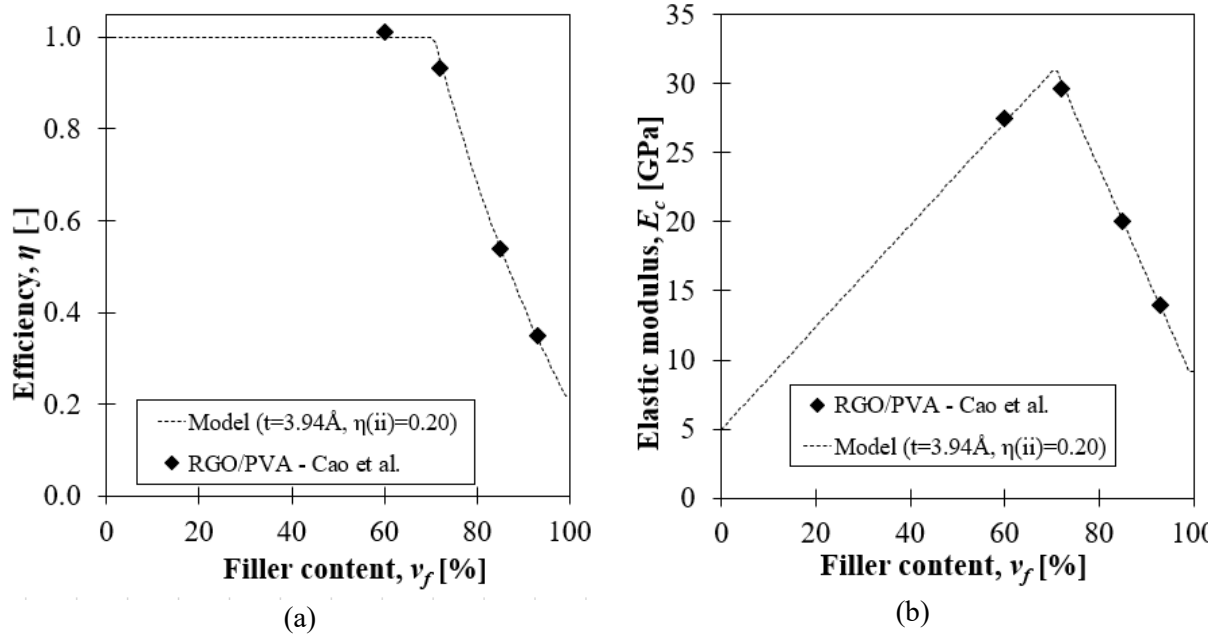
Figure 5.13. Reduced graphene oxide (RGO)/PVA system [101]. Elastic modulus vs filler content and Efficiency vs filler content: comparison between experimental data and model with t_{matrix}=0.39 nm and η^{ii}=0.2

Further evidence of the applicability of the model to other nanoplatelet/polymer systems with brick-and-mortar architecture are reported in Figure 5.13 and Figure 5.12 and model parameters are listed in Table 5.5. In both cases, the model adequately predicts the experimental data.

Table 5.5. Values of t_m and η^{ii} for different materials

	t_m [nm]	η^{ii} [-]
GNP/PEI – Li et al. [23]	15	0.30
MTM/PVA – Wang et al. [114]	1.40	0.10
RGO/PVA – Cao et al.[101]	0.39	0.20
GNP/Epoxy – Our work	10	0.43

5.4.2 *Influence of applied pressure on mechanical properties*

The wettability of the matrix layer has a significant role in the efficiency of stress transfer. In particular, the minimum stable thickness of the matrix layer identifies the filler content for which the loss of the efficacy of the reinforcement occurs: the higher the thickness, the lower the filler content for which the mechanical efficiency fails. The pocket size can be determined from wettability measurements [123] and, the ability of the matrix to cover the GNP surface and to efficiently transfer load to the particles is thus defined. As is well known, the wettability of a polymer can be regulated by varying temperature or pressure [261] and by introducing specific adhesive forces that the polymer and the solid surface may exchange. Moreover, the

wettability is strongly dependent on the effect of the molecular structure (molecular weight and reticulation) on the viscoelastic polymer properties.

In order to improve the mechanical properties of GNP/Epoxy films, strategies to increase the wettability should be employed. One possibility is to modify the fabrication process, by increasing for example the compaction pressure during the curing cycle. In this way, a physical confinement is applied to the polymer, increasing its conformal contact with the nanoplatelets. Figure 5.14 shows the comparison between tests carried out on film produced at different compaction pressures of 10 bar and 50 bar, respectively. Mechanical tests performed [43] shows that the higher is the compaction pressure during manufacturing the higher is the stress transfer efficiency at high nanoplatelet content and that the drop in efficiency can thus be shifted to higher values of nanoplatelet content.

The pressure increase from 10 to 50 bar shifts the onset of drop-off efficiency from ~58 vol% to ~67 vol% coherent with the estimated reduction of the minimum polymeric interphase thickness from 10 to 7 nm. On the other hand, the cohesive parameter increases up to 53%. The intermolecular forces contribution is higher when the compaction pressure between particles is enhanced [262]. In this way, the efficiency curve clearly shifts to higher values.
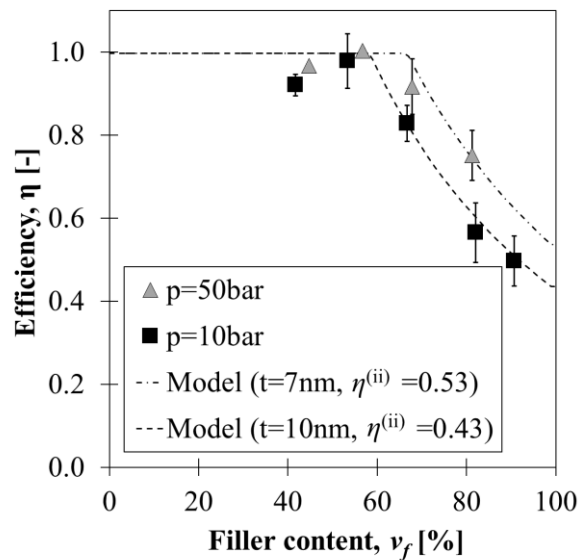
Figure 5.14. Influence of external applied pressure on mechanical behaviour of GNP/Epoxy film

5.5   Final considerations

Wettability issues and difficulties in fully covering the nanoplatelet surface with a thin and continuous polymer film are responsible of the drop of efficiency at high filler content. It is thus concluded that the reduction of available effective length for stress transfer between the matrix and the nanoparticle is responsible for the decrease of reinforcement efficiency in these composites. Modelling the matrix as a discontinuous layer better reflects the real structure of the material when filler content is high. Key parameter in the model is the minimum thickness of the polymeric matrix for which partial coverage of the nanoparticle occurs. The presented model gives very good prediction of the efficiency versus filler content, matching the experimental data presented herein and in other pertinent works [23,101,114]. Very interestingly, the proposed model combined with experimental observation have demonstrated that, at high GNP content, the efficiency of stress transfer can be improved with proper process design by promoting the wetting phenomenon and inhibiting the phenomenon of partial coverage. In fact, in light of the model design suggestion, GNP/Epoxy composite have been manufactured at higher compaction pressure (50 bar) and experimental data confirmed the model hypothesis showing an increase of the filler content for which the mechanical efficiency drops off.

6. EMPLOYMENT OF GRAPHENE PAPERS IN INDUSTRIAL APPLICATIONS

6.1 Introduction

As widely discussed in the previous chapters, brick-and-mortar materials, and specifically GNP/Polymer films, are characterized by exceptional multifunctional properties and good structural performances that make them competitive in different industrial applications. Also, they can be easily integrated into fibre reinforced polymers (FRP), without adding any additional steps in the fabrication process. Consequently, by exploiting their functionalities it is possible to improve those of FRP. In this chapter, the ability of graphene nanoplatelet coating to improve the fire performances of CFRP laminate is presented.

6.2 Fire resistance coating

Several disasters, caused by fires, in aircraft and ships demonstrated the importance of understanding the fire behaviour of composites, and the need for more flame-resistant materials. In particular, the fire performance of composites materials interests different fields, such as aerospace, marine, rail, automotive and civil infrastructure [263].

In case of fire, the main problems are associated to:

- Flame propagation;

- Smoke release and fumes, with concentration of carbon monoxide, hydrogen cyanide and other toxic gases that can reach a lethal level;

- Loss of load bearing capacity of structural element during and after a fire.

Polymer based composite materials, during fire event, exhibit poor performance: at temperatures typically above 300-400°C their organic matrix decomposes with the release of heat, smoke, and toxic volatiles and the composite irreversibly loses its mechanical performances. Carbon fibre reinforced plastics (CFRPs) are of great industrial interest due to its specific properties such as: high specific strength and stiffness, good fatigue, and chemical resistance. Thanks to these characteristics, in the last decades, CFRPs find applications in various sectors, such as: aerospace, ships, sports equipment, racing automotive, and civil engineering. However, the applications are still limited by the thermomechanical and fire behaviour of the polymer matrix and, in particular, by its high flammability and poor fire resistance [264–266]. This problem becomes particularly heavy when the composite component is placed in proximity to a radiative flux, since the material can deteriorate and experiences failure. This could produce severe consequences especially in case of aircraft, submarine and ship cabins, supercar engine compartment, structural parts of offshore platforms etc. Several methods have been proposed to preserve the mechanical performance of CFRP composites from the exposure to temperature, that include modifications of the matrices and protective coatings [267]. Modifications of the polymer matrices have been generally demonstrated to produce deterioration of the mechanical performance of the CFRP composites [268] and segregation problems in manufacturing [269]. On the contrary, the addition of a protective coating on the surface of laminate has several advantages: the fire-resistant properties are concentrated at the surface eliminating compatibility issues with the matrix and, more importantly, the functional and structural properties of the composite are not impacted.

In the latest years a great interest in the study of brick and mortar architecture to develop fire resistant coatings [28,113,115,140,185,186] has been addressed due to the intrinsic properties that such kind of architecture may exhibit: anisotropic thermal properties with in plane thermal conductivity much higher than through the thickness [30,43], and barrier to vapour and gases due to the exceptional high tortuosity factor associated to the impervious path created by oriented bricks [168,169]. All these engineered properties may favourably influence the fire resistance by managing the conductive heat exchange, block the oxygen and pyrolysis products diffusion towards the flame [171] and reflecting the incoming radiative heat flux.

In this chapter, the behaviour of CFRP composite when exposed to fire have been assessed through calorimeter test and the effect of graphene films protection has been investigated. In addition, the reaction of CFRP composite have been further investigated by laser spot heating. The effect of the protective layer thickness has been tested with different laser power (25, 50, 75, 100, 150 kW/m^2), simulating standard testing conditions (AC 20-135 and ISO 5660-1 Standards).

Finally, damage level and residual mechanical response of exposed samples have been assessed as a function of the level of protection. A significant improvement of the post-heat flexural moduli and a significant reduction of the damaged areas have been obtained in graphene films protected laminates.

6.2.1   *Requirement of fire resistance in CFRP*

ISO 5660-1 standard specifies the method for assessing the heat release rate and dynamic smoke production rate of specimens exposed in the horizontal orientation to controlled levels of irradiance with an external igniter [270]. In the test, specimens, positioned horizontally, are burned in ambient air conditions, while being subjected to a predetermined external irradiance within the range 10 to 75 kW/m^2, and placed in an aluminium mould, to avoid the polymer flow during heating. During cone calorimeter tests, the material is subjected to a heat flux by means of a heating source of conical shape, which allows a uniform irradiation of the specimen surface and also the aspiration of combustion products in a duct. The thermal degradation of the material causes gas release, which trigger the flame when in contact with the spark, initiating the measure.

The ISO 5660-1 standard suggest keeping the distance between the horizontal specimen and the heat source of 25 mm and sets the sample surface dimensions of 100x100 mm^2. The irradiance shall be uniform within the central area of 50x50 mm^2 and no prescription are made on the exposure time. The AC 20-135 standard [271] fix the sample dimension of 250x250 mm^2 and the heated area of 125x125 mm^2. The irradiated power flux should be Pd =105 kW/m^2, and the treatment times should vary from 5 minutes for fire-resistant classification and 15 minutes for fire-proof classification.

Heat Release Rate (HRR) curve is obtained from the measure of oxygen percentage that is consumed and CO/CO_2 percentages that is produced during the combustion [272]. It is one of the most used parameters to evaluate fire behaviour of a material. Cone calorimeter investigations can be used as a universal approach to ranking and comparing the fire behaviour of materials. However, the performances of the material depend on the specific characteristics

of the test, such as ignition source, ventilation, irradiance, temperature and geometry of the specimen [273]. Also, the horizontal sample positioning, melt dripping prevention, and well-ventilated combustion are crucial characteristics of the setup, as well as the distance between the cone heater and the sample surface.

6.3   Cone calorimeter tests

The ability of GNP/Epoxy films to improve the fire performances of CFRP laminate is assessed with cone calorimeter tests.

Tests were conducted on a Fire Testing Technology (FTT) oxygen consumption cone calorimeter, compliant with ISO 5660 [270], at Department of Applied Science and Technology of Polytechnic University of Turin. The value of applied heat flux is 50 kW/m^2. The distance between the horizontal specimen and the heat source is 25 mm.

GNP/Epoxy films (G-Pregs) of standard dimension 20 x 20 cm^2, average thickness of 62 ± 7 μm and with a nominal nanoplatelet/resin content ratio of 70/30 wt/wt are employed as coating. CFRPs are supplied by Technologycom S.r.l. They consist in high strength carbon fabrics twill 2/2 of 600 g/m^2, impregnated with a standard epoxy resin, suitable for autoclave and press moulding process and cured for 1 hour at 120°C with a pressure of 3 bar. The tensile strength and elastic modulus of cured laminate at room temperature are 700 MPa and 61 GPa respectively. Samples dimensions of 100 mm x 100 mm x 5 mm, coated with one graphene layer protection are fabricated by compression moulding, according to the cure cycle of the laminates. G-Pregs are easily integrated in the process, by overlaying them on CFRP surface. The adhesion is guaranteed without the addition of any binder.

Prior to the cone tests, all specimens analysed were conditioned at 23 °C for several days at 50% R.H. in a climatic chamber. All materials are tested in triplicate.

The tests have the purpose to give an assessment about the combustion behaviour under cone calorimeter conditions. During cone calorimeter tests, the material is subjected to a heat flux that is created by an electrical device: the material decomposes and releases gas products that are ignited by a spark and combustion products are aspirated in a duct.

(a)

(b)

(c)

(d)
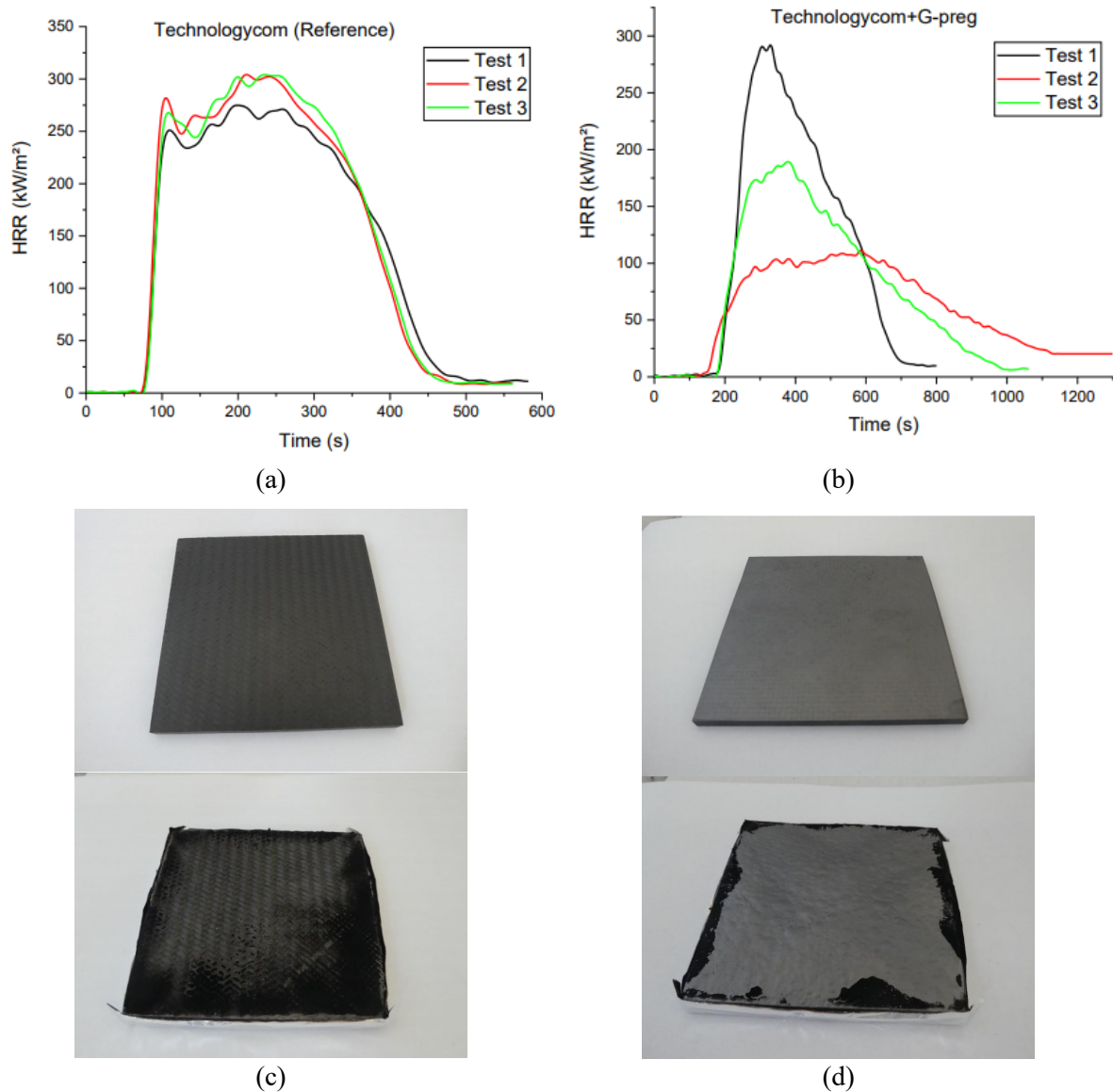
Figure 6.1 HRR curves relating to (a) Technologycom (b) Technologycom +G-preg

Figure 6.1(a-b) report the heat release curve for uncoated CFRP and CFRP coated with 1 graphene layer. The beneficial effect of the coating is relevant, since the intensity of fire (HRR) reduces of -40%, the total energy of fire (pHRR) reduces of -30%, the delays ignition time increases of +117% and the total smoke production during the fire reduces of -14.5%.

However, the results could underestimate the capacity of the material to protect the composite when exposed to fire. According to ISO 5660, the test is suitable to evaluate the fire performances of bulk materials, while may not work for a coupled material represented by CFRP panel coated with graphene layer. In fact, during the test, combustible gases are generated, but, given the good barrier properties of GPregs, they are trapped into the material and tend to flow towards the edges, triggering the flame. Therefore, since the graphene paper act as a heat spreader, dissipating heat in plane direction, the frame effects during this type of

test can be significant. Consequently, an optimized setup, aimed to minimize this effect, should be considered. A solution could be to consider samples with larger area, such that the heat flux is localized on a smaller area and the frame effects are negligible.

6.4 Laser spot analysis

To overcome these issues and to better understand the capacity of GNP/Epoxy films to protect CFRP in case of high heat flux, a new testing procedure based on laser radiation was developed at CIRTIBS Research Centre of the University of Naples Federico II [274].

Also, traditional methods of fire testing of composite materials have proven to be expensive due to material, equipment, and other costs. The costs put a limitation on the progress in developing new composite systems [275]. To overcome some of these limitations, laser heating test have been proposed [276–282]. Laser heating test is a reasonable cost method that uses a laser as the heating source to produce the desired heat flux. The test is able to simulate sub and hyper-sonic environment heating, by finely regulating the energy density generating several heating profile [278]. A small energy consumption and a limited power supply system is required during the test, thanks to the diode laser yield of about 40% and the compact case. Both energy spatial distribution and the irradiated area size can be modified, by defocusing or by properly selecting the focal length/beam expander. The sample size depends only by the available laser power, allowing the adoption of small samples, which is advantageous in case of precious materials. Consequently, since the laser energy can be concentrated on a small spot, it is possible to achieve temperature on the samples up to 3000 °C [276]. In addition, there are no limitations on the process chamber dimensions, they can be variable allowing a safe positioning of measuring equipment, such as IR cameras and pyrometers, without risking of damaging them. All these advantages enable laser heating test to become more and more popular in evaluating the behaviour of advanced materials, including composites [279–281], especially in aerospace applications [282,283].

In the follow, a preliminary study on the IR radiation shielding ability of graphene paper is presented, with the aim to produce CFRPs shielding coating.

Same sample used for cone calorimeter tests are tested. Plates of 400x400 mm^2 in plane dimension and about 1.7 mm in thickness, with a different level of protection (from 0 to 2 G-Preg layers) are fabricated by compression moulding. Also, in this case the adhesion between the laminate and the graphene paper is guaranteed without the addition of any binder. After curing, laminates are cut with a diamond saw in square samples of 50 mm side.

Specimen were tested for 15 minutes changing the power density in the range 25-150 kW/m^2, by changing the power percentage of the laser. Test conditions are reported in Table 6.1. During the laser heating tests, an IR camera (FLIR A655SC) was adopted to monitoring the temperature on the exposed surface of the specimen, while on the opposite surface, two thermocouples were used to measure temperature, bonded with epoxy adhesive at the centre of the exposed area and at 10 mm distance. In Figure 6.2 the complete set up is shown.
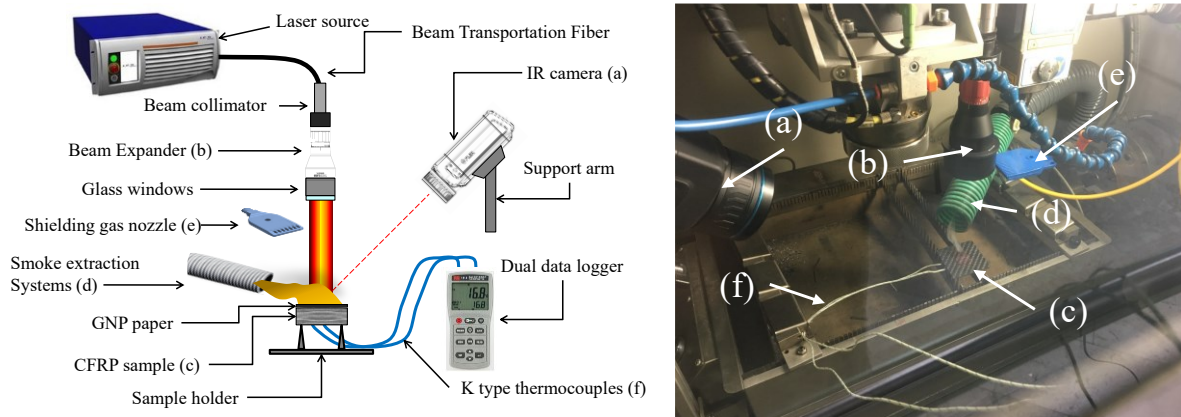
Figure 6.2 Schematic and image of experimental set-up

Table 6.1: Testing conditions and samples

Sample code	Materials		Power density [KW/m^2]				
	CFRP	GNP layers	25	50	75	100	150
G0-C8	1.7 mm	Uncoated	1	1	1	3	1
G1-C8	1.7 mm	1	1	1	1	3	1
G2-C8	1.7 mm	2	1	1	1	3	1

It is worth noting that, since it was necessary to adapt the test to the irradiation system (i.e. the laser source), the adopted procedure considers both the AC 20-135 and ISO 5660-1 standards. The proposed laser heating procedure uses a variable irradiated power flux up to 150 kW/m^2, an irradiated area about 15 mm radius over the sample surface of 50x50 mm^2 comparable to the standard AC 20-135 and an exposure time that is the maximum of AC 20-135 standard. Although the adopted procedure is not equivalent to any standard, the resulting condition is very stressful for the material, thus test at Pd=150 kW/m^2 are also performed.

Figure 6.3a-b show the temperatures trend versus time for the test performed at Pd=100 kW/m^2 on the uncoated CFRP (G0-C8) and 2 layers coated CFRP (G2-C8) samples. Temperatures are as acquired by IR camera within the circle of radius 20 mm centred in the beam of the laser spot. In both cases and for all the distances, *R*, from the centre of the laser beam, the temperatures rapidly increase up to a plateau, indicating that the thermal equilibrium is achieved and remain almost constant up to laser irradiation off. After the heating phase, the

temperature rapidly drops to the ambient one. The maximum temperatures reached at the centre of the laser beam are considerably different: T_{max}=675°C for the unprotected specimen and T_{max}=500°C for the specimen protected with 2 G-preg layers. In addition, uncoated laminates reached the maximum temperature after 60 s, while coated samples reached the maximum temperature much faster after 40 s. Figure 6.3c-d show the time-temperature recorded by the two channels' data logger on the opposite surface of the same samples Temperatures recorded on the opposite surfaces follow the same dynamic maintaining a noticeable difference of the maximum temperatures reached during the test of about 120°C. The behaviour is common for all the test conditions.
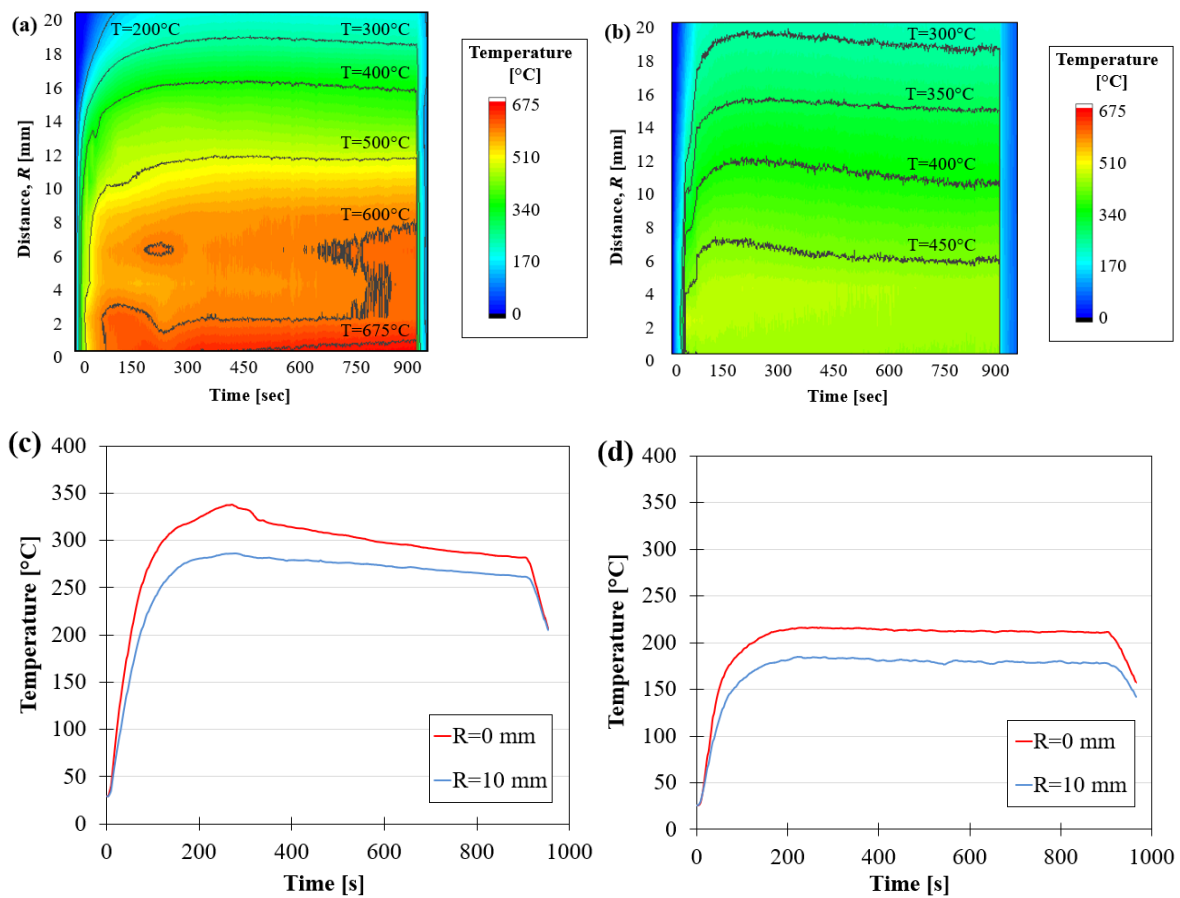
Figure 6.3 Time temperature history, in case of Pd=100 kW/m2: temperature map of upper face of (a) uncoated sample G0-C8 and (b) two graphene layers protected sample G2-C8; temperature at bottom face of (c) uncoated sample G0- C8 and (d) two graphene layers protected sample G2-C8.

Detailed temperature data analysis has been conducted by considering the average temperature reached during the last 4 min of the tests. Figure 6.4 shows the temperatures at the centre of the laser beam, R=0, on the exposed side (Figure 6.4a) and on the opposite side of the specimen (Figure 6.4b), as a function of the power density and for the different lay-up. The temperature measured on the upper surface at the centre of the laser beam (Figure 6.4a),

increases with increasing the power density, for both the uncoated and coated samples. Moreover, the protection with graphene layers reduces the maximum temperature attained: the highest is the thickness of the protection, the lowest is the temperature reached for all the power density investigated. Exception is the one-layer coated sample (G1-C8) tested at Pd=150 kW/m², that has reached a temperature, of about 1350°C, much higher than the uncoated one (about 900°C). However, this high temperature value is due to the presence of a hot spot, caused by the coating perforation and the escape of the matrix vapours formed below the coating. Thus, the IR camera erroneously reads the temperatures due to the radiation emitted by hot pyrolysis gases that is different from the gases temperature, since the latter have a different emissivity coefficient, consistently with [284]. Similar reduction of the maximum temperature reached during the tests due to the graphene layers protection is showed for the temperatures reached on the bottom side of the composite specimen (Figure 6.4b).

Figure 6.5 shows the ratio between the peak temperature for *R*=0, and the averaged value on the irradiated surface of the specimen as a function of protection level and laser power. The indicator shows the efficiency of the G-preg layer in redistributing the thermal energy.
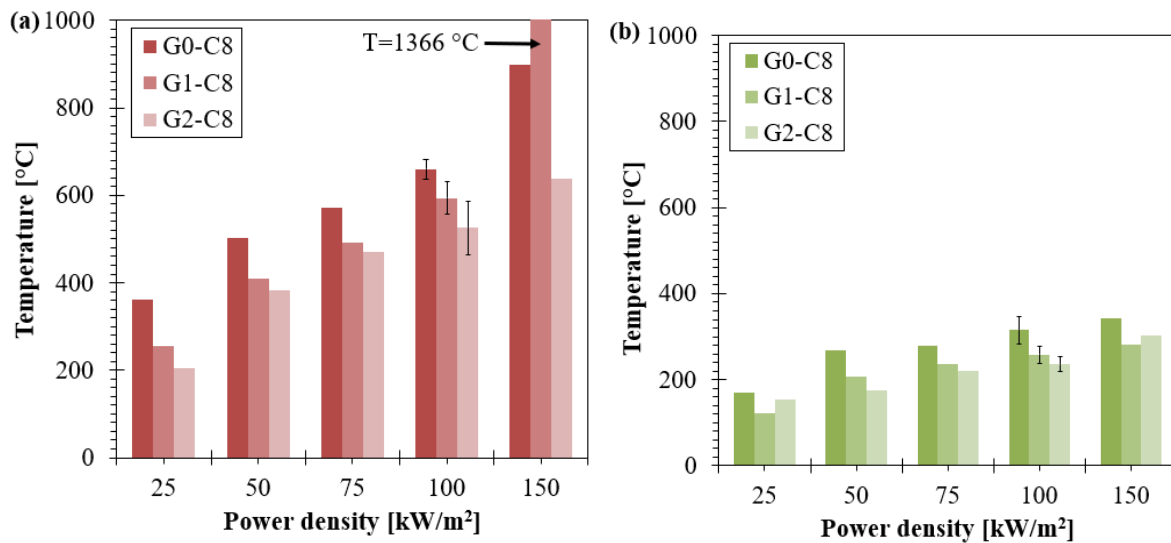
Figure 6.4. Maximum temperature against power laser density, measured on (a) upper face and (b) lower face
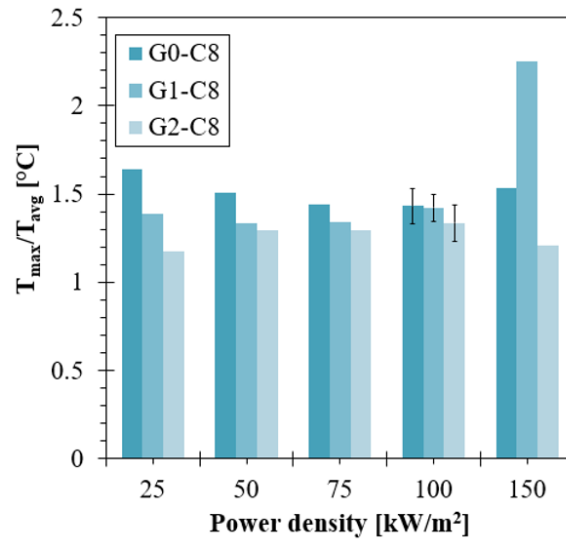
Figure 6.5 Ratio between the peak temperature at *R*=0 and the average value on the upper surface of the specimen as a function of protection level and laser power.

G-preg coating greatly reduces the temperature gradient across the sample surface exposed to the heat flux for all the power fluxes. The thickness of protecting G-preg coating increases the effect of heat spreading. In G-preg coated samples, temperatures are less localized under the gaussian laser beam, but more spread on the entire surface of the specimen, exploiting the high thermal conductivity of the material, as it is depicted in Figure 6.6. This effect would efficiently contribute to prevent a major damage of the composite by preventing the temperature peaks. This effect is showed in Figure 6.7, in the temperature profiles after 13 minutes of both uncoated and coated sample for different power laser density (25, 75, 100 kW/m^2). Since the in-plane thermal diffusivity of the graphene layer is much higher than that of CFRP, (about 100 mm^2/s [43] against 1.58 mm^2/s), the spatial distribution of temperatures in coated and uncoated samples is significantly different.
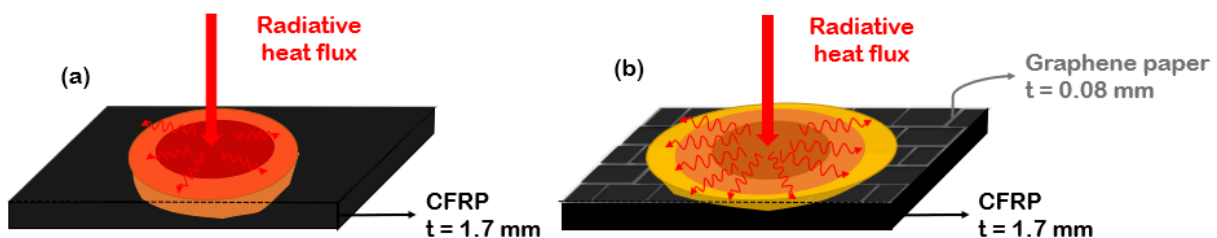
Figure 6.6 Schematic distribution of temperatures in CFRP sample (a) and CFRP sample coated with graphene layer (b)
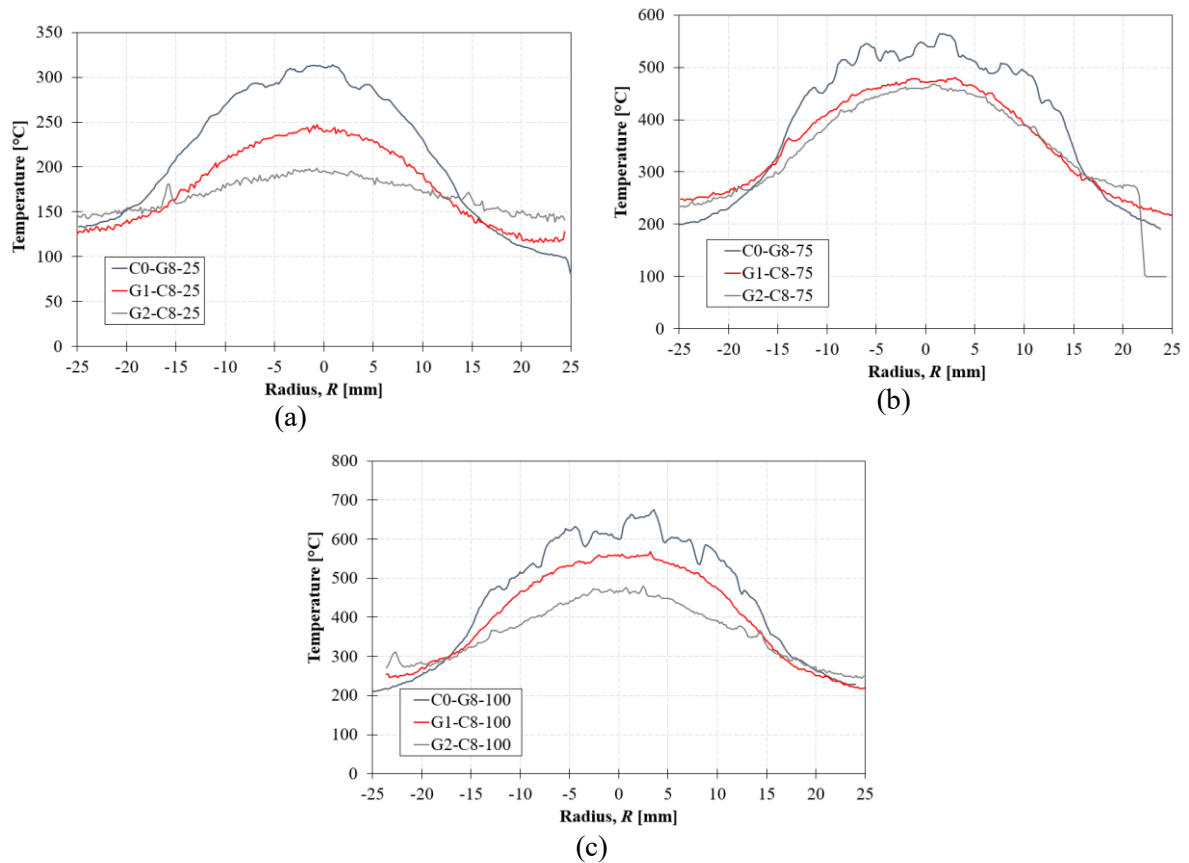
Figure 6.7. Spatial temperature profile after 13 min of uncoated sample and coated sample with 1 and 2 graphene layers in the case of (a) Pd=25 kW/m^2, (b) Pd=75 kW/m^2, (c) Pd=100 kW/m^2
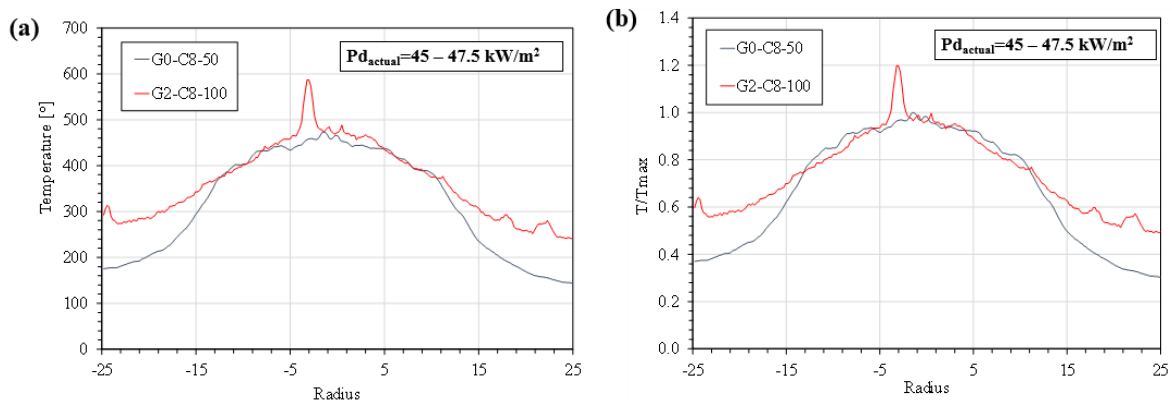
Figure 6.8. Comparison between (a) the spatial temperatures distribution and (b) the normalised temperatures distribution, at equal energy input (45-47.5 kW/m^2), for the samples G0-C8 and G2-C8

This effect is also well captured in Figure 6.8 that shows the temperature spatial distribution for uncoated sample (G0-C8) and sample coated with 2 graphene layers (G2-C8). The same energy input is considered for a better comparison, taking into account the material emissivity, which is 0.45 for the graphene paper and 0.95 for the uncoated CFRP [169]. In particular, for the uncoated and coated samples the temperature profile at Pd=50 kW/m^2 and at Pd=100

140

kW/m^2 are considered, which correspond to an actual power density of 47.5 kW/m^2 and 45 kW/m^2 respectively.

6.4.1 Damage assessment

Table 6.2. Damage phenomenology observed during the test

Phenomenon	Picture
Hot spots formation, production of fumes and/or fractures on the graphene coating	
Graphene paper swelling, followed by: (a) coating lifting (b) detachment of part of the graphene layer on G2-C8 samples	
Absence of matrix on: (a) upper surface at 25 kW/m^2 (b) bottom surface 75 kW/m^2 of the uncoated samples	
Achievement of high temperature (>1000 °C) confirmed by the presence of bright red-light emission of the sample surface on: (a) uncoated sample; (b) coated sample. for Pd ≥ 100 kW/m^2	
Formation of a white ash layer on the CFRP sample at Pd= 50 kW/m^2	

During the tests, various phenomena were observed and described in Table 6.2. The G-preg coating may swell due to its detachment from the composite sample upper surface due to pyrolysis gasses pressure or it may completely detach from the sample leaving internal surface exposed to the laser beam. Also, fractures on the G-preg coating may occur due to the production of pyrolysis gases and their escape produces IR camera hot spots. In addition, for $Pd \geq 100$ kW/m^2, temperatures above 1000°C were achieved on the samples, regardless of the coating. The achievement of so high temperatures was confirmed by the presence of bright red-light emission of the sample surface.

The tested samples are then characterized in order to assess the level of damage, both with optical and chemical analyses.

➤ *Optical damage evaluation*

Typical damage progression visually detected on both sides of the specimen as a function of the protection level is shown in Figure 6.9 for laser power density of 100 kW/m^2.
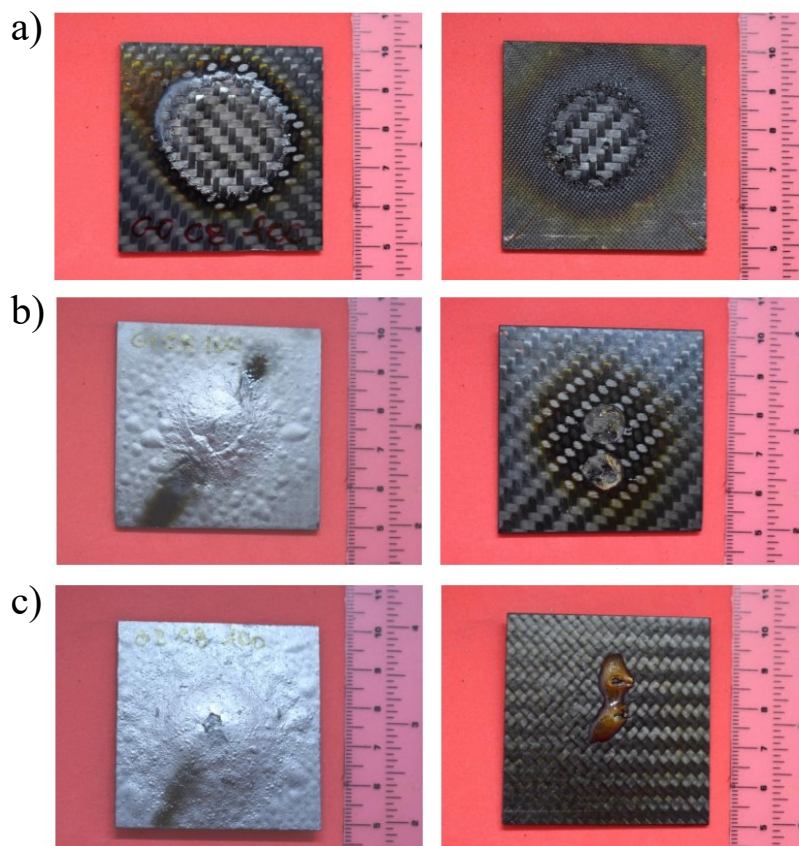
Figure 6.9. Samples tested with laser power density of 100 kW/m^2: (a) Uncoated; (b) 1 G-Preg layer; (c) 2 G-Pregs layers (upper side on the left and lower side on the right)

Due to the different optical properties of the resin rich and burned carbon textile it is possible to estimate from the photograph the damaged area for both the sides of unprotected samples.

The presence of G-preg layer makes the evaluation of upper surface damage status not straightforward, but some indications can be given.

The estimation of the damaged area for sample without protection and protected with 1 G-Preg layer is reported in Figure 6.10. In the uncoated case, the damaged area is clearly visible and identifiable from an optical analysis of the sample both on the upper and lower surface and for different laser input density. On the contrary, samples coated with 1 G-Preg layer do not experience severe damage on the lower surface, which only turns brown as shown Figure 6.10b, except for Pd=150 kW/m^2.
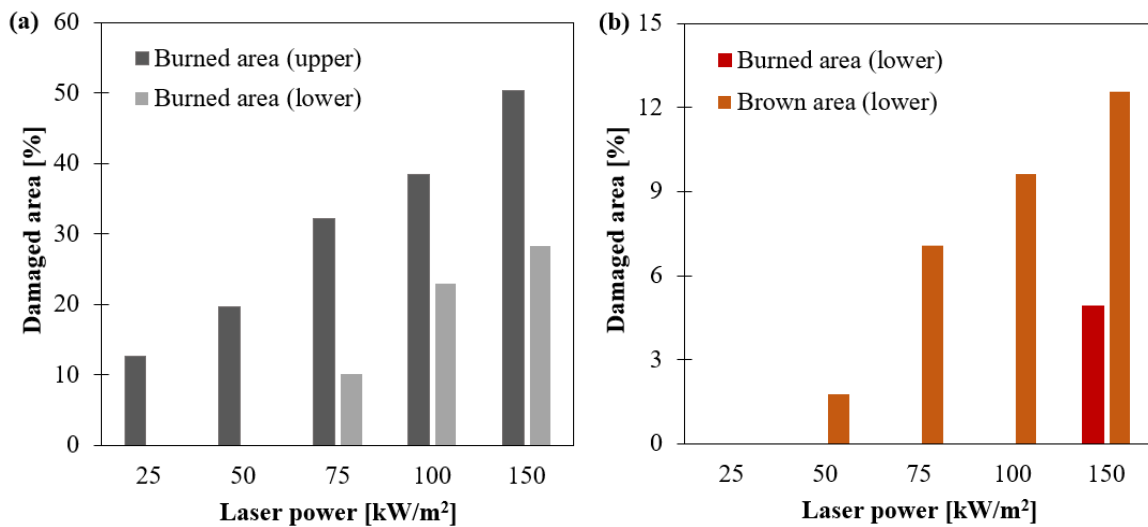
Figure 6.10. Estimation of damaged area (with respect to the sample area) of: (a) uncoated sample; (b) and protected with 1 G-Preg layer.

The damaged area linearly increases with the increasing laser power. In the case of unprotected sample, the upper side happens to be burned even at the lowest laser power, while the lower side started to be burned from 75 kW/m^2. When protected with G-pregs, the damage is significantly reduced. For laser power of 25 kW/m^2, no damage is detected either on the upper or lower surfaces and both for samples coated with 1 and 2 layers. By increasing the laser input to 100 kW/m^2, the upper side exhibits some bubbles, while the lower side turned brown in case of 1 layer protection and is undamaged in case of 2 layers protection. Further increases of laser input to 150 kW/m^2, leads to a damage on both upper and bottom surface, even in the case of sample coated with 2 G-preg layers.

➢ *Chemical assessment*

Damage assessment by visual inspection has been checked with a qualitative chemical analysis.

Infrared Spectroscopy (FT-IR) (Frontier MIR/NIR Perkin-Elmer spectrometer) is adopted to investigate the level of damage of all the samples after burning, to determine the presence of resin peaks. Spectra are acquired on both side of uncoated coupons and only on the bottom side of the coated coupons and in different points (centre and corner). The spectral window ranges from 650 cm^{-1} to 4000 cm^{-1}, and corresponds to that of the remarkable peaks of epoxy resin [285].

Figure 6.11 reports FTIR spectra taken on the surface exposed to heat flux and on the opposite side of uncoated specimen (G0 samples) after irradiation for 15 min @25 and @100 kW/m^2, a reference FTIR spectrum of an unexposed position is also reported for comparison. Typical FTIR epoxy spectrum, showing peaks @ 829 cm^{-1}, 1184 cm^{-1}, 1508 cm^{-1}, 2871 cm^{-1}, 2966 cm^{-1} are recorded in reference position [286].

In the case of the sample heated @25 kW/m^2 (Figure 6.11a) the spectrum recorded on the exposed side is flat demonstrating the absence of epoxy matrix features, while the spectrum recorded on the other side, opposite to heat flux, shows the features of the epoxy demonstrating the integrity of the matrix. In the case of the sample heated @100 kW/m^2 (Figure 6.11b) both the spectrum recorded on the side exposed to heat flux and that recorded on opposite side are flat, demonstrating the absence of epoxy matrix features. In both the cases FTIR measurements confirm the visual inspection analysis.
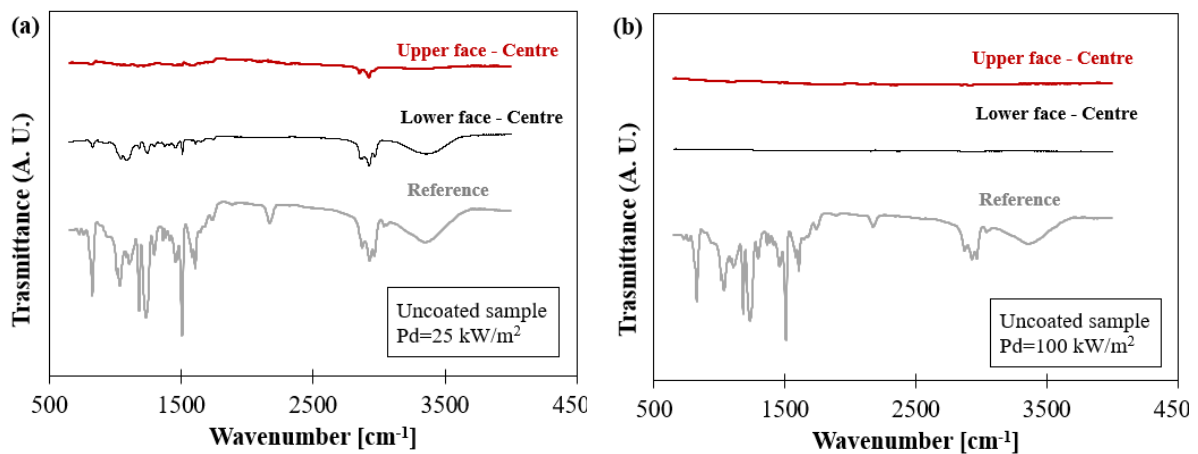
Figure 6.11. FTIR spectra on surfaces of uncoated coupons heated with laser power of (a) 25 kW/m^2 and (b) 100 kW/m^2
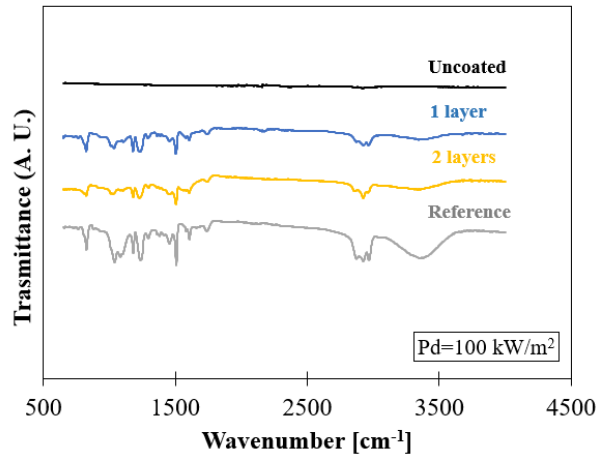
Figure 6.12. Comparison between FTIR spectra on lower surface of uncoated and coated coupons exposed to a heat flux of 100 kW/m^2

The beneficial effect of protection is shown in Figure 6.12, which reports a comparison of FTIR spectra acquired in the centre of the opposite to heat flux surface of G-preg coated and uncoated samples heated with laser power of 100 kW/m^2. The sample without protection was found fully damaged in fact the polymer signature was lost resulting in a flat curve, while the samples protected with 1 and 2 G-preg layers preserved their chemical integrity: the resin peaks of coated samples are still clearly visible, meaning that the polymer is not burnt. The G-Preg barrier improved the resistance of samples by preventing the decomposition of the polymeric matrix.

6.4.2   *Residual mechanical properties after heating*

Residual mechanical properties of tested samples are evaluated with dynamic mechanical analysis using TA Instrument DMA-Q800 equipped with dual cantilever clamp. Rectangular specimens of 35x15 mm^2 are cut from the central area of the burned coupons. Test are conducted with an initial amplitude of 20 μm and at room temperature. Data are elaborated according to the ASTM D790 standard for flexural behaviour of composites [206].

Figure 6.13 is reported the variation of storage modulus at room temperature for different levels of protection. It is found that the mechanical properties deteriorate with increasing laser power, since it corresponds to an increase of the temperature within the composites, as shown in Figure 6.13(a-c). For the uncoated sample, given the high level of damage, the residual elastic modulus is reduced of 49% with respect to the reference value, already from laser power of 25 kW/m^2. Further decreases are observed with increasing laser power, where the elastic modulus reaches 6% of its original value at 150 kW/m^2. The effect of protection is evident in the case of sample coated with 1 layer and 2 layers, where the residual elastic modulus is 81%

and 86% of the reference value respectively at 25 kW/m² and linearly decreases with increasing laser power, remaining higher than the uncoated sample (Figure 6.13b). By comparing the residual stiffness after exposure to 100 kW/m² heat flux, the G-preg protection allows to kept mechanical performances up to 40 % of the pristine value and 5 times higher respect to the unprotected sample.
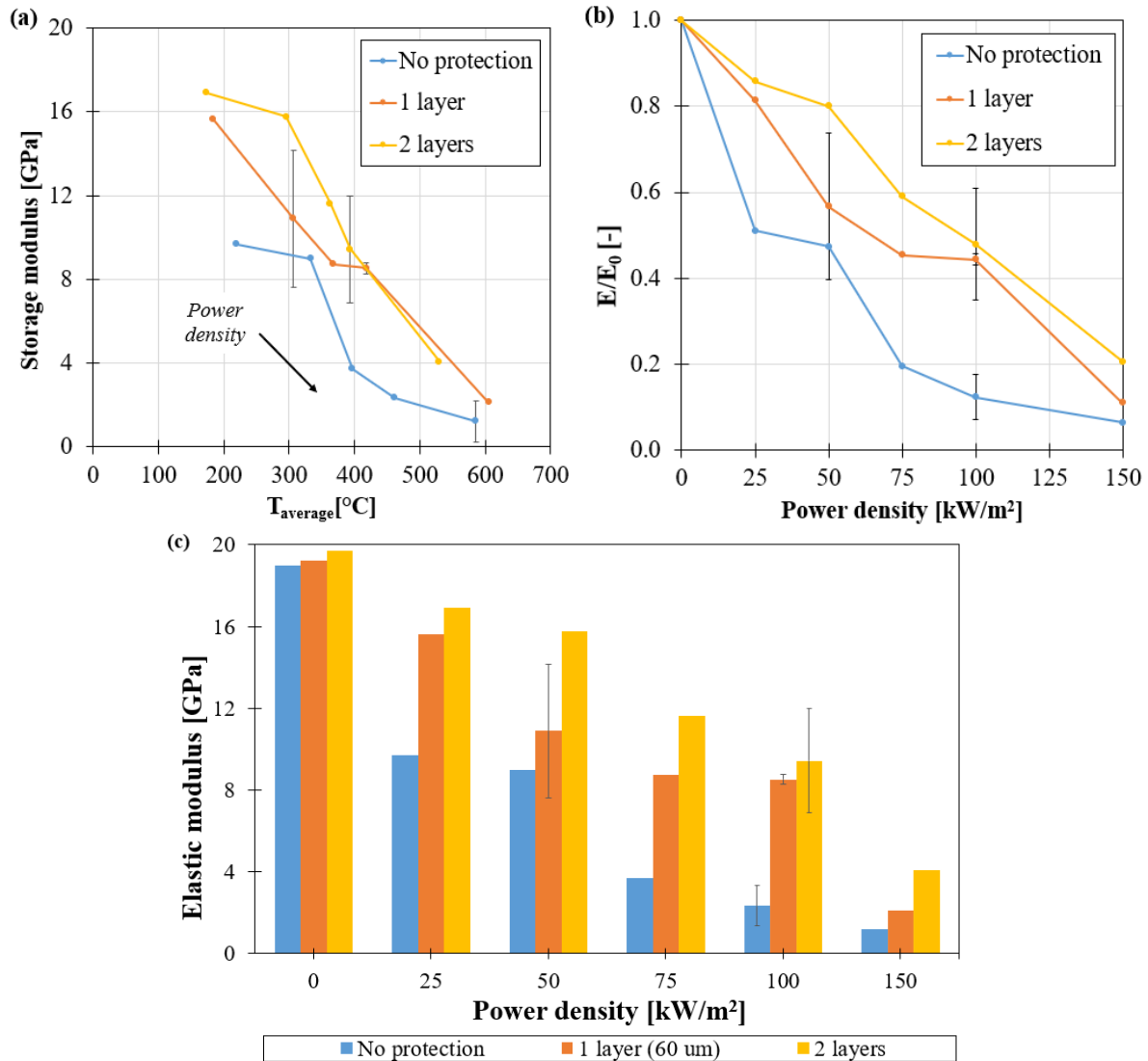
Figure 6.13. (a) Residual elastic modulus vs average temperature on the upper surface; (b) Percentage of residual elastic modulus vs laser power density; (c) Elastic modulus vs laser power density.

Pictures of the internal damage of uncoated and coated samples tested at 100 kW/m² are reported in Figure 6.14. They clearly show that G-Pregs layers act as shielding to radiative flux. In fact, uncoated sample exhibits a high level of damage, with absence of resin between plies. On the contrary, coated samples maintain their integrity, only showing lifting and detachment of the graphene layer. Resin traces can still be found between carbon fibres, especially for the sample with two G-Pregs coating.
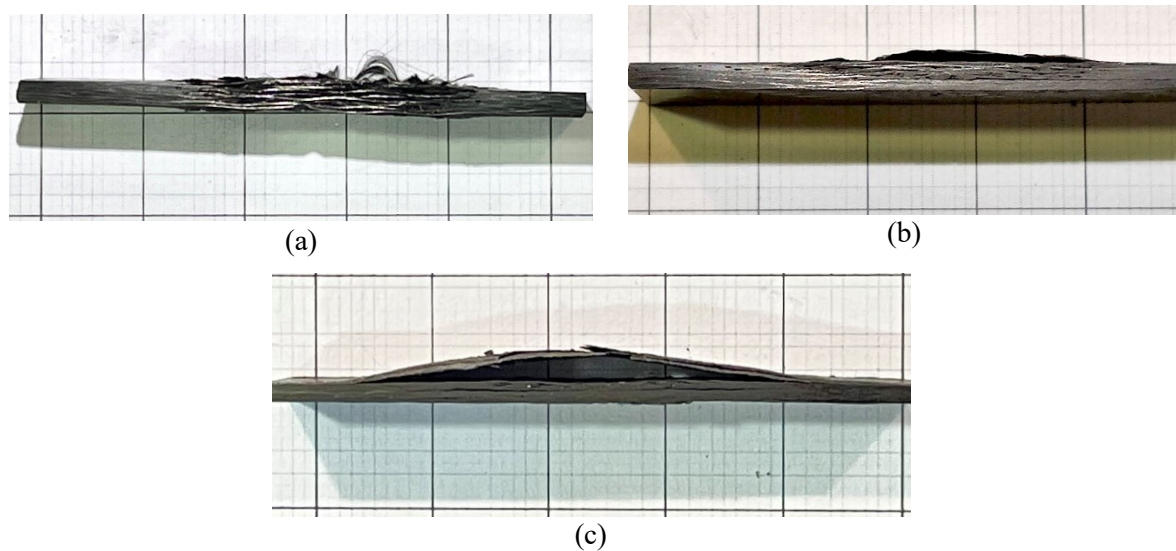
Figure 6.14. Internal damage of uncoated (a), 1 G-Preg layer (b), and 2 G-Pregs layers (c) samples at Pd=100 kW/m^2

6.5 Conclusions

In this chapter the high-power density radiative flux shielding ability of graphene papers with different thickness is showed with the aim to enhance CFRP fire protection. The experimental analysis showed that, thanks to the high degrees of orientation of highly conductive GNPs within the coating, the maximum temperature, and the temperature gradient onto the exposed to heat flux surface is mitigated by spreading the thermal energy over the sample volume. Non-destructive analysis revealed that the presence of a G-preg coating onto the surface subjected to laser beam preserve the sample from through-the-thickness damages at energy level up to 100 kW/m^2.

Finally, the IR graphene shield preserve the mechanical performance of CFRP when it is exposed to very high heat fluxes. Specimens extracted from the damaged samples at 100 kW/m^2, which is strictly related to the standard testing condition for transport industry, showed a residual mechanical performance 5 times higher than the CFRP without protection, with a residual mechanical performance up to 40 % of the pristine. The use of graphene flexible paper as IR shield was found as an effective technological solution for extend the application of composite materials when exposed to high heat fluxes such as thermal protection in critical structural parts subjected to high energy fluxes (i.e. batteries, electronic cabinets, engine nacelle) and/or protective coating for component subjected to hypersonic field (i.e. turbine inlet).

7. CONCLUSIONS AND FUTURE WORKS

7.1 Conclusions

In this work, the mechanical and multifunctional behaviour of composite reinforced with laminated nano-biomimetic architecture have been investigated. Nacre-like films with high content of graphite nanoplatelets (GNPs) have been prepared by a top-down manufacturing technology.

From, an accurate critical analysis of literature data it has been deeply studied the mechanism at the base of stress transfer in high filler content composites, identifying the parameters that influence the efficiency of stress transfer and the strategies to improve it. It has been found that the properties of a macroscopic bulk material strongly depend on the interaction at atomic levels, including Van der Waals (vdW) force, hydrogen, ionic and covalent bonds and in most cases, on their synergetic effect. In particular, the formation of highly ordered brick and mortar structure depends on the interaction forces between the two phases, which drive the self-assembly to the final highly ordered structure. Consequently, poor mechanical performances of the material are associated to interface issues, and to the low stress transfer from the matrix to the nanoparticles. Therefore, improvement of the interface at chemical level enhances the mechanical response of the material. Thus, the best mechanical performances in composites with high content of 2D nanofillers are achieved when the bonding and interactions between nanoparticles and the polymer are strong and when the matrix molecular mobility is such that the polymer intercalates between nanoplatelets, covering their

entire surface. Most importantly, it has been found that at very high filler content, brick and mortar materials exhibit an unusual behaviour. The mechanical properties of the material drop, deviating from the expected behaviour for which with the increasing filler content, the elastic modulus of the material linearly increases getting closer to that of the main constituent.

Experimental characterization of composite with high graphene content has been carried out. Firstly, a set up procedure for the mass production of graphene-based material has been assessed in collaboration with NANESA S.r.l. and then, the mechanical and thermal behaviour of the material has been investigated. In particular, different fillers and matrices have been employed, investigating the effect of nanoplatelets aspect ratio and matrix type on both mechanical and thermal properties. Also, particular attention has been paid to the variation of mechanical and functional properties of the material vis-a-vis filler content ($v_f > 50$ wt%).

Mechanical tests in tension have been performed on films with high GNPs content. It has been found that an increase in platelet aspect ratio does not modify the elastic modulus of the material, while slightly increases the tensile strength. On the other hand, the matrix behaviour, whether it is fragile or ductile, significantly influences the overall behaviour of the composite. In fact, films with epoxy exhibited pseudo-elastic behaviour with fragile rupture, while films with more ductile matrices, such as those with the vinyl copolymer and polyurethane showed an elasto-plastic behaviour.

However, for low filler content, the elastic modulus of the composite is well approximated by the rule of mixture with GNP modulus of 25 GPa, exhibiting a maximum for filler content of 67 vol%, then it drops, deviating from expected behaviour dictated by the rule of mixture. To better understand the reason of this unusual behaviour, morphological analyses are performed. SEM analyses showed that the particles are highly oriented in the longitudinal direction, with a laminated inner architecture and uniform texture and that the particles are aligned, but wrinkled. Therefore, albeit the distribution of lamellar particles is overall good, some empty areas, which can affect the bonding between the nanoplatelets, have been detected. In particular, by decreasing the resin content, the inner structure becomes organised with nanoplatelets leaned on the film plane up to a critical GNP content (70 wt%). Above this critical content the inner structure is threaten by dry spots and empty areas. Further information is collected with AFM analyses, investigating the topography of an internal layer of the GNP/Epoxy film at different filler content. These analyses verified the assembly of the material, with stacked GNPs and typical structural corrugations (wrinkles and folds). Most importantly, they reveal the presence of several droplet-like features, which indicate that the

polymeric phase is discontinuous. However, the morphology of the material does not vary with increasing filler content, but the average size of the droplets decreases with it. Consequently, the matrix partial cover the nanoplatelets' surface, affects the mechanical properties of the composite and causes the observed reduction of the elastic modulus and tensile strength at very high filler content.

On the same way, the micromechanical behaviour of GNP/Epoxy films was assessed with a microscopic investigation carried out by micro Raman spectroscopy. The analysis confirmed the results obtained from tensile test, highlighting a bad stress transfer between the two phases, starting from filler content of 50 vol%. By comparing the results obtained from tensile test, with those obtained from Raman measurements, it appears that there is a strong correlation between the results. In particular, the Raman shift linearly decreases for high filler content meaning that the stress transfer is poor. This indicates that the matrix is not able to efficiently transfer load to the particles and thus the mechanical performances of the material deteriorate.

All these experimental observations allow to better understand the behaviour of the material at high filler content and consequently to define strategies for the optimization of the mechanical performances. According to this, a model has been proposed for predicting the efficiency of stress transfer in brick and mortar systems, which accounts for a non-uniform matrix distribution over the nanoplatelets. Theoretically, as the filler content increases, the thickness of nominal matrix layer reduces to a fraction of the nanoplatelet thickness. In reality, experimental observation indicates that at high filler content, the matrix thickness is higher than the expected value. In means that exists a minimum stable thickness of the matrix layer, compatible with the gyration radius of the polymer, starting from which dewetting phenomena may occur. This critical thickness identifies the point for which the loss of the efficacy of the reinforcement occurs. The reduction of available effective length for stress transfer between the matrix and the nanoparticle is responsible for the decrease of reinforcement efficiency in these composites. Therefore, modelling the matrix as a discontinuous layer better reflects the real structure of the material when filler content is high.

The efficiency of reinforcement has been discussed by invoking a shear-lag load transfer mechanism, suitably modified to take into account the actual resin distribution between the particles. The accuracy of the proposed analytical model has been then assessed through comparison with experimental and literature data.

Furthermore, the knowledge of the mechanism at the base of stress transfer allowed to define design strategies able to improve the structural organization of the matrix, in order to produce

a more mechanically efficient composite. The efficiency of stress transfer can be improved with proper process design by promoting the wetting phenomenon and inhibiting the phenomenon of partial coverage. In fact, in light of the model design suggestions, by increasing the compaction pressure during manufacturing of GNP/Epoxy films from 10 bar to 50 bar, resulted in an improvement of the efficiency of reinforcement. A higher compaction pressure was able to improve physical confinement of the polymer and therefore to reduce the minimum matrix thickness. In this way, the drop of efficiency shifted to higher volumetric fraction as confirmed by experimental data.

At the same time, also the multi-functionalities of the material have been investigated. GNP/Epoxy films showed high anisotropic thermal behaviour thanks to the good alignment of the nanoplatelets in plane direction respect to cross plane, which reflect that of GNPs. As for the mechanical properties, also for thermal properties, the behaviour with filler content has been investigated. It has been found that the in plane thermal diffusivity of the material linearly increases with the increasing filler content as it is expected. In fact, the reduction of polymer content, improves the thermal diffusivity due to the increasing number of GNP-GNP bridges, which develop at high filler content, and which are favourable to the heat transfer. On the contrary, the cross plane thermal diffusivity is quite constant, indicating that the polymer does not affect the thermal properties in cross plane direction. Analogously, thermal conductivity showed an increasing trend with increasing filler content, reaching a maximum of 242 kW/mK for GNP content of 100 wt%.

In addition, since the electrical conductivity is dominated by lamella-lamella resistance, the material showed excellent electrical resistivity, with a sheet resistance of 0.33 Ω/sq for films with thickness 65 μm. The high electrical conductivity makes the material a good candidate for EMI shielding application. In fact, preliminary tests on GNP/Epoxy films with different filler content showed good shielding effectivness of the material in the X-band. In particular, at low filler content, given the randomly orientation of nanoplatelets within the volume, the EM waves are partly absorbed. On the contrary at high GNP content, given the high level of organization and alignment in plane of the nanoparticles, the EM waves are mostly reflected.

Finally, it has been shown the possibility of employing GNP/Epoxy film as coating to improve the fire performances of CFRPs. Adding a thin layer on the surface of FRPs, can significantly improve the performance of the material, without impacting their mechanical properties and weight, while offering a new surface protection approach for additional applications. GNP/Epoxy films can be easily integrated into common composite process, such

as autoclave, without adding any additional steps. For this purpose, the high-power density radiative flux shielding ability of GNP/Epoxy films with different thickness has been investigated with the aim to enhance CFRP fire protection.

The experimental analysis showed that thanks to their high degrees of orientation of the thin GNP/Epoxy films, parts of the incident energy is reflected, due to the lower material emissivity with respect of CFRP, but also the temperature distribution onto the surface is spread over all the sample volume. Furthermore, the coating also acts as a barrier trapping pyrolysis gas formed by the decomposition of layer closer to the laser source. This effect contributes to improve the safety, by keeping the material self-extinguish and avoiding flames rise-up. Thus, the presence of a thin graphene coating onto the surface subjected to laser beam preserves the sample from through the thickness damages at energy level up to 100 kW/m^2, which is strictly related to the standard testing condition for transport industry. Consequently, the graphene film work as shield preserving the mechanical performance of CFRP when it is exposed to very high heat fluxes. Specimens extracted from the damaged samples at 100 kW/m^2, showed a residual mechanical performance 5 times higher than the CFRP without protection, with a residual mechanical performance up to 40 % of the pristine. The fire performances of the material have been finally assessed through cone calorimeter tests. They showed a significant shift of the ignition time, passing from 80 sec for unprotected CFRP to 180 sec for CFRP protected with GNP/Epoxy film and a significant reduction of the intensity of fire and smoke production.

Therefore, the combination of all these remarkable properties makes material an effective technological solution to extend the application of composite materials to many industrial fields. In fact, the enhancement of thermal conductivity draws the attention in de-icing, heated tooling, and thermal dissipation applications, while the enhancement of electrical conductivity attracts the transportation sector with lightning strike protection, EMI shielding and electrostatic coatings.

7.2   Future works

In light of these findings, several steps could be undertaken to further improve the mechanical performances of the materials and their functionalities in order to further extend their employment in different fields and several applications.

As it has been found from literature data and then confirmed by the micromechanical model, the mechanical behaviour of the composites at very high filler content strongly depends on the

ability of the polymeric phase to spread as a continuous layer within nanoplatelets. Consequently, further steps will be aimed to the improvement of the filler/matrix compatibility. Possible strategies would regard the accurate selection of a matrix with low molecular weight, such that the critical thickness, which causes the partial coverage of the nanoplatelets, and thus the drop of efficiency, is reached at higher volumetric fractions. Another possibility would be the functionalization the nanoparticle in order to improve the chemical affinity between the two phases. An example could be the use of amino acids, such as tyrosine, as cross-linker of graphene-based materials. In fact, the excellent capacity of tyrosine to self-assemble into 2D nanosheets, has already been proven, thanks to the chemical reactivity of the side-chain phenolic –OH functional group. They would lead to good mechanical and energy-storage properties and represent a cheap and environmentally friendly reactant. Thus, amino-acids (e.g., tryptophan, tyrosine, and phenylalanine) could act as a binder in nanocomposites since their aromatic rings strongly interacts with 2D carbonaceous materials via hydrogen bonding, electrostatic, and hydrophobic interaction and can be easily adsorbed on the surface of graphene. Furthermore, the tendency of amino acids to orient in parallel with the benzene rings' plane of graphene nanoparticles, enable the assembly of hierarchical and organized nanostructures, with nanoplatelets bonded by thin peptide layers (~ 1nm)[287][286][285][285][285]. This point could be crucial, since the capacity of tyrosine to spread as a very thin layer could overcome the issues identified in composites with lamellar reinforcement in which uncovering of nanoplatelets occurs for very high filler content.

In addition, given the process flexibility, other nanoparticles and/or matrices could be employed to widen the employment of brick and mortar flexible thin films to other industrial applications, by creating hybrid nanostructures. Inorganic matrices, such as polysiloxanes and polysilanes, could be employed to improve the performances at very high temperatures. Boron nitride (BN) lamellar nanoparticles could be employed to uncouple the thermal and electrical transport behaviour. In fact, while GNPs combine both thermal and electrical conductivities, BN nanoparticles are characterized by good thermal properties and poor electrical conductivity. Thus, by varying the weight fraction of NB, it is possible to obtain a hybrid material with tunable electrical properties. Also, ferromagnetic nanoparticles could be employed to improve the attenuation of the electromagnetic waves. In particular, hybrid thin films, composed by GNPs and ferrite nanoparticles could guarantee high performances in blocking the transmittance of the electromagnetic waves, thanks to the high electrical conductivity. In fact, while GNPs give a great contribution in terms of reflection, ferrite nanoparticles are capable of

absorbing the electromagnetic waves. Consequently, these innovative materials with high shielding effectiveness could be employed for stealth application, as radar absorber material (RAM), in military field. Another possibility to enhance the absorption capacity of the material could be to act on the nanostructure. In fact, as it has showed in the preliminary tests, the absorption capacity increases when the structure is not well-organized. For this purpose, a disordered nanostructure, with nanoplatelets randomly oriented could improve the capacity of the material to dissipate the EM waves and thus, could pave the wave for the use of graphene coatings for stealth applications.

REFERENCES

[1]   J.R. Rodrigues, N.M. Alves, J.F. Mano, Nacre-inspired nanocomposites produced using layer-by-layer assembly: Design strategies and biomedical applications, Mater. Sci. Eng. C. 76 (2017) 1263–1273. https://doi.org/10.1016/j.msec.2017.02.043.

[2]   D.F. Schmidt, Nanolaminates - Bioinspired and beyond, Mater. Lett. 108 (2013) 328–335. https://doi.org/10.1016/j.matlet.2013.07.004.

[3]   J. Sun, B. Bhushan, Hierarchical structure and mechanical properties of nacre: a review, RSC Adv. 2 (2012) 7617. https://doi.org/10.1039/c2ra20218b.

[4]   H.D. Espinosa, J.E. Rim, F. Barthelat, M.J. Buehler, Merger of structure and material in nacre and bone - Perspectives on de novo biomimetic materials, Prog. Mater. Sci. 54 (2009) 1059–1100. https://doi.org/10.1016/j.pmatsci.2009.05.001.

[5]   F. Barthelat, H. Tang, P.D. Zavattieri, C.M. Li, H.D. Espinosa, On the mechanics of mother-of-pearl: A key feature in the material hierarchical structure, J. Mech. Phys. Solids. 55 (2007) 306–337. https://doi.org/10.1016/j.jmps.2006.07.007.

[6]   M.A. Meyers, A.Y.M. Lin, P.Y. Chen, J. Muyco, Mechanical strength of abalone nacre: Role of the soft organic layer, J. Mech. Behav. Biomed. Mater. 1 (2008) 76–85. https://doi.org/10.1016/j.jmbbm.2007.03.001.

[7]   A.G. Checa, J.H.E. Cartwright, M.-G. Willinger, The key role of the surface membrane in why gastropod nacre grows in towers, Proc. Natl. Acad. Sci. 106 (2009) 38 LP – 43. https://doi.org/10.1073/pnas.0808796106.

[8]   X. Li, W.C. Chang, Y.J. Chao, R. Wang, M. Chang, Nanoscale structural and mechanical characterization of a natural nanocomposite material: The shell of red abalone, Nano Lett. 4 (2004) 613–617. https://doi.org/10.1021/nl049962k.

[9]   J. Wang, Q. Cheng, Z. Tang, Layered nanocomposites inspired by the structure and mechanical properties of nacre, Chem. Soc. Rev. 41 (2012) 1111–1129. https://doi.org/10.1039/C1CS15106A.

[10]   S. Wan, J. Peng, L. Jiang, Q. Cheng, Bioinspired Graphene-Based Nanocomposites and Their Application in Flexible Energy Devices, Adv. Mater. 28 (2016) 7862–7898. https://doi.org/10.1002/adma.201601934.

[11]   Y. Zhang, S. Gong, Q. Zhang, P. Ming, S. Wan, J. Peng, L. Jiang, Q. Cheng, Graphene-based artificial nacre nanocomposites, Chem. Soc. Rev. 45 (2016) 2378–2395. https://doi.org/10.1039/C5CS00258C.

[12]   A.K. Geim, K.S. Novoselov, The rise of graphene, in: Nanosci. Technol. a Collect. Rev. from Nat. Journals, World Scientific, 2010: pp. 11–19.

[13]   C. Lee, X. Wei, J.W. Kysar, J. Hone, Measurement of the Elastic Properties and Intrinsic Strength of Monolayer Graphene, Science (80-.). 321 (2008) 385–389.

[14]   G. Tsoukleri, J. Parthenios, K. Papagelis, R. Jalil, A.C. Ferrari, A.K. Geim, K.S. Novoselov, C. Galiotis, Subjecting a graphene monolayer to tension and compression, Small. 5 (2009) 2397–2402. https://doi.org/10.1002/smll.200900802.

[15]   D. Teweldebrhan, C.N. Lau, S. Ghosh, A.A. Balandin, W. Bao, I. Calizo, F. Miao, Superior Thermal Conductivity of Single-Layer Graphene, Nano Lett. 8 (2008) 902–907. https://doi.org/10.1021/nl0731872.

[16]   E. Pop, V. Varshney, A.K. Roy, Thermal properties of graphene: Fundamentals and applications, MRS Bull. 37 (2012).

[17]   A.H.C. Neto, F. Guinea, N.M.R. Peres, K.S. Novoselov, A.K. Geim, The electronic properties of graphene, Rev. Mod. Phys. 81 (2009). https://doi.org/10.1103/RevModPhys.81.109.

[18]   P. Kumar, F. Shahzad, S. Yu, S.M. Hong, Y.H. Kim, C.M. Koo, Large-area reduced graphene oxide thin film with excellent thermal conductivity and electromagnetic interference shielding effectiveness, Carbon N. Y. 94 (2015) 494–500. https://doi.org/10.1016/j.carbon.2015.07.032.

[19]   B. Shen, W. Zhai, W. Zheng, Ultrathin flexible graphene film: An excellent thermal conducting material with efficient EMI shielding, Adv. Funct. Mater. 24 (2014) 4542–

4548. https://doi.org/10.1002/adfm.201400079.

[20] A. Yu, P. Ramesh, X. Sun, E. Bekyarova, M.E. Itkis, R.C. Haddon, Enhanced thermal conductivity in a hybrid graphite nanoplatelet - Carbon nanotube filler for epoxy composites, Adv. Mater. 20 (2008) 4740–4744. https://doi.org/10.1002/adma.200800401.

[21] N.J. Song, C.M. Chen, C. Lu, Z. Liu, Q.Q. Kong, R. Cai, Thermally reduced graphene oxide films as flexible lateral heat spreaders, J. Mater. Chem. A. 2 (2014) 16563–16568. https://doi.org/10.1039/c4ta02693d.

[22] H. Wu, L.T. Drzal, Graphene nanoplatelet paper as a light-weight composite with excellent electrical and thermal conductivity and good gas barrier properties, Carbon N. Y. 50 (2012) 1135–1145. https://doi.org/10.1016/j.carbon.2011.10.026.

[23] X. Li, A. Manasrah, A. Al-ostaz, H. Alkhateb, D. Lincoln, G. Rushing, A.H. Cheng, Preparation and Characterization of High Content Graphene Nanoplatelet-Polyetherimide Paper, J. Nanosci. Nanoeng. 1 (2015) 252–258.

[24] B.K.W. Putz, O.C. Compton, M.J. Palmeri, S.T. Nguyen, L.C. Brinson, High-Nanofiller-Content Graphene Oxide–Polymer Nanocomposites via Vacuum-Assisted Self-Assembly, Adv. Funct. Mater. 20 (2010) 3322–3329. https://doi.org/10.1002/adfm.201000723.

[25] Y. Li, T. Yu, T. Yang, L. Zheng, K. Liao, Bio-Inspired Nacre-like Composite Films Based on Graphene with Superior Mechanical , Electrical , and Biocompatible Properties, (2012) 3426–3431. https://doi.org/10.1002/adma.201200452.

[26] Y. Tian, Y. Cao, Y. Wang, W. Yang, J. Feng, Realizing Ultrahigh Modulus and High Strength of Macroscopic Graphene Oxide Papers Through Crosslinking of Mussel-Inspired Polymers, (2013) 2980–2983. https://doi.org/10.1002/adma.201300118.

[27] Y. Li, Z. Xue, Y. Luan, L. Wang, D. Zhao, F. Xu, Y. Xiao, Z. Guo, Z. Wang, Improved mechanical performance of graphene oxide based artificial nacre composites by regulating the micro-laminated structure and interface bonding, Compos. Sci. Technol. 179 (2019) 63–68.

[28] A. Walther, I. Bjurhager, J.M. Malho, J. Pere, J. Ruokolainen, L.A. Berglund, O. Ikkala, Large-area, lightweight and thick biomimetic composites with superior material properties via fast, economic, and green pathways, Nano Lett. 10 (2010) 2742–2748. https://doi.org/10.1021/nl1003224.

[29] M. Mirkhalaf, F. Barthelat, Nacre-like materials using a simple doctor blading

technique : Fabrication , testing and modeling, J. Mech. Behav. Biomed. Mater. 56 (2016) 23–33. https://doi.org/10.1016/j.jmbbm.2015.11.010.

[30] J. Han, G. Du, W. Gao, H. Bai, An Anisotropically High Thermal Conductive Boron Nitride/Epoxy Composite Based on Nacre-Mimetic 3D Network, Adv. Funct. Mater. 29 (2019) 1900412. https://doi.org/https://doi.org/10.1002/adfm.201900412.

[31] J.J. Richardson, M. Björnmalm, F. Caruso, Technology-driven layer-by-layer assembly of nanofilms, Science (80-.). 348 (2015) aaa2491.

[32] F. Barthelat, Designing nacre-like materials for simultaneous stiffness, strength and toughness: Optimum materials, composition, microstructure and size, J. Mech. Phys. Solids. 73 (2014) 22–37. https://doi.org/10.1016/j.jmps.2014.08.008.

[33] N. Abid, M. Mirkhalaf, F. Barthelat, Discrete-element modeling of nacre-like materials: Effects of random microstructures on strain localization and mechanical performance, J. Mech. Phys. Solids. 112 (2018) 385–402. https://doi.org/10.1016/j.jmps.2017.11.003.

[34] F. Barthelat, A.K. Dastjerdi, R. Rabiei, An improved failure criterion for biological and engineered staggered composites, J. R. Soc. Interface. 10 (2013). https://doi.org/10.1098/rsif.2012.0849.

[35] M.R. Begley, N.R. Philips, B.G. Compton, D. V Wilbrink, R.O. Ritchie, M. Utz, Micromechanical models to guide the development of synthetic ' brick and mortar ' composites, J. Mech. Phys. Solids. 60 (2012) 1545–1560. https://doi.org/10.1016/j.jmps.2012.03.002.

[36] S. Pimenta, P. Robinson, An analytical shear-lag model for composites with "brick-and-mortar" architecture considering non-linear matrix response and failure, Compos. Sci. Technol. 104 (2014) 111–124. https://doi.org/10.1016/j.compscitech.2014.09.001.

[37] X. Wei, M. Naraghi, H.D. Espinosa, Optimal length scales emerging from shear load transfer in natural materials: Application to carbon-based nanocomposite design, ACS Nano. 6 (2012) 2333–2344. https://doi.org/10.1021/nn204506d.

[38] D.F. Schmidt, Nanolaminates - Bioinspired and beyond, Mater. Lett. 108 (2013) 328–335. https://doi.org/10.1016/j.matlet.2013.07.004.

[39] J. Peng, Q. Cheng, High-Performance Nanocomposites Inspired by Nature, Adv. Mater. 29 (2017) 1702959. https://doi.org/10.1002/adma.201702959.

[40] J. George, H. Ishida, A review on the very high nanofiller-content nanocomposites : Their preparation methods and properties with high aspect ratio fillers, Prog. Polym. Sci. 86 (2018) 1–39. https://doi.org/10.1016/j.progpolymsci.2018.07.006.

[41] T.P. Niebel, F. Bouville, D. Kokkinis, A.R. Studart, Journal of the Mechanics and Physics of Solids Role of the polymer phase in the mechanics of nacre-like composites, J. Mech. Phys. Solids. 96 (2016) 133–146. https://doi.org/10.1016/j.jmps.2016.06.011.

[42] A.A. Balandin, Thermal properties of graphene and nanostructured carbon materials, Nat. Mater. 10 (2011) 569–581. https://doi.org/10.1038/nmat3064.

[43] F. Cilento, A. Martone, F. Cristiano, A. Fina, M. Giordano, Effect of Matrix Content on Mechanical and Thermal Properties of High Graphene Content Composites, MATEC Web Conf. 303 (2019) 01002. https://doi.org/10.1051/matecconf/201930301002.

[44] C. Lee, X. Wei, J.W. Kysar, J. Hone, Measurement of the Elastic Properties and Intrinsic Strength of Monolayer Graphene, Science (80-.). 321 (2008) 385 LP – 388. https://doi.org/10.1126/science.1157996.

[45] J.W. Suk, R.D. Piner, J. An, R.S. Ruoff, Mechanical properties of monolayer graphene oxide, ACS Nano. 4 (2010) 6557–6564.

[46] J. Chen, L. Li, Thermal conductivity of graphene oxide: A molecular dynamics study, JETP Lett. (2020) 1–5.

[47] H. Chen, M.B. Müller, K.J. Gilmore, G.G. Wallace, D. Li, Mechanically strong, electrically conductive, and biocompatible graphene paper, Adv. Mater. 20 (2008) 3557–3561. https://doi.org/10.1002/adma.200800757.

[48] L. Liu, J. Zhang, J. Zhao, F. Liu, Mechanical properties of graphene oxides, Nanoscale. 4 (2012) 5910–5916. https://doi.org/10.1039/C2NR31164J.

[49] W. Cui, M. Li, J. Liu, B. Wang, C. Zhang, L. Yiang, Q. Cheng, A Strong Integrated Strength and Toughness Arti fi cial Nacre Based on, (2014) 9511–9517. https://doi.org/10.1021/nn503755c.

[50] J.R. Cost, K.R. Janowski, R.C. Rossi, Elastic properties of isotropic graphite, Philos. Mag. 17 (1968) 851–854. https://doi.org/10.1080/14786436808223035.

[51] R. Rafiee, R. Shahzadi, Mechanical properties of nanoclay and nanoclay reinforced polymers: a review, Polym. Compos. 40 (2019) 431–445.

[52] F. Uddin, Montmorillonite: An introduction to properties and utilization, Curr. Top. Util. Clay Ind. Med. Appl. 1 (2018).

[53] K.S. Novoselov, A.K. Geim, S. V Morozov, D. Jiang, Y. Zhang, S. V Dubonos, I. V Grigorieva, A.A. Firsov, Electric field effect in atomically thin carbon films, Science (80-.). 306 (2004) 666–669.

[54] Y. Yao, L. Ren, S. Gao, S. Li, Histogram method for reliable thickness measurements

of graphene films using atomic force microscopy (AFM), J. Mater. Sci. Technol. 33 (2017) 815–820. https://doi.org/https://doi.org/10.1016/j.jmst.2016.07.020.

[55] E. Pop, V. Varshney, A.K. Roy, Thermal properties of graphene: Fundamentals and applications, MRS Bull. 37 (2012) w. https://doi.org/10.1557/mrs.2012.203.

[56] Q.-L. Zhang, S.C. O'Brien, J.R. Heath, Y. Liu, R.F. Curl, H.W. Kroto, R.E. Smalley, Reactivity of large carbon clusters: spheroidal carbon shells and their possible relevance to the formation and morphology of soot, J. Phys. Chem. 90 (1986) 525–528.

[57] P.M. Ajayan, T.W. Ebbesen, T. Ichihashi, S. Iijima, K. Tanigaki, H. Hiura, Opening carbon nanotubes with oxygen and implications for filling, Nature. 362 (1993) 522–525.

[58] J.K. Wassei, R.B. Kaner, Graphene, a promising transparent conductor, Mater. Today. 13 (2010) 52–59. https://doi.org/https://doi.org/10.1016/S1369-7021(10)70034-1.

[59] A.B. Kuzmenko, E. Van Heumen, F. Carbone, D. Van Der Marel, Universal optical conductance of graphite, Phys. Rev. Lett. 100 (2008) 117401.

[60] P. Wick, A.E. Louw-gaume, M. Kucki, H.F. Krug, K. Kostarelos, B. Fadeel, K.A. Dawson, A. Salvati, E. Vµzquez, L. Ballerini, M. Tretiach, F. Benfenati, E. Flahaut, L. Gauthier, M. Prato, A. Bianco, Classification Framework for Graphene-Based Materials, Angew. Chem. Int. Ed. 53 (2014) 7714–7718. https://doi.org/10.1002/anie.201403335.

[61] V.B. Mohan, R. Brown, K. Jayaraman, D. Bhattacharyya, Characterisation of reduced graphene oxide: Effects of reduction variables on electrical conductivity, Mater. Sci. Eng. B. 193 (2015) 49–60. https://doi.org/https://doi.org/10.1016/j.mseb.2014.11.002.

[62] M. Eizenberg, J.M. Blakely, Carbon monolayer phase condensation on Ni (111), Surf. Sci. 82 (1979) 228–236.

[63] C. Berger, Z. Song, T. Li, X. Li, A.Y. Ogbazghi, R. Feng, Z. Dai, A.N. Marchenkov, E.H. Conrad, P.N. First, Ultrathin epitaxial graphite: 2D electron gas properties and a route toward graphene-based nanoelectronics, J. Phys. Chem. B. 108 (2004) 19912–19916.

[64] M. Cai, D. Thorpe, D.H. Adamson, H.C. Schniepp, Methods of graphite exfoliation, J. Mater. Chem. 22 (2012) 24992–25002.

[65] Y.I. Zhang, L. Zhang, C. Zhou, Review of chemical vapor deposition of graphene and related applications, Acc. Chem. Res. 46 (2013) 2329–2339.

[66] Z.X. Shu, R.S. McMillan, J.J. Murray, Electrochemical intercalation of lithium into graphite, J. Electrochem. Soc. 140 (1993) 922.

[67] W.S. Hummers, R.E. Offeman, Preparation of Graphitic Oxide, J. Am. Chem. Soc. 80 (1958) 1339. https://doi.org/10.1021/ja01539a017.

[68] B.C. Brodie, XIII. On the atomic weight of graphite, Philos. Trans. R. Soc. London. (1859) 249–259.

[69] W. Gao, The chemistry of graphene oxide, in: Graphene Oxide, Springer, 2015: pp. 61–95.

[70] I.K. Moon, J. Lee, R.S. Ruoff, H. Lee, Reduced graphene oxide by chemical graphitization, Nat. Commun. 1 (2010) 1–6.

[71] F. Uddin, Clays, Nanoclays, and Montmorillonite Minerals, Metall. Mater. Trans. A. 39 (2008) 2804–2814. https://doi.org/10.1007/s11661-008-9603-5.

[72] I. Corni, T.J. Harvey, J.A. Wharton, K.R. Stokes, F.C. Walsh, R.J.K. Wood, A review of experimental techniques to produce a nacre-like structure, Bioinspiration and Biomimetics. 7 (2012). https://doi.org/10.1088/1748-3182/7/3/031001.

[73] G. Decher, Fuzzy Nanoassemblies : Toward Layered Polymeric Multicomposites, Science (80-.). 277 (1997) 1232–1237.

[74] I. Langmuir, Through a limited pressure range the degree of adsorption of gas is in fair agreement with the logarithmic isotherm equation of Freundlich , as has already been shown by previous investigators . At higher pres- sures (above 60 cm .), the adsorption rapid, Fundam. Prop. SOLIDS Liq. 468 (1917).

[75] G. Wahl, P. Davies, R. Bunshah, B. Joyce, C. Bain, G. Wegner, M. Remmers, F. Walsh, K. Hieber, J.-E. Sundgren, P. Bachman, S. Miyazawa, A. Thelen, H. Strathmann, Thin Films, 2012. https://doi.org/10.1002/14356007.a26.

[76] Van der Biest, OO, L. Van de perre, Electrophoretic deposition, Annu Rev Mater Res. 29 (1999).

[77] U.G.K. Wegst, H. Bai, E. Saiz, A.P. Tomsia, R.O. Ritchie, Bioinspired structural materials, Nat. Mater. 14 (2015) 23–36. https://doi.org/10.1038/nmat4089.

[78] M.E. Launey, E. Munch, D.H. Alsem, H.B. Barth, E. Saiz, Designing highly toughened hybrid composites through nature-inspired hierarchical complexity, Acta Mater. 57 (2009) 2919–2932. https://doi.org/10.1016/j.actamat.2009.03.003.

[79] A. Tanay, L. Bitincka, R. Shamir, E.K.O. Shea, A.I. Tschumi, R. Kishony, C.A. Telmer, S.A. Adler, C.A. Telmer, V. Subramaniam, A.J. Lopez, T.J. Mitchison, N. Perrimon, S.E. Fraser, J. Ellenberg, A.I. Lamond, J.S. Brotman, S.T. Sweeney, G. Davis, R. Daneman, M. Zavortink, W. Chia, L.F. Liu, P.D. Arpa, W.P. Pfund, V.B. Mehta, D.K.

Trask, D. Makonchuk, C. Gomes, J.J. Zheng, M. Hetman, M.S. Wold, J.A. Borowiec, T.C. Elston, W.J. Blake, J.J. Collins, A.J. Levine, E.D. Siggia, P.S. Swain, M. Thattai, I. Kurtser, A.D. Grossman, A. Van Oudenaarden, S.J. Arlander, L. Karnitz, C. Lin, S.Y. Sun, S. Zhao, Z.R. Liu, W.M. Old, K.A. Resing, N.G. Ahn, M. Mann, J. Bar, I. Glinert, T. Shlapok, Tough, Bio-Inspired Hybrid Materials, (2008) 1516–1521.

[80]   A. Walther, I. Bjurhager, J. Malho, J. Ruokolainen, L. Berglund, O. Ikkala, Supramolecular Control of Stiffness and Strength in Lightweight High- Performance Nacre-Mimetic Paper with Fire-Shielding Properties **, Angew. Chemie Int. Ed. 49 (2010) 6448–6453. https://doi.org/10.1002/anie.201001577.

[81]   H. Le Ferrand, F. Bouville, T.P. Niebel, A.R. Studart, Magnetically assisted slip casting of bioinspired heterogeneous composites, 14 (2015). https://doi.org/10.1038/NMAT4419.

[82]   C. Berndt, W. Lenling, Handbook of thermal spray technology, 2004.

[83]   W. Li, H. Assadi, F. Gaertner, S. Yin, A Review of Advanced Composite and Nanostructured Coatings by Solid-State Cold Spraying Process, Crit. Rev. Solid State Mater. Sci. 44 (2019) 109–156. https://doi.org/10.1080/10408436.2017.1410778.

[84]   J.L. Suter, R.C. Sinclair, P. V. Coveney, Principles Governing Control of Aggregation and Dispersion of Graphene and Graphene Oxide in Polymer Melts, Adv. Mater. 32 (2020). https://doi.org/10.1002/adma.202003213.

[85]   H. Pan, S. Zhu, L. Mao, Graphene Nanoarchitectonics: Approaching the Excellent Properties of Graphene from Microscale to Macroscale, J. Inorg. Organomet. Polym. Mater. 25 (2015) 179–188. https://doi.org/10.1007/s10904-014-0073-5.

[86]   C. Huang, Q. Cheng, Learning from nacre: Constructing polymer nanocomposites, Compos. Sci. Technol. 150 (2017) 141–166. https://doi.org/10.1016/j.compscitech.2017.07.021.

[87]   S. Wan, Q. Cheng, Role of Interface Interactions in the Construction of GO-Based Artificial Nacres, Adv. Mater. Interfaces. 5 (2018) 1–24. https://doi.org/10.1002/admi.201800107.

[88]   Q. Cheng, M. Wu, M. Li, L. Jiang, Z. Tang, Ultratough Artificial Nacre Based on Conjugated Cross-linked Graphene Oxide **, (2013) 3750–3755. https://doi.org/10.1002/anie.201210166.

[89]   Y. Li, Z. Xue, Y. Luan, L. Wang, D. Zhao, F. Xu, Y. Xiao, Z. Guo, Z. Wang, Improved mechanical performance of graphene oxide based artificial nacre composites by

regulating the micro-laminated structure and interface bonding, Compos. Sci. Technol. 179 (2019) 63–68. https://doi.org/10.1016/j.compscitech.2019.04.032.

[90] S. Wan, Y. Li, J. Peng, H. Hu, Q. Cheng, L. Jiang, Synergistic Toughening of Graphene Oxide-Molybdenum Disulfide-Thermoplastic Polyurethane Ternary Artificial Nacre, ACSNano. 9 (2015) 708–714. https://doi.org/10.1021/nn506148w.

[91] S. Park, D.A. Dikin, S.T. Nguyen, R.S. Ruoff, Graphene Oxide Sheets Chemically Cross-Linked by Polyallylamine, (2009) 15801–15804.

[92] L. Liu, Y. Gao, Q. Liu, J. Kuang, D. Zhou, S. Ju, B. Han, Z. Zhang, High mechanical performance of layered graphene oxide/poly(vinyl alcohol) nanocomposite films, Small. 9 (2013) 2466–2472. https://doi.org/10.1002/smll.201300819.

[93] O.C. Compton, S.W. Cranford, K.W. Putz, Z. An, L.C. Brinson, M.J. Buehler, S.T. Nguyen, Tuning the mechanical properties of graphene oxide paper and its associated polymer nanocomposites by controlling cooperative intersheet hydrogen bonding, ACS Nano. 6 (2012) 2008–2019. https://doi.org/10.1021/nn202928w.

[94] M. Wang, Q. Wang, L. Liang, H. Ding, X. Liang, G. Sun, High-content graphene-reinforced polymer with bioinspired multilayer structure, J. Mater. Sci. 55 (2020) 16836–16845. https://doi.org/10.1007/s10853-020-05233-x.

[95] T.U. Patro, H.D. Wagner, Influence of Graphene Oxide Incorporation and Chemical Cross-Linking on Structure and Mechanical Properties of Layer-by-Layer Assembled Poly (Vinyl Alcohol) -Laponite Free-Standing Films, (2016) 2377–2387. https://doi.org/10.1002/polb.24226.

[96] S. Wan, J. Peng, Y. Li, H. Hu, L. Jiang, Q. Cheng, Use of Synergistic Interactions to Fabricate Strong , Tough , and Conductive Arti fi cial Nacre Based on Graphene Oxide and Chitosan, (2015) 9830–9836. https://doi.org/10.1021/acsnano.5b02902.

[97] Y. Wu, R. Cao, L. Ji, W. Huang, X. Yang, Synergistic toughening of bioinspired artificial nacre by polystyrene grafted graphene oxide, (2015) 28085–28091. https://doi.org/10.1039/C5RA03074A.

[98] Y. Wang, T. Li, P. Ma, S. Zhang, H. Zhang, M. Du, Y. Xie, M. Chen, W. Dong, W. Ming, Artificial Nacre from Supramolecular Assembly of Graphene Oxide, ACS Nano. 12 (2018) 6228–6235. https://doi.org/10.1021/acsnano.8b03025.

[99] H. Ni, F. Xu, A.P. Tomsia, E. Saiz, L. Jiang, Q. Cheng, Robust Bioinspired Graphene Film via $\pi - \pi$ Cross-linking, (2017). https://doi.org/10.1021/acsami.7b07748.

[100] M. Zhang, L. Huang, J. Chen, C. Li, G. Shi, Ultratough , Ultrastrong , and Highly

Conductive Graphene Films with Arbitrary Sizes, (2014) 7588–7592. https://doi.org/10.1002/adma.201403322.

[101] J. Cao, C. Chen, K. Chen, Q. Lu, Q. Wang, P. Zhou, D. Liu, L. Song, Z. Niu, J. Chen, High-strength graphene composite films by molecular level couplings for flexible supercapacitors with high volumetric capacitance, J. Mater. Chem. A. 5 (2017) 15008–15016. https://doi.org/10.1039/c7ta04920j.

[102] S. Wan, H. Hu, J. Peng, Y. Li, Y. Fan, L. Jiang, Q. Cheng, Nacre-inspired integrated strong and tough reduced graphene oxide–poly(acrylic acid) nanocomposites, Nanoscale. (2016) 5649–5656. https://doi.org/10.1039/c6nr00562d.

[103] N. Zhao, M. Yang, Q. Zhao, W. Gao, T. Xie, H. Bai, Superstretchable Nacre-Mimetic Graphene/Poly(vinyl alcohol) Composite Film Based on Interfacial Architectural Engineering, ACS Nano. 11 (2017) 4777–4784. https://doi.org/10.1021/acsnano.7b01089.

[104] Y. Wang, H. Yuan, P. Ma, H. Bai, M. Chen, W. Dong, Y. Xie, Y.S. Deshmukh, Superior Performance of Artificial Nacre Based on Graphene Oxide Nanosheets, ACS Appl. Mater. Interfaces. 9 (2017) 4215–4222. https://doi.org/10.1021/acsami.6b13834.

[105] S. Wan, F. Xu, L. Jiang, Q. Cheng, Superior Fatigue Resistant Bioinspired Graphene-Based Nanocomposite via Synergistic Interfacial Interactions, 1605636 (2017) 1–7. https://doi.org/10.1002/adfm.201605636.

[106] S. Gong, Q. Zhang, R. Wang, L. Jiang, Q. Cheng, Synergistically toughening nacre-like graphene nanocomposites via gel-film transformation, J. Mater. Chem. A Mater. Energy Sustain. 5 (2017) 16386–16392. https://doi.org/10.1039/C7TA03535G.

[107] W. Yang, Z. Zhao, K. Wu, R. Huang, T. Liu, H. Jiang, F. Chen, Q. Fu, Ultrathin flexible reduced graphene oxide / cellulose nanofiber composite films with strongly anisotropic thermal conductivity and efficient, J. Mater. Chem. C. 5 (2017) 3748–3756. https://doi.org/10.1039/C7TC00400A.

[108] J. Zhu, H. Zhang, N.A. Kotov, Thermodynamic and structural insights into nanocomposites engineering by comparing two materials assembly techniques for graphene, ACS Nano. 7 (2013) 4818–4829. https://doi.org/10.1021/nn400972t.

[109] K. Hu, L.S. Tolentino, D.D. Kulkarni, C. Ye, S. Kumar, V. V Tsukruk, Written-in Conductive Patterns on Robust Graphene Oxide Biopaper by Electrochemical Microstamping **, (2013) 13784–13788. https://doi.org/10.1002/anie.201307830.

[110] Z. Tang, N.A. Kotov, S. Magonov, B. Ozturk, Nanostructured artificial nacre, Nat.

Mater. 2 (2003) 413–418. https://doi.org/10.1038/nmat906.

[111] P. Podsiadlo, A.K. Kaushik, E.M. Arruda, A.M. Waas, B.S. Shim, J. Xu, H. Nandivada, B.G. Pumplin, J. Lahann, A. Ramamoorthy, N.A. Kotov, Ultrastrong and stiff layered polymer nanocomposites, Science (80-.). 318 (2007) 80–83. https://doi.org/10.1126/science.1143176.

[112] P. Das, J.M. Malho, K. Rahimi, F.H. Schacher, B. Wang, D.E. Demco, A. Walther, Nacre-mimetics with synthetic nanoclays up to ultrahigh aspect ratios, Nat. Commun. 6 (2015) 1–14. https://doi.org/10.1038/ncomms6967.

[113] A. Liu, A. Walther, O. Ikkala, L. Belova, L.A. Berglund, Clay nanopaper with tough cellulose nanofiber matrix for fire retardancy and gas barrier functions, Biomacromolecules. 12 (2011) 633–641. https://doi.org/10.1021/bm101296z.

[114] J. Wang, Q. Cheng, L. Lin, L. Chen, L. Jiang, Understanding the relationship of performance with nanofiller content in the biomimetic layered nanocomposites, Nanoscale. 5 (2013) 6356–6362. https://doi.org/10.1039/c3nr00801k.

[115] H. Bin Yao, Z.H. Tan, H.Y. Fang, S.H. Yu, Artificial nacre-like bionanocomposite films from the self-assembly of chitosan-montmorillonite hybrid building blocks, Angew. Chemie - Int. Ed. 49 (2010) 10127–10131. https://doi.org/10.1002/anie.201004748.

[116] B. Debelak, K. Lafdi, Use of exfoliated graphite filler to enhance polymer physical properties, Carbon N. Y. 45 (2007) 1727–1734. https://doi.org/10.1016/j.carbon.2007.05.010.

[117] H. Wu, L.T. Drzal, Graphene nanoplatelet paper as a light-weight composite with excellent electrical and thermal conductivity and good gas barrier properties, Carbon N. Y. 50 (2012) 1135–1145. https://doi.org/10.1016/j.carbon.2011.10.026.

[118] F. Cilento, A. Martone, M.G.P. Carbone, M. Giordano, C. Galiotis, Load transfer in high content graphite nanoplateles composites, AIP Conf. Proc. 2196 (2019). https://doi.org/10.1063/1.5140316.

[119] K.W. Putz, O.C. Compton, C. Segar, Z. An, S.T. Nguyen, L.C. Brinson, Evolution of order during vacuum-assisted self-assembly of graphene oxide paper and associated polymer nanocomposites, ACS Nano. 5 (2011) 6601–6609. https://doi.org/10.1021/nn202040c.

[120] P. Podsiadlo, Z. Tang, B.S. Shim, N.A. Kotov, Counterintuitive effect of molecular strength and role of molecular rigidity on mechanical properties of layer-by-layer assembled nanocomposites, Nano Lett. 7 (2007) 1224–1231.

https://doi.org/10.1021/nl0700649.

[121] N. Rehse, C. Wang, M. Hund, M. Geoghegan, R. Magerle, G. Krausch, Stability of thin polymer films on a corrugated substrate, Eur. Phys. J. E. 4 (2001) 69–76.

[122] M.H. Yang, S.Y. Hou, Y.L. Chang, A.C.M. Yang, Molecular recoiling in polymer thin film dewetting, Phys. Rev. Lett. 96 (2006) 1–4. https://doi.org/10.1103/PhysRevLett.96.066105.

[123] J. Zhao, S. Jiang, Q. Wang, X. Liu, X. Ji, B. Jiang, Effects of molecular weight, solvent and substrate on the dewetting morphology of polystyrene films, Appl. Surf. Sci. 236 (2004) 131–140. https://doi.org/10.1016/j.apsusc.2004.04.019.

[124] Z. An, O.C. Compton, K.W. Putz, L.C. Brinson, S.T. Nguyen, Bio-inspired borate cross-linking in ultra-stiff graphene oxide thin films, Adv. Mater. 23 (2011) 3842–3846. https://doi.org/10.1002/adma.201101544.

[125] Z. An, O.C. Compton, K.W. Putz, L.C. Brinson, S.T. Nguyen, Bio-inspired borate cross-linking in ultra-stiff graphene oxide thin films, Adv. Mater. 23 (2011) 3842–3846. https://doi.org/10.1002/adma.201101544.

[126] S. Park, K.S. Lee, G. Bozoklu, W. Cai, S.B.T. Nguyen, R.S. Ruoff, Graphene oxide papers modified by divalent ions - Enhancing mechanical properties via chemical cross-linking, ACS Nano. 2 (2008) 572–578. https://doi.org/10.1021/nn700349a.

[127] Y. Gao, L.Q. Liu, S.Z. Zu, K. Peng, D. Zhou, B.H. Han, Z. Zhang, The effect of interlayer adhesion on the mechanical behaviors of macroscopic graphene oxide papers, ACS Nano. 5 (2011) 2134–2141. https://doi.org/10.1021/nn103331x.

[128] D.A. Dikin, S. Stankovich, E.J. Zimney, R.D. Piner, G.H.B. Dommett, G. Evmenenko, S.T. Nguyen, R.S. Ruoff, Preparation and characterization of graphene oxide paper, Nature. 448 (2007) 457–460. https://doi.org/10.1038/nature06016.

[129] K. Chen, X. Tang, Y. Yue, H. Zhao, L. Guo, Strong and Tough Layered Nanocomposites with Buried Interfaces, ACSNano. 10 (2016) 4816–4827. https://doi.org/10.1021/acsnano.6b01752.

[130] K. Krishnamoorthy, M. Veerapandian, K. Yun, S.-J. Kim, The chemical and structural analysis of graphene oxide with different degrees of oxidation, Carbon N. Y. 53 (2013) 38–49. https://doi.org/https://doi.org/10.1016/j.carbon.2012.10.013.

[131] J. Kim, J. Cha, G.H. Jun, S.C. Yoo, S. Ryu, Fabrication of Graphene Nanoplatelet / Epoxy Nanocomposites for Lightweight and High-Strength Structural Applications, 1700412 (2018) 1–7. https://doi.org/10.1002/ppsc.201700412.

[132] S. Vadukumpully, J. Paul, N. Mahanta, S. Valiyaveettil, Flexible conductive graphene / poly (vinyl chloride) composite thin films with high mechanical strength and thermal stability, 9 (2010). https://doi.org/10.1016/j.carbon.2010.09.004.

[133] G. Li, X. Tian, X. Xu, C. Zhou, J. Wu, Q. Li, L. Zhang, F. Yang, Y. Li, Fabrication of robust and highly thermally conductive nano fi brillated cellulose / graphite nanoplatelets composite papers, 138 (2017) 179–185. https://doi.org/10.1016/j.compscitech.2016.12.001.

[134] S.G. Prolongo, R. Moriche, A. Jiménez-Suárez, M. Sánchez, A. Ureña, Advantages and disadvantages of the addition of graphene nanoplatelets to epoxy resins, Eur. Polym. J. 61 (2014) 206–214. https://doi.org/10.1016/j.eurpolymj.2014.09.022.

[135] J. Malho, A. Walther, O. Ikkala, M.B. Linder, Facile Method for Stiff, Tough, and Strong Nanocomposites by Direct Exfoliation of Multilayered Graphene into Native Nanocellulose Matrix, (2012). https://doi.org/10.1021/bm2018189.

[136] S. Wan, Q. Zhang, X. Zhou, D. Li, B. Ji, L. Jiang, Q. Cheng, Fatigue Resistant Bioinspired Composite from Synergistic Two-Dimensional Nanocomponents, ACSNano. 11 (2017) 7074–7083. https://doi.org/10.1021/acsnano.7b02706.

[137] J. Wang, J. Qiao, J. Wang, Y. Zhu, L. Jiang, Bioinspired Hierarchical Alumina − Graphene Oxide − Poly(vinyl alcohol) Arti fi cial Nacre with Optimized Strength and Toughness, (2015). https://doi.org/10.1021/acsami.5b02194.

[138] J. Duan, S. Gong, Y. Gao, X. Xie, L. Jiang, Q. Cheng, Bioinspired Ternary Artificial Nacre Nanocomposites Based on Reduced Graphene Oxide and Nano fibrillar Cellulose, ACS Appl. Mater. Interfaces. 8 (2016) 10545–10550. https://doi.org/10.1021/acsami.6b02156.

[139] S. Gong, W. Cui, Q. Zhang, A. Cao, L. Jiang, Q. Cheng, Integrated Ternary Bioinspired Nanocomposites via Synergistic Toughening of Reduced Graphene Oxide and Double-Walled Carbon Nanotubes, (2015) 11568–11573. https://doi.org/10.1021/acsnano.5b05252.

[140] P. Ming, Z. Song, S. Gong, Y. Zhang, J. Duan, Q. Zhang, L. Jiang, Q. Cheng, Nacre-inspired integrated nanocomposites with fire retardant properties by graphene oxide and, J. Mater. Chem. A Mater. Energy Sustain. 3 (2015) 21194–21200. https://doi.org/10.1039/C5TA05742F.

[141] P. Li, H. Shen, Z. Qian, X. Yang, N. Zhao, C. Zhu, Facile fabrication of flexible layered GO / BNNS composite films with high thermal conductivity, J. Mater. Sci. 53 (2018)

4189–4198. https://doi.org/10.1007/s10853-017-1867-y.

[142] Z. Liu, J. Li, X. Liu, Novel Functionalized BN Nanosheets/Epoxy Composites with Advanced Thermal Conductivity and Mechanical Properties, ACS Appl. Mater. Interfaces. 12 (2020) 6503–6515. https://doi.org/10.1021/acsami.9b21467.

[143] N. Song, D. Jiao, S. Cui, X. Hou, P. Ding, L. Shi, Highly Anisotropic Thermal Conductivity of Layer-by-Layer Assembled Nano fi brillated Cellulose/Graphene Nanosheets Hybrid Films for Thermal Management, (2017). https://doi.org/10.1021/acsami.6b11979.

[144] H. Wang, S. Wang, W. Lu, M. Li, Y. Gu, Y. Zhang, Z. Zhang, Through-thickness thermal conductivity enhancement of graphite film/epoxy composite via short duration acidizing modification, Appl. Surf. Sci. 442 (2018) 170–177. https://doi.org/10.1016/j.apsusc.2018.02.125.

[145] X. Tian, M.E. Itkis, E.B. Bekyarova, R.C. Haddon, Anisotropic Thermal and Electrical Properties of Thin Thermal Interface Layers of Graphite Nanoplatelet-Based, (2013) 1–6. https://doi.org/10.1038/srep01710.

[146] P. Kumar, S. Yu, F. Shahzad, S. Man, Y. Kim, C. Min, Ultrahigh electrically and thermally conductive self-aligned graphene / polymer composites using large-area reduced graphene oxides, Carbon N. Y. 101 (2016) 120–128. https://doi.org/10.1016/j.carbon.2016.01.088.

[147] G. Xin, H. Sun, T. Hu, H.R. Fard, X. Sun, N. Koratkar, T. Borca-tasciuc, J. Lian, Large-Area Freestanding Graphene Paper for Superior Thermal Management, (2014) 4521–4526. https://doi.org/10.1002/adma.201400951.

[148] X. Huang, T. Leng, X. Zhang, J.C. Chen, K.H. Chang, A.K. Geim, K.S. Novoselov, Z. Hu, Binder-free highly conductive graphene laminate for low cost printed radio frequency applications, Appl. Phys. Lett. 106 (2015) 19–23. https://doi.org/10.1063/1.4919935.

[149] Y. Huang, Q. Gong, Q. Zhang, Y. Shao, J. Wang, Y. Jiang, M. Zhao, D. Zhuang, J. Liang, Fabrication and molecular dynamics analyses of highly thermal conductive reduced graphene oxide films at ultra-high temperatures, Nanoscale. 9 (2017) 2340–2347. https://doi.org/10.1039/c6nr06653d.

[150] C. Teng, D. Xie, J. Wang, Z. Yang, G. Ren, Y. Zhu, Ultrahigh Conductive Graphene Paper Based on Ball-Milling Exfoliated Graphene, Adv. Funct. Mater. 27 (2017) 1–7. https://doi.org/10.1002/adfm.201700240.

[151] Z. Tan, H. Xu, B. Zhou, Z. Qi, Y. Qu, Y. Zhu, Planar lighting from optimized graphite papers made of graphite oxide, Appl. Phys. Lett. 110 (2017) 1–5. https://doi.org/10.1063/1.4984132.

[152] C. Teng, C.M. Ma, C. Lu, S. Yang, S. Lee, M. Hsiao, M. Yen, K. Chiou, T. Lee, Thermal conductivity and structure of non-covalent functionalized graphene / epoxy composites, Carbon N. Y. 49 (2011) 5107–5116. https://doi.org/10.1016/j.carbon.2011.06.095.

[153] K.M.F. Shahil, A.A. Balandin, Graphene − Multilayer Graphene Nanocomposites as Highly Efficient Thermal Interface Materials, Nano Lett. 12 (2012) 861–867. https://doi.org/10.1021/nl203906r.

[154] D. Zhu, Y. Qi, L. Chen, M. Wang, H. Xie, Enhanced Thermal Conductivity for Graphene Nanoplatelets / Epoxy Resin Composites, J. Therm. Sci. Eng. Appl. 10 (2018) 1–5. https://doi.org/10.1115/1.4036796.

[155] H. Li, S. Dai, J. Miao, X. Wu, N. Chandrasekharan, H. Qiu, J. Yang, Enhanced thermal conductivity of graphene/polyimide hybrid film via a novel "molecular welding" strategy, Carbon N. Y. 126 (2018) 319–327. https://doi.org/10.1016/j.carbon.2017.10.044.

[156] I. Tseng, J. Chang, S. Huang, M. Tsai, Enhanced thermal conductivity and dimensional stability of flexible polyimide nanocomposite film by addition of functionalized graphene oxide, Polym Int. 62 (2013) 827–835. https://doi.org/10.1002/pi.4375.

[157] Y. Yao, X. Zeng, F. Wang, R. Sun, J. Xu, C. Wong, Significant Enhancement of Thermal Conductivity in Bioinspired Freestanding Boron Nitride Papers Filled with Graphene Oxide, Chem. Mater. 28 (2016). https://doi.org/10.1021/acs.chemmater.5b04187.

[158] D. Hu, W. Gong, J. Di, D. Li, R. Li, W. Lu, B. Gu, B. Sun, Q. Li, Strong graphene-interlayered carbon nanotube fi lms with high thermal conductivity, 118 (2017) 659–665. https://doi.org/10.1016/j.carbon.2017.04.005.

[159] P. Das, J.M. Malho, K. Rahimi, F.H. Schacher, B. Wang, D.E. Demco, A. Walther, Nacre-mimetics with synthetic nanoclays up to ultrahigh aspect ratios, Nat. Commun. 6 (2015) 1–14. https://doi.org/10.1038/ncomms6967.

[160] W.B. Park, P. Bandyopadhyay, T.T. Nguyen, T. Kuila, N.H. Kim, J.H. Lee, Effect of high molecular weight polyethyleneimine functionalized graphene oxide coated polyethylene terephthalate film on the hydrogen gas barrier properties, Compos. Part B Eng. 106 (2016) 316–323. https://doi.org/https://doi.org/10.1016/j.compositesb.2016.09.048.

[161] H. Liu, T. Kuila, N.H. Kim, B.-C. Ku, J.H. Lee, In situ synthesis of the reduced graphene oxide–polyethyleneimine composite and its gas barrier properties, J. Mater. Chem. A. 1 (2013) 3739–3746. https://doi.org/10.1039/C3TA01228J.

[162] S.C. Mun, J.J. Park, Y.T. Park, D.Y. Kim, S.W. Lee, M. Cobos, S.J. Ye, C.W. Macosko, O. Ok Park, High electrical conductivity and oxygen barrier property of polymer-stabilized graphene thin films, Carbon N. Y. 125 (2017) 492–499. https://doi.org/10.1016/j.carbon.2017.09.088.

[163] D. Zhuo, R. Wang, L. Wu, Y. Guo, L. Ma, Z. Weng, J. Qi, Flame Retardancy Effects of Graphene Nanoplatelet / Carbon Nanotube Hybrid Membranes on Carbon Fiber Reinforced Epoxy Composites, J. Nanomater. (2013) 1–7. https://doi.org/http://dx.doi.org/10.1155/2013/820901.

[164] F. Carosio, F. Cuttica, L. Medina, L.A. Berglund, Clay nanopaper as multifunctional brick and mortar fire protection coating-Wood case study, Mater. Des. 93 (2016) 357–363. https://doi.org/10.1016/j.matdes.2015.12.140.

[165] Y. Li, H. Zhang, Y. Liu, H. Wang, Z. Huang, T. Peijs, E. Bilotti, Synergistic effects of spray-coated hybrid carbon nanoparticles for enhanced electrical and thermal surface conductivity of CFRP laminates, Compos. Part A Appl. Sci. Manuf. 105 (2018) 9–18. https://doi.org/10.1016/j.compositesa.2017.10.032.

[166] B. Wang, Y. Duan, Z. Xin, X. Yao, D. Abliz, G. Ziegmann, Fabrication of an enriched graphene surface protection of carbon fiber/epoxy composites for lightning strike via a percolating-assisted resin film infusion method, Compos. Sci. Technol. 158 (2018) 51–60. https://doi.org/10.1016/j.compscitech.2018.01.047.

[167] I. Gaztelumendi, M. Chapartegui, R. Seddon, S. Flórez, F. Pons, J. Cinquin, Enhancement of electrical conductivity of composite structures by integration of carbon nanotubes via bulk resin and/or buckypaper films, Compos. Part B Eng. 122 (2017) 31–40. https://doi.org/10.1016/j.compositesb.2016.12.059.

[168] J. Li, S. Wang, L. Lai, P. Liu, H. Wu, J. Xu, S.J. Severtson, W.-J. Wang, Synergistic enhancement of gas barrier and aging resistance for biodegradable films with aligned graphene nanosheets, Carbon N. Y. 172 (2021) 31–40. https://doi.org/https://doi.org/10.1016/j.carbon.2020.09.071.

[169] C. Leone, S. Genna, F. Bertocchi, M. Giordano, A. Martone, A procedure to measure the emissivity of ultra-thin graphene based film in long wavelength infrared (LWIR) spectrum region, Optics and Lasers in Engineering, Opt. Laser Technol. 138 (2021)

106910. https://doi.org/10.1016/j.optlastec.2020.106910.

[170] Q.F. Guan, H. Bin Yang, C.H. Yin, Z.M. Han, K.P. Yang, Z.C. Ling, S.H. Yu, Nacre-Inspired Sustainable Coatings with Remarkable Fire-Retardant and Energy-Saving Cooling Performance, ACS Mater. Lett. 3 (2021) 243–248. https://doi.org/10.1021/acsmaterialslett.0c00509.

[171] Y.-C. Wang, T.-K. Huang, S.-H. Tung, T.-M. Wu, J.-J. Lin, Self-assembled clay films with a platelet–void multilayered nanostructure and flame-blocking properties, Sci. Rep. 3 (2013) 2621. https://doi.org/10.1038/srep02621.

[172] A. Liu, L.A. Berglund, Clay nanopaper composites of nacre-like structure based on montmorrilonite and cellulose nanofibers — Improvements due to chitosan addition, Carbohydr. Polym. 87 (2012) 53–60. https://doi.org/10.1016/j.carbpol.2011.07.019.

[173] J. Gao, Q. Yan, L. Lv, X. Tan, J. Ying, K. Yang, Lightweight thermal interface materials based on hierarchically strucntured graphene paper with superior through-plane thermal conductivity, Chem. Eng. J. 419 (2021). https://doi.org/10.1016/j.cej.2021.129609.

[174] D. Jeon, S.H. Kim, W. Choi, C. Byon, An experimental study on the thermal performance of cellulose-graphene-based thermal interface materials, Int. J. Heat Mass Transf. 132 (2019) 944–951. https://doi.org/10.1016/j.ijheatmasstransfer.2018.12.061.

[175] Love, Fältström, Graphite sheets and graphite gap pads used as thermal interface materials, 2014.

[176] S. Das, S. Sharma, T. Yokozeki, S. Dhakate, Conductive layer-based multifunctional structural composites for electromagnetic interference shielding, Compos. Struct. 261 (2021). https://doi.org/10.1016/j.compstruct.2020.113293.

[177] S. Geetha, K.K. Satheesh Kumar, C.R.K. Rao, M. Vijayan, D.C. Trivedi, EMI shielding: Methods and materials—A review, J. Appl. Polym. Sci. 112 (2009) 2073–2086. https://doi.org/https://doi.org/10.1002/app.29812.

[178] R.M. Simon, Emi Shielding Through Conductive Plastics, Polym. Plast. Technol. Eng. 17 (1981) 1–10. https://doi.org/10.1080/03602558108067695.

[179] Z. Barani, F. Kargar, A. Mohammadzadeh, S. Naghibi, C. Lo, B. Rivera, A.A. Balandin, Multifunctional Graphene Composites for Electromagnetic Shielding and Thermal Management at Elevated Temperatures, Adv. Electron. Mater. 6 (2020) 1–12. https://doi.org/10.1002/aelm.202000520.

[180] I. Ud Din, K. Naresh, R. Umer, K.A. Khan, L.T. Drzal, M. Haq, W.J. Cantwell, Processing and out-of-plane properties of composites with embedded graphene paper

for EMI shielding applications, Compos. Part A Appl. Sci. Manuf. 134 (2020) 105901. https://doi.org/10.1016/j.compositesa.2020.105901.

[181] S. Parida, R. Parida, B. Parida, S.K. Srivastava, N.C. Nayak, Exfoliated graphite nanoplatelet (xGnP) filled EVA/EOC blends nanocomposites for efficient microwave absorption in the S-band (2–4 GHz), Compos. Sci. Technol. 207 (2021) 108716. https://doi.org/10.1016/j.compscitech.2021.108716.

[182] Q. Gao, Y. Pan, G. Zheng, C. Liu, C. Shen, X. Liu, Flexible multilayered MXene/thermoplastic polyurethane films with excellent electromagnetic interference shielding, thermal conductivity, and management performances, Adv. Compos. Hybrid Mater. (2021). https://doi.org/10.1007/s42114-021-00221-4.

[183] J. Li, L. Huang, Y. Yuan, Y. Li, X. He, Mechanically strong, thermally conductive and flexible graphene composite paper for exceptional electromagnetic interference shielding, Mater. Sci. Eng. B Solid-State Mater. Adv. Technol. 263 (2021) 114893. https://doi.org/10.1016/j.mseb.2020.114893.

[184] D. Lai, X. Chen, Y. Wang, Controllable fabrication of elastomeric and porous graphene films with superior foldable behavior and excellent electromagnetic interference shielding performance, Carbon N. Y. 158 (2020) 728–737. https://doi.org/10.1016/j.carbon.2019.11.047.

[185] I. Machado, I. Hsieh, V. Calado, T. Chapin, H. Ishida, Nacre-Mimetic Green Flame Retardant: Ultra-High Nanofiller Content, Thin Nanocomposite as an Effective Flame Retardant, Polym. . 12 (2020). https://doi.org/10.3390/polym12102351.

[186] D. Zhuo, R. Wang, L. Wu, Y. Guo, L. Ma, Z. Weng, J. Qi, Flame Retardancy Effects of Graphene Nanoplatelet / Carbon Nanotube Hybrid Membranes on Carbon Fiber Reinforced Epoxy Composites, J. Nanomater. 2013 (2013). https://doi.org/http://dx.doi.org/10.1155/2013/820901.

[187] V. Kumar, S. Sharma, A. Pathak, B.P. Singh, S.R. Dhakate, T. Yokozeki, T. Okada, T. Ogasawara, Interleaved MWCNT buckypaper between CFRP laminates to improve through-thickness electrical conductivity and reducing lightning strike damage, Compos. Struct. 210 (2019) 581–589. https://doi.org/https://doi.org/10.1016/j.compstruct.2018.11.088.

[188] J. Liang, Y. Huang, L. Zhang, Y. Wang, Y. Ma, T. Cuo, Y. Chen, Molecular-level dispersion of graphene into poly(vinyl alcohol) and effective reinforcement of their nanocomposites, Adv. Funct. Mater. 19 (2009) 2297–2302.

https://doi.org/10.1002/adfm.200801776.

[189] T. Cheng-An, Z. Hao, W. Fang, Z. Hui, Z. Xiaorong, W. Jianfang, Mechanical properties of Graphene Oxide/Polyvinyl Alcohol Composite Film, Polym. Polym. Compos. 25 (2017) 11–16. https://doi.org/10.1177/096739111702500102.

[190] NANESA, G2Nan - Technical Datasheet, (n.d.) 2–3.

[191] RTM6 - Technical Datasheet, Hexcel Corp. (2018) 1–4. https://www.hexcel.com/user_area/content_media/raw/HexFlowRTM6DataSheetPDF.pdf.

[192] ICAFLEX ADB562 - Technical datasheet, 520 (2015) 5–6.

[193] Vinnol® h 40/50 - Technical Datasheet, (2015) 9–11.

[194] ASTM D3418 - Standard Test Method for Transition Temperatures and Enthalpies of Fusion and Crystallization of Polymers by Differential Scanning Calorimetry, (n.d.).

[195] C. Formicola, Insight of thermo-mechanical and fire properties of an aerospace epoxy matrix loaded with micro and nano fillers . Insight of thermo-mechanical and fire properties of an aerospace epoxy matrix loaded with micro and nano fillers ., 2008.

[196] M.R. Ricciardi, F. Cristiano, F. Bertocchi, A. Martone, M. Giordano, Manufacturing and properties of biomimetic graphite nanoplatelets foils, Polym. Eng. Sci. 59 (2019) 2443–2448. https://doi.org/https://doi.org/10.1002/pen.25200.

[197] M.R. Ricciardi, A. Martone, F. Cristiano, F. Bertocchi, M. Giordano, Nacre-like composites made by graphite nanoplatelets, AIP Conf. Proc. 1981 (2018) 6–9. https://doi.org/10.1063/1.5045934.

[198] F. Cilento, A. Martone, M.G. Pastore Carbone, C. Galiotis, M. Giordano, Nacre-like GNP/Epoxy composites: Reinforcement efficiency vis-à-vis graphene content, Compos. Sci. Technol. 211 (2021) 108873. https://doi.org/10.1016/j.compscitech.2021.108873.

[199] A. Martone, C. Formicola, M. Giordano, M. Zarrelli, Reinforcement efficiency of multi-walled carbon nanotube/epoxy nano composites, Compos. Sci. Technol. 70 (2010) 1154–1160. https://doi.org/https://doi.org/10.1016/j.compscitech.2010.03.001.

[200] ASTM 3039, Standard Test Method for Tensile Properties of Polymer Matrix Composite Materials, ASTM Int. 35 (2002) 36–38.

[201] W.J. Parker, R.J. Jenkins, C.P. Butler, G.L. Abbott, Flash Method of Determining Thermal Diffusivity, Heat Capacity, and Thermal Conductivity, J. Appl. Phys. 32 (1961) 1679–1684. https://doi.org/10.1063/1.1728417.

[202] ASTM E1461, Standard Test Method for Thermal Diffusivity by the Flash Method,

(n.d.).

[203] G. Sheets, Panasonic - "PGS" Graphite Sheets, (2017). https://na.industrial.panasonic.com/products/thermal-management/thermal-management/thermal-management-products/series/pgs-graphite-sheet-ssm/AYA0002?reset=1.

[204] W.J. and S. Bird R. B., Stewart W. E., and Lightfoot E. N., Transport phenomena, AIChE J. 7 (1961) 268. https://doi.org/doi:10.1002/aic.690070245.

[205] S. Pandit, K. Gaska, V.R.S.S. Mokkapati, E. Celauro, A. Derouiche, S. Forsberg, M. Svensson, R. Kádár, I. Mijakovic, Precontrolled Alignment of Graphite Nanoplatelets in Polymeric Composites Prevents Bacterial Attachment, Small. 16 (2020) 1–11. https://doi.org/10.1002/smll.201904756.

[206] ASTM D 790-17, Standard Test Methods for Flexural Properties of Unreinforced and Reinforced Plastics and Electrical Insulating Materials1, (2017).

[207] I.M. Robinson, M.J. Zakikhani, R.J. Day, R.J. Young, C. Galiotis, Strain dependence of the Raman frequencies for different types of carbon fibres, J. Mater. Sci. Lett. 6 (1987) 1212–1214.

[208] B. Schrader, Infrared and Raman spectroscopy: methods and applications, John Wiley & Sons, 2008.

[209] P. Larkin, Infrared and Raman spectroscopy: principles and spectral interpretation Elsevier, 2011.

[210] C. Kittel, P. McEuen, P. McEuen, Introduction to solid state physics, Wiley New York, 1996.

[211] I.R. Lewis, H. Edwards, Handbook of Raman spectroscopy: from the research laboratory to the process line, CRC press, 2001.

[212] D.A. Long, D.A. Long, Raman spectroscopy, McGraw-Hill New York, 1977.

[213] K. Tashiro, W. Gang, M. Kobayashi, Quasiharmonic Treatment of Infrared and Raman Vibrational Frequency Shifts Induced by Tensile Deformation of Polymer Chains, J. Polym. Sci. Part B Polym. Phys. 28 (1990) 2527–2553.

[214] R.P. Wool, Infrared Studies of Deformation in Semicrystalline Polymers, Polym. Eng. Sci. 20 (1980) 805–815.

[215] R.S. Bretzlaff, R.P. Wool, Frequency Shifting and Asymmetry in Infrared Bands of Stressed Polymers, Macromolecules. 16 (1983) 1907–1917. https://doi.org/10.1021/ma00246a019.

[216] C. Galiotis, R.J. Young, D.N. Batchelder, A resonance Raman spectroscopic study of the strength of the bonding between an epoxy resin and a polydiacetylene fibre, J. Mater. Sci. Lett. 2 (1983) 263–266.

[217] G. Gouadec, P. Colomban, Raman Spectroscopy of nanomaterials : How spectra relate to disorder , particle size and mechanical properties, Prog. Cryst. Growth Charact. Mater. 53 (2007) 1–56. https://doi.org/10.1016/j.pcrysgrow.2007.01.001.

[218] C. Galiotis, A. Paipetis, C. Marston, Unification of fibre/matrix interfacial measurements with Raman microscopy, J. Raman Spectrosc. 30 (1999) 899–912.

[219] C. Galiotis, Interfacial Studies on Model Composites by Laser Raman Spectroscopy, Compos. Sci. Technol. 42 (1991) 125–150.

[220] V.K. Mitra, W.M. Risen Jr, R.H. Baughman, A laser Raman study of the stress dependence of vibrational frequencies of a monocrystalline polydiacetylene, J. Chem. Phys. 66 (1977) 2731–2736.

[221] R.J. Young, Polymer single crystal fibres, in: Dev. Oriented Polym., Springer, 1987: pp. 1–38.

[222] C. Galiotis, R.J. Young, P.H.J. Yeung, D.N. Batchelder, The study of model polydiacetylene/epoxy composites, J. Mater. Sci. 19 (1984) 3640–3648.

[223] A.C. Ferrari, J.C. Meyer, V. Scardaci, C. Casiraghi, M. Lazzeri, S. Piscanec, K.S. Novoselov, S. Roth, A.K. Geim, The Raman Fingerprint of Graphene, 1 (2008) 1–5.

[224] A.C. Ferrari, J.C. Meyer, V. Scardaci, C. Casiraghi, M. Lazzeri, F. Mauri, S. Piscanec, D. Jiang, K.S. Novoselov, S. Roth, A.K. Geim, Raman Spectrum of Graphene and Graphene Layers, Phys. Rev. Lett. 187401 (2006) 1–4. https://doi.org/10.1103/PhysRevLett.97.187401.

[225] A. Kaniyoor, S. Ramaprabhu, A Raman spectroscopic investigation of graphite oxide derived graphene, Aip Adv. 2 (2012) 32183.

[226] A.C. Ferrari, J. Robertson, Interpretation of Raman spectra of disordered and amorphous carbon, Phys. Rev. B. 61 (2000) 14095.

[227] F. Tuinstra, J.L. Koenig, Raman Spectrum of Graphite, J. Chem. Phys. 53 (1970) 1126–1130. https://doi.org/10.1063/1.1674108.

[228] R.J. Nemanich, S.A. Solin, First-and second-order Raman scattering from finite-size crystals of graphite, Phys. Rev. B. 20 (1979) 392.

[229] R.P. Vidano, D.B. Fischbach, L.J. Willis, T.M. Loehr, Observation of Raman band shifting with excitation wavelength for carbons and graphites, Solid State Commun. 39

(1981) 341–344.

[230] T.M.G. Mohiuddin, A. Lombardo, R.R. Nair, A. Bonetti, G. Savini, R. Jalil, N. Bonini, D.M. Basko, C. Galiotis, N. Marzari, Uniaxial strain in graphene by Raman spectroscopy: G peak splitting, Grüneisen parameters, and sample orientation, Phys. Rev. B. 79 (2009) 205433.

[231] L. Gong, R.J. Young, I.A. Kinloch, I. Riaz, R. Jalil, K.S. Novoselov, Optimizing the Reinforcement of Polymer-Based Nanocomposites by Graphene, ACSNano. 6 (2012) 2086–2095. https://doi.org/10.1021/nn203917d.

[232] R.J. Young, M. Liu, I.A. Kinloch, S. Li, X. Zhao, C. Vallés, D.G. Papageorgiou, The mechanics of reinforcement of polymers by graphene nanoplatelets, Compos. Sci. Technol. 154 (2018) 110–116. https://doi.org/10.1016/j.compscitech.2017.11.007.

[233] S.R. Ahmad, C. Xue, R.J. Young, The mechanisms of reinforcement of polypropylene by graphene nanoplatelets, Mater. Sci. Eng. B. (2016). https://doi.org/10.1016/j.mseb.2016.10.003.

[234] O. Frank, M. Bouša, I. Riaz, R. Jalil, K.S. Novoselov, G. Tsoukleri, J. Parthenios, L. Kavan, K. Papagelis, C. Galiotis, Phonon and structural changes in deformed Bernal stacked bilayer graphene, Nano Lett. 12 (2012) 687–693.

[235] M. Huang, H. Yan, C. Chen, D. Song, T.F. Heinz, J. Hone, Phonon softening and crystallographic orientation of strained graphene studied by Raman spectroscopy, Proc. Natl. Acad. Sci. 106 (2009) 7304–7308.

[236] I. Crivelli Visconti, G. Caprino, A. Langella, Materiali compositi, Hoepli, 2009.

[237] H. Krenchel, Fibre Reinforcement Akademisk Forlag, Copenhagen, Denmark. (1964).

[238] H. Liu, L.C. Brinson, Reinforcing efficiency of nanoparticles: A simple comparison for polymer nanocomposites, Compos. Sci. Technol. 68 (2008) 1502–1512.

[239] Z. Li, R.J. Young, I.A. Kinloch, N.R. Wilson, A.J. Marsden, A.P.A. Raju, Quantitative determination of the spatial orientation of graphene by polarized Raman spectroscopy, Carbon N. Y. 88 (2015) 215–224.

[240] Z. Li, J. Chu, C. Yang, S. Hao, M.A. Bissett, I.A. Kinloch, R.J. Young, Effect of functional groups on the agglomeration of graphene in nanocomposites, Compos. Sci. Technol. 163 (2018) 116–122.

[241] M. Omidi, H.R.D. T, R.J. Seethaler, R. Arasteh, Prediction of the mechanical characteristics of multi-walled carbon nanotube / epoxy composites using a new form of the rule of mixtures, Carbon N. Y. 48 (2010) 3218–3228.

https://doi.org/10.1016/j.carbon.2010.05.007.

[242] C. Androulidakis, E.N. Koukaras, J. Rahova, K. Sampathkumar, J. Parthenios, K. Papagelis, O. Frank, C. Galiotis, Wrinkled few-layer graphene as highly efficient load bearer, ACS Appl. Mater. Interfaces. 9 (2017) 26593–26601.

[243] H.L. Cox, The elasticity and strength of paper and other fibrous materials, Br. J. Appl. Phys. 3 (1952) 72–79.

[244] A. Kelly, Fibre reinforcement, Strong Solids. (1966) 121–163.

[245] S.P. Kotha, S. Kotha, N. Guzelsu, A shear-lag model to account for interaction effects between inclusions in composites reinforced with rectangular platelets, Compos. Sci. Technol. 60 (2000) 2147–2158.

[246] J.C. Halpin, J.L. Kardos, The Halpin-Tsai equations: a review, Polym. Eng. Sci. 16 (1976) 344–352.

[247] T. Mori, K. Tanaka, Average stress in matrix and average elastic energy of materials with misfitting inclusions, Acta Metall. 21 (1973) 571–574.

[248] E.T. Thostenson, T.-W. Chou, On the elastic properties of carbon nanotube-based composites: modelling and characterization, J. Phys. D. Appl. Phys. 36 (2003) 573.

[249] L.E. Nielsen, Simple Theory of Stress-Strain Properties of Filled Polymers, J. Appl. Polym. Sci. 10 (1966) 97–103.

[250] L.E. Nielsen, Mechanical Properties of Polymer and Composites, 1994.

[251] M.R. Begley, N.R. Philips, B.G. Compton, D. V. Wilbrink, R.O. Ritchie, M. Utz, Micromechanical models to guide the development of synthetic "brick and mortar" composites, J. Mech. Phys. Solids. 60 (2012) 1545–1560. https://doi.org/10.1016/j.jmps.2012.03.002.

[252] W. Wu, K. Sadeghipour, K. Boberick, G. Baran, Predictive modeling of elastic properties of particulate-reinforced composites, Mater. Sci. Eng. A332 (2002) 362–370.

[253] B. Bhushan, Biomimetics: bioinspired hierarchical-structured surfaces for green science and technology, Springer, 2016.

[254] M.G.P. Carbone, D. Tammaro, A.C. Manikas, G. Paterakis, E. Di Maio, C. Galiotis, Wettability of graphene by molten polymers, Polymer (Guildf). 180 (2019) 121708.

[255] N. Melanitis, C. Galiotis, Interfacial micromechanics in model composites using laser Raman spectroscopy, Proc. R. Soc. London. Ser. A Math. Phys. Sci. 440 (1993) 379–398.

[256] G.E. Padawer, N. Beecher, On the strength and stiffness of planar reinforced plastic

resins, Polym. Eng. Sci. 10 (1970) 185–192.

[257] G. Decher, J.B. Schlenoff, Multilayer thin films: sequential assembly of nanocomposite materials, John Wiley & Sons, 2006.

[258] L. Xue, Y. Han, Inhibition of dewetting of thin polymer films, Prog. Mater. Sci. 57 (2012) 947–979. https://doi.org/10.1016/j.pmatsci.2012.01.003.

[259] Z. Liu, S.-M. Zhang, J.-R. Yang, J.Z. Liu, Y.-L. Yang, Q.-S. Zheng, Interlayer shear strength of single crystalline graphite, Acta Mech. Sin. 28 (2012) 978–982.

[260] F. RozpAlocha, J. Patyka, J. Stankowskib, Graphenes bonding forces in graphite, (2007).

[261] M. Yekta-Fard, A.B. Ponter, Factors affecting the wettability of polymer surfaces, J. Adhes. Sci. Technol. 6 (1992) 253–277.

[262] J. Zhao, L. Yang, F. Li, R. Yu, C. Jin, Structural evolution in the graphitization process of activated carbon by high-pressure sintering, Carbon N. Y. 47 (2009) 744–751.

[263] A.P. Mouritz, A.G. Gibson, Fire Properties of Polymer Composite Materials, Springer, 2006.

[264] S. Feih, A.P. Mouritz, Z. Mathys, A.G. Gibson, Fire structural modeling of polymer composites with passive thermal barrier, J. Fire Sci. 28 (2010) 141–160. https://doi.org/10.1177/0734904109340878.

[265] P. Tran, Q.T. Nguyen, K.T. Lau, Fire performance of polymer-based composites for maritime infrastructure, Compos. Part B Eng. 155 (2018) 31–48. https://doi.org/10.1016/j.compositesb.2018.06.037.

[266] Y. Bai, T. Keller, High Temperature Performance of Polymer Composites, Wiley, Wiley-VCH Verlag GmbH & Co. KGaA, Singapore, 2013. https://doi.org/10.1002/9783527654147.

[267] E. Kandare, B.K. Kandola, P. Myler, Evaluating the influence of varied fire-retardant surface coatings on post-heat flexural properties of glass/epoxy composites, Fire Saf. J. 58 (2013) 112–120. https://doi.org/https://doi.org/10.1016/j.firesaf.2013.01.009.

[268] E. Kandare, B.K. Kandola, P. Myler, G. Edwards, Thermo-mechanical Responses of Fiber-reinforced Epoxy Composites Exposed to High Temperature Environments. Part I: Experimental Data Acquisition, J. Compos. Mater. 44 (2010) 3093–3114. https://doi.org/10.1177/0021998310373511.

[269] Á. Pomázi, A. Toldy, Particle Distribution of Solid Flame Retardants in Infusion Moulded Composites, Polym. . 9 (2017). https://doi.org/10.3390/polym9070250.

[270] ISO, ISO 5660-1: Reaction-to-fire tests — Heat release, smoke production and mass loss rate - Part 1: Heat release rate (cone calorimeter method), Int. Stand. (2002).

[271] AC 20-135 Powerplant installation and propulsion system component fire protection test methods, Standard and criteria, Fed. Aviat. Adm. USA. (1990).

[272] B. Schartel, T.R. Hull, Development of fire-retarded materials—Interpretation of cone calorimeter data, Fire Mater. 31 (2007) 327–354. https://doi.org/https://doi.org/10.1002/fam.949.

[273] B. Schartel, M. Bartholmai, U. Knoll, Some comments on the use of cone calorimeter data, Polym. Degrad. Stab. 88 (2005) 540–547. https://doi.org/10.1016/j.polymdegradstab.2004.12.016.

[274] Fabrizia Cilento, C. Leone, S. Genna, M. Giordano, A. Martone, Protection from high-power radiative flux of Carbon Fiber Reinforced Plastic by Graphene NanoPlatelet - based coating, Compos. Part B Eng. (n.d.) Submitted June 2021.

[275] W. Liang, A.O. Bonsu, H. Lv, B. Yang, C. Liu, J. Deng, Intumescent coating thickness effect on the post-heat mechanical properties of composites, Structures. 28 (2020) 2056–2072. https://doi.org/https://doi.org/10.1016/j.istruc.2020.10.045.

[276] D.D. Jayaseelan, H. Jackson, E. Eakins, P. Brown, W.E. Lee, Laser modified microstructures in ZrB2, ZrB2/SiC and ZrC, J. Eur. Ceram. Soc. 30 (2010) 2279–2288. https://doi.org/10.1016/j.jeurceramsoc.2010.03.001.

[277] L. Larrimbe, M. Pettinà, K. Nikbin, E.L. Jones, A.P. Katz, C.J. Hawkins, J. DeCerbo, P. Brown, L.J. Vandeperre, M.A. White, High Heat Flux Laser Testing of HfB2 Cylinders, J. Am. Ceram. Soc. 100 (2017) 293–303. https://doi.org/10.1111/jace.14474.

[278] F. Monteverde, J.M. Cordoba, R. Savino, A. Cecere, S. Genna, C. Leone, Thermal stability under laser heating of hot-pressed (Hf1-X ZrX)B2/SiC powder mixtures obtained by mechano-synthesis, J. Eur. Ceram. Soc. 39 (2019) 4575–4587. https://doi.org/10.1016/j.jeurceramsoc.2019.06.050.

[279] L.C. Long, T.T. Wang, L.T. Liu, Tensile and compression test of carbon/epoxy composite laminate under combined action of laser irradiation and load, Mater. Res. Innov. 19 (2015) S9171–S9176. https://doi.org/10.1179/1432891715Z.0000000001953.

[280] F. Lacroix, V. Allheily, K. Diener, A. Eichhorn, M. Gillet, G. L'Hostis, Thermomechanical behavior of aeronautic structural carbon epoxy composite submitted to a laser irradiation, Compos. Struct. 143 (2016) 220–229. https://doi.org/10.1016/j.compstruct.2016.02.009.

[281] P. Nan, Z. Shen, B. Han, X. Ni, The influences of laminated structure on the ablation characteristics of carbon fiber composites under CW laser irradiation, Opt. Laser Technol. 116 (2019) 224–231. https://doi.org/10.1016/j.optlastec.2019.03.015.

[282] Y.X. Zhang, Z. Zhu, R. Joseph, I.J. Shihan, Damage to aircraft composite structures caused by directed energy system: A literature review, Def. Technol. (2020) In press, Available online 26 August 2020. https://doi.org/10.1016/j.dt.2020.08.008.

[283] J. Wolfrum, S. Eibl, E. Oeltjen, J. Osterholz, M. Wickert, High-energy laser effects on carbon fiber reinforced polymer composites with a focus on perforation time, J. Compos. Mater. Article fi (2021). https://doi.org/10.1177/0021998320988885.

[284] P.R. Griffiths, Infrared Emission Spectroscopy. I. Basic Considerations, Appl. Spectrosc. 26 (1972) 73–76. https://doi.org/10.1366/000370272774352650.

[285] G. Nikolic, S. Zlatkovic, M. Cakic, S. Cakic, C. Lacnjevac, Z. Rajic, Fast fourier transform IR characterization of epoxy GY systems crosslinked with aliphatic and cycloaliphatic EH polyamine adducts, Sensors. 10 (2010) 684–696. https://doi.org/10.3390/s100100684.

[286] P. Maity, S. V. Kasisomayajula, V. Parameswaran, S. Basu, N. Gupta, Improvement in surface degradation properties of polymer composites due to pre-processed nanometric alumina fillers, IEEE Trans. Dielectr. Electr. Insul. 15 (2008) 63–72. https://doi.org/10.1109/T-DEI.2008.4446737.

[287] J. Lee, M. Ju, O.H. Cho, Y. Kim, K.T. Nam, Tyrosine-Rich Peptides as a Platform for Assembly and Material Synthesis, Adv. Sci. News. 1801255 (2019). https://doi.org/10.1002/advs.201801255.

PUBLICATIONS

Fabrizia Cilento, Alfonso Martone, Francesco Cristiano, Alberto Fina, Michele Giordano, Effect of Matrix Content on Mechanical and Thermal Properties of High Graphene Content Composites" MATEC Web Conf., 303 (2019) 01002 DOI: https://doi.org/10.1051/matecconf/201930301002

Fabrizia Cilento, Alfonso Martone, Maria Giovanna Pastore Carbone, Michele Giordano, and Costas Galiotis , "Load transfer in high content graphite nanoplateles composites", AIP Conference Proceedings 2196, 020043 (2019) https://doi.org/10.1063/1.5140316

Fabrizia Cilento, Alfonso Martone, Maria Giovanna Pastore Carbone, Costas Galiotis, Michele Giordano, Nacre-like GNP/Epoxy Composites: Reinforcement Efficiency vis-à-vis Graphene Content, Composites Science and Technology, 2021, 108873, ISSN 0266-3538, https://doi.org/10.1016/j.compscitech.2021.108873

Fabrizia Cilento, Claudio Leone, Silvio Genna, Michele Giordano, Alfonso Martone, Protection from high-power radiative flux of Carbon Fiber Reinforced Plastic by Graphene NanoPlatelet -based coating, Composites Part B Engineering. Submitted (June 2021).